Mechanistic and Structural Insights into the Type VI Secretion System Tail of *Vibrio cholerae*

Inauguraldissertation

zur
Erlangung der Würde eines Doktors der Philosophie
vorgelegt der
Philosophisch-Naturwissenschaftlichen Fakultät
der Universität Basel

von
Maximilian Brackmann
aus Deutschland

BASEL, 2018

Genehmigt von der Philosophisch-Naturwissenschaftlichen Fakultät

auf Antrag von:

Prof. Dr. Marek Basler

Fakultätsverantwortlicher, Dissertationsleiter

Prof. Dr. Markus Seeger

Korreferent

Basel, den 20.06.2017

Prof. Dr. Martin Spiess

Dekan

Abstract

Bacteria use many different types of secretion systems to interact with and modulate their environment. Secretion systems are involved in these tasks with a wide variety of functions. Their substrate proteins mediate motility, phagosomal escape, host modulation or interbacterial competition. Various different mechanisms exist, how the transport across membranes is mediated. Some substrates are secreted in two steps, others in only one step. Some secretion systems just export their cargo into the extracellular medium, whereas others deliver their substrates under specific circumstances into other cells.

The Type VI Secretion System (T6SS) is the largest secretion system and can span the entire length of a bacterium. It contracts a long sheath and pushes an inner tube with associated effectors into a target cell. The tail is anchored to the cell envelope by a membrane complex and consists of sheath, tube and baseplate. The baseplate initiates polymerization of the sheath-tube complex and connects the sheath to the membrane complex.

The membrane complex is formed by the membrane proteins TssJ, TssL and TssM. TssJ is located in the outer membrane, whereas TssL and TssM are inner membrane proteins. The baseplate is formed by TssE, TssF, TssG and TssK. TssK connects the baseplate to the membrane complex. TssF and TssG form the baseplate wedge and TssE connects the sheath to the baseplate. The central part of the baseplate consists of VgrG and PAAR-proteins. A trimer of VgrG-proteins forms the spike and the monomeric Zinc-containing PAAR-protein forms the spike tip. The inner Hcp-tube polymerizes on VgrG and the sheath polymerizes on TssE and wraps around the Hcp-tube. Polymerization of the sheath is mediated by a TssA cap at the growing end of the sheath, opposite of the baseplate. The sheath is a six-start helix of TssB and TssC (VipA and VipB) and its protomers form an interlaced network that is essential for stability of the sheath. Presumably, the baseplate triggers contraction of the sheath, which leads to an increase in the helical twist, widening of the diameter and shortening of the length of the sheath. The contraction pushes the inner tube with the associated spike and effectors into target cells. The contracted sheath is specifically recognized by the AAA^{+}-protein ClpV that disassembles it.

In recent years our understanding regarding structure and function of the T6SS advanced rapidly. However, certain aspects are not yet understood. This thesis will address progress on understanding different aspects of the T6SS mostly from a structural and mechanistic perspective.

First, I will briefly describe other bacterial secretion systems and then present our findings on (i) the structure of the T6SS sheath in a contracted state, (ii) the mechanism of contraction of the sheath, (iii) the structure of the sheath in an extended state and (iv) structures of associated components, namely the baseplate and the cap.

We solved the structure of the T6SS-sheath in a contracted state, discovered that it forms an interlaced helix and that the interlacing linkers are important for its function. We also proposed how specificity of ClpV binding to the contracted sheath is achieved. Further targeted mutagenesis lead to a model of how sheath contraction is propagated through the sheath. Some mutations stabilized the sheath in an extended state and made it possible to isolate it. Extended sheaths contain the inner Hcp-tube. We then structurally characterized the extended sheath-tube assembly and gained further insights into the rearrangement of domains as well as a deeper understanding of the binding mode of ClpV. The extended sheaths were also specifically associated with proteins of the baseplate and the cap. We described the structural arrangement of baseplate proteins and the cap and gained first insights in the relative orientation with the sheath in a near-native assembly.

I will provide insights into the complete assembly of the cytosolic part of the T6SS. The knowledge about the T6SS that is presented here, can likely be transferred to related systems as contractile tailed phages or R-type pyocins.

Contents

CONTENTS

Chapter I

Introduction

I.1 Bacterial Secretion Systems

Bacteria interact with and manipulate their surroundings by the secretion of proteins. The bacterial envelope serves as a natural diffusion barrier and shields the bacteria against various factors. However, bacteria have to adhere to surfaces, be motile, sense their environment, import nutrients, export toxins, invade host tissues but also kill other bacteria and modulate eukaryotic cells in their surroundings. To circumvent the intrinsic challenge of transport through membranes, bacteria evolved a plethora of membrane channels and active transporters as well as secretion systems. The number of discovered protein secretion systems is still expanding and from 2006 to 2017, four new protein secretion systems have been discovered and await characterization.

Secretion of proteins across membranes is achieved by secretion systems. In the simplest case, a secretion system only consists of one membrane spanning protein whose primary purpose is the transport of a cognate cargo protein. Transported proteins are involved in many different processes and thus also have different fates. Some are secreted into the extracellular milieu, others reside on the outer membrane or reach their target in another cell. Some secretion systems are widespread between species and translocate a wide variety of target proteins whereas others are confined to fewer species or translocate a narrower spectrum of proteins. In the most extreme case, one secretion system translocates one protein. Additionally, several secretion systems of pathogenic bacteria are often required for pathogenesis and play crucial roles in manipulating the host cell in favor of the invading bacterium.

Historically, Gram-staining was used to divide bacteria into gram-negative and gram-positive, depending on if they are able to be stained (gram-positive) or not (gram-negative) [1]. Gram-staining relies on crystal violet that stains peptidoglycan and for many bacteria this is sufficient and enables easy classification, however, some bacteria, notably *Mycobacteria*, cannot be classified using Gram-staining. For the scope of this thesis, the term monoderm or diderm will be used instead to indicate if the bacterium discussed has one or two membranes, respectively [2,3].

Protein secretion in monoderm and diderm bacteria works fundamentally different, as in monoderm bacteria, proteins have to be transported through one membrane and pass a thick peptidoglycan layer whereas in diderm bacteria, a second membrane further complicates protein transport.

I.1 Protein Secretion across the Cytoplasmic Membrane

Protein secretion across the cytoplasmic membrane is achieved by the Secretion (Sec-) and Twin arginine translocation (Tat-) pathways [4,5]. The Sec-pathway is responsible for

transport of proteins across the membrane in an unfolded state, whereas the Tat-pathway transports proteins in a folded conformation. Both pathways recognize a signal sequence in the secretory protein. For the Tat-pathway, this is the presence of a 30 amino acid long N-terminal peptide containing a twin arginine motif and for Sec a 20 amino acid long N-terminal stretch without significant conservation, however, common characteristics can be deduced [6]. Both signal sequences have an n-region with a positive net charge, an h-region that is hydrophobic and has a certain propensity to form an α-helix and a short polar c-region, often followed by a peptidase cleavage site. Based on the signal sequence, substrates of both pathways can be predicted by online tools [7].

I.1.1 The Sec-Pathway

The Sec-pathway is an essential and universally conserved protein translocation pathway of the inner membrane [8–10]. Protein targeting towards the Sec-pathway already starts co-translationally and can be achieved by two different and independent mechanisms. Either SecB binds to the nascent polypeptide chain and stabilizes it in an unfolded conformation or targeting is mediated by the signal recognition particle (SRP). It appears that the final destination of the substrate dictates the pathway by which it is targeted to the Sec-translocon [11]. Whereas inner-membrane proteins are targeted via SRP, periplasmic and outer-membrane proteins rely on SecB [12–15].

SRP is a protein-RNA complex that binds nascent peptide chains at the exit tunnel of the ribosome and targets it to FtsY, an inner membrane-bound protein [13, 16–20]. FtsY serves as signal recognition particle receptor (SRP-R), recognizing SRP and delivers the nascent chain to the SecYEG complex where the target protein is inserted into the SecYEG-complex with the help of SecA [20,21]. SRP-mediated targeting to the SecYEG-complex leads to co-translational translocation of substrates and translocation is thought to be powered by the translating ribosome [22].

SecB is involved in the post-translational translocation of unfolded proteins and binds the N-terminal signal sequence of its target protein and directs it to the cytoplasmic protein SecA that in turn interacts with proteins of the translocation machinery SecYEG [23–25]. In this context, SecB serves as a chaperone and the ATPase SecA powers translocation of proteins through the SecYEG pathway in an ATP-dependent manner [26]. The SecYEG-complex forms the actual protein translocation channel in the cytoplasmic membrane that is formed mostly by isoleucines [27, 28]. The complex is an all α-helical structure in which SecY is the central protein, both for SecA-recognition as well as for formation of the protein conductive channel. SecY also plugs the structure to avoid leakage of other cellular components [27]. ATP-hydrolysis by SecA when bound to SecYEG

induces conformational changes in the protein translocation channel and prepares the channel for transport. The SecYEG complex is functional as a dimer (or higher order oligomer) and binds either one or two copies of SecA, however, the exact orientation of the SecYEG protomers towards each other remains unknown [22, 29–31]. Interestingly, both SecYEG subassemblies are involved in translocation, however, only one of them is actively translocating and the other subassembly has a supportive function [30, 32, 33]. In a first step of translocation, SecA binds to the SecYEG complex as well as to SecB, which is bound to the secretory protein. ATP-binding to SecA leads to a conformational change in SecA that inserts a 30 kDa domain of itself into the membrane together with the signal sequence into SecYEG [34]. SecD and SecF stabilize SecA in the membrane-inserted state [34]. ATP-hydrolysis by SecA leads to dissociation of the secretory protein from SecA and SecA dissociates from SecYEG, is replaced by a cytoplasmic SecA and further protein translocation is achieved by the proton motive force [26, 34–36]. By this, the whole protein is threaded through the translocon and after successful translocation, the channel is closed by an α-helical plug of SecY [28, 35].

The Sec-pathway has been well-characterized and is studied in great detail, however, a recent study challenges the existing model that co-translational translocation is mediated by SRP, whereas post-translational translocation is achieved with the help of SecB, as an interaction of SecA with the nascent polypeptide chain has been detected [11, 37]. The study shows that SecA can bind to the nascent peptide independent of SecB and proposes an intermediate between co- and post-translational translocation in which translocation is powered by SecA (instead of the ribosome) while the mRNA is still translated [37].

I.1.2 The Tat-Pathway

The Tat-Pathway transports folded proteins across the cytoplasmic membrane. Whereas the Sec-pathway is essential, the Tat-pathway is dispensable in most species, which is also reflected in a lower number of substrate proteins [10, 38, 39]. However, the Tat-pathway plays crucial roles in pathogenesis of plant and animal pathogens and is involved in many diverse cellular processes as motility, iron acquisition or biofilm formation [40–43]. A very prominent example is the export of Shiga toxin (Stx) by the Tat-pathway of *Shigella dysenteriae* and Shiga-like toxins (SLTs) of enterohemorrhagic *E. coli* strains [41, 44]. The most striking difference to the Sec-pathway is the ability of the Tat-pathway to translocate proteins across the inner bacterial membrane in a folded conformation [38, 45]. The transport of folded substrates has the advantage that proteins that require specific chaperones for their correct folding can be folded in the cytoplasm or that hetero-oligomers of which only one protomer contains a signal sequence can be translocated

together [46]. Additionally, proteins that need co-factors like iron-sulfur clusters or certain ions can be assembled correctly and can be shielded from competing ions in the periplasm [47, 48].

After emergence from the ribosomal exit tunnel, nascent peptide chains are first targeted by trigger factor, a general bacterial ribosomally associated chaperone [49, 50]. For some Tat-secretory proteins, trigger factor is crucial for stabilization by binding to the signal sequence of the substrate protein, probably to prevent premature binding of the signal sequence to the membrane-bound translocon [49]. Folding is achieved by Tat-signal sequence specific chaperones as well as general cytosolic chaperones like SlyD and DnaK [51–53].

Once folded, substrate proteins of the Tat-pathway associate with the inner membrane due to the intrinsic affinity of the signal sequence to the inner membrane [54]. Before substrate recognition, TatA of the the Tat-complex is thought to be present in the membrane in a monomeric form, whereas TatB and TatC form oligomers [55,56]. The signal sequence of the secretory protein is recognized by TatC and although several copies of TatC are present in a hetero-oligomer, only one TatC is involved in recognition of the secretory protein [56,57]. Upon substrate protein binding to TatC, protomers of TatA are recruited into the complex and form the actual protein translocation channel [58, 59]. In *E. coli*, TatA forms a homo-oligomeric membrane channel that allows passage of target proteins in which one helix of a protomer is involved in formation of the channel and another amphipathic helix is associated with the cytoplasmic side of the inner membrane [58]. The substrate is translocated through the channel fomed by TatA, mediated by TatC and regulated by TatB, however, the signal sequence stays attached to the TatBC-complex until the target is completely translocated and the signal sequence is cleaved by a periplasmic signal peptidase [60–63]. The fate of the signal peptide remains unclear [38]. In contrast to the Sec-translocase, the Tat-machinery is powered not directly by ATP-hydrolysis but rather by the proton motive force and is not equipped with a plug but disassembles into monomers after the translocation process [62, 64, 65]. The model of an oligomeric membrane channel also implies that substrates with different sizes can be transported by variation of the numbers of protomers that form the channel [62].

I.2 Secretion Systems of Diderm Bacteria

Bacteria with an inner, cytoplasmic membrane and additionally an outer membrane face one more challenge. They need to transport a subset of proteins across two membranes. This can be achieved in a one-step (Type I, III, IV, VI and VII Secretion Systems) or in a two-step process (Type II, IV, V and IX Secretion System). All of the secretion sys-

tems that transport proteins via a two-step mechanism rely on either the Sec- or the Tat pathway by which the proteins are first transported into the periplasm where they are then recognized by the respective secretion apparatus. Proteins that are transported in a two-step process and Sec-dependent are challenged by a further requirement: They need to be maintained in an unfolded but folding- and secretion-competent state, yet have to be resistant to degradation. For some secretion systems, parts of the transport substrate however, have to fold to allow efficient transport and/or recognition by the cognate secretion system. This is especially the case for Type V Secretion System autotransporters that rely on periplasmic chaperones like SurA, Skp or FkpA [66–71]. Additional to secretion system substrates that can depend on the Sec- or the Tat-Pathway, also the assembly of the secretion apparatus itself can depend on either Sec- or Tat-Pathway as also some proteins of the machinery have to be translocated into the periplasm.

I.2.1 The Type I Secretion System

The Type I Secretion System (T1SS) consists of three different proteins, all of which are essential for its function [72]. Two proteins are located at the inner membrane, a homodimeric ATP-binding cassette (ABC-) protein with a transmembrane domain (TMD) and a membrane fusion protein (MFP). The inner membrane proteins are usually specific for their substrate, whereas an additional outer membrane protein, TolC is a multi-purpose protein that is very common in bacterial membranes and involved in many different processes [73]. Interestingly, the inner membrane proteins and the cargo are encoded in the same operon and regulated together, whereas the outer membrane protein is encoded elsewhere and regulated independently [73].

Secretion via T1SSs is Sec- and Tat-independent and thus proteins are transported across both membranes in one step. Substrates of T1SS harbor a C-terminal signal sequence that is not cleaved and neither its sequence is conserved nor clear common structural features were identified [74–76]. The *E. coli* Hemolysin A (HlyA) Type I Secretion was the first described and is the best characterized T1SS to date and thus nomenclature of this machinery will be used here [72]. All proteins of the machinery were found to be essential for export of HlyA, a protein responsible for lysis of immune cells and thus involved in immune evasion and in virulence of uropathogenic *E. coli* (UPEC) strains [77]. Before secretion, HlyA is acylated by HlyC at two different positions of which both are necessary for its hemolytic activity [78, 79].

Assembly of the machinery starts with the inner membrane proteins HlyB (ABC-protein) and HlyD (MFP) that form a complex and recognize the substrate protein HlyA [80, 81]. Upon substrate recognition, the outer membrane protein TolC is recruited, thus,

the translocation channel is established and substrate transfer starts [82–84]. Translocation is powered by ATP-hydrolysis by HlyB [80].

HlyB is a member of the family of ABC-proteins, which are involved in the transport of small molecules, notably antibiotics, across the inner membrane. ABC-proteins bind intracellular small molecules, then, ATP-binding induces a conformational change from an inward-facing to an outward-facing conformation with lower affinity to the substrate and releases it to the periplasm [85–89]. ATP-hydrolysis then reverts the conformation to inward-facing [86]. Even though, the mechanism of action of ABC-proteins as drug efflux pumps is established, it remains elusive, how whole proteins can be exported.

The membrane fusion protein HlyD resides with one transmembrane helix in the inner membrane, has a small 60 residue cytoplasmic and a large α-helical and β-strand domain that is expected to bridge ABC-transporter and the outer membrane protein TolC [83,90]. The substrate protein then traverses the outer membrane through a channel formed by TolC [91].

Besides the C-terminal signal sequence, some T1SS-substrates also contain a repeats-in-toxin-(RTX)-domain, which contains repeats of a nonapeptide rich in glycine and aspartate. These repeats have been shown to promote folding when bound to Ca^{2+} [92]. As cytosolic levels of Ca^{2+} are lower than the affinity of the repeats (300 nM to 100 M), the domain can only promote folding once the peptide reached the extracellular surface, where Ca^{2+}-concentrations in the range of mM are encountered [93, 94]. Extracellular folding has recently been shown to facilitate translocation by blocking the way back as well as energizing the translocation [94, 95].

I.2.2 The Type II Secretion System

Substrates of the Type II Secretion System rely on either the Sec- or the Tat-pathway for transport from the bacterial cytosol into the periplasm [96]. The Type II Secretion System transports folded proteins across the outer membrane and is the only known export system for folded periplasmic proteins [96–98]. For this reason, several proteins requiring cofactors or periplasmic chaperones are transported by this mechanism [97,99]. Secretion via T2SS is implicated in many diverse cellular processes ranging from nutrient uptake, motility and adhesion to pathogenesis and colonization of hosts [100–106]. Early studies of the Cholera Toxin (CT) export showed that even oligomers can be exported by T2SS [102,107]. CT is a heterohexameric AB_5-toxin, which is composed of one enzymatic subunit (A) and five receptor-binding subunits (B) that mediate entry of the A-subunit into the target cell [107,108]. Many proteins of the T2SS itself depend on the Sec-pathway to be translocated across the inner membrane into the periplasm [109, 110].

T2SSs are composed of many different (≈15) often oligomeric proteins, which form a pilus-like structure called pseudopilus that is anchored to both bacterial membranes [111, 112]. Even though several proteins show some homology to Type IV pili proteins, they have distinct functions and carry therefore the prefix "pseudo-" [113–115]. As the Type II Secretion System was discovered very early and initially thought to be responsible for the export of most secretory proteins, it was termed General Secretion Pathway (GSP) and thus proteins involved are named Gsp*X* [116].

Assembly of T2SS starts with GspS, a protein also referred to as pilotin, which is a lipoprotein of the outer membrane and involved in recruiting more proteins of the complex. The secretin GspD is first recruited by GspS and forms the outer membrane channel that in turn leads to the accumulation of pseudopilins, which still contain the hydrophobic patch of the signal sequence that anchors them to the inner membrane [109,117]. GspD forms a dodecameric outer membrane-spanning channel with two constrictions, one lies at the height of the inner and the other one at the outer leaflet of the outer bacterial membrane [118]. The constrictions are expected to prevent leakage of cellular contents.

Even though the T2SS only transports proteins through the outer membrane, it is also anchored in the inner membrane by GspC, -F, -L and -M and assembly of the inner membrane protein complex is supported by the secretin in the outer membrane [119]. Once the outer and inner membrane protein complexes are assembled, the essential translocation ATPase, GspE is recruited [120]. The ATPase binds to GspL in the inner membrane and is activated by this interaction, which also induces hexamerization [120–123]. The major pseudopilin GspG as well as the minor pseudopilins GspH, -I, -J and -K assemble on the inner membrane complex with an unknown stoichiometry [109,124,125]. The minor pseudopilins form the tip of the pseudopilus and the major pseudopilins form the rest of the pseudopilus [125]. Minor pseudopilins could also be incorporated between subunits of the major pseudopilin [126].

Once assembled, the ATPase GspE binds to a cleft between two domains at the cytoplasmic side of GspL [120]. ATP-hydrolysis leads to conformational changes, first in the ATPase that are then transmitted to other proteins of the complex and lead to translocation of pseudopilins and further incorporation of more pseudopilins and thus to elongation of the pseudopilus [120, 122, 123, 127]. The assembly and architecture of the outer membrane components of T2SS as well as the general mode of secretion are well established, however, how substrates are translocated is still not completely understood [105, 126]. Two mechanisms of effector secretion have been proposed [126, 128]. One model, the "piston model" states that substrate proteins are loaded onto minor pseudopilins, which form the spike of the pseudopilus. Assembly of the pseudopilus then pushes the secretory proteins through the membrane channel protein GspD into the extracellular space.

In a second model, the "Archimedes' screw model", minor pseudopilins are incorporated between major pseudopilins and substrate proteins associate with minor pseudopilins.

In contrast to Type IV Pili, in T2SSs, no retraction ATPase has been found [113]. Thus, pseudopili have to be expelled or degraded to allow reuse of all proteins that are not part of the pseudopilus. How reuse of the machinery is achieved or whether it happens at all is under debate [126].

I.2.3 The Type III Secretion System

Type III Secretion Systems or Injectisomes are, regarding the number of proteins involved, the most complicated secretion systems described to date [129,130]. Substrates of T3SSs have an uncleaved N-terminal signal sequence that targets them to the ATPase of the injectisome [131–133]. The substrates are exported across both bacterial membranes through a narrow channel that only allows export of partially folded proteins [134, 135]. Injectisomes are one of few examples of secretion systems that directly inject toxins into the host cell cytoplasm across the membrane of the target cell [136].

The injectisome can be divided in two distinct parts. One is the basal body consisting to a large extent of membrane spanning rings of proteins as well as an export apparatus. The second part is the translocon with its needle that is anchored to the rod in the basal body. The needle reaches into the extracellular space with a defined length and is responsible to establish contact with the eukaryotic target cell as well as for pore formation in the membrane of its host [135, 137].

Type III Secretion Systems have been mostly described in the context of pathogenesis, especially cell and tissue invasion as well as phagosome remodelling and escape. The best described T3SSs are those of *Yersinia enterocolitica* and *Salmonella enterica*, both of which have 2 different T3SSs [135, 138–141]. Here, only the T3SSs of *Salmonella* will be discussed. Both secretion systems are encoded on *Salmonella* pathogenicity island-1 or 2 (SPI) [139].

Salmonella uses its T3SS of SPI-1 for the invasion of non-phagocytic cells by remodelling of the actin cytoskeleton modulated by Rho-GTPase targeting effectors [142–144]. The remodelling leads to engulfment of the bacterium and subsequent macropinocytosis. The resulting vesicles in which Salmonella resides are called *Salmonella*-containing vacuoles (SCV). Once internalized, *Salmonella* uses its SPI-2 T3SS to translocate a different set of effectors from the SCV into the cytoplasm of the host cell to prevent recruitment of hydrolases to the SCV and interfere with host tubulin-dependent transport among others [138, 145–147].

Assembly of the injectisome starts with the inner membrane-associated proteins SpaP

and SpaR, which then recruit SpaQ and SpaS and together form the export apparatus [98]. The export apparatus assembles in the inner membrane and is the basal structure of the protein conduit [148]. Then, PrgH and PrgK form an oligomeric ring around the export apparatus in the inner membrane with a 24-fold rotational symmetry [134]. A lipidated chaperone called pilotin (InvH) recruits the Sec-dependent secretin InvG to the outer membrane that then forms the periplasmic part of the outer membrane ring structure with a 15-fold symmetry [134, 149]. PrgJ is recruited to form the inner rod that connects the needle with the basal body [150, 151]. The needle protein PrgI then assembles a helix with defined length into the extracellular space [135, 152, 153]. The ruler protein InvJ is responsible for determination of the length and presumably is inserted relatively early in the needle assembly process, as the distal end adopts a globular fold and thus cannot be secreted through the needle [153–155]. The needle complex with all components mentioned before was resolved at medium resolution using single-particle cryo-electron microscopy (cryo-EM) and revealed important features of the architecture [134].

At the tip of the needle, the translocon is located [156–158]. The translocon connects to and senses the host membrane, triggers a conformational change in the ruler protein, which in turn leads to autocatalytic cleavage of a protease, enabling secretion of effector proteins [159–162]. The translocon is composed of three proteins, of which two are hydrophobic and one is a hydrophilic protein. The hydrophilic protein SipD forms the cap on the translocon and serves as a scaffold for later pore formation of the two hydrophobic membrane proteins SipB and SipC that form a pore in the membrane of the target cell through which the effectors are then translocated [163, 164].

On the cytoplasmic side of the secretion system, a sorting platform as well as the machinery powering translocation is located [161, 165, 166]. The ATPase InvC is located in the export apparatus and is responsible for substrate recognition [167, 168]. Whereas the ATPase is essential for detachment of effector proteins from their cognate chaperones, the actual driver of protein translocation seems to be the proton motive force (PMF) [168–171].

The cytoplasmic portion of the secretion system can only be visualized using whole cell cryo-electron tomography (cryo-ET) as several components detach from the rest of the machinery during isolation [129, 134, 137, 161, 172]. Recently, gene-deletion and -tagging studies combined with cryo-ET revealed the architecture and composition of this part of the secretion system in great detail [172]. A relatively large cytoplasmic sorting platform was described to have a structure with six pods, whose assembly is independent of the export apparatus. The six-fold symmetric sorting platform is attached to the N-terminal cytoplasmic part of PrgH that is present in 24-fold symmetry. To accomodate this symmetry mismatch, the cytoplasmic domains of four protomers of PrgH form a patch, to

which the pods of the sorting platform then attach [172]. The exact role of the sorting platform remains unclear and further work will focus on elucidation of the function of this sub-assembly.

I.2.4 The Type IV Secretion System

The Type IV Secretion System is the sole bacterial secretion system that is capable of translocating substrate proteins from the cytoplasm as well as the periplasm through its needle into the target cell [173]. However, most substrates pass through the T4SS directly from the cytoplasm [174]. T4SSs can also target both, eukaryotic as well as prokaryotic cells [175, 176].

Two families of T4SSs exist, with one being conjugation systems and the other one being protein translocation systems. Both types of systems are closely related to each other and in fact, conjugation systems also translocate proteins and recognize proteins as their substrate, whereby ssDNA is coupled to the protein substrate [177, 178]. Both families can be further divided into plasmid-encoded and chromosomally located subtypes. T4SSs show a certain variety of architectures and are also different in the range of substrates that they translocate. The most extreme examples are the T4SS of *Helicobacter pylori* that only transports one substrate, and the T4SS of *Legionella pneumophila* that exports about 140 different effectors [179–181].

Secretion via T4SS is either Type 4 Coupling Protein-dependent (T4CP) (secretion from cytoplasm) or Sec-dependent (secretion from periplasm). To date, one example of Sec-dependent T4S has been discovered in *Bordetella pertussis* which is the secretion of the Pertussis Toxin [173]. The Pertussis Toxin (PTX) is a heterohexameric toxin of which all components are translocated across the cytoplasmic membrane through the Sec-pathway and enter the T4SS laterally [182, 183]. Some experimental evidence also exists for a transient periplasmic intermediate of substrates of the *Agrobacterium* T4SS. These proteins lack a signal sequence and thus are transported in a Sec-independent manner, which is currently not understood [184].

Here, the *Agrobacterium tumefaciens* VirB/D4 T4SS will serve as an archetypal T4SS and nomenclature of this system will be used [185, 186].

Components of the Ti-plasmid-encoded VirB/D4 T4SSs of *Agrobacterium tumefaciens* are encoded in two operons [187]. All 11 VirB proteins are encoded in one operon and the T4CP VirD4 is encoded elsewhere on the plasmid [188]. Additionally, effectors called Vir*E*X are encoded downstream of the *virD4*-gene [187]. VirD4 is a hexameric ATPase that recognizes cytoplasmic secretory proteins via their unstructured C-terminus harboring positively charged or hydrophobic patches [189]. Another possibility of substrate

recognition is mediated by the tertiary structure of domains [190]. Both mechanisms of recognition by T4CP can further be supported by chaperones that interact with both the substrate and T4CP [191–193]. The diverse nature of the recognition signal and the potential need for a additional chaperones complicates subtrate prediction.

VirD4 also powers secretion of substrates and is a component of the inner membrane complex (IMC) that additionally composes VirB3, VirB4, VirB6, VirB8, VirB11. The outer membrane complex (OMC) composes VirB7, VirB9, VirB10 and VirB2, of which VirB2 also builds the extracellular pilus.

VirB4 and VirB11 are additional ATPases located at the cytoplasmic face of the assembly. VirB11 is located in the center and VirB4 at the opposite side as VirD4.

Assembly of the secretion system starts with the IMC in which VirB4 stabilizes VirB8 in an ATP-independent manner [194, 195]. Then, VirB8 recruits the OMC components VirB10 as well as VirB5 that serves as a first step in pilus assembly. As many proteins depend on each other for stability and complex formation, information on the exact and complete order of assembly is lacking.

The pilins are first synthesized as propilins with a leader peptide that is cleaved off, followed by acetylation and cyclization, which leads to high mechanical stability [196–198]. A single particle cryo-EM reconstruction of a VirB3-VirB10 complex at a resolution of 18 Å gave detailed insight into the architecture of the complex [199]. Interestingly, two hexamers of the ATPase VirB4 were found to be localized on the cytoplasmic side of the complex. These hexamers were postulated to be potentially exchanged by hexamers of other ATPases (VirD4 or VirB11) to allow substrate switching [199]. Another hypothesis would be that VirB4 is involved in recognition of the substrate, whereas processivity and actual translocation are then achieved by other ATPases.

Even though the order of assembly is only partially clear, the way of the substrate through the machinery is resolved in great detail [200]. First, the relaxase VirD2 that is bound to its target DNA, contacts VirD4 ATPase, which then transfers the substrate to another ATPase VirB11. After this, the substrate is transferred to a complex of VirB6 and VirB8 and then enters the VirB2 pilus via interactions with VirB9 [200]. No direct substrate interactions have been observed for VirB3, 4, 5, 7 and 10. VirB1 is a lytic transglycosylase that is proteolytically cleaved and can be detected associated with target cells and in culture supernatants [201, 202]. It is also the only dispensable protein of the assembly, but its exact role, besides promotion of pilus formation, is not entirely clear [203, 204]. VirB5 localizes to the tip of the pilus and is involved in incorporation of pilin-subunits into the growing pilus [205–207].

Initial recognition and transfer of substrates from one ATPase to another one is ATP-independent [194]. ATP binding to either one of the ATPases induces conformational

changes in VirB10 that are presumably involved in gating the T4SS-pore [178, 208–210]. The substrate is then passed to other components of the IMC, VirB6 and VirB8 and afterwards enters the OMC and finally the VirB2 pilus through which it is translocated into the target cell [178, 198]. The exact interplay of many components, especially those that are not resolved in the cryo-EM structure, remains elusive [199]. Additionally, it is unclear how the T4SS recognizes a target cell.

I.2.5 The Type V Secretion System

Type V Secretion Systems are two-step secretion systems that are Sec-dependent [211]. A β-barrel protein forms the translocation channel in the outer membrane and facilitates translocation of its substrate [212]. Five different subclasses of Type V Secretion Systems have been discovered to date; Va to Ve [213, 214]. Type Vb Secretion is also called Two-partner Secretion (TPS) [213, 214]. All subclasses besides Vb are composed of different flavors of autotransporters, in which the outer membrane channel and the secreted protein (the passenger domain) are encoded in one gene. In contrast to autotransporters, TPS is achieved by two proteins; a membrane channel protein and a substrate protein. They are usually encoded adjacent to each other. Thus, most substrate proteins have a dedicated transport protein. As Type V Secretion is Sec-dependent, substrate proteins have an N-terminal signal sequence that is cleaved by an inner-membrane anchored signal peptidase [25].

In all autotransporters, the C-terminal β-domain forms a transmembrane β-barrel structure that enables transport of the passenger domain [215]. To integrate into the outer membrane, most autotransporters rely on the presence of either BamA or TamA that also form a β-barrel in the outer membrane and assist in insertion of the autotransporters β-domain [216, 217]. The inner diameter of the 16-stranded β-barrel protein TamA is 1.8 nm [217]. Once the β-barrel is inserted into the outer membrane, translocation of the passenger domain is expected to be driven by passenger domain folding in the extracellular space [218]. After export of the passenger domain, most substrates autocatalytically cleave themselves and some stay non-covalently associated with the outer membrane while others are released [212,218–220]. Currently, it is unclear what the fate of the inserted β-barrel in the outer membrane is. It was postulated that they potentially perform other functions after secretion of the respective passenger domain [221]. To avoid leakage of cellular contents through the remaining β-barrel, the autotransporter is closed by an α-helical plug [212, 222–225].

Less experimental evidence exists for a second model of Type V Secretion that proposes that several β-barrels form a multimeric complex with a pore of $\approx$2 nm in their center

[226]. However, this pore can potentially vary its size by incorporating more protomers and thus would allow the export of folded substrates through the outer membrane [226].

Autotransporters and substrate proteins of TPS systems need to be maintained in a secretion-competent state in the periplasm, yet need to be protected from degradation but also should not accumulate in the periplasm to allow normal functioning of the cell envelope. For autotransporters, the β-domain has to be able to fold and insert into the membrane and the passenger domain remains unfolded. Periplasmic chaperones like Skp, SurA, FkpA or DegP are crucial for maintaining this balance [66–71, 227]. To a certain extent, DegP assists in chaperoning HbpA, an exported *E. coli* effector, however, if HbpA accumulates in the periplasm, DegP acts as a protease and degrades its substrate [227–229].

Substrates of the TPS system are widespread in pathogenic bacteria and many of them have been characterized as cytotoxins, adhesins or heme-binding proteins and thus are involved in host colonization and invasion [221]. The two partners are named TpsA and TpsB, of which TpsB forms a β-barrel membrane channel, with polypeptide transport-associated (POTRA) domains and the substrate is referred to as TpsA. In contrast to autotransporters, TpsB can have more than one substrate protein. Specificity of TpsB is achieved by the periplasmic POTRA-domains that recognize the TPS-domain of its substrate, TpsA. Interestingly, contact dependent inhibition (CDI) is mediated by TPS [230]. *E. coli* secretes the nuclease CdiA by TPS and upon contact to BamA of the target cell CdiA is cleaved off from the outer membrane, internalized into the periplasm and enters the cytoplasm mediated by AcrB, a multidrug efflux pump [231, 232].

I.2.6 The Type VI Secretion System

Secretion by the Type VI Secretion System is achieved by a long contractile machinery that is anchored to cell envelope [233]. It can be divided in three major parts; membrane complex and tail [233–236]. Furthermore, the tail is composed of a baseplate, a sheath and an inner tube. The membrane complex spans both membranes and anchors the nanomachine to the envelope [233, 235]. The baseplate serves as an adaptor for sheath and tube and triggers contraction of the sheath that surrounds an inner tube [233, 237]. By contraction of the sheath, the inner tube is expelled and delivers its cargo effector proteins into the target cell [233]. Effectors that can target eukaryotes, prokaryotes or both, are located at the tip of the inner tube or can also be contained in the hollow and narrow tube [238–241]. After contraction, the sheath is in a low-energy state that is specifically recognized by the AAA^+-protein ClpV [237, 242]. ClpV disassembles the sheath and allows reuse of the sheath proteins TssB and TssC (VipA and VipB in *V. cholerae*) [243, 244].

The exact mechanism of sheath disassembly as well as the fate of membrane complex and baseplate after contraction remains unclear [245, 246].

Further aspects of T6SSs are discussed in Section I.3.

I.2.7 The Type VII Secretion System

The T7SS was first discovered in 2003 as the only secretion system in *Mycobacterium tuberculosis* [247]. It was found to be a virulence determinant required for efficient macrophage subversion during acute infection in mice [247]. *Mycobacterium tuberculosis* encodes five T7SS (ESX1-5) that export different sets of proteins and the substrates of ESX-1, -3 and -5 are required for virulence [248–250]. Interestingly, one of these systems (ESX-1) is missing in the attenuated vaccine strain, *Mycobacterium bovis* BCG and complementation restores virulence [251]. Homologs of T7SS-proteins of *Mycobacteria* have also been identified in monoderm bacteria like *Staphylococcus aureus* and *Listeria monocytogenes* [252–255]. Secretory proteins of T7SSs comprise effectors of many different functions, ranging from nutrient scavenging to immune evasion or macrophage subversion by phagosomal escape [247, 248, 256, 257]. Many secreted proteins of the PE and PPE-families (characterized by a Pro-Glu or Pro-Pro-Glu motif at the C-terminus) are expected to reside at the mycobacterial outer membrane, to bind host receptors and by this mediate entry into host cells [258, 259]. Substrates are recognized via a C-terminal signal peptide that is cleaved in the periplasm by the essential inner membrane-anchored protease MycP encoded at the same locus [260].

EccA is a cytoplasmic AAA^+-protein that is essential for T7SS. It recognizes substrates and presumably transports them to the export machinery [261–263]. All other known components of T7SS, EccB-EccE are integral inner membrane proteins and the structure of the periplasmic part of EccB has been solved [264–266]. EccB potentially connects the IMC to a postulated OMC. However, to date, no component of a potential OMC has been identified. EccC and EccD have been suggested to be located at the periphery of the IMC based on limited proteolysis studies [264]. Additionally, EccC, with 170 kDa the largest protein of the complex, has also been shown to be essential for stability and integrity of the membrane complex. Mechanism of secretion and the route of assembly are largely unclear due to lack of information on the organisation of the complex within the membrane as well as the interactions of its components.

I.2.8 The Type IX Secretion System

The T9SS is a two step secretion system and was first discovered in *Porphyromonas gingivalis* as Phorphyromonas secretion system (PorSS) [267, 268]. Up to now, T9SSs have

only been found in Bacteroidetes and have been implicated in very diverse functions. Being first only implicated in the secretion of gingipains by *Porphyromonas gingivalis* and proteins involved in gliding motility in *Flavobacterium johnsoniae*, later, secretion of more diverse proteins has been described [267–271].

Porphyromonas gingivalis is a human pathogen involved in periodontal diseases and a major cause of tooth loss [272,273]. Gingipains are cysteine proteases secreted by *Porphyromonas gingivalis* that are considered to be important virulence factors and act by degradation of fibrinogen, CD14 receptor of macrophages as well as activation of the blood coagulation system and enhancement of vascular permeability [274–277]. The main components of the machinery in *Porphyromonas* are PorK, -L, -M, -N and -P. All of these proteins are membrane associated proteins. PorL and PorM reside in the inner membrane, PorK and PorN are associated with the outer membrane and PorP is predicted to be a β-barrel protein und thus located in the outer membrane [267, 278, 279]. The inner membrane proteins PorL and PorM have predicted transmembrane helices that are also expected to mediate interaction of these two proteins [278]. PorK has an N-terminal lipobox motif, whereas PorN has an N-terminal SEC-signal sequence that directs it to the periplasm. However, sequence analysis of PorN does not predict it to be associated to membranes [267, 278, 279]. Additionally, PorV is involved in secretion of some substrate proteins and PorU is a signal peptidase that cleaves a C-terminal β-sandwich domain [270, 280].

Recently, first insights into the architecture of the secretion system have emerged from electron microscopy studies as well as protein interaction studies. PorN and PorK form together a ring structure with 32 to 36-fold symmetry, of which the part, where PorK is located appears to be wider [279]. The inner diameter of the observed structures is $\approx$35 nm and the outer diameter is $\approx$50 nm [279]. In this complex, PorN and PorK have been shown to be present in a 1:1 stoichiometry, however, due to limitations in resolution, no further information can be deduced [279].

I.2 *Vibrio cholerae* and its Type VI Secretion System

I.1 Biology of *Vibrio cholerae*

Vibrio cholerae is a motile diderm and human-pathogenic bacterial species [281, 282]. It is an aquatic bacterium that can survive in fresh- as well as seawater and is often found in rivers and brackish water as well as on coast lines [283]. *Vibrio* species are facultative anaerobes with two chromosomes [284].

Critical virulence factors of *Vibrio cholerae* are the Cholera Toxin (CT) and the Toxin

coregulated pilus (TCP). Genes for CT have been acquired by horizontal gene transfer by phage CTX, which binds to the TCP and subsequently transports its DNA into the bacterial cytoplasm [285, 286]. Genes of the TCP are encoded on the *Vibrio* pathogenicity island (VPI) on chromosome 1 [287]. The genome of the phage (including genes for CT, *ctxA* and *ctxB*) can either be integrated on chromosome 1 or remain as a plasmid [285, 286, 288]. Cholera Toxin is a heterohexameric AB_5-toxin secreted by T2SS, which recognizes the B-part of the toxin [106, 289, 290]. AB_5-toxins are composed of 5 similar or identical subunits of the B-components that assemble with one copy of component A [291]. B subunits are responsible for translocation of the A subunit across the membrane of the eukaryotic host, which then exerts its respective enzymatic function. Other prominent examples include the Iota-toxin of *Clostridium perfringens*, Pertussis toxin of *Bordetella pertussis*, Shiga toxin of *Shigella dysenteriae* or Shiga-like toxins of enterohemorrhagic *Escherichia coli* [118, 290, 292–294].

In intestinal epithelial cells, the A subunit of CT catalyzes the ADP-ribosylation of a G-protein that in turn stimulates adenylate cyclase to produce cAMP [295]. High cAMP levels induce the expression of cystic fibrosis transmembrane conductance regulator (CFTR) which leads to uncontrolled ion efflux into the lumen of the intestine and to watery diarrhea [108, 296, 297].

In the intestine, *Vibrio cholerae* senses bile and downregulates expression of CT and TCP but enhances motility [298]. Increased motility is expected to lead to penetration of the bacteria into the mucus, where then the expression of CT and TCP is upregulated again and infection is established [298–301]. The TCP is closely related to Type 4 pili and crucial for self-aggregation of *Vibrio* which promotes retention in the mucus [302, 303]. After initial retention, *V. cholerae* escapes the mucus into the lumen, presumably to prepare for the next infection [301].

V. cholerae is often transmitted via the fecal-oral route by insufficient hygiene in food-preparation or washing and bathing in rivers [304]. Cause of death by *Vibrio cholerae* infection is severe dehydration with a mortality rate of $\approx$5% that decreases to $<$1% when treated [305, 306]. Cholera can easily be treated by sufficient oral or intravenous hydration and in severe cases may be supported by antibiotics [307–309].

I.2 Regulation of the T6SS in *V. cholerae*

Already in the first publication describing the T6SS in *V. cholerae*, VasH was identified as a transcriptional regulator that is encoded in the T6SS main cluster [239]. Subsequently, many other transcriptional regulators and environmental stimuli, which influence T6SS-expression have been identified, among them quorum sensing, chitin-induced competency,

nucleoside scavenging and catabolite repression [310–314]. Additionally, it is also regulated by bile and mucin [315]. Many of these pathways are interconnected, as for example chitin utilization by *Vibrio* depends on biofilm formation that the bacteria can efficiently adhere to chitinous surfaces. The second messenger cyclic di-GMP has also been shown to be involved in activation of T6SS gene expression [316].

Interestingly, growth on chitinous surfaces is interconnected with a natural competence pathway leading to increased competence of *V. cholerae,* when growing on chitin [317–319]. It has been shown earlier that the core set of genes of T6SS in *V. cholerae* is conserved, however, the effectors vary between species [320]. These studies indicate that formation of biofilms on chitinous surfaces leads to increased T6SS activity and thus to increased target cell killing and DNA release that then can be taken up efficiently by natural competence using the ComEA/EC system [317]. Thereby new effectors are potentially taken up by the attacking Vibrio strain.

Quorum sensing affects transcription of T6SS genes so that at low cell densities, T6SS expression is decreased and increased at higher cell densities [311, 312, 321, 322]. Another study showed that at high cyclic di-GMP levels, at which biofilm formation occurs, the expression of the main cluster of T6SS is inhibited. This inhibition is released again at lower cyclic di-GMP levels [316, 323]. Further studies will discriminate between the different regulatory cascades and elucidate their impact on T6SS-dependent virulence [316, 324].

In the host, T6SS gene expression appears to be reduced by bile and activated by mucins, indicating that when *V. cholerae* is not yet attached to the epithelium, T6SS activity is off. As soon as *Vibrio* attaches to the mucus layer, both T6SS expression and flagellar motility is turned on to efficiently colonize a niche by killing resident bacterial species [298, 300, 322, 325, 326].

All pathways discussed before, influence expression level of T6SS genes. For *P. aeruginosa*, a regulatory network of transcriptional and post-transcriptional regulation but also post-translational modification has been identified and the activation of T6SS appears to be much more regulated [327–331]. So far, no post-translational regulation has been identified in *V. cholerae*.

I.3 The Type VI Secretion System

The Type VI Secretion System (T6SS) is a contractile apparatus, parts of which share functional and structural homology to contractile tails of some phages, R-type pyocins as well as some other extracellular contractile protein complexes with diverse functions [237, 241, 332–336]. Although first hints to a new protein secretion system were already

present in 1996, it was in 2006 that the T6SS was discovered in a screen for novel virulence factors of *Vibrio cholerae* using a *Dictyostelium discoideum* model system [239, 337–339]. Shortly after, it was also described to be present in *Pseudomonas aeruginosa* [328]. It is found in ≈25% of all sequenced diderm bacteria of which many are important pathogens [339, 340]. However, more and more reports imply a function of the T6SS not directly in pathogenesis but rather indirectly by a competitive advantage in polymicrobial communities [341–343]. Its effectors can target eukaryotic, prokaryotic or also both cell types [239, 329, 331, 341, 344, 345].

Some pathogens like *Francisella* critically depend on a functional T6SS as it is absolutely crucial for phagosomal escape during infection [346]. Avian pathogenic *E. coli* upregulate their T6SS during infection [347]. In *V. cholerae,* T6SS is not involved in infection in an infant mouse model, however, many clinical and environmental isolates of *V. cholerae* encode a T6SS [334, 338, 346–349]. In *Burkholderia*, even five T6SS-clusters are found [350, 351]. Other studies highlighted the inflammatory effects of T6SS effectors during infection that potentially promote effective host colonization [325].

Nomenclature of T6SS proteins has been harmonized and different groups have been assigned [351]. A core set of genes that is present in virtually all clusters of T6SS is designated as Tss (*T*ype *s*ix *s*ecretion *X*), whereas accessory components are named Tag (*T*ype six *a*ssociated *g*ene *X*) [351]. Additionally, effectors are named Tse (*T*ype *s*ix *e*ffector) and their respective immunity proteins are called Tsi (*T*ype *s*ix *i*mmunity), both are denoted with a number [352]. In other cases, effectors with known functions carry a letter based on their function, which is exemplified in TseL, which is a lipase (*T*ype *s*ix *e*ffector *l*ipase) or Tae, which is an amidase (*T*ype six *a*midase *e*ffector) [353, 354].

Most T6SS effectors have been shown to be associated with the tip-complex or are extensions thereof [355]. However, effectors can also be localized inside the inner Hcp tube [238, 356]. In *V. cholerae*, all identified effectors localize to the tip and none has yet been identified that associates with Hcp.

In *V. cholerae*, the T6SS is organized in four genetic clusters. The main cluster encodes sheath proteins, membrane complex proteins, most baseplate proteins, ClpV, VgrG-3 and an effector-immunity pair [239, 357]. Thus, most structural components and core components are encoded in the main cluster, whereas Hcp-1 and VgrG-1 are encoded together with another effector, its immunity protein and an adaptor for binding to VgrG-1 elsewhere on the chromosome in auxiliary cluster 1 [355, 358, 359]. Auxiliary cluster 2 contains VgrG-2 and Hcp-2, as well as effectors and immunity proteins and another adaptor protein [360]. Lastly, auxiliary cluster 3 encodes an effector-immunity pair and a PAAR-protein [357].

I.3.1 The Membrane Complex

The membrane complex of the T6SS is a protein complex composed of TssJ, TssL and TssM and functions as an anchor and protein conduit for the cytosolic part of the T6SS. Computational analysis predicted its topology and localization of components which was further verified by cysteine accessibility studies [361, 362]. TssJ is a lipoprotein that connects the protein complex to the outer bacterial membrane, TssL is a transmembrane protein of the inner membrane and TssM, the biggest protein, also spans the inner membrane [236, 363, 364]. In some cases a fourth protein called TagJ, containing a peptidoglycan binding domain can accompany the other membrane complex proteins and additionally anchors the complex to the cell wall, when the TssL does not have a C-terminal domain with a predicted peptidoglycan binding site [364].

No protein of the membrane complex has homology to proteins in contractile tailed phages or other contractile nanomachines. Structures of the periplasmic domain of TssJ, TagL and of the cytoplasmic domain of TssL have been solved individually but details of the assembly are missing [236,362–368]. Interactions of these proteins or domains thereof have been tested. TssM has been shown to be the central protein that interconnects TssL and TssJ with its periplasmic domain [363]. TssL and TssJ self interact at unknown stoichiometry and TssL additionally interacts with TagL, if present, and with TssK of the baseplate [236, 361, 362, 364].

The insertion of the membrane complex is supported by a peptidoglycan hydrolase that enzymatically digests the peptidoglycan layer to allow establishment of the transmembrane conduit [207]. Furthermore, insertion of TssL into the inner membrane relies on YidC, an insertase of the inner membrane [361, 369].

Recently, a structure of the membrane complex at a resolution of ≈12 Å has been published and shows an overall five-fold symmetry with a central cavity, a height of 300 Å and a width of 205 Å [235]. Based on the electron microscopy reconstruction and the overall molecular weight of 1.7 MDa, TssL, TssJ and TssM are expected to be present in 10 copies [235, 236]. A capping structure is located in the outer membrane and is formed by TssJ, which is connected to TssM that forms pillars and arches that bridge the periplasm [235,363]. A crystal structure of the periplasmic domain of TssM has also been solved and could be placed in the electron density map [235,363]. TssL and TssM interact with baseplate components to anchor the contractile sheath [234, 235, 365, 370, 371].

During contraction of the sheath, the internal pillars of TssM are expected to move outwards and by this widen the inner diameter of the membrane complex to permit passage of the tip-spike-complex with associated effectors and subsequently the Hcp-tube [235]. In the closed state, the central cavity in the membrane complex is not large

enough to encompass the VgrG-tip, meaning that the tip-spike-complex with associated effectors has to be localized outside the membrane complex [235,241]. Molecular details of the interactions between the components of the membrane complex are still lacking due to limits in resolution of the electron microscopy reconstruction. Further studies will reveal a better understanding of the interactions between components of membrane complex as well as components of the baseplate with the membrane complex.

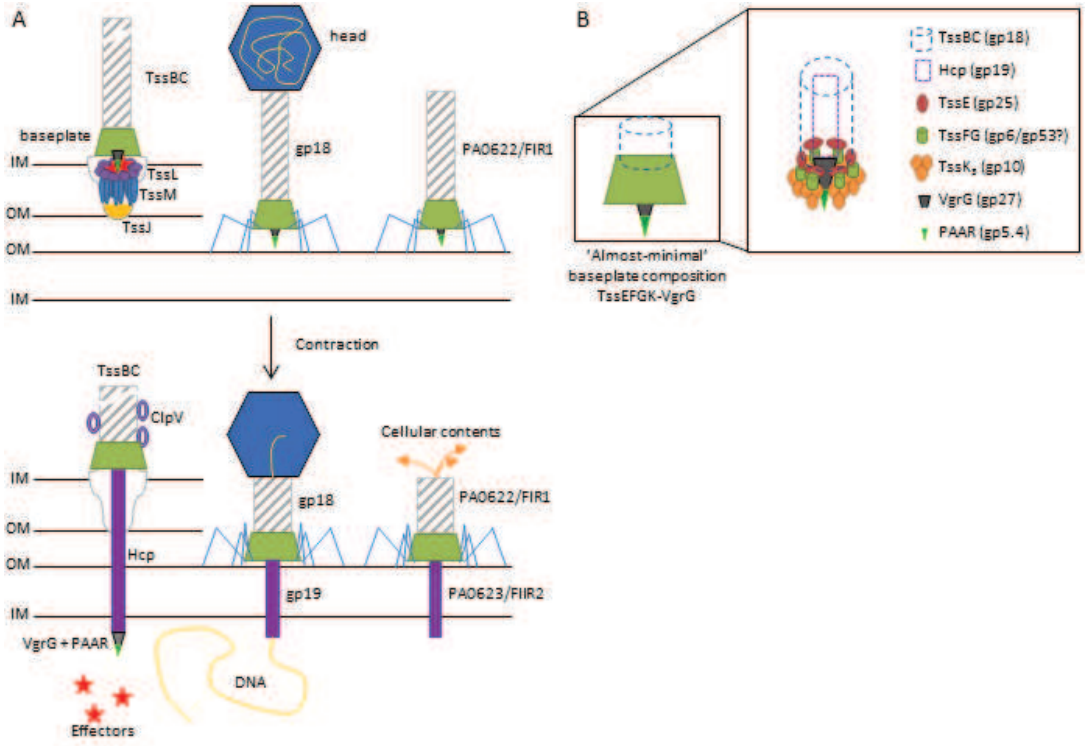

Figure I.2.1 Scheme of contractile nanomachines. (A) Type VI Secretion System delivers toxins from the cytosol to the cytosol of a target cell. Phage T4 delivers its DNA into the recipient and R-type pyocins generate holes in the cell envelope of closely related species. (B) Close-up view of the baseplate of T6SS. TssK presumably attaches the baseplate to the membrane complex. TssF and TssG form a wedge and a core bundle of the baseplate and TssE is the sheath initiator. VgrG and PAAR-proteins form the spike and spike tip complex. Respective phage proteins (gp) are in parentheses. IM: Inner membrane, OM: Outer membrane

I.3.2 The Baseplate

The baseplate of the T6SS serves as an adaptor for the contractile sheath to the membrane complex [234]. Studies from phage T4 showed that the baseplate is also involved in triggering the contraction of the sheath and thus is expected to be a central player for correct functioning of the T6SS [372–375]. VgrG and PAAR-protein together with TssE, F, G and K form the baseplate of the T6SS. VgrG and PAAR-protein form the central

part of the baseplate and the spike that is expelled [241]. VgrG forms a trimer which is tipped by a monomer of the PAAR-protein [241]. TssE, F, G and K are assembled around the spike and presumably stay attached to the membrane complex during contraction of the sheath [234,241,333]. Potentially, another protein, TssA, is also present in the baseplate [376]. Yeast-two-hybrid together with co-immuno precipitation experiments revealed a dense interaction network of the different baseplate components in which TssF and TssE interact with TssG, and TssF and TssG together interact with TssK and VgrG, the central spike protein [234,363,377].

Functions and potential localizations can be deduced from the role of the T4 phage homologs [372]. TssE is a homolog of sheath initiator gp25 and thus expected to serve as a direct anchor for the sheath, which has also been proposed by structural studies on the sheath [237,372]. The T4 wedge proteins gp6 and gp7 are proposed to be homolog to TssF and TssG, respectively [372]. TssG is expected to be localized peripherally with respect to TssF. TssF is expected to be present in 12 copies in two different conformations, whereas TssG is thought to be present in 6 copies [372,378,379]. Spike and hub proteins gp5 and gp27 are resembled by VgrG in T6SS and the spike tip protein gp5.4 is the PAAR-repeat protein [241, 333, 372]. The T6SS proteins are all homologous to proteins of the inner baseplate of phage T4, meaning that the T6SS baseplate is less complex than the one of phage [372]. Instead of being connected to the peripheral baseplate and the tail fiber network, the baseplate of T6SS is connected to the membrane complex.

TssG interacts with TssM of the membrane complex and TssF and TssG also interact with Hcp, the tube protein of the tail [234, 370, 380]. TssE is expected to serve as a direct anchor of the sheath to the baseplate [237, 372]. The baseplate is structurally very poorly described for the T6SS. Up to now, only the central spike has been resolved at atomic resolution and the TssK trimer has been described to have a triangle shape by negative stain electron microscopy (EM) and small angle X-ray scattering (SAXS) [241, 377, 381]. Baseplates of related contractile nanomachines, show six-fold symmetry, which is also expected for the T6SS baseplate [332, 372, 382]. Currently it is not clear if the five-fold symmetry of the membrane complex is a true biological feature or an artifact from protein over-expression in a heterologous host. Further studies will focus on this potential symmetry mismatch or a different configuration of the membrane complex. More details about structure and assembly as well as our findings describing the structure of the baseplate can be found in Section II.6 on page 75.

I.3.3 The Sheath-Tube Complex

The sheath is the dynamic structure of the T6SS [233]. In *Vibrio*, it first assembles in ≈30 s a long (up to several m) tubule inside cells that then quickly contracts to about 50% of its original length [233, 383]. The contraction is, similarly to contractile tailed phages, expected to lead to delivery of effectors into the target cell [233].

The contractile sheath is made up of two proteins, VipA (or TssB) and VipB (or TssC). The inner Hcp tube starts assembling on the baseplate on the VgrG trimer and serves as a template for sheath assembly. Structures of several Hcp proteins of different organisms have been elucidated [328, 358, 384, 385]. The tube protein forms hexameric rings with an outer diameter of ≈100 Å and an inner diameter of ≈40 Å [328, 358, 384, 385]. The rings are also able to form tubes *in vitro*, however with low affinity and are presumably stabilized by the sheath *in vivo* [333]. The inner diameter is sufficient to accomodate small folded proteins or domains.

The sheath proteins are encoded adjacent to each other in all T6SS-clusters and assemble a six-start helix around the inner Hcp tube and form an interlaced network of β-strands that is responsible for the high stability of the sheath [237, 334, 340, 386, 387] (Section II.4). Upon an unknown trigger, presumably from the baseplate, the sheath contracts, expells the inner tube with its tip and and delivers tip-associated effectors [233]. The contracted sheath is specifically recognized by the AAA^+-protein ClpV, which disassembles it [233, 243, 244, 331, 388]. To date, it was not possible to purify sheath in an extended state, likely due to its inherently unstable nature.

My PhD project lead us to propose a model of how the mechanism of contraction works and how this is propagated through the sheath. Using this model, we could also isolate mutant sheaths in an extended conformation and resolve their structure. More on the mechanism of contraction and the structure of the sheath in an extended state can be found in Section II.2 on page 51 and in Section II.4 on page 64, respectively.

I.3.4 Type VI Secretion System Effectors

T6SS-effectors can target either pro- or eukaryotic cells but also both domains of life, depending on the cellular target [239, 345]. In 2013, the multiple effector translocation VgrG (MERV) model was proposed [241]. The model proposed five different possible effector binding modalities in which effectors can be either C- or N-terminal extensions of PAAR or VgrG proteins or non-covalently linked to either one of them [241]. Another possibility is the association of effectors into the VgrG cavity that faces the Hcp tube [241]. Additionally, effectors can also reside in the inner Hcp tube [238].

In *Vibrio*, no Hcp-associated effectors have been identified yet. The first effector de-

scribed in *V. cholerae* has an actin-crosslinking activity and is found as a C-terminal extension of VgrG-1 [239, 389]. Subsequently, transposon sequencing experiments identified TseL, a putative lipase and its cognate immunity protein TsiV1 and the previously identified pore forming effector VasX and its immunity protein TsiV2 [353, 360]. Additionally, VgrG-3 was identified as an effector that contains a peptidoglycan hydrolase domain with an immunity protein encoded downstream [353]. This study also showed that VgrG-3 directly interacts with TseL and is essential for its secretion [353]. Later however, TseL was shown to be loaded onto VgrG-1 with the help of an adaptor protein [390]. Another approach used mass spectrometry based experiments and identified a putative peptidoglycan hydrolase TseH and its immunity protein encoded downstream of a PAAR-protein [357].

Recently, two other studies showed another mode of how T6SS-effectors can be loaded onto the tip complex [359, 390]. Both studies showed that a conserved chaperone domain helps to load proteins onto the tip. The chaperone serves as an adaptor and has binding sites for both VgrG and the effector protein that is located downstream of the chimeric adaptor [359, 390]. The adaptor proteins have been named T6SS effector chaperones (TEC) or T6SS adaptor protein (Tap) and are often encoded downstream of a PAAR- or VgrG-protein, however are not secreted [359, 390].

I.3 Other Contractile Tail Machines

In the past decades more and more phage tail-like protein translocation systems (PLTS) have been discovered and their biological function has been described [386, 391]. Namesake for these structures are phages of the family *Myoviridae* that have contractile tails that pierce the membrane of target cells and deliver DNA. PLTS comprise assemblies with a variety of functions; the extracellular metamorphosis-associated contractile (MAC) structures that are expressed by *Pseudoalteromonas luteoviolacea* and induce metamorphosis in the marine tubeworm *Hydroides elegans* or antifeeding prophages (Afp) of *Serratia entomophila* that induce cessation of feeding in a grass grub [335,336,392]. Other examples are R-type pyocins that are bacteriocins expressed by *Pseudomonas aeruginosa* and pierce the membrane of other *Pseudomonas* strains leading to cell lysis or the *Photorabdus* virulence cassette (PVC) that efficiently kills larvae of the wax moth by actin condensation [393–396]. The T6SS is structurally and functionally related to these assemblies, however, it is the only structure that works from inside bacteria and is not released. All these structures use a common contractile tail to pierce bacterial or eukaryotic membranes and in most cases also deliver toxins. R-type pyocins and contractile tailed phages are discussed below as they are the best described systems and exhibit close homology

to T6SSs [237, 332, 379]. A more detailed description including a comparison of T6SS, T4-phage and R-type pyocins can be found in Section IV.1 on page 157.

I.1 R-type Pyocins

Pyocins are bacteriocins released from *Pseudomonas aeruginosa* and can be classified in R-, F- and S-type pyocins [395, 397, 398]. They are classified according to shape and contractability. R-type pyocins are non-flexible contractile structures that are homologous to contractile phage tails and the tail of the bacterial Type VI Secretion System and F-type pyocins are flexible and non-contractile and show homology to phage λ [395]. In contrast, S-type pyocins do not form long structures, but consist of only two proteins for an effector that induces DNA-breakdown and its cognate immunity protein [399, 400]. Structures similar to R-type pyocins have also been found in *Clostridium difficile* or *Proteus vulgaris* and other strains [401–403]. Pyocins are released by a subset of cells from a particular bacterial strain and target related strains based on their lipopolysaccharide (LPS)(only R- and F-type pyocins) [393]. For the scope of this thesis, only R-type pyocins are of relevance and thus will be discussed further.

R-type pyocins are 120 nm long contractile structures and can be considered as the simplest contractile nanomachine [237, 332, 393–395]. As contractile tailed phages and the T6SS, they are composed of a baseplate and a sheathed tube [393]. They also possess a cap and have a defined length [332]. R-type pyocins are organized in one genetic cluster and are expressed under stress for example by UV-light or drugs like Mitomycin C that induce the SOS-response, which correlates with lysis of the producing cell [393, 394, 398, 404, 405]. The SOS-response leads to cell lysis that releases the mature R-type pyocin particle [404]. Upon recognition of the target cell, tail fibers bind to LPS, the baseplate triggers contraction of the sheath, which then expells a spiked inner tube into the target cell [332, 406, 407]. Once the hollow inner tube breached the membrane it allows leakage of cytoplasmic contents and ultimately leads to cell death [332, 408].

R-type pyocin sheaths have a similar interlaced network of β-strands as the T6SS sheath and their proteins a similiar conserved fold [237, 332, 334]. In the extended state, the outer sheath protein contacts the inner tube with an attachment helix that is the major point of interaction between sheath and tube [332]. Interlacing of sheath protomers is maintained during contraction [332]. The high killing efficiency lead to the development of R-type pyocins as targeted antimicrobials [406, 408–410].

I.2 Contractile Tailed Phages

Myoviridae belong to the order *Caudovirales* that encompasses tailed phages [411]. Phages of the family of *Myoviridae* have conserved long contractile tails that show significant structural homology to tails of R-type pyocins and T6SSs [333, 395, 411, 412]. Of this family, phage T4 is the best characterized and will be described in more detail.

Myoviridae like T4 are composed of a long contractile tail and a head [411]. The genome of phage T4 consists of dsDNA and its natural host is *E. coli* [413, 414]. On the end of the tail, the baseplate is localized and serves with its tail fibers for attachment of the phage to its target cell [372, 415, 416]. The tail sheath powers the penetrations of the host cell and is connected to the head via a neck [379, 412, 417–421]. The head (capsid) is a reservoir for the DNA and associated proteins [373, 422, 423]. The neck at the interface between head and tail has different functions in maturation of the phage and release of DNA [417, 424–426]. During maturation it is responsible for efficient packaging of DNA into the head and after host recognition and contraction it mediates the release of the DNA into the host cytoplasm [417, 424–426]. For infection, the long tail fibers recognize LPS and reversibly attach to the host and bring the short tail fibers in close proximity to the host [427–429]. Binding of the short tail fibers to LPS is irreversible and leads to a conformational change in the baseplate from a dome- to a star-shape [372–374, 430]. The conformational change in the baseplate leads to contraction of the sheath, which in turn expells the inner tube with a spiked tip and drills it through the membranes of the host [372, 374, 375, 419, 430]. Then the neck opens and releases the DNA from the head through tube and baseplate into the target cell, where replication of the phage starts [417, 421, 426].

T4-phage has a well described six-fold symmetric baseplate that is connected to a tail fiber network of which the atomic structure is known [372, 415]. The baseplate can be divided into inner-, intermediate- and peripheral baseplate [372]. The tail fiber network composed of gp9, gp10, gp11 and gp12 (short tail fiber, LPS receptor) is attached to the peripheral baseplate [372]. The intermediate baseplate transmits conformational changes occurring in the peripheral baseplate through target interaction to the inner baseplate (wedge) composed of gp6, gp7, gp53 and gp25 [372, 415]. gp25 is the sheath initiator protein from which sheath assembly starts. The innermost part of the baseplate is the central spike composed of gp5 (spike), gp5.4 (spike tip) and gp27 (hub) [372, 415, 416, 431].

The first two layers of the six-start helical tube are formed by gp48 and gp54 and the rest of the sheath is formed by gp19 [432]. Sheath assembly is initiated by gp25 and the sheath is formed by gp18 [378, 391, 412, 418, 433, 434]. The sheath is expected to form the same interlaced network as T6SS-sheath and the sheath of R-type pyocin

[237, 332, 334, 391, 418]. Length of the tail is determined by the ruler protein gp29 and finishes upon incorporation of tail terminator protein gp15 [435, 436]. At the distal end of the tail, the neck connects the tail and the head. The neck forms a ring like structure mainly composed of gp13 and gp14 that attaches to the tail terminator gp15 and regulates DNA release [417, 421]. The head forms a prolate icosahedron and is mainly composed of the major capsid protein gp23* and the vertex protein gp24* (* denotes the protease processed, mature form) [422, 437]. Other components are small outer capsid (soc) and highly antigenic outer capsid (hoc) proteins [422]. Gp24* forms pentamers at the corners of the icosahedron, whereas gp23* forms hexamers on the sides and edges [423, 438]. DNA is packed into the head by packaging motors at the neck before the tail is anchored to the neck [421, 424, 425, 437, 439].

Early studies on the mechanism of contraction of the tail of T4-phage showed that it contracts in a wave-like fashion [440]. A prerequisite for this model is that not all sheath rings contract at the same time but rather ring by ring. Sheath protomers have been shown to undergo rigid-body movements during contraction but otherwise, no major structural rearrangements occur [418, 419, 434]. Upon contraction, the sheath decreases its length from 925 Å to 420 Å and increases its outer diameter from 240 Å to 330 Å [418, 419, 434]. Consequently, also the inner diameter widens from 100 Å to 120 Å and detaches from the inner tube that has an outer diameter of 90 Å [418, 419, 434]. Further studies will reveal atomic structures of the sheath and tube and reveal their molecular interactions with the baseplate and by this lead to deeper insights into how contraction is triggered and propagated through the sheath.

Aims of this work

I started my PhD with the aim to characterize the T6SS sheath structurally and mechanistically. *V. cholerae* and *Pseudomonas aeruginosa* were well established model organisms for studying different aspects of the T6SS. *V. cholerae* has a constitutively active T6SS, that does not aim. In contrast, the T6SS of *P. aeruginosa* is tightly regulated by a membrane-spanning kinase and a phosphatase and is able to sense an attack and aim at this direction. For structural and mechanistic studies, T6SS of *V. cholerae* has advantages of being easily detectable by fluorescence microscopy, as both sheath assembly and disassembly can be monitored with fusions of fluorescent proteins to the sheath component VipA or the disassembly ATPase ClpV.

In the first project, the structure of the contracted T6SS sheath was solved using cryo-electron microscopy to atomic resolution using advances in camera technology as well as image processing algorithms. The structural studies were further supported by mutational analyses that highlighted the importance of specific linker regions in the overall assembly of the sheath. Furthermore, insights into ClpV-binding to sheath were gained and we were able to propose how the sheath attaches to the baseplate. Comparison to known structures of phage sheath proteins highlighted their common evolutionary origin. Due to low stability of the sheath-tube complex in the extended state, it was only possible to characterize the contracted state.

Based on insights we gained from the structure of the sheath in the contracted state and studies on the related R-type pyocins of *P. aeruginosa*, we identified critical features of the sheath that potentially contribute to propagation of contraction through the extended sheath and others that stabilize the sheath in a contracted conformation. We introduced several mutations, of which two changes stabilized the sheath in a non-contracted state, which lead us to propose a model of how contraction is propagated from the baseplate throughout the sheath. We confirmed the model using fluorescence live-cell imaging and could show that the proposed linker and residues are involved in triggering propagation of contraction and stability of the sheath. Furthermore, we showed that mutant sheaths co-assemble with wild-type proteins into the same structure and these assemblies critically

depend on the presence of a functional baseplate. The non-contractile sheaths stably associate with proteins of the membrane complex and a potential cap and additionally contain large amounts of the tube protein Hcp.

Non-contractile mutant sheaths can be isolated from *V. cholerae* which enabled us to solve the structure of the complete sheath-tube assembly. Further experiments using cryo-electron tomography validated that the structure of the mutant non-contractile sheath is similar to wild-type extended sheaths. The structure of the sheath in its extended state highlighted important differences to the contracted state and led to insights into the recognition of contracted sheath by ClpV.

In a fourth project, we structurally characterized both ends of the extended T6SS tail that were previously shown to contain baseplate proteins and a cap on the other end. Challenges in sample preparation limited the resolution to ≈8 Å, however, we were able to reveal a 3-fold symmetry for the central spike and a three-fold symmetry for a peripheral density at the baseplate. Overall the baseplate has a clear six-fold symmetry. The cap shows a central pore and also a clear six-fold symmetry. Due to limitations in resolution no further information can be deduced.

Chapter II

Results

II.1 Research Article I

Structure of the Type VI Secretion System Contractile Sheath.

Mikhail Kudryashev, Ray Yu-Ruei Wang, Maximilian Brackmann, Sebastian Scherer, Timm Maier, David Baker, Frank DiMaio, Henning Stahlberg, Edward H. Egelman and Marek Basler

Cell, Volume 160, Issue 5, 26 February 2015, pages 952–962, DOI: 10.1016/j.cell.2015.01.037

Statement of contribution

I constructed strains, performed bacterial competition assays, immunoblots and isolated mutant sheaths. I performed fluorescence microscopy analysis of mutant *V. cholerae* strains and contributed to data interpretation and manuscript preparation.

Article

Cell

Structure of the Type VI Secretion System Contractile Sheath

Graphical Abstract

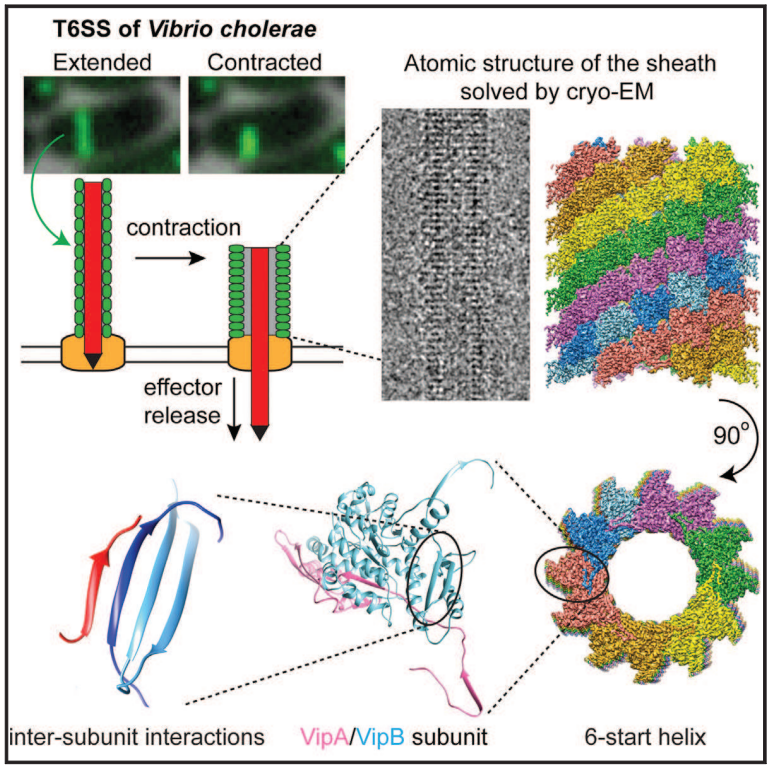

Authors

Mikhail Kudryashev, Ray Yu-Ruei Wang, ..., Edward H. Egelman, Marek Basler

Correspondence

egelman@virginia.edu (E.H.E.), marek.basler@unibas.ch (M.B.)

In Brief

The atomic structure of a bacterial type VI secretion system shows similarities to phage homologs in the sheath core architecture while a distinct outer layer facilitates interactions with the ClpV ATPase that enables multiple rounds of sheath use.

Highlights

- Atomic structure of the bacterial T6SS sheath was solved by cryo-EM
- β-strand-mediated intermolecular interactions stabilize six-start helical assembly
- Structural alignments with phage sheaths indicate conserved mechanism of assembly
- Arrangement of the outer domain of the sheath facilitates recycling by ClpV ATPase

Accession Numbers

EMD-2699
EMPIAR-10019
3J9G

Kudryashev et al., 2015, Cell *160*, 952–962
February 26, 2015 ©2015 Elsevier Inc.
http://dx.doi.org/10.1016/j.cell.2015.01.037

Cell

Article

Structure of the Type VI Secretion System Contractile Sheath

Mikhail Kudryashev,[1,2] Ray Yu-Ruei Wang,[3,4] Maximilian Brackmann,[1] Sebastian Scherer,[2] Timm Maier,[5] David Baker,[3] Frank DiMaio,[3] Henning Stahlberg,[2] Edward H. Egelman,[6,*] and Marek Basler[1,*]

[1]Focal Area Infection Biology, Biozentrum, University of Basel, Klingelbergstrasse 50/70, CH-4056 Basel, Switzerland
[2]Center for Cellular Imaging and NanoAnalytics, Biozentrum, University of Basel, Mattenstrasse 26, CH-4058 Basel, Switzerland
[3]Department of Biochemistry, University of Washington, 1705 NE Pacific Street, Seattle, WA 98195, USA
[4]Graduate Program in Biological Physics, Structure and Design, University of Washington, Box 357350, Seattle, WA 98195, USA
[5]Focal Area Structural Biology, Biozentrum, University of Basel, Klingelbergstrasse 50/70, CH-4056 Basel, Switzerland
[6]Department of Biochemistry and Molecular Genetics, University of Virginia, Charlottesville, VA 22908, USA
*Correspondence: egelman@virginia.edu (E.H.E.), marek.basler@unibas.ch (M.B.)
http://dx.doi.org/10.1016/j.cell.2015.01.037

SUMMARY

Bacteria use rapid contraction of a long sheath of the type VI secretion system (T6SS) to deliver effectors into a target cell. Here, we present an atomic-resolution structure of a native contracted *Vibrio cholerae* sheath determined by cryo-electron microscopy. The sheath subunits, composed of tightly interacting proteins VipA and VipB, assemble into a six-start helix. The helix is stabilized by a core domain assembled from four β strands donated by one VipA and two VipB molecules. The fold of inner and middle layers is conserved between T6SS and phage sheaths. However, the structure of the outer layer is distinct and suggests a mechanism of interaction of the bacterial sheath with an accessory ATPase, ClpV, that facilitates multiple rounds of effector delivery. Our results provide a mechanistic insight into assembly of contractile nanomachines that bacteria and phages use to translocate macromolecules across membranes.

INTRODUCTION

Several critical components of the type VI secretion system (T6SS) are structurally and functionally related to components of contractile tails of bacteriophages. Secreted VgrG and PAAR proteins form a complex similar to phage spike, secreted Hcp is a structural homolog of a phage tube protein, and TssE (type six secretion E) is a homolog of T4 phage baseplate protein gp25 (Leiman et al., 2009; Pukatzki et al., 2007; Shneider et al., 2013). VipA and VipB (TssB and TssC) proteins were shown to form a cog-wheel-like tubular structure in *V. cholerae* (Bönemann et al., 2009) that was noticed to resemble T4 phage gp18 polysheath (Leiman et al., 2009). The VipA/VipB sheath assembles around an inner Hcp tube and is attached to a structure called a baseplate that spans the bacterial membranes (Basler et al., 2012; Brunet et al., 2014; Zoued et al., 2013). Importantly, the VipA/VipB sheath was shown to form a long contractile organelle in *V. cholerae* (Basler et al., 2012; Kapitein et al., 2013) and in *E. coli* (Brunet et al., 2013), suggesting that sheath contraction powers the secretion. In vivo, the contracted sheath is specifically recognized by the ClpV ATPase, which disassembles the sheath by unfolding VipB from the N terminus (Basler and Mekalanos, 2012; Kapitein et al., 2013; Pietrosiuk et al., 2011). Even though sheath contraction has been implicated in powering protein translocation across a membrane for phages, pyocins, and T6SS (Leiman and Shneider, 2012), a mechanistic understanding of this process is currently limited, mostly due to the lack of a high-resolution structure of a native and fully assembled sheath.

There is no high-resolution information available for the T6SS sheath, but several crystal structures are available for fragments of phage sheath proteins (Aksyuk et al., 2009a, 2011). However, a major limitation of these atomic structures is that monomeric proteins were used for crystallization and thus, in principle, cannot reveal atomic details of inter-subunit interactions in a native fully assembled sheath polymer. The structure of the T4 phage sheath polymer was so far solved only at low resolution using electron microscopy (Kostyuchenko et al., 2005; Leiman et al., 2004), again not providing the necessary details to fully understand sheath assembly.

Native T6SS sheath has only been isolated from *V. cholerae* in a contracted form (Basler et al., 2012). Even though the sheath was isolated without the inner Hcp tube, Hcp and other components of T6SS were shown to be necessary for sheath assembly (Basler et al., 2012; Brunet et al., 2014; Kapitein et al., 2013). Indeed, in contrast to a long and regular T6SS sheath that can be isolated from T6SS-positive *V. cholerae* (Basler et al., 2012), VipA/VipB from *P. aeruginosa* and *V. cholerae* heterologously expressed in *E. coli* only form short tubes (Bönemann et al., 2009; Kube et al., 2014; Lossi et al., 2013); electron microscopy of these tubes provided low-resolution density maps (Kube et al., 2014; Lossi et al., 2013). Nonetheless, a recent ~6 Å resolution structure of *V. cholerae* sheath provided insights into a possible mechanism of ClpV-specific disassembly of the contracted sheath (Kube et al., 2014).

Due to recent advances in direct electron detection cameras and software tools (Egelman, 2010; Faruqi et al., 2003; Li et al., 2013; Lu et al., 2014), it is now possible to obtain density maps

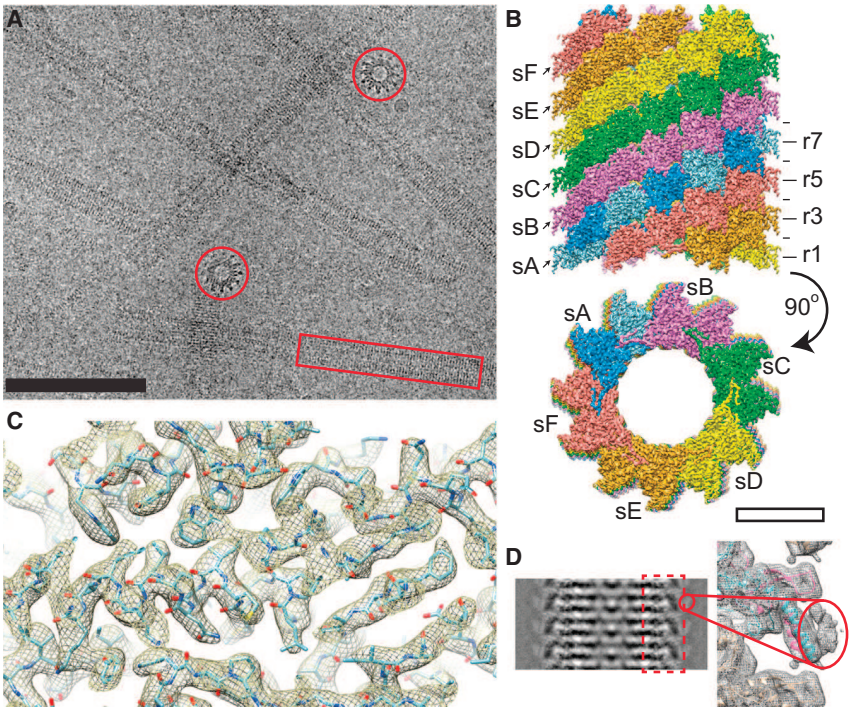

Figure 1. Cryo-EM Structure of the T6SS Sheath

(A and B) (A) A representative low-dose cryo-EM micrograph with side (red box) and top (red circle) views of the sheath. Scale bar, 100 nm; (B) assembly of the protomers into a six start helix; s, individual strands; r, horizontal rings. Scale bar, 10 nm.

(C) An example of the atomic model fitted into the protein density.

(D) Left: a class average of the sheath showing a density on the surface; right: protein density filtered to low resolution showing density of the VipB N terminus and VipA C terminus.

See also Figure S1 and Movie S1.

with a resolution that allows de novo building of atomic models (Kühlbrandt, 2014). These technical advances allowed for directly generating atomic models of the subunit of the mitochondrial ribosome (Amunts et al., 2014) or the ribosome-Sec61 complex (Voorhees et al., 2014) and provided fundamental insights into mechanisms of those macromolecular machines. Here, we used the state-of-the-art electron microscopic approaches and the Rosetta density-guided structural modeling methods to reveal the structure of the contracted VipA/VipB sheath from *V. cholerae* in atomic detail.

RESULTS AND DISCUSSION

Atomic Structure of the VipA/VipB Protomer

We purified the native contracted sheath from *Vibrio cholerae* and imaged it by cryo-electron microscopy (Figure 1A). Fourier transforms of recorded images showed Thon rings up to ~3 Å with layer lines in single micrographs up to a resolution of 5 Å (Figure S1A). Helical reconstruction was performed by the iterative helical real space reconstruction (IHRSR) method (Egelman, 2000) with the final helical parameters being a 21.8 Å axial rise, 29.4° rotation, and a C6 rotational symmetry about the helical axis (Figures 1B, S1B, and S1C and Movie S1). Helical parameters and an overall shape of the sheath are similar to the previously reported structure (Kube et al., 2014); however, our approach allowed us to obtain a resolution of ~3.5–4.0 Å, which improved up to ~3.2 Å for the inner and middle layers of the sheath (Figure S1D). Most of the amino acid side chains and some oxygen atoms in the backbone were resolved in the most ordered parts of the structure (Figure 1C and Movie S1). Even though the resolution of our protein density decreased for the outer surface layer, we were able to de novo trace residues 2 to 126 (out of 168) of VipA and residues 61 to 492 of VipB (Figures 2A, 2B, and S2A–S2E). The VipA C terminus and the VipB N terminus were clearly localized to a less ordered layer on the surface of the sheath as shown in class averages of sheath images (Figures 1D, S1E, and S1F). To further improve the geometry of the side chains, the model was subject to Rosetta density-guided all-atom refinement using a physically realistic energy function (Song et al., 2013; DiMaio et al., 2015). An atomic model built into an independently generated electron microscopy (EM) map of lower resolution had a Cα root-mean-square deviation (RMSD) to the original atomic model of 0.34 Å (see Experiential Procedures), suggesting that model building is highly reliable. Analysis of the conservation and coevolution of VipA/VipB protein residues shows that the conserved residues are generally facing the inner part of the protomer, variable residues are exposed on the protomer surface, and distances between most coevolving residues are within 10 Å (Figure S3 and Table S1).

The atomic model allowed us to calculate energies of protein-protein interactions using PISA (Proteins Interfaces Structures and Assemblies) (Krissinel and Henrick, 2007) and understand how the sheath structure is stabilized in its contracted form. The strongest intermolecular interaction was calculated between VipA and VipB to form a heterodimeric sheath protomer with 1:1 stoichiometry (Table 1 and Figures 2A, 2B, and S2F). Two β strands of VipA and four β strands of VipB intertwine, forming the middle layer of the sheath (domain 2, Figure 2D). VipA further binds to one side of VipB, forming 35 hydrogen bonds and 14 salt bridges. The total interfacial area for this interaction is 3,493 $Å^2$, and ΔG = −54.8 kcal/mol/protomer represents more than half of all the interaction energy within the assembled sheath (Table 1).

Interprotomer Interactions

The interaction surface between VipB proteins on the same helical strand covers ~2,444 $Å^2$, represents about 20% of the total interaction energy, and stabilizes the protomers within the strand. The interface area between VipA and VipB from adjacent

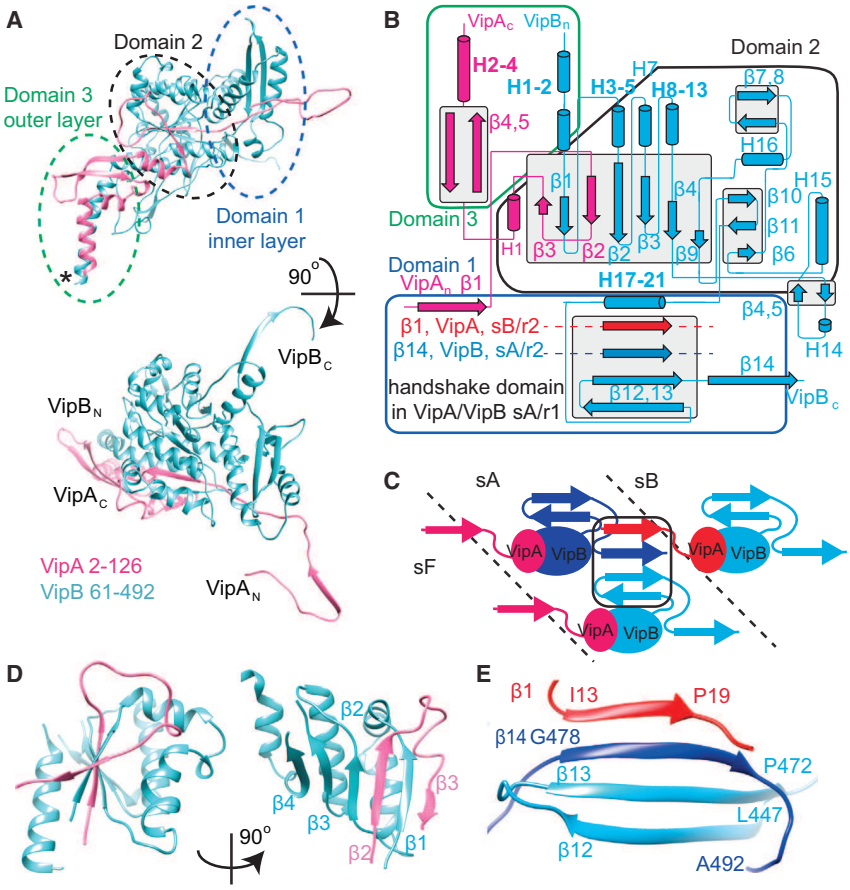

Figure 2. Atomic Model of the Sheath Protomer

(A) An atomic model for VipA (pink) and VipB (blue) with the outlined domains. Domain 3 contains untraced residues predicted to form 5 α helices (location marked with an asterisk [*]).

(B–E) (B) Interactions of secondary structure elements in the protomer; (C) scheme of the handshake domain assembly by three protomers of VipA/VipB; (D) two views of domain 2, six β strands surrounded by 5 α helices stabilizing the interaction between VipA and VipB in the protomer; (E) a "handshake domain" in the domain 1 connecting four β strands: β12 and β13 of VipB in strand A, ring 1 (light blue) with β14 of VipB in strand A, ring 2 (blue), and β1 of VipA in strand B, ring 2 (red). See also Figure S2 and Movie S1.

helical strands is 1,143 Å^2 and contributes ~14.7 kcal/mol/protomer energy to the stabilization of the individual strands within the six-start helix. Together, these interactions represent an energy of 34 kcal/mol/protomer and are the major contributors to sheath stability (Table 1).

Resolution limitations of the previous study (Kube et al., 2014) led to an imprecise segmentation of a sheath subunit from the low-resolution density map (Figure S1G). Interestingly, we show that the subunits are connected by a unique set of interactions in the innermost layer of the sheath. This "handshake" domain is assembled from two anti-parallel β strands (β12 and β13) of one VipB molecule, one parallel β strand (β14) of a second VipB on the same six-start helical strand, and one parallel β strand (β1) of a VipA molecule from a neighboring strand in the six-start helix (Figures 2B, 2C, and 2E).

T6SS and Phage Sheaths Evolved from a Common Ancestor

To understand the evolution of T6SS sheath, we performed a structural alignment between VipA/VipB and a model of T4 phage sheath protein gp18 (Aksyuk et al., 2009a; Fokine et al., 2013) and a crystal structure of *Listeria innocua* phage sheath protein Lin1278 (Aksyuk et al., 2011). In contrast to sequence-based alignments that only detect homology between VipB and phage sheath proteins, we show that domains 1 and 2, composed of both VipA and VipB, are highly conserved and the outer domains 3 and 4 are divergent (Figures 3 and S4). Domain 1 of T6SS sheath and the domain 1 of a model of gp18 or a crystal structure of Lin1278 align with RMSD of 2.7 Å and 2.2 Å, respectively. RMSDs between the domain 2 of the T6SS sheath and the crystal structures of the domain 2 of gp18 or Lin1278 are 3.7 Å and 2.8 Å, respectively.

Interestingly, the architecture of domain 1 differs between phage and T6SS. In both phage sheath proteins, the first two β strands have the same orientation as in the T6SS sheath, but the third β strand has an opposite orientation, and the fourth β strand is missing (Figures 3A and 3B). Because the phage sheath structures were solved for monomers and not for fully assembled polymers, it is tempting to speculate that, in a fully assembled phage sheath, the corresponding handshake domain has the same architecture as in the native T6SS sheath and connects subunits and strands in the same manner as in T6SS.

The fundamental difference between phage and T6SS sheath is that phage sheath is used only once, whereas T6SS sheath is recycled in vivo by ClpV (Basler and Mekalanos, 2012; Kapitein et al., 2013). Moreover, phages act in an extracellular space, whereas the T6SS sheaths are functioning in bacterial cytoplasm. Here, we show that the major difference between phage and T6SS sheaths is in the outer layer, which is not only structurally different but also positioned differently on the sheath surface. In the case of the T4 phage sheath, the domains 3 and 4 are inserted between β1 and H3 of VipB in the domain 2 (Figures 3A, 3B, and S4). On the other hand, the T6SS sheath has its domain 3 inserted between H1 of VipA and H2 of VipB (Figures 3A, 3B, and S4). This leads to a major difference in the angle between domain 3 and domain 2 compared to phage sheath architecture. Furthermore, the outermost layer of the phage sheaths is formed mostly by β strands (Aksyuk et al., 2009a, 2011), whereas the T6SS sheath outer layer is predicted to be composed of five α helices (Figures S2A and S2B).

Table 1. Energy of Interactions between VipA/VipB in the Sheath Assembly

	Interface Area, Å^2	Number of H-H Bonds	Number of Salt Bridges	ΔG kcal/mol	% of Interaction Energy
VipA-B main interface	3493	35	14	−54.8	57
VipB-B interaction in the strand	2444	33	14	−19.3	20
VipA-B between the strands	1143	7	2	−14.7	15
VipA-B in the horizontal ring	634	11	4	−4.5	5
VipB-B vertical interaction	454	5	2	−3.0	3

Even though the overall fold of domains 1 and 2 of phage and T6SS is conserved, the T6SS sheath has several potentially functional insertions compared to phage sheath (Figure 4A). The VipA/VipB protomer has two weakly conserved extra helices in the domain 1: VipB H17 and VipB H21. VipB H17 (aa 374–386) interacts with a loop of the next VipA in a strand (aa 18–24, originating from the handshake domain). A weakly conserved loop and a short VipB H21 interact with a loop (aa 412–415) close to VipB H19.

As hypothesized previously (Basler and Mekalanos, 2012; Kapitein et al., 2013; Kube et al., 2014), after the sheath contraction, the VipB N terminus is likely exposed on the sheath surface to allow disassembly by ClpV. Although an atomic model of an extended T6SS sheath is not available yet, it is likely that the N terminus of VipB is not accessible for binding by ClpV in the extended state to prevent disassembly of the extended sheath. We show that domain 3 is exposed on the surface of the contracted sheath, aligning the domains 3 from the neighboring strands on top of one another. This is in agreement with the recently proposed model (Kube et al., 2014); however, here we show that two helices from $VipA_C$ and three from $VipB_N$ are exposed on the surface. This indeed makes the VipB N terminus fully accessible for disassembly by ClpV (Figure 3D), as suggested previously (Kube et al., 2014), but raises a possibility that VipA is involved in properly positioning VipB on the sheath surface. Furthermore, our atomic model suggests that precise positioning of domain 3 could be stabilized by interactions of three T6SS-specific insertions into the surface of VipB in domain 2: short helices H8–H13, a loop R246–N276, and an outward facing hairpin β7–β8. These insertions appear to form a network of hydrophobic interactions with the domain 3 at the outer surface of the sheath (Figure 4B). Hairpin β7–β8 forms an interaction with the H8-H13 of the VipB in the neighboring strand and with the loop VipB246-276. Loop VipB246-276 interacts with the two long helices VipA H4 and VipB H1 of the domain 3 from the inside, whereas the other hairpin VipA β3-β4 stabilizes them from the outside. The two long helices are further stabilized by a helix-helix interaction with the conserved interfaces (Figure 4A).

Attachment of the Sheath to the Baseplate

Whole-cell cryo-electron tomography provided only a low-resolution structure of the sheath (Basler et al., 2012), and therefore it is not possible directly from those data to orient the VipA/VipB structure relative to a baseplate in the bacterial cell wall. However, considering the degree of structural similarity between T6SS and phage, it is likely that VipA and VipB are oriented relative to the baseplate in the same way as gp18 in T4 phage (Aksyuk et al., 2009a). In Figure 3A, and all other similar top views, the baseplate would be located behind the plane of view; on all side views, like the inset of Figure 3A, the baseplate would be located on the bottom. This orientation of the VipA/VipB protomer suggests that two β strands per subunit are free to bind to an unknown T6SS component in the baseplate (Figure 3A). A natural interacting partner for those two β strands would be a structure similar to an "empty" 2-β-stranded handshake domain organized in a hexameric ring similarly to an actual sheath ring.

A search for structural homologs of the T6SS sheath revealed that protein NP_952040.1 from *Geobacter sulfurreducens* (PDB: 2IA7), a homolog of the T4 phage baseplate protein gp25, aligns with the T6SS sheath domain 1 with an RMSD of 2.7 Å (Figure 5A). As noted previously (Leiman and Shneider, 2012), phage sheath domain 1 has a fold that is similar to that of gp25-like protein (Figure 5B). Importantly, gp25 is positioned near the sheath in the T4 phage baseplate (Aksyuk et al., 2009b).

In a fully assembled handshake domain of T6SS sheath, the orientation of the third β strand (counting from the lumen of the sheath) is parallel to the second β strand but antiparallel in crystal structures of gp25 and its homolog (Figures 5A and S5). We detected significantly coevolving, and thus potentially interacting, residues only between the first two β strands of gp25 (Figure S5). This suggests that, similarly to the sheath handshake domain, only two β strands of gp25 are present in a native assembly. The third β strand of the gp25 could flip out of the domain and interact with yet another component of the baseplate. Therefore, gp25 could accept two additional β strands from interacting proteins in a similar mechanism to the mechanism of sheath subunit interaction.

Interestingly, T6SS component TssE was suggested to be a homolog of gp25 (Leiman et al., 2009; Lossi et al., 2011), co-purifies with the T6SS sheath in *V. cholerae* (Basler et al., 2012), and is important for sheath assembly (Basler et al., 2012; Kapitein et al., 2013). We therefore speculate that the TssE protein could be the part of the T6SS baseplate that accepts VipA-β1 and VipB-β14 strands of the first sheath ring and thus initiates the sheath assembly and also anchors the sheath to the baseplate (Figure 5C). Moreover, TssG and TssK were shown to copurify with sheath in *V. cholerae* (Basler et al., 2012), and VipB was shown to interact with TssK in *E. coli* (Zoued et al., 2013), suggesting that additional proteins are likely involved in attaching the sheath to the baseplate as well. A stable attachment of a contractile sheath to a baseplate is likely crucial for generation of the force needed to deliver substrates across target cell membranes. The sheath has to bind to the baseplate as strongly as individual sheath rings bind together—otherwise, the sheath would likely detach from the baseplate during a rapid contraction.

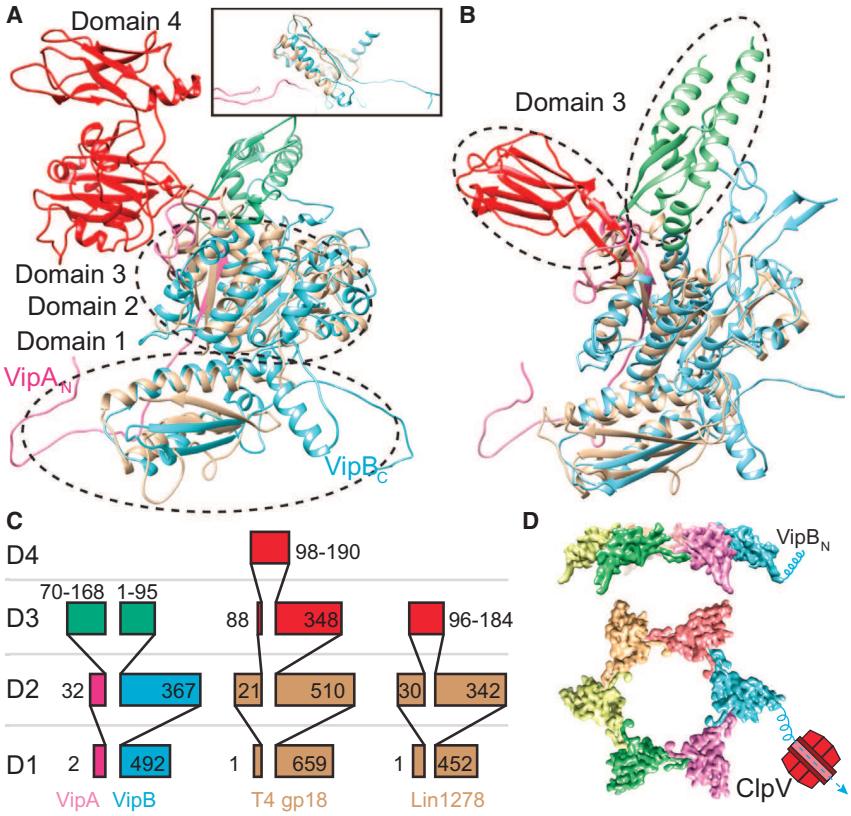

Figure 3. Structural Homology between the T6SS and Phage Sheaths

(A and B) Structural alignment of VipA/VipB (pink/blue) with (A) model of full-length T4 phage sheath gp18 (PDB: 3J2N), the inset shows a side view from the sheath lumen; (B) *L. innocua* phage sheath Lin1278 (PDB: 3LML). Structurally homologous domains 1 and 2 of phage sheaths are shown in brown; divergent domains 3 are shown in red for phage tails and in green for VipA/VipB.

(C) A scheme depicting domain organization of VipA/VipB, gp18, and Lin1278 (partially adapted from Leiman and Shneider [2012]).

(D) One ring of protomers showing N terminus of VipB exposed to the outer surface of the sheath making it accessible to be disassembled by ClpV. See also Figure S4.

Interactions in the Handshake Domain Are Critical for T6SS Sheath Assembly and Dynamics

Our structural data indicate that interactions between β strands in domain 1 are important for initiation of sheath polymerization, extension, and potentially also for sheath contraction. To test this, we generated truncated versions of VipA and VipB lacking β1 and β14, respectively. In a background of a fully functional VipA-msfGFP chromosomal fusion, we show that deletion of *vipB* abolishes sheath assembly and target cell killing (Figures 6A and 6C and Movie S2). As shown in Figures 6A–6C and Movie S2, sheath assembly and target cell killing can be restored by a wild-type level of expression of a full-length VipB from a plasmid, but not by a similar level of expression of a mutant lacking β14 (VipB-ΔC). This indicates that a connection between the sheath protomers on the same strand is essential for sheath assembly and T6SS function.

To assess the role of β1 strand of VipA, we compared dynamics of a full-length VipA-sfGFP expressed in *vipA* deletion background with dynamics of β1 strand deletion mutant (VipA-ΔN). As shown on Figure 6D and Movie S3, the wild-type sheaths rapidly assemble and contract in almost all cells during 5 min. Sheaths with disrupted domain 1 are capable of assembling into structures resembling extended wild-type sheaths but exhibit very little dynamics (Figures 6D and 6E and Movie S3). On average, we observe only one assembly event per ~500 cells over 5 min. Furthermore, the time of sheath assembly is increased for the VipA-ΔN sheath to about 2 min (Figure 6E), whereas most of wild-type sheaths fully assemble in 20 to 40 s under the same conditions. This clearly indicates that a fully assembled handshake domain is critical for efficient sheath assembly initiation and the fast assembly rate of the T6SS sheath. Interestingly, even though we inspected sheath dynamics in ~50,000 cells over 5 min, we identified only 5 examples of unambiguous sheath contraction and disassembly (one example is given in Figure 6E). This suggests that the ability to contract is preserved to some degree but raises the possibility that domain 1 is involved in triggering sheath contraction in vivo. Alternatively, the rate of sheath assembly may play a role in triggering sheath contraction. Target cell killing in *vipA* deletion background was restored by expression of VipA-sfGFP, but not by expression of VipA-ΔN-sfGFP mutant (Figure 6C), suggesting that mere ability to assemble sheaths is not sufficient for T6SS-dependent killing.

Concluding Remarks

The unusual four-strand β sheet handshake domain assembled from three molecules invites comparisons with other protein polymers. In most protein filaments that have been intensively studied, such as F-actin (von der Ecken et al., 2014; Galkin et al., 2015), microtubules (Alushin et al., 2014), bacterial flagellar filaments (Yonekura et al., 2003), or type IV pili (Craig et al., 2006), subunits can be treated as compact, and the assemblies are held together by the exclusion of solvent at the buried interfaces (Miller et al., 1987). In contrast to these, type I pili from bacteria have a polymerization mechanism that involves an N-terminal extension of one subunit that becomes a β strand within a β sheet of an adjacent subunit (Waksman and Hultgren, 2009). This β sheet formed by two subunits gives a remarkable stability to the filaments and allows type I pili to resist very large shear forces (Castelain et al., 2011; Miller et al., 2006). We expect that this architecture allows the sheath to transfer a large force and remain intact during its rapid contraction.

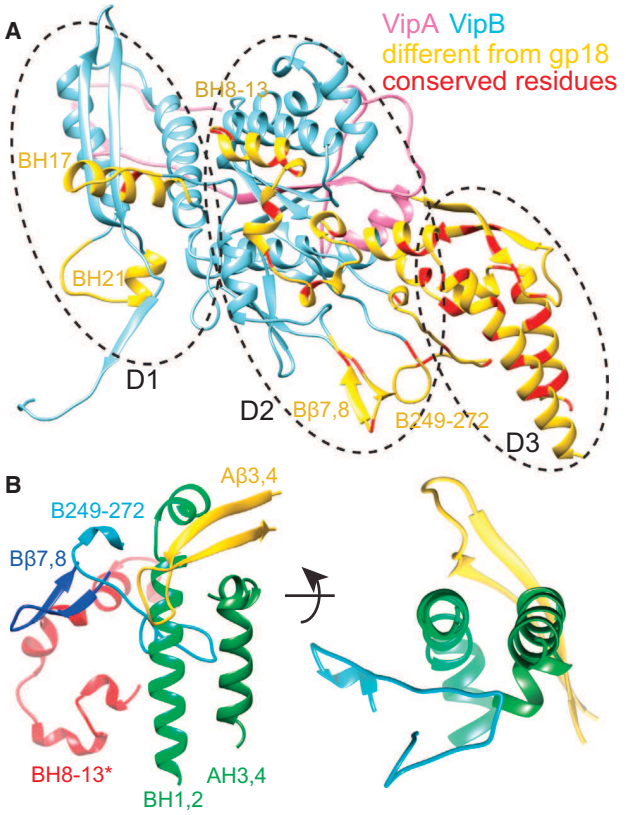

Figure 4. Divergence of the T6SS Sheath from the Phage Sheath

(A) VipA/VipB protomer (pink/blue) with the additional insertions compared to phage sheath Lin1278 marked in yellow; residues with sequence conservation over 70% are marked in red.

(B) Interaction network in the outer domain of VipA/VipB. BH 8–13* are part of VipB in the neighboring subunit.

See also Figure S3.

EXPERIMENTAL PROCEDURES

Bacterial Strains and DNA Manipulations

V. cholerae 2740-80 parental and *ΔvipA* strains and the pBAD24-VipA-sfGFP plasmid were described previously (Basler et al., 2012). pBAD24-VipA-ΔN-sfGFP plasmid was created by replacing *vipA* gene in pBAD24-VipA-sfGFP plasmid with a gene lacking codons encoding 23 N-terminal amino acids using standard methods. *V. cholerae* 2740-80 *vipA-msfGFP* strain was created by replacing *vipA* on the chromosome with *vipA-msfGFP* fusion by *sacB*-mediated allelic exchange using the pWM91 suicide plasmid as described previously (Basler and Mekalanos, 2012; Basler et al., 2012; Bina and Mekalanos, 2001; Metcalf et al., 1996). msfGFP differs from previously used sfGFP by Val 206 to Lys substitution, which was previously described to reduce dimerization of GFP (Zacharias et al., 2002). Comparison of VipA-msfGFP to VipA-sfGFP expressed from pBAD24 plasmid in *ΔvipA* strain revealed no difference in dynamics of the fusion proteins (data not shown). The linker between VipA and msfGFP was 3xAla 3xGly, as used previously on pBAD24 plasmid (Basler et al., 2012). To limit effects of the fusion gene on the downstream genes in the T6SS locus, we added the last 21 bp of *vipA* at the end of *vipA-msfGFP*. *V. cholerae* 2740-80 *vipA-msfGFP ΔvipB* strain was created by replacing *vipB* with a gene encoding "MMSTTEKGRLDQA" peptide (first seven and last six residues of *vipB* fused in frame) by allelic exchange as described above and was done previously (Basler et al., 2012). Standard techniques were used to clone a PCR-amplified *vipB* or the first 477 codons of *vipB* to pBAD24 plasmid (Guzman et al., 1995) to generate pBAD24-VipB and pBAD24-VipB-ΔC plasmids, respectively. All PCR-generated products were verified by sequencing. Plasmids were transformed to *V. cholerae* by electroporation. Gentamicin-resistant *E. coli* MG1655 strain was used in bacterial killing assays. Strain list provided as Table S2.

Antibiotic concentrations used were streptomycin (100 μg/ml), ampicillin (200 μg/ml), and gentamicin (15 μg/ml). Luria-Bertani (LB) broth was used for all growth conditions. Liquid cultures were grown aerobically at 37°C.

Fluorescence Microscopy

Procedures similar to those described previously (Basler et al., 2012) were used to detect fluorescence signal in *V. cholerae*. Overnight cultures of *V. cholerae* carrying pBAD24-vipA-sfGFP, pBAD24-vipA-ΔN-sfGFP, pBAD24-vipB, or pBAD24-vipB-ΔC were washed by LB and diluted 50× into fresh LB supplemented with ampicillin, streptomycin, and 0.003% arabinose for VipA and 0.006% arabinose for VipB and cultivated for 2.5–3.0 hr to optical density (OD) at 600 nm of about 0.8–1.2. Strains without plasmid were grown similarly, but no ampicillin and arabinose was added. Cells from 100 μl of the culture were re-suspended in 5–10 μl of fresh LB (to OD ~10), spotted on a thin pad of 1% agarose in LB, and covered with a glass coverslip. Cells were immediately imaged at room temperature using an objective heated to 37°C. Microscope configuration similar to the one described previously (Basler et al., 2013) was used: Nikon Ti-E inverted motorized microscope with Perfect Focus System and Plan Apo 100× Oil Ph3 DM (NA 1.4) objective lens. SPECTRA X light engine (Lumencore), ET-GFP (Chroma #49002) filter set was used to excite and filter fluorescence. sCMOS camera pco.edge 4.2 (PCO, Germany) (pixel size 65 nm) and VisiView software (Visitron Systems, Germany) were used to record images. Fiji (Schindelin et al., 2012) was used for all image analysis and manipulations as described previously (Basler et al., 2013). Contrast on compared sets of images was adjusted equally. All imaging experiments were performed with three biological replicates.

Bacterial Killing Assay

V. cholerae 2740-80 strains and *E. coli* MG1655 strain were incubated overnight at 37°C in LB supplemented with appropriate antibiotics. Cultures were washed in fresh LB, diluted 100×, and grown to OD 0.8–1.2 in presence of appropriate antibiotics and 0.01% arabinose for strains with pBAD24 plasmids. Cells were washed and mixed at final OD of ~10 in 10:1 ratio (*V. cholerae* to *E. coli*) as specified, and 5 μl of the mixture was spotted on a dry LB agar plate containing 0.01% arabinose but no antibiotics. After 3 hr, bacterial spots were cut out and the cells were re-suspended in 0.5 ml LB. The cellular suspension was serially diluted (1:10) in LB, and 5 μl of the suspensions were spotted on selective plates (gentamicin for *E. coli* and streptomycin for *V. cholerae*). Colonies were counted after ~16 hr incubation at 30°C. Three biological replicates were analyzed.

VipA/VipB Sheath Purification

Sheath was purified similarly to a previous method (Basler et al., 2012). An overnight culture of *flgG* in-frame deletion mutant of the parental *V. cholerae* 2740-80 strain (Basler et al., 2012) was diluted 1:200 into 1,000 ml of fresh LB and then shaken at 37°C for 2.5–3.0 hr to reach an OD of 1.0–1.5. Cells were cooled on ice, centrifuged for 10 min 7,000 × *g* and lysed in 50 ml lysis buffer (150 mM NaCl, 20 mM Tris [pH 8], lysozyme 200 μg/ml, DNase I 50 μg/ml, 5 mM EDTA, 0.1% SDS, 0.5% Triton X-100). Cell lysis was complete after 5–10 min incubation at 37°C. To activate DNase to cleave DNA, $MgCl_2$ was added to 10 mM final concentration and, after 2–5 min incubation at 37°C, EDTA was added to reach 15 mM final concentration. Cell debris was removed by centrifugation for 20 min at 10,000 × *g*. Cleared lysates were subjected to ultraspeed centrifugation at 150,000 × *g* for 1 hr at 4°C. Pellets were re-suspended in 1 ml in TND buffer (150 mM NaCl, 20 mM Tris [pH 8], 0.5% Triton-100, 0.1% SDS), and insoluble material was removed by centrifugation for 1 min at 10,000 × *g*. Supernatant was diluted to 50 ml in TND buffer and subjected to ultraspeed centrifugation at 150,000 × *g* for 1 hr at 4°C. Pellet was washed with 2 ml of PBS and resuspended in 2 ml PBS. Insoluble material was removed by centrifugation for 1 min at 10,000 × *g*. Supernatant was diluted to 50 ml by PBS and subjected to ultraspeed centrifugation at 150,000 × *g* for 1 hr at 4°C. Pellet was washed by 2 ml of PBS and resuspended in 1 ml PBS, and insoluble material

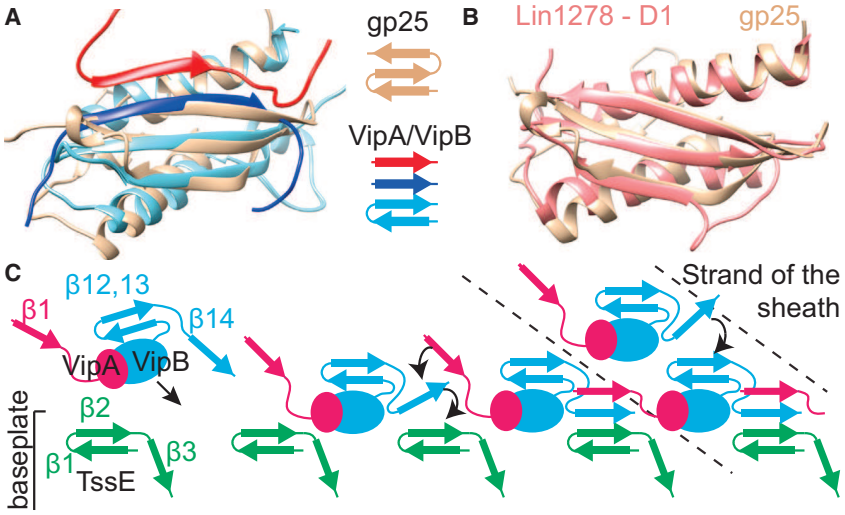

Figure 5. Evolutionary Conservation of the Handshake Interactions and Sheath Assembly Initiation

(A) Structural alignment of the gp25-like phage protein from *G. sulfurreducens* (brown, PDB: 2IA7) and a T6SS sheath handshake domain containing VipB (light blue), VipB from the next subunit on the same strand (blue), and VipA from the next strand (red).

(B) Alignment of the gp25-like phage protein from *G. sulfurreducens* (brown) and domain 1 of phage sheath Lin1278 (red).

(C) A model for sheath assembly initiation and polymerization as viewed from inside the tube: recruitment of VipA/VipB protomers (through their free β strand) to the baseplate protein TssE (providing 2 β strands); establishment of the full 4-β-stranded handshake domain starting with VipB, followed by VipA; recruitment of additional VipA/VipB protomers to the newly formed ring.

See also Figure S5.

was removed by centrifugation for 1 min at 10,000 × *g*. Supernatant contained pure sheath. Purity was assessed by Coomassie stained gel, and protein concentration was measured by standard approaches.

Peptide-Specific Antibodies

Antigen-purified rabbit polyclonal antibodies raised against VipB peptide QENPPADVRSRRPL were obtained commercially (GenScript, USA). Specificity of the antibodies was tested on *V. cholerae* strains expressing or lacking *vipB*.

Cell Fractionation and Immunoblot Analysis

Cells from 250 μl culture prepared for imaging as described above were resuspended in 100 μl PBS and subjected to sonication (20 cycles, 100% amplitude, 0.5 s cycle) (UIS215V Hielscher Ultrasonics GmbH, Germany). Then 10 μl of 10% SDS was added, and the sample was sonicated as before. Samples were incubated for 10 min at 95°C, centrifuged, and 17 μl were mixed with 7 μl 4× NuPAGE LDS Sample Buffer (Life Technologies) and 2 μl 1 M DTT. Samples were heated again for 10 min at 72°C, centrifuged, and loaded on 4%–12% pre-cast polyacrylamide gels (Life Technologies) and transferred to nitrocellulose membrane (Amersham Biosciences, UK). Membrane was blocked by 5% milk in Tris buffered saline (pH 7.4) containing Tween 0.1% (TBST), incubated with primary peptide antibody for 16 hr at 4°C, washed with TBST, incubated for 1.5 hr with horseradish peroxidase-labeled anti-rabbit antibody (Jackson Lab), and washed with TBST, and peroxidase was detected by LumiGLO Chemiluminescent Substrate (Cell Signaling Technology, USA).

Cryo-Electron Microscopy

Sample was placed on holey carbon grids (Quantifoil GmbH, Germany) and plunge frozen into liquid ethane cooled down to LN_2 temperature using a Vitrobot MK4 (FEI Corp, the Netherlands). Frozen grids were stored in LN_2 and directly observed in a Titan Krios (FEI Corp, the Netherlands) operated at 300 kV and quipped with a K2 Summit direct electron detector (Gatan, Pleasanton, CA). All images were acquired in a single 2 day session at a defocus range of 0.5–1.5 μm. Images were recorded in dose fractionation mode, with a dose rate 3–4 e^-/pix/s, exposures per image sub-frames between 1 and 1.5 $e^-/Å^2$ and a cumulative dose for the entire image series of 30 $e^-/Å^2$. The final pixel size for the resulting 3838×3710 pix^2 images was 1.0 Å/pix.

Image Processing and 3D Reconstruction

Alignment for beam-induced movement was performed by 2 dx_automator (Scherer et al., 2014) that provides on-the-fly drift correction based on the algorithm implemented by Li et al. (2013). Images recorded as movie data in "counting mode" were drift corrected with the algorithm by Li et al. (2013). The quality of the images drastically improved after drift correction, especially at high resolution (Figure S1A). Drift on the order of 10 Å could be fixed and resulted in Thon rings up to 3–3.5 Å. All recorded frames up to 30 $e^-/Å^2$ were used, and no weighting was performed. From the recorded ~250 images, the best 77 were selected based on ice thickness and the quality of the Thon rings. Contrast transfer function (CTF) determination was performed by CTFFIND3 (Mindell and Grigorieff, 2003). This led to exclusion of one image, due to a poor fit between the theoretical and observed Thon ring pattern. The images were then multiplied by the estimated CTF in SPIDER to both correct phases and to improve the SNR. Filaments were boxed using the e2helixboxer function within EMAN2 (Tang et al., 2007), using a box width of 600 pixels for the initial alignment and 384 pixels for the final reconstruction. The SPIDER software package (Frank et al., 1996) was used for most subsequent steps. From the long boxes, overlapping segments were cut that were 600 pixels long with a shift of 30 pixels between boxes, where the shift (yielding 95% overlap) was chosen to be ~1.5× the axial rise per subunit. A total of 10,203 segments were obtained. The segments were then padded to 600 × 600 pixels and decimated to 200 × 200 pixels size (3 Å/pix) for initial alignments and reconstruction using IHRSR (Egelman, 2000). Once these were reconstructed, the original images were subsequently decimated to 300 × 300 pixels for further processing that included out-of-plane tilts. Finally, the initial boxes were windowed to 384 × 384 pixels for several cycles of IHRSR with 1.0 Å/pix until convergence. At the end of each iteration, helical symmetry with a rise of 21.8 Å and a rotation of 29.4 degrees with C6 symmetry was applied. Class averages for Figures 1D and S1F were generated using Spring (Desfosses et al., 2014).

To test reproducibility of the atomic model building, a completely independent EM-density map was generated, starting from the initial micrographs followed by independent particle picking using the e2helixboxer function within EMAN2 (Tang et al., 2007). Square boxes of 400 Å length (1 Å/pix) were picked with a step of 30 Å. Iterative real space helical reconstruction (Egelman, 2000) was performed with Spring (Desfosses et al., 2014), starting with a featureless cylinder as an initial model. At the end of each iteration, C6 symmetry was applied to the reference. All segments were processed as one data set, and resolution estimated by Fourier Shell Correlation between the half data sets was 4.3 Å (FSC = 0.5).

Atomic Model Building

Model building was done de novo, with initial models of a single subunit built first, and then the system was refined in a symmetrical complex with all the interacting subunits present. A model of a single-subunit VipA/VipB was manually built in Coot (Emsley et al., 2010), guided by an initial partial model from Buccaneer (Cowtan, 2006), which placed a total of 513 residues into the density map. In parallel, automated model building was carried out independently

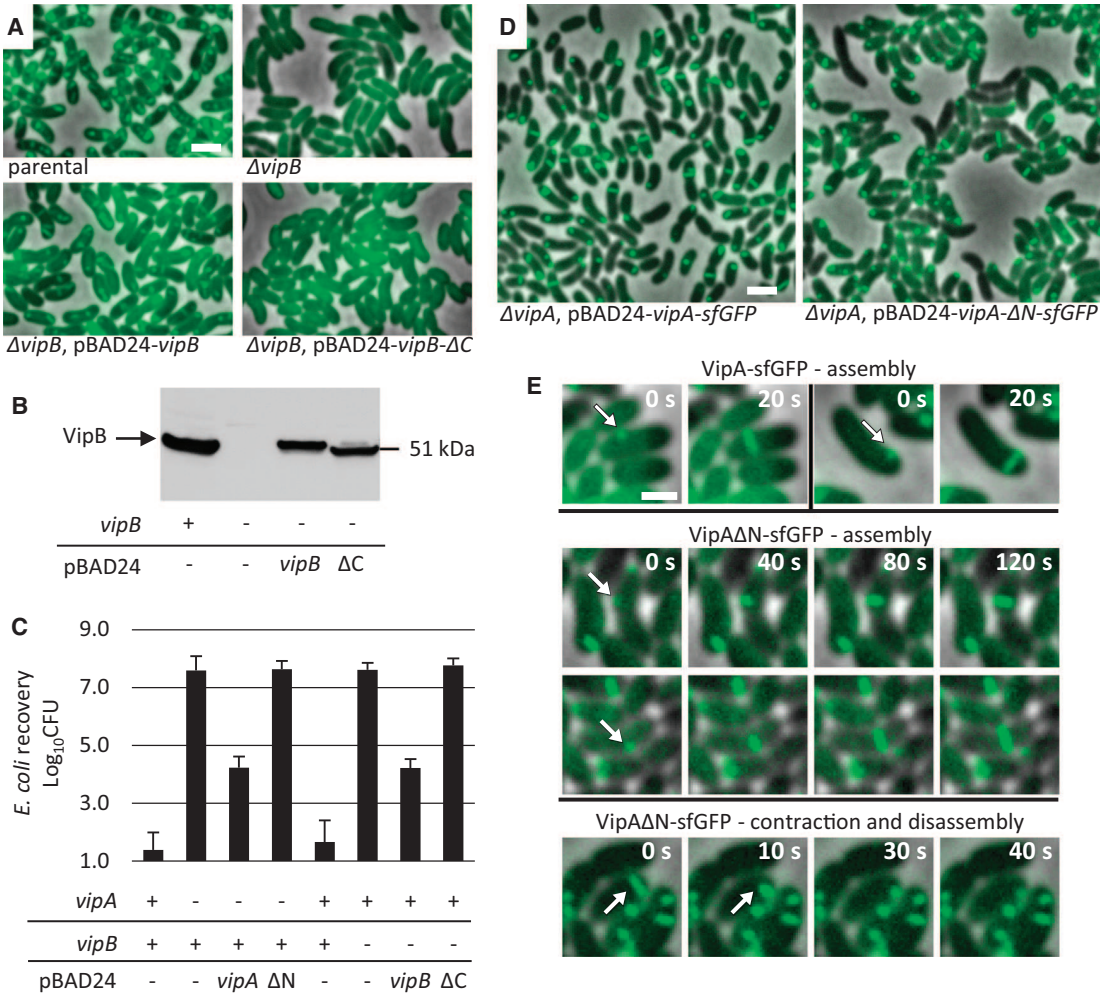

Figure 6. Handshake Domain Integrity Is Important for Sheath Dynamics

(A) Sheath assembly was detected by fluorescence microscopy. Parental strain, *V. cholerae* with VipA-msfGFP fusion encoded in the native locus. Deletion of *vipB* gene was complemented by expression of either WT *vipB* or *vipB* lacking C-terminal β strand (VipB-ΔC) from pBAD24 plasmid. 15 × 10 μm fields of cells are shown. Bar is 1 μm. See also Movie S2.

(B) Expression of VipB or VipB-ΔC was detected in the indicated strains prepared as for the imaging shown in (A) by western blotting using VipB-specific antibody.

(C) Level of *E. coli* killing on a plate was measured for indicated strains after 3 hr of incubation at 10:1 ratio. Presence or absence of *vipA* or *vipB* on the chromosome is indicated by "−" or "+," respectively. Complementation was from pBAD24 plasmid carrying indicated genes. ΔN, *vipA* lacking N-terminal β strand; ΔC, *vipB* lacking C-terminal β strand. Data are represented as mean ± SD.

(D) Sheath assembly was detected by fluorescence microscopy. Parental strain, *V. cholerae vipA*$^{-}$. Deletion of *vipA* gene was complemented by expression of either WT *vipA* or *vipA* lacking N-terminal β strand (VipA-ΔN) from pBAD24 plasmid. 20 × 20 μm field of cells shown. Bar is 1 μm. See also Movie S3.

(E) Dynamics of sheath assembly for WT VipA (two examples, top) and VipA lacking N-terminal β strand (VipA-ΔN) (two examples, middle). An example of sheath contraction and disassembly is shown for VipA-ΔN (bottom).

using a newly developed approach (Wang et al., 2015). The automated method uses sequence-derived backbone conformations with side-chain density fit to accurately assign sequence into density maps. Starting with a map segmented to containing a single subunit, the computational method was able to place 466 residues into the density.

The two independently derived models showed reasonably good agreement: 394 residues were assigned in both models with a Cα RMSD of 1.05 Å. However, there were parts of the protein assigned in each model that were unassigned in the other. Thus, to build and refine the final model, we used RosettaCM (Song et al., 2013), a comparative modeling protocol that assembles protein structures by recombining portions of several models; in this case, the inputs were the two independently traced models. RosettaCM was guided by experimental density data, with agreement to the density map as an additional score term while building and refining models. A total of 1,000 models were generated, and a best model was selected based on the all-atom energy plus the "fit to density" energy.

Using this model, a final refinement step was carried out in the context of the symmetrical assembly, improving model geometry and relieving clashes at the symmetric interfaces (DiMaio et al., 2015). The final model shows very good agreement to the density, with 504 of 558 traced residues matching the map with real-space correlations of 0.60 or greater (using *density_tools* in Rosetta), and very good model geometry, with 0.36% Ramachandran outliers, 0% rotamer outliers, a Molprobity clash score of 2.15, and an overall Molprobity score of 1.38 (Chen et al., 2010).

To test for overfitting during model building, we uniformly perturbed the final model and refined it against the independently generated EM map. A long refinement cycle (1,000 cycles of backbone rebuilding) was used to ensure the refined model is unbiased from the model fit to the original reconstruction. The resulting model had 0.34 Å Cα RMSd to the original model.

Atomic B factors were capped to 600 for heavy atoms and to 720 for H atoms. Methionine in position 1 of VipA was not included in the model due to a lack of EM density and evidence from mass spectrometry analysis of isolated sheath (data not shown) that it is not present on the N terminus.

Molecular Analysis

Interaction energy was calculated using PISA (Krissinel and Henrick, 2007). Secondary structure prediction for the Figures S2A and S2B was performed by Jnet (Cole et al., 2008). Structural alignments were performed by RaptorX (Wang et al., 2013), and the RMSD presented in the text are calculated from these alignments. Structural homologs were found using PDB Structure Navigator (http://pdbj.org/strucnavi).

Evolutionary Constraints

Evolutionary constraints were generated by the Gremlin server (http://gremlin.bakerlab.org/) (Ovchinnikov et al., 2014) or FreeContact software (Kaján et al., 2014). All reliable constraints with scores over 1.5 are listed in Table S1. The distance in 3D was measured between the weighted centers of mass of the contacting residues. The distance was also estimated between the contacting residues in the neighboring protomers, and in case the inter-protomer distance was less than intra-protomer distance, the inter-protomer distance was used in Table S1. This was implemented using Matlab (Mathworks).

Coloring of the EM maps was done with Dynamo package for electron tomographic image processing (Castaño-Díez et al., 2012). The visualization of atomic models, evolutionary constraints, and rendering of the Movie S1 was performed in UCSF Chimera (Pettersen et al., 2004).

ACCESSION NUMBERS

The EM map was deposited to EMDB (http://www.emdatabank.org/) with an accession number EMD-2699. Electron micrographs used for processing were deposited to EMPIAR (http://www.ebi.ac.uk/pdbe/emdb/empiar/) with an accession number EMPIAR-10019. Atomic coordinates were deposited to PDB (http://www.rcsb.org) with an accession number 3J9G.

SUPPLEMENTAL INFORMATION

Supplemental Information includes five figures, two tables, and three movies and can be found with this article online at http://dx.doi.org/10.1016/j.cell.2015.01.037.

AUTHOR CONTRIBUTIONS

M.K. performed cryo-EM analysis, built a manual atomic model with T.M., interpreted the data, and wrote the manuscript. R.Y.-R.W., F.D., and D.B. performed automated model building and refinement and contributed to data interpretation. M. Brackmann generated new plasmids and strains, imaged sheath dynamics, performed bacterial killing assays, analyzed protein levels by western blot, and contributed to data analysis and interpretation. S.S. contributed to data collection and processing. T.M. built a manual atomic model with M.K. H.S. supervised data collection and contributed essential analytical tools. E.H.E. performed cryo-EM image analysis and made critical contributions to data interpretation. M. Basler analyzed and interpreted the data and wrote the manuscript. All authors participated in writing the manuscript.

ACKNOWLEDGMENTS

We thank Mihai Ionescu for excellent technical assistance in preparation of the sheath sample. We thank Kenneth Goldie and Bill Anderson for expert assistance with cryo-EM and Venkat Dandey for support with software. Grant support was from NIH EB001567 (to E.H.E.), Swiss systems biology initiative SystemsX.ch grant CINA, and NIH R01GM092802 (to R.Y.-R.W. and D.B.).

Received: September 5, 2014
Revised: November 17, 2014
Accepted: January 20, 2015
Published: February 26, 2015

REFERENCES

Aksyuk, A.A., Leiman, P.G., Kurochkina, L.P., Shneider, M.M., Kostyuchenko, V.A., Mesyanzhinov, V.V., and Rossmann, M.G. (2009a). The tail sheath structure of bacteriophage T4: a molecular machine for infecting bacteria. EMBO J. *28*, 821–829.

Aksyuk, A.A., Leiman, P.G., Shneider, M.M., Mesyanzhinov, V.V., and Rossmann, M.G. (2009b). The structure of gene product 6 of bacteriophage T4, the hinge-pin of the baseplate. Structure *17*, 800–808.

Aksyuk, A.A., Kurochkina, L.P., Fokine, A., Forouhar, F., Mesyanzhinov, V.V., Tong, L., and Rossmann, M.G. (2011). Structural conservation of the myoviridae phage tail sheath protein fold. Structure *19*, 1885–1894.

Alushin, G.M., Lander, G.C., Kellogg, E.H., Zhang, R., Baker, D., and Nogales, E. (2014). High-resolution microtubule structures reveal the structural transitions in αβ-tubulin upon GTP hydrolysis. Cell *157*, 1117–1129.

Amunts, A., Brown, A., Bai, X.C., Llácer, J.L., Hussain, T., Emsley, P., Long, F., Murshudov, G., Scheres, S.H.W., and Ramakrishnan, V. (2014). Structure of the yeast mitochondrial large ribosomal subunit. Science *343*, 1485–1489.

Basler, M., and Mekalanos, J.J. (2012). Type 6 secretion dynamics within and between bacterial cells. Science *337*, 815.

Basler, M., Pilhofer, M., Henderson, G.P., Jensen, G.J., and Mekalanos, J.J. (2012). Type VI secretion requires a dynamic contractile phage tail-like structure. Nature *483*, 182–186.

Basler, M., Ho, B.T., and Mekalanos, J.J. (2013). Tit-for-tat: type VI secretion system counterattack during bacterial cell-cell interactions. Cell *152*, 884–894.

Bina, J.E., and Mekalanos, J.J. (2001). Vibrio cholerae tolC is required for bile resistance and colonization. Infect. Immun. *69*, 4681–4685.

Bönemann, G., Pietrosiuk, A., Diemand, A., Zentgraf, H., and Mogk, A. (2009). Remodelling of VipA/VipB tubules by ClpV-mediated threading is crucial for type VI protein secretion. EMBO J. *28*, 315–325.

Brunet, Y.R., Espinosa, L., Harchouni, S., Mignot, T., and Cascales, E. (2013). Imaging type VI secretion-mediated bacterial killing. Cell Rep. *3*, 36–41.

Brunet, Y.R., Hénin, J., Celia, H., and Cascales, E. (2014). Type VI secretion and bacteriophage tail tubes share a common assembly pathway. EMBO Rep. *15*, 315–321.

Castaño-Díez, D., Kudryashev, M., Arheit, M., and Stahlberg, H. (2012). Dynamo: a flexible, user-friendly development tool for subtomogram averaging of cryo-EM data in high-performance computing environments. J. Struct. Biol. *178*, 139–151.

Castelain, M., Ehlers, S., Klinth, J., Lindberg, S., Andersson, M., Uhlin, B.E., and Axner, O. (2011). Fast uncoiling kinetics of F1C pili expressed by uropathogenic Escherichia coli are revealed on a single pilus level using force-measuring optical tweezers. Eur. Biophys. J. *40*, 305–316.

Chen, V.B., Arendall, W.B., 3rd, Headd, J.J., Keedy, D.A., Immormino, R.M., Kapral, G.J., Murray, L.W., Richardson, J.S., and Richardson, D.C. (2010). MolProbity: all-atom structure validation for macromolecular crystallography. Acta Crystallogr. D Biol. Crystallogr. *66*, 12–21.

Cole, C., Barber, J.D., and Barton, G.J. (2008). The Jpred 3 secondary structure prediction server. Nucleic Acids Res. *36*, W197–W201.

Cowtan, K. (2006). The Buccaneer software for automated model building. 1. Tracing protein chains. Acta Crystallogr. D Biol. Crystallogr. *62*, 1002–1011.

Craig, L., Volkmann, N., Arvai, A.S., Pique, M.E., Yeager, M., Egelman, E.H., and Tainer, J.A. (2006). Type IV pilus structure by cryo-electron microscopy and crystallography: implications for pilus assembly and functions. Mol. Cell *23*, 651–662.

Desfosses, A., Ciuffa, R., Gutsche, I., and Sachse, C. (2014). SPRING - an image processing package for single-particle based helical reconstruction from electron cryomicrographs. J. Struct. Biol. *185*, 15–26.

DiMaio, F., Song, Y., Li, X., Brunner, M.J., Xu, C., Conticello, V., Egelman, E., Marlovits, T., Cheng, Y., and Baker, D. (2015). Atomic- accuracy models from 4.5-Å cryo-electron microscopy data with density-guided iterative local refinement. Nat. Methods. Published online February 23, 2015. http://dx.doi.org/10.1038/NMETH.3286.

Egelman, E.H. (2000). A robust algorithm for the reconstruction of helical filaments using single-particle methods. Ultramicroscopy *85*, 225–234.

Egelman, E.H. (2010). Reconstruction of helical filaments and tubes. Methods Enzymol. *482*, 167–183.

Emsley, P., Lohkamp, B., Scott, W.G., and Cowtan, K. (2010). Features and development of Coot. Acta Crystallogr. D Biol. Crystallogr. *66*, 486–501.

Faruqi, A.R., Cattermole, D.M., Henderson, R., Mikulec, B., and Raeburn, C. (2003). Evaluation of a hybrid pixel detector for electron microscopy. Ultramicroscopy *94*, 263–276.

Fokine, A., Zhang, Z., Kanamaru, S., Bowman, V.D., Aksyuk, A.A., Arisaka, F., Rao, V.B., and Rossmann, M.G. (2013). The molecular architecture of the bacteriophage T4 neck. J. Mol. Biol. *425*, 1731–1744.

Frank, J., Radermacher, M., Penczek, P., Zhu, J., Li, Y., Ladjadj, M., and Leith, A. (1996). SPIDER and WEB: processing and visualization of images in 3D electron microscopy and related fields. J. Struct. Biol. *116*, 190–199.

Galkin, V.E., Orlova, A., Vos, M.R., Schröder, G.F., and Egelman, E.H. (2015). Near-atomic resolution for one state of f-actin. Structure *23*, 173–182.

Guzman, L.M., Belin, D., Carson, M.J., and Beckwith, J. (1995). Tight regulation, modulation, and high-level expression by vectors containing the arabinose PBAD promoter. J. Bacteriol. *177*, 4121–4130.

Kaján, L., Hopf, T.A., Kalaš, M., Marks, D.S., and Rost, B. (2014). FreeContact: fast and free software for protein contact prediction from residue co-evolution. BMC Bioinformatics *15*, 85.

Kapitein, N., Bönemann, G., Pietrosiuk, A., Seyffer, F., Hausser, I., Locker, J.K., and Mogk, A. (2013). ClpV recycles VipA/VipB tubules and prevents non-productive tubule formation to ensure efficient type VI protein secretion. Mol. Microbiol. *87*, 1013–1028.

Kostyuchenko, V.A., Chipman, P.R., Leiman, P.G., Arisaka, F., Mesyanzhinov, V.V., and Rossmann, M.G. (2005). The tail structure of bacteriophage T4 and its mechanism of contraction. Nat. Struct. Mol. Biol. *12*, 810–813.

Krissinel, E., and Henrick, K. (2007). Inference of macromolecular assemblies from crystalline state. J. Mol. Biol. *372*, 774–797.

Kube, S., Kapitein, N., Zimniak, T., Herzog, F., Mogk, A., and Wendler, P. (2014). Structure of the VipA/B type VI Secretion complex suggests a contraction-state-specific recycling mechanism. Cell Rep. *8*, 20–30.

Kühlbrandt, W. (2014). Biochemistry. The resolution revolution. Science *343*, 1443–1444.

Leiman, P.G., and Shneider, M.M. (2012). Contractile tail machines of bacteriophages. Adv. Exp. Med. Biol. *726*, 93–114.

Leiman, P.G., Chipman, P.R., Kostyuchenko, V.A., Mesyanzhinov, V.V., and Rossmann, M.G. (2004). Three-dimensional rearrangement of proteins in the tail of bacteriophage T4 on infection of its host. Cell *118*, 419–429.

Leiman, P.G., Basler, M., Ramagopal, U.A., Bonanno, J.B., Sauder, J.M., Pukatzki, S., Burley, S.K., Almo, S.C., and Mekalanos, J.J. (2009). Type VI secretion apparatus and phage tail-associated protein complexes share a common evolutionary origin. Proc. Natl. Acad. Sci. USA *106*, 4154–4159.

Li, X., Mooney, P., Zheng, S., Booth, C.R., Braunfeld, M.B., Gubbens, S., Agard, D.A., and Cheng, Y. (2013). Electron counting and beam-induced motion correction enable near-atomic-resolution single-particle cryo-EM. Nat. Methods *10*, 584–590.

Lossi, N.S., Dajani, R., Freemont, P., and Filloux, A. (2011). Structure-function analysis of HsiF, a gp25-like component of the type VI secretion system, in Pseudomonas aeruginosa. Microbiology *157*, 3292–3305.

Lossi, N.S., Manoli, E., Förster, A., Dajani, R., Pape, T., Freemont, P., and Filloux, A. (2013). The HsiB1C1 (TssB-TssC) complex of the Pseudomonas aeruginosa type VI secretion system forms a bacteriophage tail sheathlike structure. J. Biol. Chem. *288*, 7536–7548.

Lu, A., Magupalli, V.G., Ruan, J., Yin, Q., Atianand, M.K., Vos, M.R., Schröder, G.F., Fitzgerald, K.A., Wu, H., and Egelman, E.H. (2014). Unified polymerization mechanism for the assembly of ASC-dependent inflammasomes. Cell *156*, 1193–1206.

Metcalf, W.W., Jiang, W., Daniels, L.L., Kim, S.K., Haldimann, A., and Wanner, B.L. (1996). Conditionally replicative and conjugative plasmids carrying lacZ alpha for cloning, mutagenesis, and allele replacement in bacteria. Plasmid *35*, 1–13.

Miller, S., Lesk, A.M., Janin, J., and Chothia, C. (1987). The accessible surface area and stability of oligomeric proteins. Nature *328*, 834–836.

Miller, E., Garcia, T., Hultgren, S., and Oberhauser, A.F. (2006). The mechanical properties of E. coli type 1 pili measured by atomic force microscopy techniques. Biophys. J. *91*, 3848–3856.

Mindell, J.A., and Grigorieff, N. (2003). Accurate determination of local defocus and specimen tilt in electron microscopy. J. Struct. Biol. *142*, 334–347.

Ovchinnikov, S., Kamisetty, H., and Baker, D. (2014). Robust and accurate prediction of residue-residue interactions across protein interfaces using evolutionary information. eLife *3*, e02030.

Pettersen, E.F., Goddard, T.D., Huang, C.C., Couch, G.S., Greenblatt, D.M., Meng, E.C., and Ferrin, T.E. (2004). UCSF Chimera—a visualization system for exploratory research and analysis. J. Comput. Chem. *25*, 1605–1612.

Pietrosiuk, A., Lenherr, E.D., Falk, S., Bönemann, G., Kopp, J., Zentgraf, H., Sinning, I., and Mogk, A. (2011). Molecular basis for the unique role of the AAA+ chaperone ClpV in type VI protein secretion. J. Biol. Chem. *286*, 30010–30021.

Pukatzki, S., Ma, A.T., Revel, A.T., Sturtevant, D., and Mekalanos, J.J. (2007). Type VI secretion system translocates a phage tail spike-like protein into target cells where it cross-links actin. Proc. Natl. Acad. Sci. USA *104*, 15508–15513.

Scherer, S., Kowal, J., Chami, M., Dandey, V., Arheit, M., Ringler, P., and Stahlberg, H. (2014). 2dx_automator: implementation of a semiautomatic high-throughput high-resolution cryo-electron crystallography pipeline. J. Struct. Biol. *186*, 302–307.

Schindelin, J., Arganda-Carreras, I., Frise, E., Kaynig, V., Longair, M., Pietzsch, T., Preibisch, S., Rueden, C., Saalfeld, S., Schmid, B., et al. (2012). Fiji: an open-source platform for biological-image analysis. Nat. Methods *9*, 676–682.

Shneider, M.M., Buth, S.A., Ho, B.T., Basler, M., Mekalanos, J.J., and Leiman, P.G. (2013). PAAR-repeat proteins sharpen and diversify the type VI secretion system spike. Nature *500*, 350–353.

Song, Y., DiMaio, F., Wang, R.Y.-R., Kim, D., Miles, C., Brunette, T., Thompson, J., and Baker, D. (2013). High-resolution comparative modeling with RosettaCM. Structure *21*, 1735–1742.

Tang, G., Peng, L., Baldwin, P.R., Mann, D.S., Jiang, W., Rees, I., and Ludtke, S.J. (2007). EMAN2: an extensible image processing suite for electron microscopy. J. Struct. Biol. *157*, 38–46.

von der Ecken, J., Müller, M., Lehman, W., Manstein, D.J., Penczek, P.A., and Raunser, S. (2014). Structure of the F-actin—tropomyosin complex. Nature. Published online December 1, 2014. http://dx.doi.org/10.1038/nature14033.

Voorhees, R.M., Fernández, I.S., Scheres, S.H.W., and Hegde, R.S. (2014). Structure of the mammalian ribosome-Sec61 complex to 3.4 Å resolution. Cell *157*, 1632–1643.

Waksman, G., and Hultgren, S.J. (2009). Structural biology of the chaperone-usher pathway of pilus biogenesis. Nat. Rev. Microbiol. *7*, 765–774.

Wang, S., Ma, J., Peng, J., and Xu, J. (2013). Protein structure alignment beyond spatial proximity. Sci. Rep. *3*, 1448.

Wang, R.Y.-R., Kudryashev, M., Li, X., Egelman, E.H., Basler, M., Cheng, Y., Baker, D., and DiMaio, F. (2015). De novo protein structure determination from near-atomic-resolution cryo-EM maps. Nat. Methods. Published online February 23, 2015. http://dx.doi.org/10.1038/NMETH.3287.

Yonekura, K., Maki-Yonekura, S., and Namba, K. (2003). Complete atomic model of the bacterial flagellar filament by electron cryomicroscopy. Nature *424*, 643–650.

Zacharias, D.A., Violin, J.D., Newton, A.C., and Tsien, R.Y. (2002). Partitioning of lipid-modified monomeric GFPs into membrane microdomains of live cells. Science *296*, 913–916.

Zoued, A., Durand, E., Bebeacua, C., Brunet, Y.R., Douzi, B., Cambillau, C., Cascales, E., and Journet, L. (2013). TssK is a trimeric cytoplasmic protein interacting with components of both phage-like and membrane anchoring complexes of the type VI secretion system. J. Biol. Chem. *288*, 27031–27041.

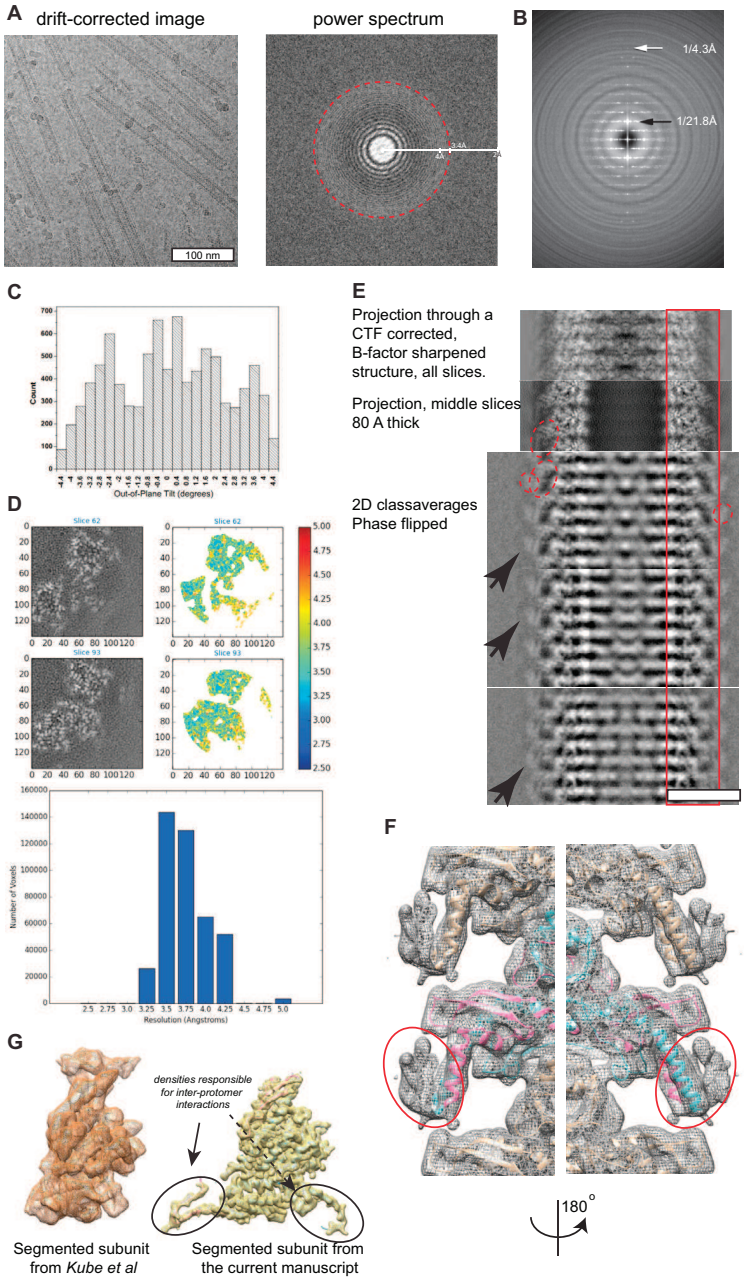

Figure S1. Cryo-EM Imaging, Image Processing, and EM-Map Resolution, Related to Figure 1

(A) An example micrograph showing Thon rings up to the water ring and beyond. Scale bar: 100 nm.

(B) Average power spectrum and out-of plane tilt of the segments. Overlapping filament segments (384 pix long) with an out-of-plane tilt of less than 2 degrees (n = 4045) were used to create this averaged power spectrum. The log of the intensities is shown in order to display the large dynamic range. The black arrow shows the meridional reflection at 1/(21.8 Å), while the gray arrow shows the fifth order of this meridional at 1/(4.3 Å).

(C). Histogram of out-of plane tilt of all segments used in the final reconstruction.

(D) Right: slices through the structure, view from the top. Voxel length is 1 Å. Left: local resolution estimated by Resmap corresponding to the slices from (right) colored accordingly to the heat map on the right. Note that solvent typically has lower resolution than the density suggesting that the reported average value is lower than the best resolved parts of the structure. Bottom: histogram of the local resolution values.

(E) Slices through the 3D map (top) and class averages (bottom) show density at the outer surface of the sheath. Scale bar: 10 nm.

(F) Isosurface visualization of the map filtered to low resolution reveals density at the outer surface of the sheath.

(G) Comparison of segmented protomers from low (Kube et al., 2014; left) and high (current manuscript, right) resolution structures of VipA/VipB.

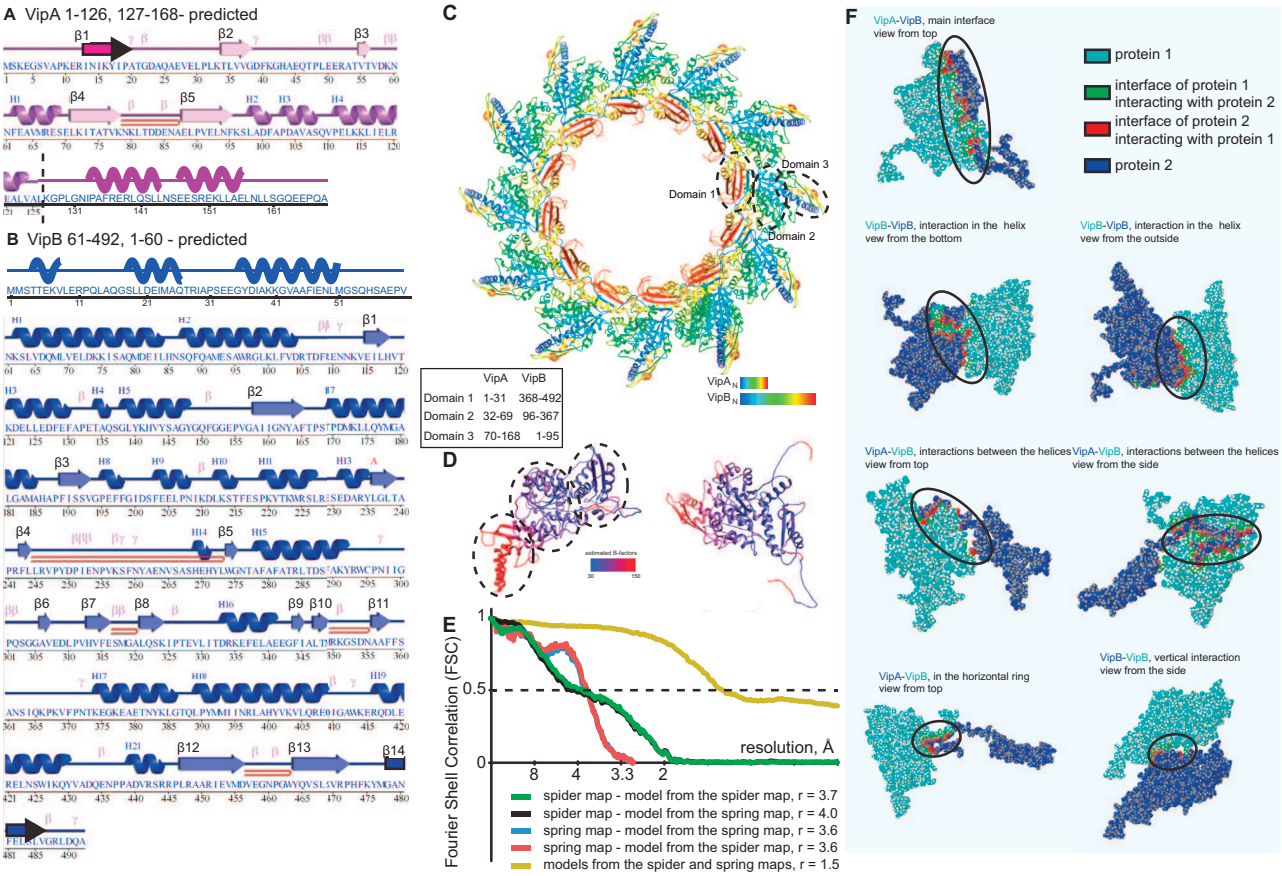

Figure S2. Atomic Model of the VipA/VipB Sheath, Related to Figure 2

(A and B) Secondary structure prediction done with Jnet (Cole et al., 2008). The beta strands 1 for VipA and 14 for VipB are parts of the handshake domain of the neighboring dimers. Secondary structure elements match Figure 2B.

(C) Arrangement of the protomers in the helix. The residues are color-coded starting from N-term; two rings are shown.

(D) Atomic model color-coded according to the estimated B-factors of residues.

(E) Fourier Shell Correlations between the atomic models built into the independently generated EM maps.

(F) Interfaces were calculated by PISA based on the structure of the helical assembly. For the corresponding energies see Table 1.

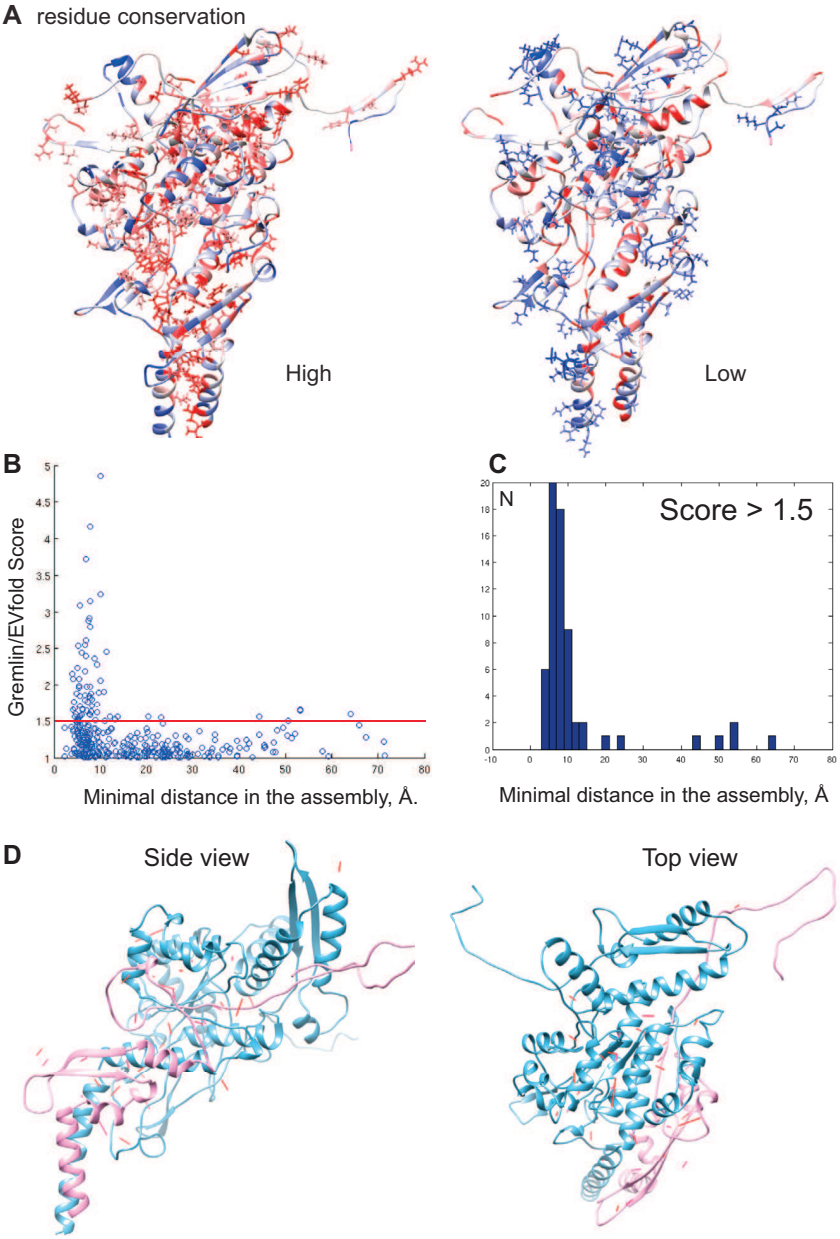

Figure S3. Conservation and Evolution of the VipA/VipB Residues, Related to Figure 4

(A) Atomic model color-coded according to conservation (red – conserved, blue – variable). Non-conserved residues are typically located at the surface, their side chains point outside. Side chains of residues with conservation above 70% (red) or below 30% (blue) are displayed.

(B–D) Analysis of co-evolving residues: (B) a scatter plot of all the 3D distances against the coupling score. Horizontal line indicated a coupling score threshold of 1.5. (C) Histogramof all the 3D distances with the prediction scores over 1.5. (D) The evolutionary connections between VipA-VipA, VipB-VipB and VipA-VipB with a score over 1.5 and distance less than 10 Å are displayed on the 3D structures with red lines. The full list of reliable constraints is in Table S1.

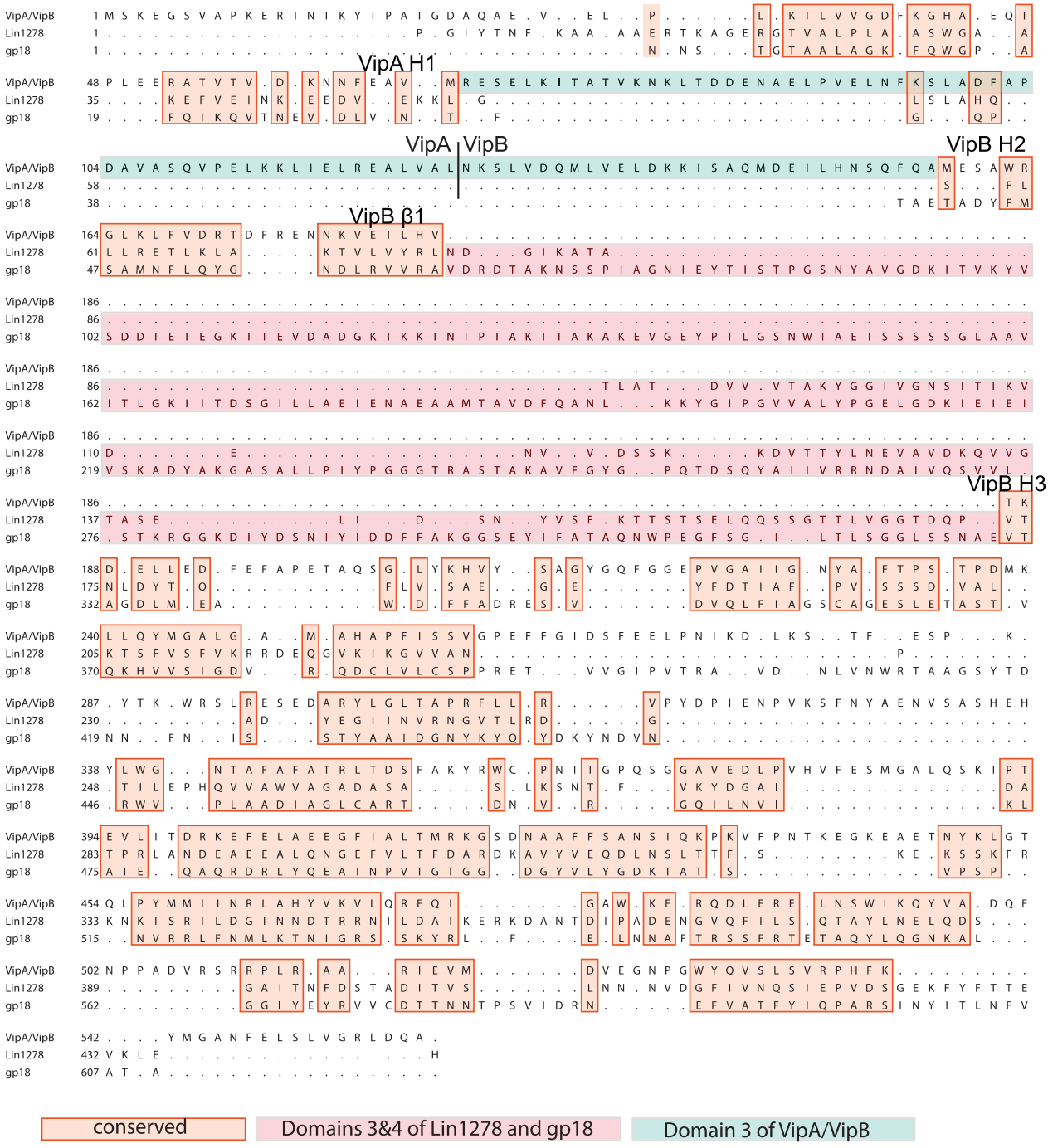

Figure S4. Sequence Alignment of VipA/VipB, Lin1278, and gp18 Based on Structural Homology in Figure 3, Related to Figure 3

Structurally conserved residues are boxed with orange, variable outer domains – red and green. Corresponding secondary structures are labeled according to text and Figure S2.

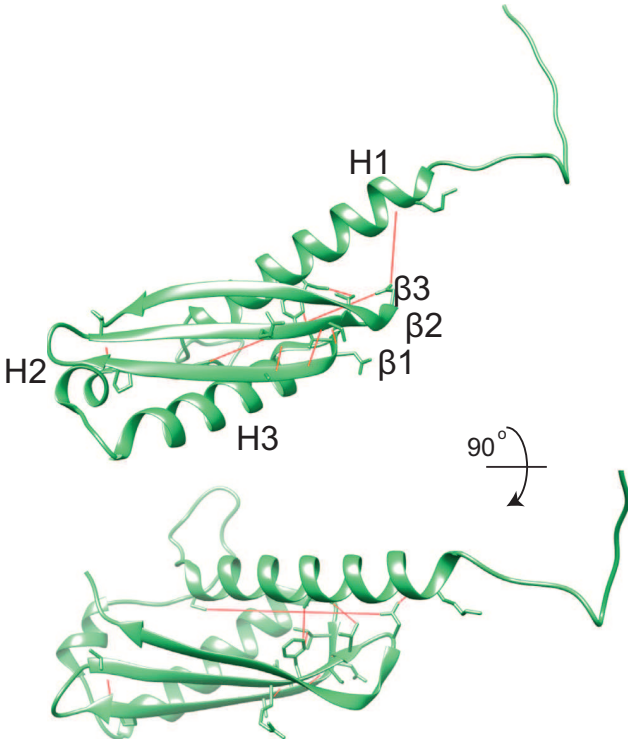

Evolutionary constraints for β2

Residue 1		Residue 2		Gremlin Scaled Score	Secondary structure element
112	V	32	I	1.913	Helix 1
111	S	91	L	1.795	Beta 1
109	R	92	A	1.705	Beta 1
110	F	88	I	1.408	Beta 1
111	S	89	D	1.176	Beta 1
110	F	32	I	1.13	Helix 1
114	D	55	C	1.061	loop
103	T	97	P	1.034	Beta 1
114	D	21	K	1.006	Helix 1

Figure S5. Evolutionary Constraints of the T4 Phage Protein gp25, Related to Figure 5

Evolutionary constraints for the gp25 protein from the T4 phage were generated by Gremlin; the constraints for β2 are displayed with the red lines on the crystal structure 4HRZ and are listed in the table. Note presence of evolutionary connections between β1 and β2 and no connections between β2 and β3. N = 351, Seq/len = 2.9.

II.2 Research Article II

Type VI secretion system sheath inter-subunit interactions modulate its contraction.

Maximilian Brackmann, Jing Wang and Marek Basler

EMBO Reports, 8 December 2017, e201744416, DOI: 10.15252/embr.201744416

Statement of contribution

I planned, designed and constructed sheath mutations, analyzed T6SS dynamics with fluorescence microscopy, isolated mutant sheaths and analyzed them by electron microscopy, immunoblot and mass spectrometry. I analyzed and interpreted data, wrote the initial draft and contributed to finalization of the manuscript.

Scientific Report

SOURCE DATA | OPEN ACCESS

EMBO reports

Type VI secretion system sheath inter-subunit interactions modulate its contraction

Maximilian Brackmann, Jing Wang & Marek Basler*

Abstract

Secretion systems are essential for bacteria to survive and manipulate their environment. The bacterial type VI secretion system (T6SS) generates the force needed for protein translocation by the contraction of a long polymer called sheath. The sheath is a six-start helical assembly of interconnected VipA/VipB subunits. The mechanism of T6SS sheath contraction is unknown. Here, we show that elongating the N-terminal VipA linker or eliminating charge of a specific VipB residue abolishes sheath contraction and delivery of effectors into target cells. Mass spectrometry analysis identified the inner tube protein Hcp, spike protein VgrG, and other components of the T6SS baseplate significantly enriched in samples of the stable non-contractile sheaths. The ability to lock the T6SS in the pre-firing state opens new possibilities for understanding its mode of action.

Keywords contractile tails; microbiology; phages; type VI secretion system
Subject Categories Microbiology, Virology & Host Pathogen Interaction; Structural Biology
DOI 10.15252/embr.201744416 | Received 27 April 2017 | Revised 7 November 2017 | Accepted 17 November 2017

Introduction

Bacteria have evolved various protein nanomachines to translocate macromolecules across biological membranes. A subset of these nanomachines is composed of a rigid tube surrounded by a contractile sheath, which is attached to a baseplate. The sheath is initially assembled in a high-energy, extended state and then quickly transits to a low-energy, contracted state. The sheath contraction pushes the inner tube, through a membrane complex into the target cell, where it delivers its cargo. The bacterial type VI secretion system (T6SS) uses this mechanism to deliver proteins across membranes [1–5].

Biogenesis of the T6SS starts by formation of an integral membrane complex of TssJ, TssL, and TssM on which the baseplate assembles [6,7]. TssE, TssF, TssG, and TssK constitute the baseplate with a trimer of the spike protein VgrG in the center [6,8]. Baseplate assembly is required to initiate polymerization of the hexameric tube protein Hcp. The tube serves as a template for rapid polymerization of the extended sheath composed of heterodimeric protomers of VipA (TssB) and VipB (TssC) [9–13]. In addition, two different classes of TssA proteins are important for the initiation of T6SS sheath assembly and its elongation [14,15], which progresses throughout the whole cell and thus allows the use of live-cell fluorescence microscopy to monitor sheath dynamics [1,7,16–19]. Contraction of the T6SS sheath pushes the spike and the inner tube out of the cell into a neighboring cell, which leads to the delivery of effectors that are associated with the spike or the inner tube [20–22]. Among substrates of the T6SS are anti-eukaryotic as well as anti-bacterial effectors that are used for host interaction and inter-bacterial competition [23–25].

The sheath can be described as a six-start helix and thus with six strands or as a stack of rings composed of six VipA/VipB heterodimeric subunits, which are interconnected by N- and C-terminal linkers in the inner domain of the sheath [26,27]. Inner domains of sheaths of contractile phage, R-type pyocin, and T6SS likely maintain the connectivity of the sheath during contraction and are evolutionarily related to each other; however, the surface-exposed domains are distinct [12,26–32]. Specifically, T6SS sheath contains a surface-exposed Domain 3 that plays a crucial role in sheath recycling [26,27,31,32]. The mechanism of T6SS sheath contraction is largely unknown because the sheath contracts during isolation from cells, and thus, characterization of the extended sheath was not possible until recently [1,32].

Here, we identified two structural features of the T6SS sheath that play a critical role in its contraction. Using live-cell fluorescence microscopy, we show that a single negatively charged residue located on the surface of the middle domain of the T6SS sheath is required for sheath contraction but not sheath assembly. We further show that the VipA N-terminal linker is critical for sheath contraction. Insertion of two and more amino acid residues into this linker completely abrogated contraction and allowed us to isolate non-contractile sheaths from cells for mass spectrometry and electron microscopy analysis. This analysis revealed that non-contracted sheaths are stably associated with the inner Hcp tube and components of the T6SS baseplate. Overall, comparison of T6SS sheaths of *Francisella novicida* and *Vibrio cholerae* and the sheath of R-type pyocins shows that conserved structural features are involved in sheath contraction and provides insights into T6SS assembly and its mode of action.

Focal Area Infection Biology, Biozentrum, University of Basel, Basel, Switzerland
*Corresponding author. Tel: +41 61 207 21 10; E-mail: marek.basler@unibas.ch

Results and Discussion

VipB residue D333 is important for contraction *in vivo*

Interactions of charged residues were previously suggested to be important for contraction of T4 phage sheath and R-type pyocin sheath [28,30]. Analysis of interfaces that are expected to be present only in the contracted form of the T6SS sheath of *V. cholerae* suggested that VipB residues K223 and D333 located on two different VipB–VipB interfaces, one between protomers of a single sheath strand and the second between protomers on two adjacent strands, significantly contribute to the stability of the contracted structure [27]. This suggests that the energy released by the formation of these interactions could contribute to the sheath contraction.

To test this hypothesis, we mutated K223 and D333 to alanine and expressed the mutated *vipB* in a *vipA-msfGFP*, *ΔvipB* background to allow monitoring of sheath dynamics in live cells. The K223A mutation impaired assembly of the sheath, and no elongated sheaths were observed (Fig 1C and Movie EV1). This was also reflected in the inability of the VipB-K223A mutant to kill target cells (Fig 1A). Interestingly, the VipB-D333A mutant assembled into non-dynamic sheath structures that were stable *in vivo* over more than one hour of imaging (Fig 1B and Movie EV1 and EV2). The number of sheath structures per cell was comparable to the number of structures assembled in wild-type cells suggesting that D333 residue is not critical for sheath assembly. Similarly to the extended wild-type sheaths, the VipB-D333A sheaths were stable even in the presence of ClpV. Importantly, the VipB-D333A mutation also completely blocked target cell killing (Fig 1A).

VipA linker is critical for sheath contraction *in vivo*

Recent atomic models of T6SS sheaths in a contracted state and structures of the R-type pyocin in an extended and contracted state identified intermolecular linkers important for sheath function [26,27,30]. Interestingly, the N-terminal linker of the R-type pyocin sheath appears more stretched in the contracted sheath than in the extended sheath (Fig EV1). We hypothesized that stretching of the N-terminal sheath linker of a basal ring upon contraction results in pulling on the VipA N-terminal linker of the next sheath ring, which in turn triggers its contraction. Such a mechanism would lead to propagation of contraction through the whole sheath, as suggested earlier for the T4 phage sheath [33]. We decided to test this hypothesis by generating a series of mutant *V. cholerae* T6SS sheaths with longer VipA linkers. We inserted 1–7 amino acids of the native "AEVELPL" sequence of the linker after residue 25 of VipA wild-type protein (labeled here as VipA-N1 to VipA-N7). To monitor the assembly and contraction, we fused VipA and its variants to msfGFP and expressed it from pBAD24 plasmid in the absence of chromosomal *vipA* [1,27].

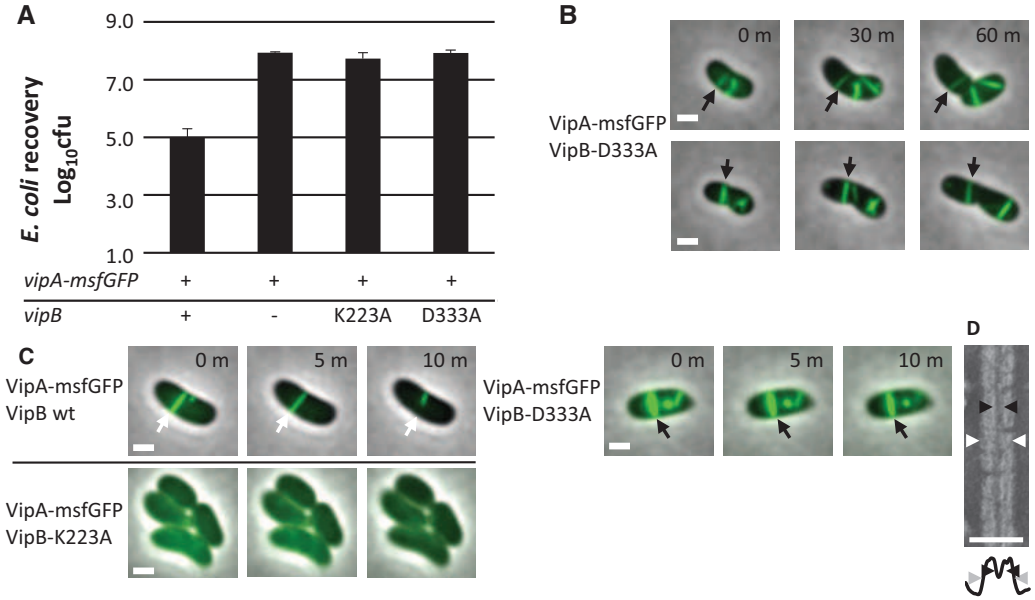

Figure 1. Charged residues of VipB are essential for sheath assembly and contraction.

A *Escherichia coli* survival (± SD, $N = 3$) after 3-h competition with indicated *Vibrio cholerae* strains in a 1:10 ratio on plate; the first column is significantly different from the rest ($P < 0.01$).

B One-hour timelapses of *V. cholerae vipA-msfGFP*, *vipB*$^-$ complemented with *vipB*-D333A on pBAD24. Two examples of stable T6SS sheaths are highlighted with arrows. Images are composite images of phase contrast and fluorescence channels. Scale bars are 1 μm.

C Ten-minute timelapse images of *V. cholerae vipA-msfGFP*, *vipB*$^-$ complemented with *vipB* wild type, *vipB*-K223A, or *vipB*-D333A on pBAD24. A dynamic, contracting (VipB wild type, white arrow) and a stable, static (VipB-D333A, black arrow) sheath are highlighted with arrows. VipB-K223A does not assemble T6SS sheaths. Images are composite images of phase contrast and fluorescence channels. Scale bars are 1 μm.

D Crop of an electron micrograph of purified VipB-D333A sheath and below a plot of the summed intensities. The inner diameter is marked with black arrowheads and the outer diameter with white or gray arrowheads. Scale bar is 50 nm.

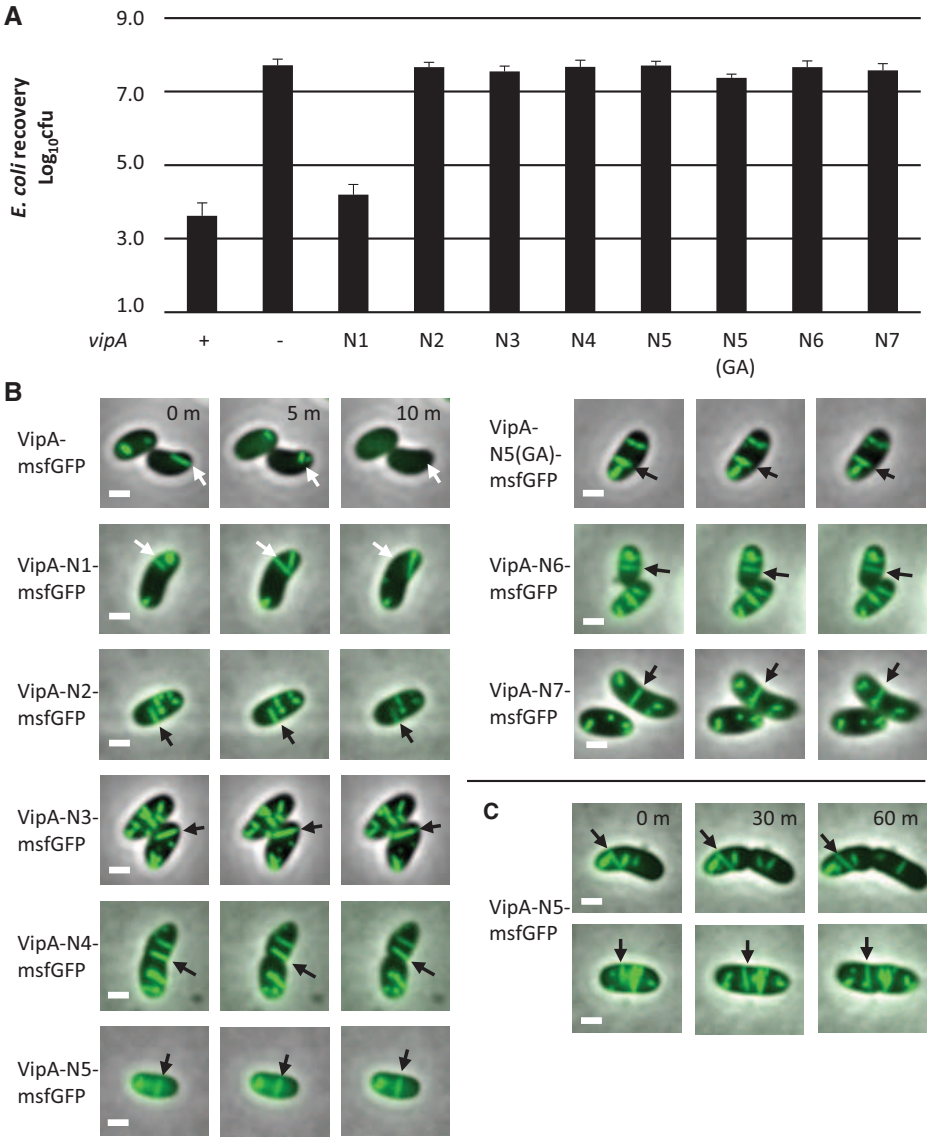

Figure 2. Length of N-terminal linker of VipA controls sheath contraction.

A *Escherichia coli* survival (± SD, $N = 3$) after 3-h competition with indicated *Vibrio cholerae* strains in a 1:10 ratio on plate; the first and third columns are significantly different from the rest ($P < 0.01$).

B Fluorescence timelapse images of *V. cholerae vipA*⁻ complemented with indicated msfGFP-tagged-*vipA* variants on pBAD24. Arrows highlight sheaths that contract (wild type, N1, white arrows) or are static (N2 or higher, black arrows). Images are composite images of phase contrast and fluorescence channels.

C Long timelapse of *V. cholerae vipA*⁻ complemented with *vipA-N5-msfGFP* on pBAD24. Images are composite images of phase contrast and fluorescence channels.

Data information: Scale bars are 1 μm.

All mutant T6SS sheaths assembled with a frequency similar to that of the wild-type sheath (Fig 2B); however, the frequency of sheath contraction was strongly dependent on the linker length (Fig 2B, Movie EV3). Whereas insertion of one amino acid (VipA-N1) had almost no effect on sheath dynamics, an elongation by two or more amino acids (VipA-N2-7) reduced the fraction of sheaths that contract within 5 min from 50% (of 159 VipA wild-type structures counted, 85 contracted) to 0% (of 204 VipA-N3 structures counted, none contracted). Many of these mutant sheaths were stable over one hour of imaging (Fig 2C and Movie EV4). Sheaths that occasionally broke after extensive bending caused by the movement and growth of cells were however quickly disassembled (Movie EV4). VipA with "AGAGA" sequence inserted, labeled as VipA-N5(GA), also assembled stable full-length sheaths (Fig 2B, Movie EV3), suggesting that VipA linker length, but not its sequence, is specifically critical for sheath stability. Furthermore, the killing of *Escherichia coli* MG1655 by *V. cholerae* T6SS (Fig 2A) was strongly dependent on the length of the VipA linker. Whereas an extension of this linker by one amino acid had no effect on the killing efficiency, an elongation by two amino acids completely abolished the killing of target cells.

The length of the sheaths *in vivo* did not differ between wild-type and the non-contractile sheaths VipB-D333A or VipA-N3. The mean length of sheaths was between 0.53 μm and 0.59 μm for all measured mutants (Table EV1). This suggests that the length of sheaths is limited by the size of the cell and the orientation of the T6SS inside cells as shown previously [19] rather than by the mutations that were introduced.

Stable sheaths assemble from baseplate and around Hcp

To analyze the stable mutant sheaths in more detail, we isolated them by using an approach similar to the one used for the isolation of the wild-type contracted sheath [1,27]. Mutant sheaths were expressed in a non-flagellated *V. cholerae* strain, cells were lysed, and sheaths were purified from soluble proteins and cell debris using ultra-centrifugation. The isolated sheaths were analyzed by negative staining electron microscopy.

Analysis of VipB-D333A sheath sample revealed partially fragmented hollow structures with an outer diameter of 260 nm, thus resembling contracted sheaths (Fig 1D). This suggests that during isolation, the VipB-D333A sheaths contract and the D333A mutation destabilizes the contracted structure, which leads to partial fragmentation. Similarly, VipA-N2 sheaths closely resembled the wild-type contracted sheaths as they appeared hollow, had the inner diameter of 100 Å, and the outer diameter of 260 Å (Figs 3A and B, and EV2). Interestingly, VipA-N3, VipA-N5, and VipA-N5(GA) mutant sheath diameters were ≈200 Å and thus narrower than wild type (Figs 3A and B, and EV2). Importantly, uranyl acetate stain was clearly unable to penetrate the sheaths, suggesting that VipA-N3, VipA-N5, and VipA-N5(GA) mutant sheaths were filled with additional proteins (Fig 3A and B).

To identify the proteins that were associated with the mutant sheaths, we subjected the VipA wild-type, N1, 2, 3, 5, and 5 (GA) samples to mass spectrometry analysis (Table EV2 and Dataset EV1). Besides VipA and VipB proteins, VipA-N3, VipA-N5, and VipA-N5(GA) sheath preparations contained large amounts of Hcp, as further confirmed by Western blot (Fig 3C, lower panel). The presence of Hcp in these mutant sheath samples explains the solid appearance on negative-stain EM (Fig 3A). Altogether, 10 of 16 T6SS-related proteins were identified in all independently purified triplicates. Interestingly, six of these proteins were specifically enriched in samples with a linker elongated by three or more amino acids ($P < 0.02$). Among the enriched proteins are baseplate proteins TssE, TssF, TssG, and TssK but also the tip component VgrG-3 (Fig EV3). VgrG-1 and VgrG-2 as well as most other proteins of the membrane complex have not been identified in all replicates and thus were excluded from the analysis.

Interestingly, VipA-N2 sheaths are stable in the cell cytosol in the presence of ClpV, however, can only be isolated in a conformation closely resembling contracted sheath. To test whether VipA-N2 sheaths contract during isolation, we imaged the mutant sheaths on an agarose pad containing low concentrations of CelLytic B and EDTA, the lytic agents that we use for bacterial cell lysis. We found that VipA-N2 sheaths shorten their length by ≈50% shortly before, during, or immediately after lysis, which indicates that VipA-N2 sheaths indeed assemble in an extended state but may contract during cell lysis (Fig EV4 and Movie EV5).

Mutant sheaths assemble only from a functional baseplate and the non-contractile phenotype is dominant

To exclude the possibility that the non-contractile sheaths are aberrant polymers that assemble independently of other T6SS components, we imaged their assembly in a strain that lacks the baseplate component TssE. In agreement with the previous observations that TssE is required for efficient sheath assembly [1,34], the frequency of wild-type T6SS sheath assembly decreased by 140-fold in the absence of *tssE*. Similarly, the assembly of D333A or VipA-N5 sheaths was clearly dependent on the presence of a functional baseplate since the number of structures assembled in the cells lacking *tssE* was reduced by at least 100-fold (Fig 4A and B). This indicates that stable mutant sheaths assemble from a baseplate similarly to the wild-type sheaths.

To test whether the mutant sheath subunits can block T6SS activity also in the presence of the wild-type subunits, we induced expression of the VipA-N5 mutant from pBAD24 plasmid in a strain expressing wild-type sheath from the chromosome and measured the efficiency of *E. coli* killing. Low-level induction of VipA-N5 by 0.01% arabinose decreased the T6SS-dependent killing of *E. coli* by 100-fold. The T6SS activity was almost completely blocked by increasing the concentration of arabinose to 0.1% (Fig 4C) indicating that the ratio of wild-type VipA to VipA-N5 is important for effector delivery. No such inhibition was observed when wild-type

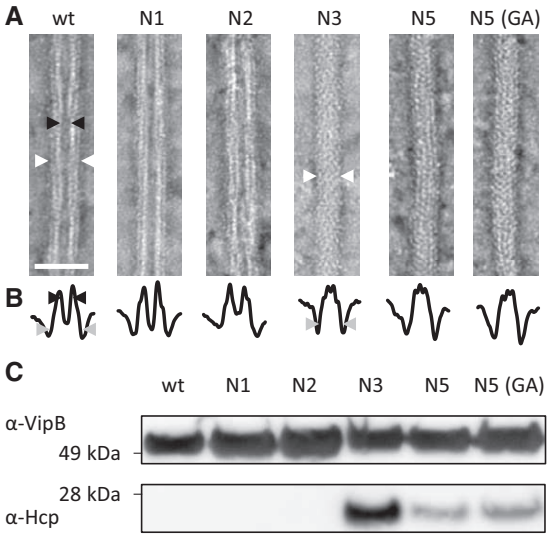

Figure 3. Hcp is enriched in VipA mutants with a linker elongated by three or more amino acids.

A Electron micrographs of isolated sheath samples. Wild-type sheath and those with additional one or two amino acids inserted are hollow but with three or more amino acids show a protein density in the center. Black arrowheads mark the inner diameter, and white arrowheads mark the outer diameter. Arrowheads are shown for one example of the two different types of structures. Scale bar is 50 nm.

B Plot of summed intensities of the micrographs in (A). The inner diameter is marked with black arrowheads and the outer diameter with gray arrowheads. Arrowheads are shown for one example of the two different types of structures.

C Immunoblots against Hcp and VipB of the samples in (A).

Source data are available online for this figure.

VipA was expressed from the plasmid (Fig 4C). Similarly, low-level expression of VipB-D333A decreased T6SS activity by 100-fold and high level of expression blocked the T6SS activity completely (Fig 4C). This dominant negative phenotype suggests that the mutant subunits are structurally compatible with the wild-type subunits, co-assemble into the same structures, and thus block T6SS function.

Concluding remarks

The T6SS is a highly dynamic system, and this complicates detailed biochemical and biophysical characterization of its mode of action. Here, we show that the system can be locked in the pre-contraction state by mutagenesis of the linker connecting sheath subunits or changing interactions contributing to the stability of the contracted state. Importantly, some non-contractile sheaths are stable during isolation from cells, assemble around Hcp tube, associate with many T6SS baseplate components, and co-assemble with wild-type extended sheath. This suggests that the structure of non-contractile sheaths is very similar to the wild-type sheath. Moreover, similarly to the wild-type extended sheath, the non-contractile sheaths form in the presence of ClpV and are therefore different from the previously described polysheath-like structures, which form independently of other T6SS components but only in the absence of ClpV [11].

Early electron micrographs of partially contracted T4 phage particles suggested that sheath contraction progresses in a wave of contracting sheath rings from the baseplate toward the phage head [33]. However, it is currently unclear how contraction of one sheath ring triggers contraction of the next ring. As we show here, insertion of two residues into the VipA N-terminal linker prevents T6SS sheath contraction *in vivo*, suggesting that the exact length of the linker connecting the subunits is essential for sheath contraction initiation or propagation of the contraction along the sheath (Figs 5 and EV1). In addition, T6SS, T4 phage, and R-type pyocin sheath structures indicated charged residues potentially important for the stability of contracted structures [27,28,30]. Many of these

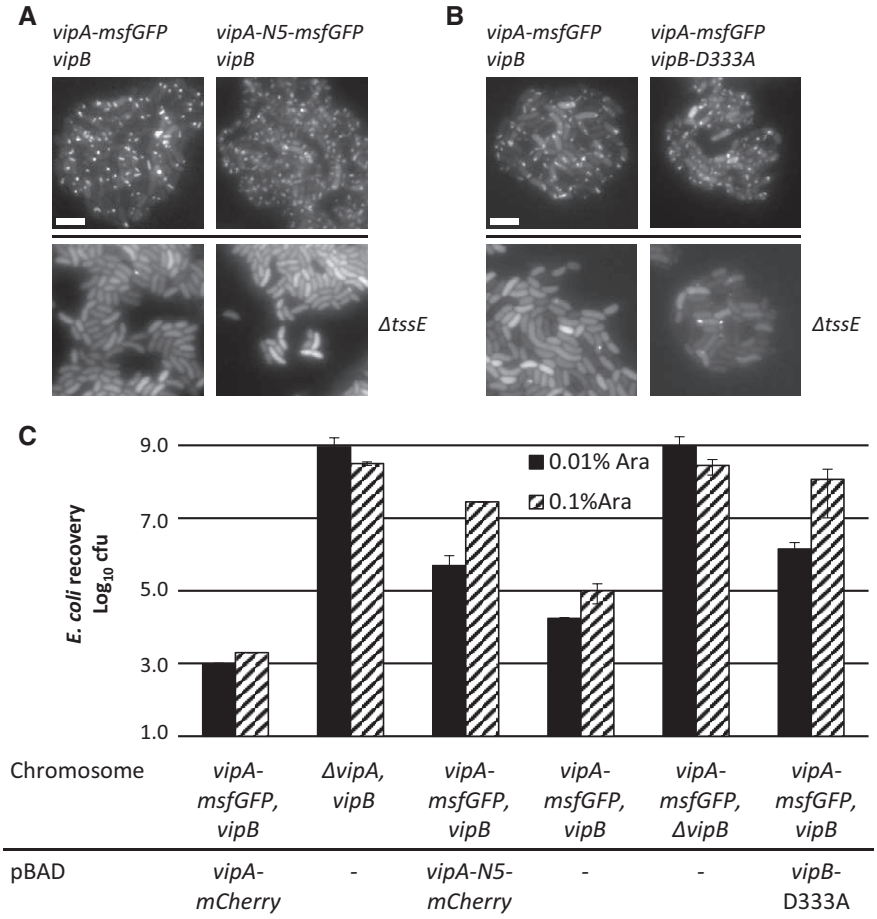

Figure 4. Assembly of non-contractile sheaths depends on the presence of TssE and mutant sheath subunits are dominant.

A Fluorescence microscopy images of *Vibrio cholerae vipA*$^{-}$ (upper panels) or *vipA*$^{-}$, *tssE*$^{-}$ (lower panels) complemented with *vipA-msfGFP* (left panels) or *vipA-N5-msfGFP* (right panels) on pBAD24.

B Fluorescence microscopy images of *V. cholerae vipA*$^{-}$, *vipB*$^{-}$ (upper panels) or *vipA*$^{-}$, *vipB*$^{-}$, *tssE*$^{-}$ (lower panels) complemented with *vipA-msfGFP* on pBAD24 and *vipB* (left panels) or *vipB*-D333A (right panels) on pBAD33.

C *Escherichia coli* survival (± SD, $N = 2$) after 3-h competition with indicated *V. cholerae* strains in a 1:10 ratio on plates at two different arabinose concentrations.

Data information: Scale bars are 5 μm.

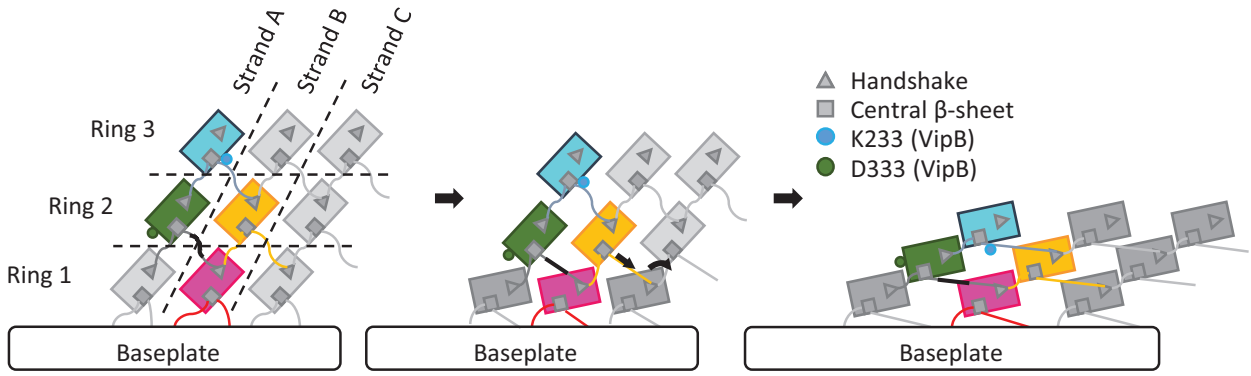

Figure 5. Model of the mechanism of contraction of contractile sheaths.

Scheme representing the connections between strands and rings in R-type pyocin and T6SS sheaths. Ring 1 contracts after an initial trigger coming from the baseplate. Ring 1 pulls on a linker region (black) of ring 2 and by this propagates the contraction throughout the sheath. After contraction, protomers are fixed by electrostatic interactions of residue D333 of VipB. The model is depicted as viewed from the outside of the sheath.

interactions specifically form during contraction and were thus proposed to drive sheath contraction [28,30]. Together with our data, this suggests that the newly formed interactions of VipB residue D333 stabilize the quaternary structure of the contracted state and prevent reversal of the contraction, especially when contraction is not yet completed throughout the sheath.

Interestingly, many baseplate components are enriched in the samples of the isolated stable non-contractile sheaths as compared to the samples of contracted sheaths (Table EV2 and Dataset EV1 and Fig EV3) [1,27]. This suggests that after sheath contraction, the baseplate is destabilized and dissociates from the sheath. Live-cell imaging of sheath dynamics and localization indeed showed that few seconds after contraction, but before disassembly, sheaths often dissociate from the initial cell envelope attachment site [16]. This is consistent with the observation that T6SS assemble repeatedly inside cells and the components of the baseplate are likely reused for new rounds of assembly. In related contractile nanomachines, which are only used once, the contracted sheaths remain stably associated with the baseplates and likely provide mechanical stability to the contracted particles. In the case of contractile phages, the sheath connects baseplate and the phage head as the DNA is translocated and in the case of R-type pyocin, the sheath might be needed to stabilize the tube, which allows ion leakage and the killing of target bacterial cell [12,30,35].

The approach used here to stabilize the pre-contraction state of T6SS will likely be invaluable for further attempts to dissect T6SS mode of action at the molecular level in various bacteria and may be also used to study related contractile nanomachines with a major relevance for viral infection, bacterial competition, and pathogenicity.

Materials and Methods

Bacterial strains and DNA manipulations

Vibrio cholerae 2740-80 parental, *vipA-msfGFP*, *ΔvipA*, *ΔvipB*, *ΔtssE* strains and the pBAD24-*vipA-sfGFP* plasmid were described previously [1,27]. *vipA* mutants on pBAD24 plasmid were generated using standard techniques. Mutant *vipA* genes encode "A, AE, AEV, AEVE, AEVEL, AGAGA, AEVELP, or AEVELPL" residues inserted right after residue 25 of wild-type *vipA*. The insertions represent either duplication of the native sequence or a sequence encoding "AGAGA". *V. cholerae* 2740-80 *ΔvipA-vipB* strain was created by replacing *vipA* and *vipB* with a gene encoding "MSKEGSVGRLDQA" peptide (first seven residues of *vipA* and last six residues of *vipB* fused in frame) and *V. cholerae* 2740-80 *ΔvipA-vipB-tssE* strain was created by replacing *vipA*, *vipB,* and *tssE* with a gene encoding "MSKEGSVRKYRVF" peptide (first seven residues of *vipA* and last six residues of *tssE* fused in frame) by allelic exchange as was done previously. *vipB* (wild type) was cloned into pBAD24 and pBAD33 plasmids using standard techniques. K223A and D333A mutations were introduced into *vipB* using mutagenic primers. All PCR-generated products were verified by sequencing. Plasmids were transformed into *V. cholerae* by electroporation. Gentamicin-resistant *E. coli* MG1655 strain with pUC19 plasmid was used in bacterial killing assays. Antibiotic concentrations used were streptomycin (50 μg/ml), ampicillin (200 μg/ml), chloramphenicol (20 μg/ml), and gentamicin (15 μg/ml). Lysogeny broth (LB) was used for all growth conditions. Liquid cultures were grown aerobically at 37°C.

Bacterial killing assay

Vibrio cholerae 2740-80 strains as indicated and *E. coli* MG1655 with empty pUC19 plasmid were incubated overnight at 37°C in LB supplemented with appropriate antibiotics. Cultures were diluted 100-fold, and grown to OD 0.8–1.2 in presence of appropriate antibiotics and 0.01% arabinose for strains with pBAD plasmids (or 0.1% arabinose for sheath co-assembly experiments). Cells were washed and mixed at final OD of ≈10 in 10:1 ratio (*V. cholerae* to *E. coli*) as specified, and 5 μl of the mixture was spotted on a pre-dried LB agar plate containing 0.01% arabinose and ampicillin or no antibiotic. After 3 h, bacterial spots were cut out and the cells were re-suspended in 0.5 ml LB. The cellular suspension was serially diluted (1:10) in LB, and 5 μl of the suspensions were spotted on selective plates (gentamicin for *E. coli* and streptomycin for *V. cholerae*). Colonies were counted

after ≈16-h incubation at 30°C. Two or more biological replicates were analyzed.

Fluorescence microscopy

Procedures similar to those described previously [16] were used to detect fluorescence signal in *V. cholerae*. Overnight cultures of *V. cholerae* carrying pBAD24 plasmid with the respective inserts were diluted 100-fold into fresh LB supplemented with ampicillin, streptomycin, and 0.01% or 0.03% arabinose and cultivated for 2.5–3.0 h to optical density (OD) at 600 nm of about 0.8–1.2. Cells from 1 ml of the culture were re-suspended in ≈50 µl LB (to OD ≈20), spotted on a thin pad of 1% agarose in LB, and covered with a glass coverslip. For experiments in which cell lysis was induced to test the stability of VipA-N2 sheaths, an agarose pad (1% agarose in PBS and LB 1:1) containing 0.0625× CelLytic B and 0.3 mM EDTA was used. Cells were immediately imaged at room temperature. A previously described microscope setup was used [27]. VisiView software (Visitron Systems, Germany) was used to record images. Fiji [36] was used for all image analysis and manipulations as described previously [37]. Bleach correction was used if necessary [38]. Contrast on compared sets of images was adjusted equally. All imaging experiments were performed with three biological replicates.

VipA/VipB sheath preparation

Overnight cultures of the indicated strains were diluted 1:1,000 in 0.5 l of fresh LB supplemented with appropriate antibiotics and then shaken at 37°C and 250 rpm to an OD of ≈1.2. Cells were centrifuged for 20 min at 5,000 *g* and 4°C, re-suspended in 20 ml PBS, and centrifuged again for 30 min at 3,214 *g* and 4°C. Pellets were frozen until further processing. The cell pellets were thawed, re-suspended in 20 ml of TN buffer (20 mM Tris, 150 mM NaCl, pH 8.3), and lysed by addition of (0.75×) CelLytic™ B, lysozyme (200 µg/ml), EDTA (5 mM), and incubation at 37°C. DNase (50 µg/ml) and $MgCl_2$ (10 mM) were added to cleave DNA. After 15-min incubation at 37°C, cell debris was removed by centrifugation for 20 min at 10,000 *g*. Cleared supernatants were subjected to ultraspeed centrifugation for 1 h at 104,000 *g* and 4°C, and the resulting pellet was washed with 1 ml TN buffer and subsequently re-suspended in 1 ml TN buffer; insoluble material was removed by centrifugation for 1 min at 10,000 *g*. Cleared supernatants were subjected to a second round of ultraspeed centrifugation for 1 h at 104,000 *g* and 4°C, and the resulting pellet was washed with 1 ml TN buffer and subsequently re-suspended in 1 ml TN buffer; insoluble material was removed by centrifugation for 1 min at 10,000 *g*. The supernatant was subjected to a third round of ultraspeed centrifugation for 1 h at 104,000 *g* and 4°C, and the resulting pellet was re-suspended in 70 µl of TN buffer for further analysis. Purity of the sample was assessed by Coomassie-stained SDS–PAGE.

Mass spectrometry

Sheath samples (30–100 µg) were reduced with 5 mM Tris(2-chloroethyl)phosphate, shaking for 1 h at 37°C and alkylated with 10 mM iodoacetamide, shaking for 30 min at 25°C in the dark. Proteins were digested using sequencing-grade modified trypsin (1/250, w/w; Promega, USA) overnight at 37°C. After digestion, the samples were supplemented with trifluoroacetic acid to a final concentration of 1%. Peptides were desalted on C18 reversed-phase spin columns according to the manufacturer's instructions (Microspin, Harvard Apparatus, Holliston, Massachusetts, USA), dried under vacuum and re-suspended in LC-MS buffer (0.15% formic acid, 2% acetonitrile in HPLC water) at ≈0.5 mg/ml. 1 µg of peptides of each sample was subjected to LC-MS analysis using a dual-pressure LTQ-Orbitrap Elite mass spectrometer connected to an electrospray ion source (both Thermo Fisher Scientific, Waltham, Massachusetts, USA) as described recently [39] with a few modifications. In brief, peptide separation was carried out using an EASY nLC-1000 system (Thermo Fisher Scientific, Waltham, Massachusetts, USA) equipped with a RP-HPLC column (75 µm × 30 cm) packed in-house with C18 resin (ReproSil-Pur C18–AQ, 1.9 µm resin; Dr. Maisch GmbH, Ammerbuch-Entringen, Germany) using a linear gradient from 95% solvent A (0.15% formic acid, 2% acetonitrile) and 5% solvent B (98% acetonitrile, 0.15% formic acid) to 28% solvent B over 75 min at a flow rate of 0.2 µl/min. The data acquisition mode was set to obtain one high-resolution MS scan in the FT part of the mass spectrometer at a resolution of 240,000 full width at half maximum (at m/z 400) followed by MS/MS scans in the linear ion trap of the 20 most intense ions. The charged state screening modus was enabled to exclude unassigned and singly charged ions, and the dynamic exclusion duration was set to 20 s. The ion accumulation time was set to 300 ms (MS) and 50 ms (MS/MS). The collision energy was set to 35%, and one microscan was acquired for each spectrum. For all LC-MS measurements, singly charged ions and ions with unassigned charge state were excluded from triggering MS2 events. MS raw files were imported into the Progenesis LC-MS software (Nonlinear Dynamics, Version 4.0, Newcastle upon Tyne, UK) and processed using the default parameter settings. MS/MS data were exported directly from Progenesis in mgf format and analyzed using Mascot (Matrix Science, Version 2.4.0, Boston, Massachusetts, USA), searching a concatenated target-decoy database including forward and reversed sequences of the protein entries included in the Uniprot *Vibrio cholerae* proteome database (www.uniprot.org, release date 11/07/2016, 3,784 target sequences). The Mascot search criteria were set as follows: 10 ppm precursor ion mass tolerance, 0.6 Da fragment ion mass tolerance, full tryptic specificity required (cleavage after lysine or arginine residues); maximum three missed cleavages; fixed modification: carbamidomethylation (C), variable modification: oxidation (M). Results from the database search were imported into Progenesis. The database search results were filtered, limiting the peptide and protein level FDR to 1%. The Progenesis analysis results were further processed using the SafeQuant R package [40], to obtain protein relative abundances. This analysis included summation of MS1 peak areas per protein followed by global normalization of protein abundances, per LC-MS run, based on the abundances of proteins VipA (VC_A0107) and VipB (VC_A0108). Finally, protein abundance ratios in Table EV2 were calculated with respect to the wild-type condition, upon averaging across biological replicates. Testing for protein differential abundance was done using empirical Bayes method [41]. The resulting *P*-values, reflecting the probability of detecting a given mean abundance difference across sample conditions by chance alone, were corrected for multiple testing using the Benjamini–Hochberg method [42].

Statistical testing

Unpaired Student's *t*-test was used to evaluate statistical significance of biological replicates for the bacterial killing assays and mass spectrometry.

Negative staining electron microscopy

300-mesh copper grids were glow-discharged for 20 s, and samples (5 µl, protein concentration approx. 0.1 µg/ml) were adsorbed for 1 min and blotted using Whatman #1 filter paper. The grids were washed five times with ddH_2O, and once using 2% uranyl acetate, followed by a 20-s staining with 2% uranyl acetate. Grids were imaged on a CM-100 microscope (Philips N.V., Amsterdam, Netherlands) equipped with a Veleta 2 k × 2 k camera (Olympus K.K., Tokyo, Japan) at 80 keV and a magnification of 64,000× (7.4 Å pixel size, 1,376 × 1,032 pixel) or a KeenView camera (Olympus K.K., Tokyo, Japan) at a magnification of 20,000× (9.1 Å pixel size) and the iTEM user interface. Fiji [36] was used for all image analysis.

Immunoblot analysis

5–10 µl of purified sheath samples was mixed with 1.2–2.4 µl 4× NuPAGE® LDS Sample Buffer (Life Technologies, Carlsbad, California, USA). Samples were incubated for 10 min at 95°C, centrifuged, cooled, and 2 µl 1 M DTT was added. Samples were heated again for 10 min at 72°C, centrifuged, loaded on 10% polyacrylamide gels, and stained with InstantBlue Protein Stain (Expedeon, San Diego, California, USA) or transferred to nitrocellulose membrane (GE Healthcare, Little Chalfont, UK). The membrane was incubated with Ponceau S (Sigma-Aldrich, Darmstadt, Germany) to check blotting efficiency. Membrane was blocked with 5% milk in Tris-buffered saline (pH 7.4) containing Tween 0.1% (TBST), incubated with primary peptide antibody against Hcp ("QSGQPSGQRVHKPF", Genscript, Piscataway, New Jersey, USA [1]), or peptide antibody against VipB ("QENPPADVRSRRPL", Genscript, Piscataway, New Jersey, USA [27]) for 16 h at 4°C or 1 h at room temperature, washed with TBST, incubated for 1 h with horseradish peroxidase-labeled anti-rabbit antibody (Jackson ImmunoResearch Inc., USA), and washed with the recommended buffer, and peroxidase was detected by LumiGLO® Chemiluminescent Substrate (KPL, Inc., Gaithersburg, Maryland, USA). Nitrocellulose membrane was stripped using Restore™ Western Blot Stripping Buffer (Thermo Fisher Scientific, Waltham, Massachusetts, USA) and reprobed using the same protocol.

Molecular analysis

Structures of PA0622 in the contracted state (PDB ID: 3J9R) [30] and of VipA and VipB in the contracted state (PDB ID: 3J9G) [27] were aligned based on their 3D structures using UCSF Chimera [43].

Expanded View for this article is available online.

Acknowledgements
The work was supported by Swiss National Science Foundation (SNSF) grant 31003A_159525 and the University of Basel. We acknowledge the Biozentrum proteomics core facility for mass spectrometry measurements and the Biozentrum BioEM Lab for access to their microscopes.

Author contributions
MBr generated and characterized the mutant sheaths, performed fluorescence microscopy, isolated and purified the sheaths, and performed negative-stain electron microscopy, mass spectrometry, and Western blot analysis of their structure and composition. JW contributed to electron microscopy data analysis. MBa conceived the project and analyzed the data. MBr and MBa wrote the manuscript.

Conflict of interest
The authors declare that they have no conflict of interest.

References

1. Basler M, Pilhofer M, Henderson GP, Jensen GJ, Mekalanos JJ (2012) Type VI secretion requires a dynamic contractile phage tail-like structure. *Nature* 483: 182 – 186
2. Hood RD, Singh P, Hsu F, Güvener T, Carl MA, Trinidad RRS, Silverman JM, Ohlson BB, Hicks KG, Plemel RL, *et al* (2010) A type VI secretion system of *Pseudomonas aeruginosa* targets a toxin to bacteria. *Cell Host Microbe* 7: 25 – 37
3. MacIntyre DL, Miyata ST, Kitaoka M, Pukatzki S (2010) The *Vibrio cholerae* type VI secretion system displays antimicrobial properties. *Proc Natl Acad Sci USA* 107: 19520 – 19524
4. Mougous JD, Cuff ME, Raunser S, Shen A, Zhou M, Gifford CA, Goodman AL, Joachimiak G, Ordoñez CL, Lory S, *et al* (2006) A virulence locus of *Pseudomonas aeruginosa* encodes a protein secretion apparatus. *Science* 312: 1526 – 1530
5. Pukatzki S, Ma AT, Sturtevant D, Krastins B, Sarracino D, Nelson WC, Heidelberg JF, Mekalanos JJ (2006) Identification of a conserved bacterial protein secretion system in *Vibrio cholerae* using the Dictyostelium host model system. *Proc Natl Acad Sci USA* 103: 1528 – 1533
6. Brunet YR, Zoued A, Boyer F, Douzi B, Cascales E (2015) The type VI secretion TssEFGK-VgrG phage-like baseplate is recruited to the TssJLM membrane complex via multiple contacts and serves as assembly platform for tail tube/sheath polymerization. *PLoS Genet* 11: e1005545
7. Durand E, Nguyen VS, Zoued A, Logger L, Péhau-Arnaudet G, Aschtgen M-S, Spinelli S, Desmyter A, Bardiaux B, Dujeancourt A, *et al* (2015) Biogenesis and structure of a type VI secretion membrane core complex. *Nature* 523: 555 – 560
8. Zoued A, Durand E, Bebeacua C, Brunet YR, Douzi B, Cambillau C, Cascales E, Journet L (2013) TssK is a trimeric cytoplasmic protein interacting with components of both phage-like and membrane anchoring complexes of the type VI secretion system. *J Biol Chem* 288: 27031 – 27041
9. Arisaka F, Tschopp J, van Driel R, Engel J (1979) Reassembly of the bacteriophage T4 tail from the core-baseplate and the monomeric sheath protein P18: a co-operative association process. *J Mol Biol* 132: 369 – 386
10. Brunet YR, Henin J, Celia H, Cascales E (2014) Type VI secretion and bacteriophage tail tubes share a common assembly pathway. *EMBO Rep* 15: 315 – 321
11. Kapitein N, Bonemann G, Pietrosiuk A, Seyffer F, Hausser I, Locker JK, Mogk A (2013) ClpV recycles VipA/VipB tubules and prevents non-productive tubule formation to ensure efficient type VI protein secretion. *Mol Microbiol* 87: 1013 – 1028

12. Leiman PG, Shneider MM (2012) Contractile tail machines of bacteriophages. *Adv Exp Med Biol* 726: 93 – 114
13. Tschopp J, Arisaka F, van Driel R, Engel J (1979) Purification, characterization and reassembly of the bacteriophage T4D tail sheath protein P18. *J Mol Biol* 128: 247 – 258
14. Planamente S, Salih O, Manoli E, Albesa-Jové D, Freemont PS, Filloux A (2016) TssA forms a gp6-like ring attached to the type VI secretion sheath. *EMBO J* 35: 1613 – 1627
15. Zoued A, Durand E, Brunet YR, Spinelli S, Douzi B, Guzzo M, Flaugnatti N, Legrand P, Journet L, Fronzes R, *et al* (2016) Priming and polymerization of a bacterial contractile tail structure. *Nature* 531: 59 – 63
16. Basler M, Mekalanos JJ (2012) Type 6 secretion dynamics within and between bacterial cells. *Science* 337: 815
17. Brunet YR, Espinosa L, Harchouni S, Mignot T, Cascales E (2013) Imaging type VI secretion-mediated bacterial killing. *Cell Rep* 3: 36 – 41
18. Gerc AJ, Diepold A, Trunk K, Porter M, Rickman C, Armitage JP, Stanley-Wall NR, Coulthurst SJ (2015) Visualization of the serratia type VI secretion system reveals unprovoked attacks and dynamic assembly. *Cell Rep* 12: 2131 – 2142
19. Vettiger A, Winter J, Lin L, Basler M (2017) The type VI secretion system sheath assembles at the end distal from the membrane anchor. *Nat Commun* 8: 16088
20. Brackmann M, Nazarov S, Wang J, Basler M (2017) Using force to punch holes: mechanics of contractile nanomachines. *Trends Cell Biol* 27: 623 – 632
21. Cianfanelli FR, Monlezun L, Coulthurst SJ (2016) Aim, load, fire: the type VI secretion system, a bacterial Nanoweapon. *Trends Microbiol* 24: 51 – 62
22. Zoued A, Brunet YR, Durand E, Aschtgen M-S, Logger L, Douzi B, Journet L, Cambillau C, Cascales E (2014) Architecture and assembly of the Type VI secretion system. *Biochim Biophys Acta* 1843: 1664 – 1673
23. Alcoforado Diniz J, Liu Y-C, Coulthurst SJ (2015) Molecular weaponry: diverse effectors delivered by the Type VI secretion system. *Cell Microbiol* 17: 1742 – 1751
24. Durand E, Cambillau C, Cascales E, Journet L (2014) VgrG, Tae, Tle, and beyond: the versatile arsenal of Type VI secretion effectors. *Trends Microbiol* 22: 498 – 507
25. Russell AB, Peterson SB, Mougous JD (2014) Type VI secretion system effectors: poisons with a purpose. *Nat Rev Microbiol* 12: 137 – 148
26. Clemens DL, Ge P, Lee B-Y, Horwitz MA, Zhou ZH (2015) Atomic structure of T6SS reveals interlaced array essential to function. *Cell* 160: 940 – 951
27. Kudryashev M, Wang RY-R, Brackmann M, Scherer S, Maier T, Baker D, DiMaio F, Stahlberg H, Egelman EH, Basler M (2015) Structure of the Type VI secretion system contractile sheath. *Cell* 160: 952 – 962
28. Aksyuk AA, Leiman PG, Kurochkina LP, Shneider MM, Kostyuchenko VA, Mesyanzhinov VV, Rossmann MG (2009) The tail sheath structure of bacteriophage T4: a molecular machine for infecting bacteria. *EMBO J* 28: 821 – 829
29. Aksyuk AA, Kurochkina LP, Fokine A, Forouhar F, Mesyanzhinov VV, Tong L, Rossmann MG (2011) Structural conservation of the myoviridae phage tail sheath protein fold. *Struct Lond Engl 1993* 19: 1885 – 1894
30. Ge P, Scholl D, Leiman PG, Yu X, Miller JF, Zhou ZH (2015) Atomic structures of a bactericidal contractile nanotube in its pre- and postcontraction states. *Nat Struct Mol Biol* 22: 377 – 382
31. Kube S, Kapitein N, Zimniak T, Herzog F, Mogk A, Wendler P (2014) Structure of the VipA/B type VI secretion complex suggests a contraction-state-specific recycling mechanism. *Cell Rep* 8: 20 – 30
32. Wang J, Brackmann M, Castaño-Díez D, Kudryashev M, Goldie KN, Maier T, Stahlberg H, Basler M (2017) Cryo-EM structure of the extended type VI secretion system sheath-tube complex. *Nat Microbiol* 2: 1507 – 1512
33. Moody MF (1973) Sheath of bacteriophage T4. 3. Contraction mechanism deduced from partially contracted sheaths. *J Mol Biol* 80: 613 – 635
34. Vettiger A, Basler M (2016) Type VI secretion system substrates are transferred and reused among sister cells. *Cell* 167: 99 – 110.
35. Hu B, Margolin W, Molineux IJ, Liu J (2015) Structural remodeling of bacteriophage T4 and host membranes during infection initiation. *Proc Natl Acad Sci USA* 112: E4919 – E4928
36. Schindelin J, Arganda-Carreras I, Frise E, Kaynig V, Longair M, Pietzsch T, Preibisch S, Rueden C, Saalfeld S, Schmid B, *et al* (2012) Fiji: an open-source platform for biological-image analysis. *Nat Methods* 9: 676 – 682
37. Basler M, Ho BT, Mekalanos JJ (2013) Tit-for-Tat: type VI secretion system counterattack during bacterial cell-cell interactions. *Cell* 152: 884 – 894
38. Miura K, Rueden C, Hiner M, Schindelin J, Rietdorf J (2014) ImageJ Plugin CorrectBleach V2.0.2. http://doi.org/10.5281/zenodo.30769
39. Glatter T, Ludwig C, Ahrné E, Aebersold R, Heck AJR, Schmidt A (2012) Large-scale quantitative assessment of different in-solution protein digestion protocols reveals superior cleavage efficiency of tandem Lys-C/trypsin proteolysis over trypsin digestion. *J Proteome Res* 11: 5145 – 5156
40. Ahrné E, Glatter T, Viganò C, von Schubert C, Nigg EA, Schmidt A (2016) Evaluation and improvement of quantification accuracy in isobaric mass tag-based protein quantification experiments. *J Proteome Res* 15: 2537 – 2547
41. Smyth GK (2004) Linear models and empirical bayes methods for assessing differential expression in microarray experiments. *Stat Appl Genet Mol Biol* 3: Article 3
42. Benjamini Y, Hochberg Y (1995) Controlling the false discovery rate: a practical and powerful approach to multiple testing. *J R Stat Soc Series B Stat Methodol* 57: 289 – 300
43. Pettersen EF, Goddard TD, Huang CC, Couch GS, Greenblatt DM, Meng EC, Ferrin TE (2004) UCSF Chimera—A visualization system for exploratory research and analysis. *J Comput Chem* 25: 1605 – 1612

II.3 Additional Results Related to Research Article II

II.1 VipA-N5 co-assembles with wild-type VipA

Studies from phage sheath protein gp19 showed that truncated sheath proteins can form aberrant polymers, so-called "polysheaths", when truncated variants are expressed heterologously [441]. To further investigate if the dominant phenotype arises from co-assembling structures or from preferential polymerization of mutant sheaths from baseplates, we decided to observe wild-type VipA-msfGFP and VipA-N5-mCherry by fluorescence microscopy (Figure II.3.1).

Signals from both fluorophores were observed in the same structures (Figure II.3.1, white arrowhead). This suggests that mutant sheath protein can readily co-assemble with wild-type VipA to form the T6SS-sheath (Figure II.3.1). Interestingly, structures that co-assembled did not contract, whereas structures only composed of wild-type sheath proteins were still able to contract. This implies that above a certain fraction of mutant VipA in the sheath, it is not able to contract anymore.

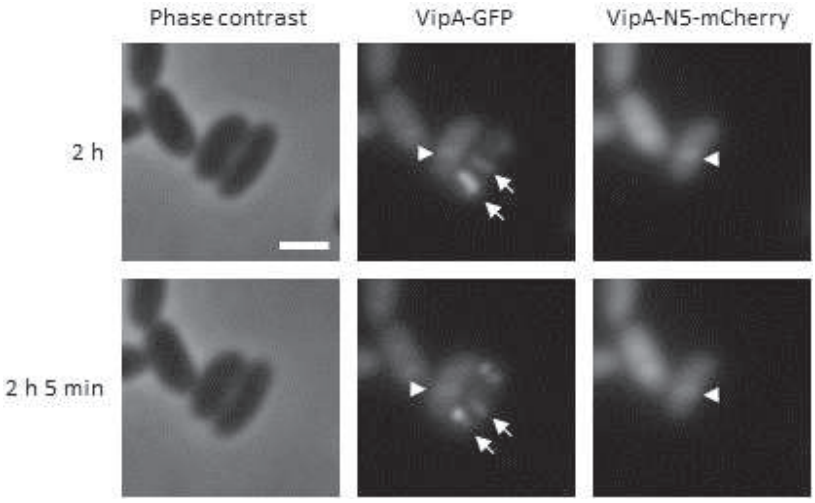

Figure II.3.1 VipA-N5 and VipA wt co-assemble in the same T6SS tail. *V. cholerae vipA-msfGFP* pBAD24_*vipA-N5-mCherry* was imaged after 2 hours of induction of protein expression from plasmid with 0.03% arabinose. Stalling of T6SS-activity is observed in structures with mCherry signal (arrowheads) but not for structures that only incorporated VipA-msfGFP. Scale bar is 1 μm

To characterize co-assembling mutant and wild-type sheaths in more detail, we wanted to image their dynamics on longer time-scales. However, long-term imaging of co-assembling sheaths with two fluorescent proteins proved challenging, as photoconversion can occur for GFP [442]. Photoconversion of GFP has been described to red-shift the absorption and emission spectra of GFP that they appear red and thus overlap with the signal from

mCherry [442].

II.2 Mutant R-type pyocin sheaths do not assemble a functional R-type pyocin

As discussed before, the introduction of a linker at the N-terminus of VipA inhibits contraction of the T6SS-sheath (Section II.2). To check if this is a general mechanistic feature of contractile sheaths, we introduced the corresponding linker in the sheath protein of R-type pyocins of *P. aeruginosa* (PA0622). The mutant sheath genes were introduced on a plasmid in a strain lacking the sheath gene (*pa0622*). Mitomycin C or UV-radiation lead to DNA-damage, which induces production of pyocins and subsequent cell lysis. After lysis, pyocins can be isolated from *P. aeruginosa* by precipitation and ultracentrifugation [332, 406, 409, 410, 443].

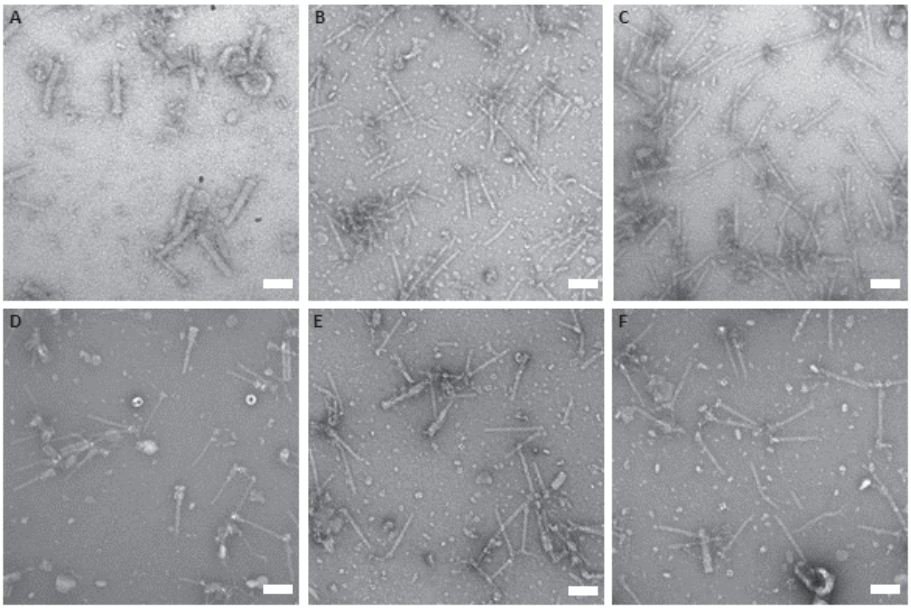

Figure II.3.2 Pyocin sheath protein expressed from plasmid does not complement. A, wild type R-type pyocins from *P. aeruginosa*. B, R-type pyocins from *P. aeruginosa* lacking pyocin sheath protein *pa0622*. C, As in B but with *pa0622* complemented from plasmid pPSV35. D, As in C but with one amino acid inserted after residue T18 in the pyocin sheath protein. D, As in C but with two amino acids inserted after residue T18 in the pyocin sheath protein. E, As in C but with three amino acid inserted after residue T18 in the pyocin sheath protein. F, As in C but with four amino acid inserted after residue T18 in the pyocin sheath protein. Scale bars are 200 nm

Purified pyocins can be tested for their activity by spotting a pyocin-containing solution and dilutions thereof on a bacterial lawn and the activity of the isolated pyocins was confirmed (data not shown and [406, 410]). Expression of *pa0622 (wt)* from plasmid does

not complement the deletion of the chromosomal gene (Figure II.3.2). Only baseplates with the inner tube or sometimes partially assembled tails are detectable in electron microscopy.

Expression of phage proteins has earlier been shown to be tightly regulated [444]. This might also be true for the expression of pyocin genes and thus, expression of pyocin genes from plasmid might not complement the deletion phenotype due to improper timing of expression.

Complementation of pyocins with mutant sheath proteins remains inconclusive, as they do not assemble mature R-type pyocins and thus cannot be tested for activity nor structurally characterized.

II.4 Research Article III

Cryo-EM structure of the extended type VI secretion system sheath-tube complex.

Jing Wang, Maximilian Brackmann, Daniel Castaño-Díez, Mikhail Kudryashev, Kenneth Goldie, Timm Maier, Henning Stahlberg and Marek Basler

Nature Microbiology, Volume 2, 25 September 2017, pages 1507–1512, DOI: 10.1038/s41564-017-0020-7

Statement of contribution

I performed initial proof-of-concept experiments and showed presence of Hcp protein in the sample. I constructed sheath mutants and performed sheath isolations. I designed and constructed mutations as well as performed experiments to test the validity of the model. I contributed to cryo-electron microscopy data interpretation.

nature microbiology

LETTERS

DOI: 10.1038/s41564-017-0020-7

Cryo-EM structure of the extended type VI secretion system sheath–tube complex

Jing Wang[1], Maximilian Brackmann[1], Daniel Castaño-Díez[2,3], Mikhail Kudryashev[4,5], Kenneth N. Goldie[2], Timm Maier[6], Henning Stahlberg[2,6] and Marek Basler[1*]

The bacterial type VI secretion system (T6SS) uses contraction of a long sheath to quickly thrust a tube with associated effectors across membranes of eukaryotic and bacterial cells[1–5]. Only limited structural information is available about the inherently unstable precontraction state of the T6SS. Here, we obtain a 3.7 Å resolution structure of a non-contractile sheath–tube complex using cryo-electron microscopy and show that it resembles the extended T6SS inside *Vibrio cholerae* cells. We build a pseudo-atomic model of the complete sheath–tube assembly, which provides a mechanistic understanding of coupling sheath contraction with pushing and rotating the inner tube for efficient target membrane penetration. Our data further show that sheath contraction exposes a buried recognition domain to specifically trigger the disassembly and recycling of the T6SS sheath by the cognate ATP-dependent unfoldase ClpV.

The type VI secretion system (T6SS) is a cytosolic phage tail-like structure connected to a transmembrane complex[1,6,7]. The phage tail-like components include a baseplate complex and a tube of Hcp hexamers surrounded by a contractile sheath assembled from VipA/VipB (TssB/TssC) heterodimers. The current model suggests that the energy released during sheath contraction is converted into movement of the inner Hcp tube through the baseplate, which results in physical puncturing of the target membrane in close contact[8–10]. A similar mechanism is used by many other nanomachines to breach membranes during various biological processes[11]: (1) R-type pyocins punch holes into bacterial membranes[12,13], (2) contractile phages translocate proteins and DNA[14–16] and (3) certain nanomachines deliver toxins and signalling molecules to eukaryotic cells[17,18]. Although the T6SS sheath is evolutionarily related to the sheaths of contractile phage tails and R-type pyocins[12,15,19–23], it contains a distinct surface-exposed Domain 3 important for sheath recycling. Upon contraction, the VipB N terminus within Domain 3 is recognized by the cognate ATPase ClpV, which unfolds the contracted sheath to allow assembly of new extended sheaths[1,24–28].

It has so far been impossible to isolate an extended T6SS sheath from cells likely because it is inherently unstable. Therefore, we first analysed the structure of T6SS sheaths inside of *Vibrio cholerae* cells using cryo-electron tomography (cryo-ET). To obtain samples as thin as possible to increase the resolution, bacterial cells were incubated with ampicillin to destabilize the cell wall, which has no influence on T6SS function[29], however leads to partial lysis of cells during sample preparation for cryo-ET. We identified two distinct types of long polymers resembling T6SS sheaths previously described within *V. cholerae* cells [1]. The first type of structure was hollow and approximately 30 nm wide. The second type was only 20 nm wide and filled with additional density (Supplementary Fig. 1a).

To further improve the resolution, we performed subtomogram averaging for both identified structures. The final subtomogram average of the hollow structure had 17.4 Å (Fourier shell correlation (FSC) $_{0.143}$) resolution and resembled a six-start helix, with a 21.8 Å rise and a 29.4-degree twist (Supplementary Fig. 1b,e,g), which is identical to that of the isolated contracted sheath[22]. The second class of structures, resolved to 15.8 Å (FSC $_{0.143}$) resolution, resembled a six-start helix with 38.0 Å rise and 23.6-degree twist (Fig. 1a,b, Supplementary Fig. 1b,f,h, Supplementary Video 1). Since live-cell fluorescence microscopy of T6SS sheath contraction previously showed that sheath contracts to about 50% of the extended length[1,29], the 38.0 Å rise per subunit is consistent with the expected rise of an extended sheath structure. The same analysis was performed for both green fluorescent protein-labelled and wild-type structures and no difference was detected for both contracted and extended states of the sheaths. Overall, only 18 out of 71 imaged cells (25%) contained extended sheath structures, whereas all of them contained contracted sheaths, indicating that the extended structure is partially unstable during sample preparation for cryo-ET. The overall structure of the extended *V. cholerae* sheath is similar to the structure of the extended T6SS sheath inside *Myxococcus xanthus* cells with 37 Å rise and 22-degree twist[30].

We recently showed that sheath contraction can be abrogated by an insertion of two or more amino acid residues into the N-terminal linker of VipA, which connects sheath strands[31]. VipA-N2 sheath (two residues inserted) was stable in vivo but contracted during isolation, whereas VipA-N3 sheath (three residues inserted) resembled extended sheath and copurified with Hcp[31]. To obtain a high-resolution structure of the non-contractile sheath, we isolated the VipA-N3 sheath (without green fluorescent protein) from *V. cholerae* cells and analysed it using cryo-electron microscopy (cryo-EM) (Fig. 1c,d, Supplementary Video 1). The diffraction patterns of straight filaments were indexed to provide an initial estimate of helical symmetry (Supplementary Fig. 2b). The helical parameters were further refined in RELION2[32] to 23.5-degree twist per subunit and 37.8 Å rise per subunit. Importantly, the helical parameters of the isolated VipA-N3 structure matched those obtained for the wild-type extended sheaths inside cells (Supplementary Table 1). We also compared their structures by FSC and the extended sheath subtomogram

[1]Focal Area Infection Biology, Biozentrum, University of Basel, Klingelbergstrasse 50/70, CH-4056 Basel, Switzerland. [2]Center for Cellular Imaging and NanoAnalytics, Biozentrum, University of Basel, Mattenstrasse 26, CH-4058 Basel, Switzerland. [3]BioEM Lab, Biozentrum, University of Basel, Mattenstrasse 26, CH-4058 Basel, Switzerland. [4]Max Planck Institute of Biophysics, Max-von-Laue Str. 3, 60438 Frankfurt am Main, Germany. [5]Buchmann Institute for Molecular Life Sciences, Max-von-Laue Str. 17, 60438 Frankfurt am Main, Germany. [6]Focal Area Structural Biology, Biozentrum, University of Basel, Klingelbergstrasse 50/70, CH-4056 Basel, Switzerland. *e-mail: marek.basler@unibas.ch

average correlated with the VipA-N3 reconstruction to 20.5 Å resolution (Fig. 1, Supplementary Fig. 2e). This suggests that the VipA-N3 sheath is stable during purification from cells and its overall structure closely resembles the extended wild-type sheath.

The final resolution of the VipA-N3 sheath structure ranged from 3.5 Å (centre of the structure) to 8 Å (outer surface), with an average of 3.7 Å (Supplementary Fig. 2d,f). This allowed us to use the structure of the VipA/VipB subunit of the contracted sheath[22] as a template to build most of the extended sheath residues into the cryo-EM density. The final pseudo-atomic model of the VipA-N3 sheath subunit comprising VipA and VipB (Fig. 1f) showed a Cα root mean squared deviation of 1.0 Å for all residues participating in the alignment with the contracted VipA/VipB subunit (Supplementary Fig. 3a). However, we also identified multiple rearrangements at the interfaces of the sheath subunits (Supplementary Fig. 3b–f).

Surprisingly, the most significant difference between the non-contractile VipA-N3 sheath and the wild-type contracted sheath is the connectivity between the subunits. In the wild-type contracted sheath, each subunit connects to the two closest subunits on the previous sheath ring, one on the same strand through VipB linker and the second on the neighbouring strand through VipA linker[22]. In contrast, the VipA-N3 sheath is connected to the previous ring only through VipB linker and the elongated VipA linker connects to a neighbouring subunit on the same sheath ring (Figs. 1g,h and 2a). Connectivity of sheath subunits is unlikely to change during contraction and was indeed shown to be identical for the extended and contracted R-type pyocin sheath[12]. The altered connectivity therefore explains the stability of VipA-N3 sheaths because the VipA linker on the sheath with such connectivity is unable to stretch further as would be necessary during sheath contraction (Fig. 2b). This also suggests that the proper connectivity is required for contraction, however, not for sheath assembly. We generated a pseudo-atomic model of the extended wild-type sheath by remodelling the VipA linker in the VipA-N3 structure to have the same connectivity as in the wild-type contracted sheath (Fig. 2c). This model likely closely represents the actual structure of the extended wild-type sheath; however, the model is derived from the structure of the non-contractile mutant and therefore will have to be confirmed by future analysis of the wild-type extended sheath.

Unlike other contractile nanomachines, the T6SS is a cytosolic component of bacteria and the sheath is recycled for multiple rounds of assembly by ClpV, which recognizes the N terminus of VipB within Domain 3[28]. The Domain 3 was poorly resolved on the contracted sheath structure[21–23], however, is resolved to 5–8 Å resolution on the VipA-N3 structure (Fig. 3a,b, Supplementary Video 1). This allowed us to propose a structural model composed of two N-terminal α-helices of VipB and two C-terminal α-helices of VipA. The Domain 3 is embedded into a groove between two VipB subunits (residues T120-Y140 and K210-K220, respectively) on the neighbouring sheath strand and thus is sterically blocked from ClpV binding (Fig. 3c). The Domain 3 specifically interacts with Domain 2 residues that are present only in T6SS sheath[22], suggesting that these evolved to bind the T6SS-specific Domain 3.

Interestingly, VipB N terminus (residues G17-A25) and VipA C terminus (residues F136-N145) are packed as antiparallel α-helices, potentially protecting the ClpV binding residues in the hydrophobic patch on the buried side of the two helices (Fig. 3c–e, Supplementary Video 1). This position of the ClpV-binding α-helix explains why the VipA-N3 and likely also the wild-type extended sheath is not recognized and disassembled by ClpV. Since Domain 3 interacts with subunits that are on the two rings closer to the baseplate, our data also suggest that the Domain 3 of the first sheath ring might interact with baseplate components to prevent ClpV binding.

The density inside of the VipA-N3 sheath is a tube composed of hexamers with the same helical parameters as the sheath (Fig. 4a,c, Supplementary Video 1). The tube is predicted to be formed from

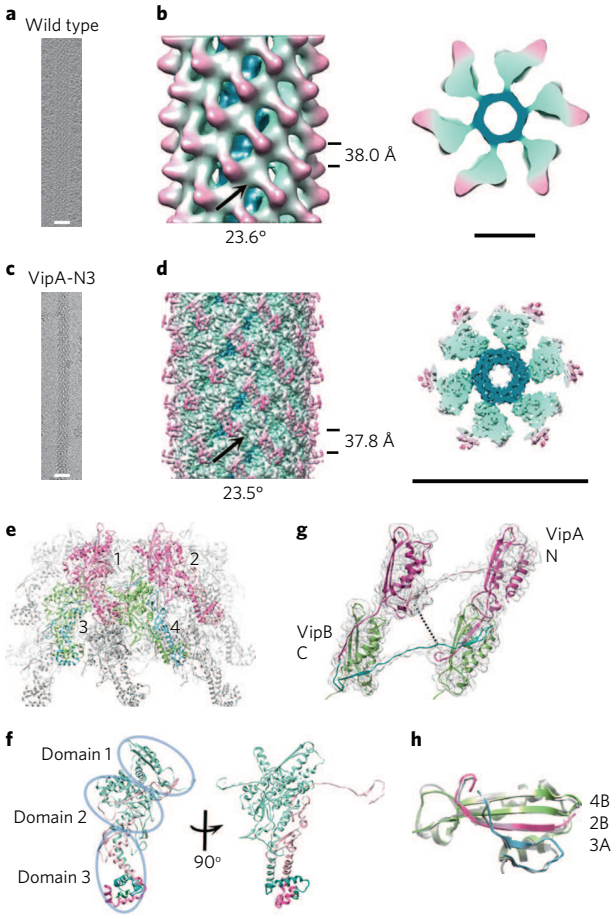

Fig. 1 | Cryo-EM structure of the VipA-N3 sheath–tube complex closely resembles the intracellular wild-type extended sheath–tube complex. **a**, Tomogram section of intracellular extended T6SS. Scale bar, 250 Å. **b**, Subtomogram average of the extended structure. Both the sheath and the tube follow a helical symmetry of 38.0 Å per rise, 23.6 ° per rotation, with C6 symmetry around the helical axis. The cross-section of the subtomogram shows the Hcp density in the centre of the sheath. Outer diameter of the Hcp tube is 80 Å (scale bar). **c**, Cryo-electron micrograph of an isolated VipA-N3 filament. Scale bar, 250 Å. **d**, Front and top views of the reconstructed VipA-N3 sheath–tube complex, which follows a helical symmetry of 37.8 Å per rise, 23.5 ° per rotation. Scale bar, 250 Å. **e**, Pseudo-atomic model of the VipA-N3 sheath. Three hexamers (rings) of sheath subunits are shown, with four adjacent protomers highlighted. **f**, Side and front views of sheath protomer (pink: VipA, green: VipB) within the outlined domains. Domain 3 contains four additional α-helices that are disordered in the contracted sheath. **g**, Non-contractile VipA-N3 sheath shows altered connectivity compared with the contracted wild-type sheath. Only Domain 1 is shown. Protomers within the same ring are connected by the VipA N-terminal linker (N), although the contracted structure predicts the VipA N-terminal linker connects subunit from the adjacent ring (dotted line). Protomers in adjacent rings are connected by the VipB C-terminal linker (C). **h**, The handshake domain connects three sheath subunits (two β-strands from VipB of subunit 4 (4B), one β-strand from VipB of subunit 2 (2B) and one β-strand from VipA of subunit 3 (3A). Numbers match those in panel **e**. The arrangement and structure of the handshake domain in extended sheath resemble that of the contracted sheath (superimposed in grey). Panels **a**–**g** are side views oriented with baseplate end towards the bottom.

Hcp molecules; however, the atomic structure of *V. cholerae* Hcp is unavailable. Therefore, we first generated a model of Hcp monomer based on crystal structures of homologous Hcp proteins using

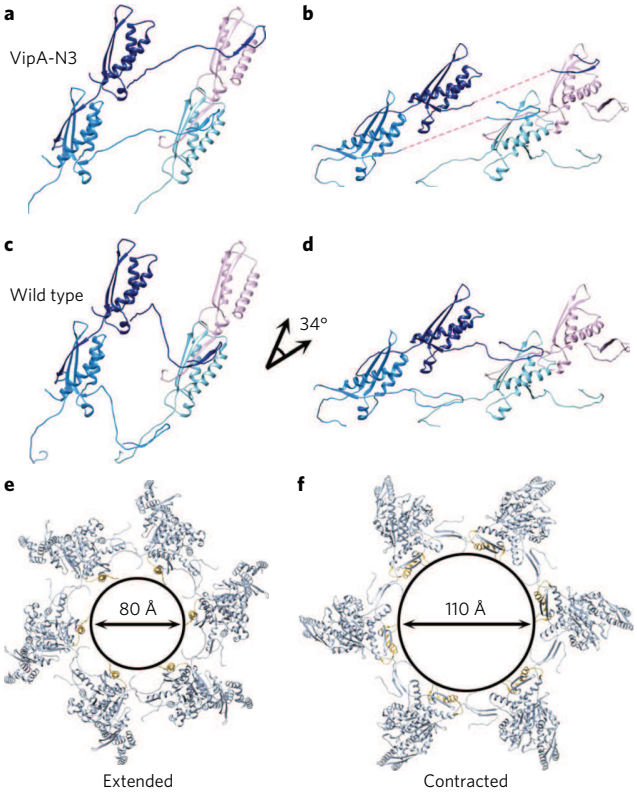

Fig. 2 | Model of T6SS sheath contraction. a, In the VipA-N3 mutant sheath, VipA linker is long enough to connect the adjacent protomers within the same sheath ring. **b**, Altered connectivity prevents the sheath from contracting. **c**, Assuming wild-type (WT) extended sheath has the same connectivity as the contracted sheath, a sharp kink has to be introduced to the VipA linker in the extended state. **d**, The sheath ring near the baseplate pulls on VipA linker to bring closer the sheath ring above, so that the sheath lattice becomes more compact after contraction. Simultaneously, the attachment helix of VipB rotates 34° to detach from the Hcp. Panels **a**–**d** are shown with baseplate connections oriented towards the bottom. **e**, Top view of an extended sheath hexamer. The inner diameter is 80 Å, matching the outer diameter of the Hcp ring. **f**, Top view of a contracted sheath hexamer. The sheath subunits expand outwards to detach from the Hcp tube.

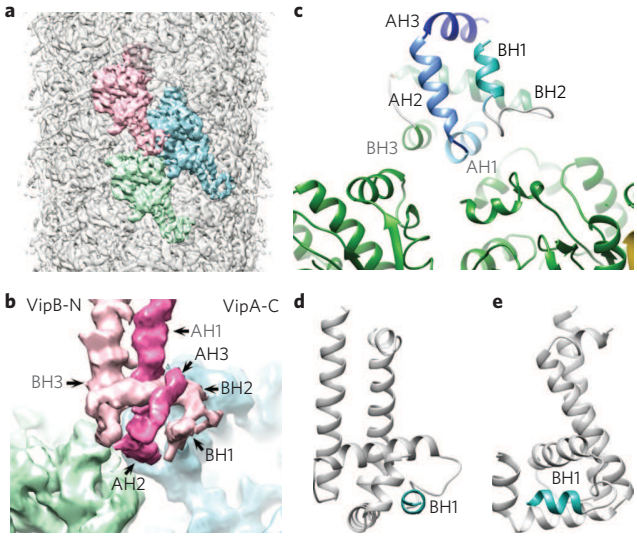

Fig. 3 | Domain 3 of the VipA-N3 sheath is inaccessible to ClpV. a, Side view of the sheath EM density (baseplate end towards the bottom) shows the Domain 3 at the outmost tip of a sheath protomer (pink) embedded between two protomers (green and blue) on the adjacent helical strand. **b**, EM density of the Domain 3 comprises two α-helices (AH2 and AH3) from VipA C terminus and two α-helices (BH1 and BH2) from VipB N terminus. AH1 and BH3 of Domain 3 are visible in both the contracted and extended sheath. **c**, Pseudo-atomic model of the Domain 3. View from **b** is rotated 90° to reveal how Domain 3 of one sheath protomer sits in between two protomers below it. **d**,**e**, Front (**d**) and side views (**e**) of the ClpV binding helix of VipB (BH1).

Modeller[33]. Then we built an atomic model of the Hcp tube into the cryo-EM map. We show that the Hcp folds as a β-sheet roll and each Hcp hexameric ring is in total composed of 24 β-strands at the inner surface (Fig. 4a,b, Supplementary Video 1). Interestingly, the inner diameter of *V. cholerae* T6SS Hcp hexamer ranges from 20 to 35 Å because an Hcp loop (residue P128-N141) protrudes to the centre of the tube (Fig. 4b), which is specific to the *V. cholerae* Hcp (Supplementary Fig. 4a–c). Importantly, as in R-type pyocin[12] or T4 phage[34], the Hcp tube and the surrounding sheath display identical helical symmetry that gives rise to a single diffraction pattern (Supplementary Fig. 2b); therefore, the interactions between sheath and tube are the same along the whole sheath–tube polymer. A similar conclusion was reached by analysis of an extended T6SS sheath of *M. xanthus* by cryo-ET[30]. This is in contrast to Hcp tubes formed in crystal lattices where Hcp hexamers stack without any helical twist[4,35,36]. However, Hcp tubes with no twist may assemble from Hcp rings in head-to-tail configuration when Cys are introduced at certain positions on Hcp[37,38].

The Hcp N-terminal side of the ring is predominantly negatively charged, and the C-terminal side of the hexamer contains positively charged residues (Supplementary Fig. 4e). Each Hcp interacts with three subunits from the next layer of Hcp ring, contributing −14.9 kcal mol^{-1} subunit^{-1} solvation free energy to stabilize the Hcp tube (Supplementary Table 2, calculated by PISA[39] including the contributions of hydrogen bonds and salt bridges). This is weaker than the corresponding tube interactions in T4 phage (−17.7 kcal mol^{-1} subunit^{-1})[34] and R-type pyocin (−18.5 kcal mol^{-1} subunit^{-1})[12].

The rings of Hcp and sheath display complementary surface charges on their contacting interfaces with an overall energy of −3.3 kcal mol^{-1} subunit^{-1} (Supplementary Fig. 4h), which is similar to that in R-type pyocin with −1.4 kcal mol^{-1} subunit^{-1} [12] (Supplementary Table 4). We identified key residues involved in interactions between Hcp and sheath (Fig. 4d, Supplementary Video 1). VipB binds the Hcp hexamer by an α-helix (VipB residue N417-E435), similarly to the 'attachment helix' in R-type pyocin[12]. Interestingly, the top of the attachment helix is overreaching to the next Hcp ring so that each copy of VipB bridges three copies of Hcp (Fig. 4d and Supplementary Fig. 4h). Both the VipA-N3 sheath and the subtomogram average of the wild-type extended sheath show the same connectivity between sheath and the edge of the hexameric Hcp ring (Supplementary Fig. 4f), implying that the interactions observed in VipA-N3 are identical to the interactions in the wild-type extended sheath.

To provide an explanation of why VipA-N2 sheaths are unable to contract in vivo[31], we obtained a 4.0 Å structure of isolated VipA-N2 sheaths using cryo-EM (Supplementary Fig. 5). VipA-N2 sheath contracts during isolation and shows a helical symmetry of 29.4° per twist and 21.7 Å per rise, identical to that of the wild-type contracted sheath. Importantly, the atomic model of the contracted wild-type sheath[22] resembles the VipA-N2 sheath protein density up to 4.1 Å resolution ($FSC_{0.5}$, Supplementary Fig. 5g). The only significant difference between the wild-type contracted sheath and VipA-N2 sheath was identified in the VipA N-terminal linker, where two

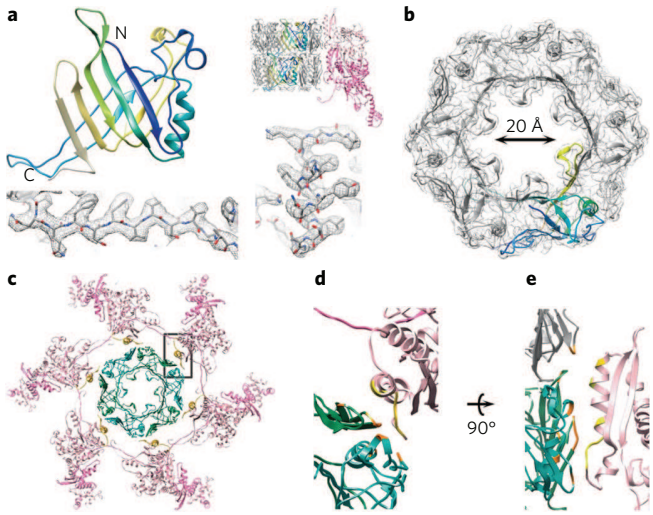

Fig. 4 | Structure of the Hcp tube and its interaction with the sheath. **a**, T6SS Hcp monomer. Six Hcp monomers assemble ring-like structures that stack on top of each other, following the same helical symmetry as the surrounding sheath. Examples of the model fitting are shown for the α-helix (residues 77–87) and one of the β-strands (residues 45–50). **b**, Top view of one Hcp hexamer. The central channel of the Hcp tube is constricted to 20 Å by the loop 128–141 that protrudes inwards. **c**, Top view of one ring of Hcp with associated VipA/VipB. The attachment helix of VipB contacts the Hcp ring at the edge of the hexamer. **d**, Close-up view of the Hcp–VipA/VipB interface, boxed in (**c**), shows each VipB interacting with two Hcp molecules in the same sheath–tube stack. **e**, Each VipB also contacts a third Hcp (grey) located one ring above. C, Hcp C-terminus; N, Hcp N-terminus.

additional residues (alanine and glutamate) are located (Supplementary Fig. 5d). Introducing two extra amino acids (AE after E27) pushed the E27 towards the VipA N terminus and changed the linker bending after the previous handshake domain. The inner layer of the sheath, including the handshake domain, assembled with the same topology as in the wild-type sheath (Supplementary Fig. 5e). This shows that elongating the VipA N-terminal linker by two amino acids abolishes sheath contraction in live cells while maintaining the same sheath subunit connectivity as in the wild-type sheath. This implies that the precise length and topological connectivity of the linker are important for sheath contraction in vivo.

Comparison of the extended T6SS sheath–tube complex with the structure of the contracted sheath[22] suggests a mechanism by which sheath contraction is coupled with the translocation of the inner tube. Upon contraction, the VipB linker maintains the handshake contacts within the same helical strand and the VipA linker swings as a hinge to pull the adjacent strands closer to the baseplate (Fig. 2c,d). Each sheath subunit rotates 34° and moves outwards 15 Å relative to the Hcp tube during contraction. As a result, the sheath expands radially (Fig. 2e,f), compresses vertically and detaches from the tube. Since the sheath contraction likely propagates from the baseplate, the remaining interactions between distal sheath and tube subunits may be sufficient to couple movement of the inner tube with the movement of the contracting sheath (Supplementary Video 2). However, a cap may further stabilize the end of the extended sheath distal to the baseplate and thus promote tube expulsion[40].

By comparing the sheath residues accessible to solvent on both extended and contracted structures, each sheath subunit in the contracted state buries about 1,293 Å^2 more of its surface than in the extended state (Supplementary Table 2). The total free energy of contacts of each subunit in the contracted sheath is −161.2 kcal mol^{-1}[22], lower than that of the extended sheath shown here to be −129.4 kcal mol^{-1} (considering only the portions of VipA and VipB proteins resolved in the contracted state). If we account for breaking the interaction between tube and sheath subunits, the free energy gained during contraction is 28.5 kcal mol^{-1} subunit^{-1}, more than 9.1 kcal mol^{-1} subunit^{-1} calculated for R-type pyocin (Supplementary Table 5, calculated by PISA[39] including the contributions of hydrogen bonds and salt bridges). However, this estimation is imprecise because Domain 3 was not resolved in the contracted sheath structure[22] and thus was excluded in this comparison.

Finally, comparison of the helical parameters of the extended and contracted sheath shows that contraction of a single sheath ring moves and rotates the tube by 16.2 Å and 5.8° (Supplementary Table 1). Therefore, contraction of a 1 µm long sheath, composed of 260 rings, would push the inner tube by 420 nm and rotate it by 4.2 turns (Supplementary Video 2). The overall amount of energy released during a single sheath contraction could be close to 44,000 kcal mol^{-1}. Considering that contraction happens within a few milliseconds[1,29], T6SS functions as a powerful drill.

Methods

VipA/VipB sheath preparation. Overnight cultures of the indicated strains were diluted 1:1,000 in 0.5 l of fresh LB medium supplemented with appropriate antibiotics, and then shaken at 37 °C and 250 rpm to an optical density (OD) of ≈ 1.2. Cells were centrifuged for 20 min at 5,000 x *g* and 4 °C, resuspended in 20 ml PBS and centrifuged again for 30 min at 3,214 x g and 4 °C. Pellets were frozen until further processing. The cell pellets were thawed, resuspended in 20 ml of TN buffer (20 mM Tris, 150 mM NaCl, pH 8.3) and lysed by addition of (0.75x) CelLytic B, Lysozyme (200 µg ml^{-1}) and EDTA (5 mM) and incubation at 37 °C. DNase (50 µg ml^{-1}) and $MgCl_2$ (10 mM) were added to cleave DNA. After 15 min incubation at 37 °C, cell debris was removed by centrifugation for 20 min at 10,000 x *g*. Cleared supernatants were subjected to ultraspeed centrifugation for 1.5 h at 104,000 x *g* and 4 °C and the resulting pellet was washed with 1 ml TN buffer and subsequently resuspended in 1 ml TN buffer; insoluble material was removed by centrifugation for 1 min at 10,000 x *g*. The supernatant was subjected to another round of ultraspeed centrifugation for 1 h at 104,000 x *g* and 4 °C and the resulting pellet was resuspended in 70 µl of TN buffer for further analysis. Purity of the sample was assessed by Coomassie-stained SDS-PAGE.

Preparation of *V. cholerae* spheroplasts. *V. cholerae* 2740-80 wild-type stain was grown aerobically at 37 °C in LB medium. A single colony was picked from an overnight-cultured plate and incubated in 3 ml LB medium to OD_{600} ≈ 1. The culture was further diluted 100-fold and grown to OD_{600} of 0.6–1. Bacteria were resuspended in LB medium supplemented with 100 µg ml^{-1} ampicillin to OD_{600} of 1 and incubated at 37 °C for another 0.5–1 h with shaking at 300 rpm. Bacteria were pelleted again at 2,000 x *g* for 2 min and suspended in PBS to OD_{600} of 5.

Cryo-ET. Bacteria were mixed with 10 nm gold particles covered with Protein A (University Medical Center Utrecht, Utrecht, The Netherlands) (20:1 v/v) in PBS immediately before plunge freezing. An aliquot of 4 µl of the mixture was applied to the glow-discharged holey carbon film grids (R2/2; Quantifoil Micro Tools GmbH, Großlöbichau, Germany), blotted for 0.5 sec and plunge-frozen by vitrification in liquid nitrogen-cooled liquid ethane, using a Vitrobot MK4 (FEI Company, Eindhoven, The Netherlands). Tilt series were collected using a Titan Krios (FEI Company) equipped with an energy filter (zero-loss energy filtering, slit width 20 eV; Gatan Inc., Pleasanton, USA) on a K2 Summit direct electron detector operated in counting mode (Gatan Inc.) at a nominal magnification of 26,000 x, corresponding to a calibrated pixel size of 5.22 Å. The tilt series were recorded from −60° to 60° using the continuous tilt scheme or from 0° to both −60° and 60° using the dose-symmetric tilt scheme[41], with increment of 3° at 5–10 µm defocus. Tilt images were acquired as 4 K by 4 K movies of eight frames, taken at 0.5 s per frame with a dose rate of 8 e$^-$ per pixel s^{-1}, corresponding to a cumulative dose 40e$^-$ per Å^2 for each tilt series. SerialEM was used for automatic tilt-series acquisition[42]. Movie frame alignment, contrast transfer function (CTF) correction and tomographic reconstruction were performed using the IMOD software package [43].

Subtomogram averaging. *Dynamo* catalogue was used to manually generate filament models in the tomograms[44,45]. Overlapping subvolumes with a size of (666)^3 Å^3 were extracted along the tube axis with 20 Å or 40 Å offset from the tomograms of the contracted or extended sheaths, respectively. Iterative alignment of subtomograms to the average was performed by *Dynamo* projects[44]. For

contracted sheaths, 67 filaments were picked from six tomograms, yielding 5,848 subtomograms. For extended sheaths, 71 filaments were picked from 18 tomograms, yielding 6,337 subtomograms. The contracted sheath helical reconstruction was low-pass-filtered to 50 Å and provided as the initial reference for aligning the contracted subtomograms (Supplementary Fig. 1c). The average of subtomograms without alignment was provided as the initial reference for aligning the extended subtomograms (Supplementary Fig. 1d). To improve the polarity convergence within an individual filament, a pair of identical templates with opposite polarity was provided for multireference alignment to classify the subtomograms (Supplementary Fig. 1i). Only the C6 symmetry was applied during subtomogram averaging and the helical symmetries of the resulting maps were determined with the *Dynamo* function *dynamo_symmetry_scan*.

Sample preparation of isolated T6SS sheaths for cryo-EM. Sheaths were purified as described above. An aliquot of 2.5 µl of sheath sample was applied onto freshly glow-discharged Quantifoil R2/1 holey carbon grids (Quantifoil Micro Tools GmbH), blotted for 2–3 seconds and vitrified using a Vitrobot MK4 (FEI Company). The chamber was maintained at 4 °C and 100% humidity during the blotting process.

Data of the isolated sheaths were acquired using Titan Krios microscope (FEI Company) equipped with an energy filter (slit width 20 eV) on a K2 Summit direct electron detector (Gatan Inc.) in counting mode, operated at 300 kV and at a nominal magnification of 130,000 x, corresponding to a calibrated pixel size of 1.04 Å, and a defocus ranging from 0.5 to 3 µm. Between 200 and 500 movie series for each of the VipA-N2, N3 were collected automatically using the SerialEM software[42]. For each movie, 30-frame exposures were taken at 0.3 s per frame (9 s total exposure time), using a dose rate of $4e^{-}$ per pixel s^{-1}, corresponding to a total dose of approximately $30e^{-}$ per $Å^{2}$ on the specimen.

Helical reconstruction. Movie frames were aligned using MotionCorr to correct for specimen motion[46]. The averages of the aligned frames were used for data processing within SPIDER[47], SPRING[48] and RELION2[32]. Filaments were manually selected from the micrographs using EMAN2 helixboxer[49]. From the filament, overlapping segments were extracted along the helical axis with a step size of one axial rise per subunit. For the VipA-N2 filaments, we selected 186 movies at 1.04 Å per pixel and manually picked 270 filaments of a box size of 512 pixels. After two-dimensional (2D) and three-dimensional (3D) classification, a total of 7,000 segments were used for 3D refinement. For the VipA-N3 filament, 420 movies collected at 1.04 Å per pixel were selected and 650 filaments were manually picked with a box size of 512 pixels. A total of 12,000 segments was selected for 3D refinement.

The contrast transfer function of each micrograph was estimated using the CTFFIND4 program[50]. Helical symmetries of the T6SS were estimated with the EMIP software and further refined using IHRSR and the RELION-2 helical module[32,51,52]. Briefly, 2D classes that showed layer lines of even intensity for both the near and far sides of the helix were selected for subsequent 3D classification. The majority of the segments belong to a single 3D class, which is low-pass-filtered to 60 Å as reference model for 3D auto-refinement. C6 symmetry was imposed during 3D refinement. The helical symmetry estimated from EMIP was real-space optimized during each iteration of 3D refinement until convergence to the final values of 21.7 Å (rise) and 29.4° (twist) for the VipA-N2, and 37.8 Å (rise) and 23.5° (twist) for VipA-N3. Class averages were generated using SPRING. Local resolution of the EM density map was computed by Resmap[53].

Atomic model building and refinement. *V. cholerae* Hcp model was generated based on known crystal structures using Modeller as template and the flexible loop regions were built into EM density by RosettaCM[33,54]. COOT was used to manually refine the polypeptide chains of Hcp, VipA and VipB directly, using available or generated models as starting poin[55]. The models built from COOT were subsequently refined in real space with PHENIX[56].

Molecular analysis. Interaction energy was calculated using PISA[39]. Secondary structure prediction was performed by Jpred[57]. The colouring of the EM maps, visualization of the atomic model and rendering of movies were performed in UCSF Chimera[58].

Data availability. The EM maps have been deposited to EMDB (http://www.emdatabank.org/) with accession numbers: EMD-3563 (subtomogram average of the wild-type extended sheath), EMD-3564 (subtomogram average of the wild-type contracted sheath), EMD-3566 (helical reconstruction of VipA-N3) and EMD-3567 (helical reconstruction of VipA-N2). Electron micrographs used for processing were deposited to EMPIAR (http://www.ebi.ac.uk/pdbe/emdb/empiar/) with accession numbers: EMPIAR-10085 (VipA-N2) and EMPIAR-10086 (VipA-N3). Atomic coordinates were deposited to PDB (http://www.rcsb.org) with accession numbers: 5MYU (VipA-N2/VipB), 5MXN (VipA-N3/VipB/Hcp) and 5OJQ (modelled structure of wild-type VipA/VipB/Hcp).

Received: 13 February 2017; Accepted: 2 August 2017;
Published online: 25 September 2017

References

1. Basler, M., Pilhofer, M., Henderson, G. P., Jensen, G. J. & Mekalanos, J. J. Type VI secretion requires a dynamic contractile phage tail-like structure. *Nature* **483**, 182–186 (2012).
2. Hood, R. D. et al. A type VI secretion system of *Pseudomonas aeruginosa* targets a toxin to bacteria. *Cell Host Microbe* **7**, 25–37 (2010).
3. MacIntyre, D. L., Miyata, S. T., Kitaoka, M. & Pukatzki, S. The *Vibrio cholerae* type VI secretion system displays antimicrobial properties. *Proc. Natl Acad. Sci. USA* **107**, 19520–19524 (2010).
4. Mougous, J. D. et al. A virulence locus of *Pseudomonas aeruginosa* encodes a protein secretion apparatus. *Science* **312**, 1526–1530 (2006).
5. Pukatzki, S. et al. Identification of a conserved bacterial protein secretion system in *Vibrio cholerae* using the *Dictyostelium* host model system. *Proc. Natl Acad. Sci. USA* **103**, 1528–33 (2006).
6. Durand, E. et al. Biogenesis and structure of a type VI secretion membrane core complex. *Nature* **523**, 555–560 (2015).
7. Leiman, P. G. et al. Type VI secretion apparatus and phage tail-associated protein complexes share a common evolutionary origin. *Proc. Natl Acad. Sci. USA* **106**, 4154–4159 (2009).
8. Cianfanelli, F. R., Monlezun, L. & Coulthurst, S. J. Aim, load, fire: the type VI secretion system, a bacterial nanoweapon. *Trends Microbiol.* **24**, 51–62 (2016).
9. Zoued, A. et al. Architecture and assembly of the type VI secretion system. *Biochim. Biophys. Acta* **1843**, 1664–1673 (2014).
10. Basler, M. Type VI secretion system: secretion by a contractile nanomachine. *Philos. Trans. R. Soc. Lond. B. Biol. Sci.* **370**, (2015).
11. Brackmann, M., Nazarov, S., Wang, J. & Basler, M. Using Force to Punch Holes: Mechanics of Contractile Nanomachines. *Trends Cell Biol.* 623–632 (2017).
12. Ge, P. et al. Atomic structures of a bactericidal contractile nanotube in its pre- and postcontraction states. *Nat. Struct. Mol. Biol.* **22**, 377–382 (2015).
13. Nakayama, K. et al. The R-type pyocin of *Pseudomonas aeruginosa* is related to P2 phage, and the F-type is related to lambda phage. *Mol. Microbiol.* **38**, 213–231 (2000).
14. Kostyuchenko, V. A. et al. The tail structure of bacteriophage T4 and its mechanism of contraction. *Nat. Struct. Mol. Biol.* **12**, 810–813 (2005).
15. Leiman, P. G. & Shneider, M. M. Contractile tail machines of bacteriophages. *Adv. Exp. Med. Biol* **726**, 93–114 (2012).
16. Leiman, P. G., Chipman, P. R., Kostyuchenko, V. A., Mesyanzhinov, V. V. & Rossmann, M. G. Three-dimensional rearrangement of proteins in the tail of bacteriophage T4 on infection of its host. *Cell* **118**, 419–429 (2004).
17. Heymann, J. B. et al. Three-dimensional structure of the toxin-delivery particle antifeeding prophage of *Serratia entomophila*. *J. Biol. Chem.* **288**, 25276–25284 (2013).
18. Shikuma, N. J. et al. Marine tubeworm metamorphosis induced by arrays of bacterial phage tail-like structures. *Science* **343**, 529–533 (2014).
19. Aksyuk, A. A. et al. The tail sheath structure of bacteriophage T4: a molecular machine for infecting bacteria. *EMBO J.* **28**, 821–829 (2009).
20. Aksyuk, A. A. et al. Structural conservation of the *myoviridae* phage tail sheath protein fold. *Structure* **19**, 1885–1894 (2011).
21. Clemens, D. L., Ge, P., Lee, B.-Y., Horwitz, M. A. & Zhou, Z. H. Atomic structure of T6SS reveals interlaced array essential to function. *Cell* **160**, 940–951 (2015).
22. Kudryashev, M. et al. Structure of the type VI secretion system contractile sheath. *Cell* **160**, 952–962 (2015).
23. Kube, S. et al. Structure of the VipA/B type VI secretion complex suggests a contraction-state-specific recycling mechanism. *Cell Rep.* **8**, 20–30 (2014).
24. Basler, M. & Mekalanos, J. J. Type 6 secretion dynamics within and between bacterial cells. *Science* **337**, 815 (2012).
25. Bönemann, G., Pietrosiuk, A., Diemand, A., Zentgraf, H. & Mogk, A. Remodelling of VipA/VipB tubules by ClpV-mediated threading is crucial for type VI protein secretion. *EMBO J.* **28**, 315–325 (2009).
26. Förster, A. et al. Coevolution of the ATPase ClpV, the sheath proteins TssB and TssC, and the accessory protein TagJ/HsiE1 distinguishes type VI secretion classes. *J. Biol. Chem.* **289**, 33032–33043 (2014).
27. Kapitein, N. et al. ClpV recycles VipA/VipB tubules and prevents non-productive tubule formation to ensure efficient type VI protein secretion. *Mol. Microbiol.* **87**, 1013–1028 (2013).
28. Pietrosiuk, A. et al. Molecular basis for the unique role of the AAA+ chaperone ClpV in type VI protein secretion. *J. Biol. Chem.* **286**, 30010–30021 (2011).
29. Vettiger, A., Winter, J., Lin, L. & Basler, M. The type VI secretion system sheath assembles at the end distal from the membrane anchor. *Nat. Commun.* **8**, 16088 (2017).
30. Chang, Y.-W., Rettberg, L. A., Ortega, D. R. & Jensen, G. J. *In vivo* structures of an intact type VI secretion system revealed by electron cryotomography. *EMBO Rep.* **18**, 1090–1099 (2017).

31. Brackmann, M., Wang, J. & Basler, M. VipA N-terminal linker and VipB-VipB interaction modulate the contraction of type VI secretion system sheath. Preprint at http://www.biorxiv.org/content/early/2017/06/21/152785 (2017).
32. Kimanius, D., Forsberg, B. O., Scheres, S. H. & Lindahl, E. Accelerated cryo-EM structure determination with parallelisation using GPUs in RELION-2. *eLIFE* **5**, (2016).
33. Webb, B. & Sali, A. Comparative protein structure modeling using MODELLER. *Curr. Protoc. Bioinformatics* **54**, 5.6.1–5.6.37 (2002).
34. Taylor, N. M. I. et al. Structure of the T4 baseplate and its function in triggering sheath contraction. *Nature* **533**, 346–352 (2016).
35. Osipiuk, J. et al. Crystal structure of secretory protein Hcp3 from Pseudomonas aeruginosa. *J. Struct. Funct. Genomics* **12**, 21–26 (2011).
36. Jobichen, C. et al. Structural basis for the secretion of EvpC: a key type VI secretion system protein from *Edwardsiella tarda*. *PLoS ONE* **5**, e12910 (2010).
37. Ballister, E. R., Lai, A. H., Zuckermann, R. N., Cheng, Y. & Mougous, J. D. *In vitro* self-assembly of tailorable nanotubes from a simple protein building block. *Proc. Natl Acad. Sci. USA* **105**, 3733–3738 (2008).
38. Brunet, Y. R., Henin, J., Celia, H. & Cascales, E. Type VI secretion and bacteriophage tail tubes share a common assembly pathway. *EMBO Rep.* **15**, 315–321 (2014).
39. Krissinel, E. & Henrick, K. Inference of macromolecular assemblies from crystalline state. *J. Mol. Biol.* **372**, 774–797 (2007).
40. Zoued, A. et al. Priming and polymerization of a bacterial contractile tail structure. *Nature* **531**, 59–63 (2016).
41. Hagen, W. J. H., Wan, W. & Briggs, J. A. G. Implementation of a cryo-electron tomography tilt-scheme optimized for high resolution subtomogram averaging. *J. Struct. Biol.* **197**, 191–198 (2016).
42. Mastronarde, D. N. Automated electron microscope tomography using robust prediction of specimen movements. *J. Struct. Biol.* **152**, 36–51 (2005).
43. Kremer, J. R., Mastronarde, D. N. & McIntosh, J. R. Computer visualization of three-dimensional image data using IMOD. *J. Struct. Biol.* **116**, 71–76 (1996).
44. Castaño-Díez, D., Kudryashev, M., Arheit, M. & Stahlberg, H. Dynamo: a flexible, user-friendly development tool for subtomogram averaging of cryo-EM data in high-performance computing environments. *J. Struct. Biol.* **178**, 139–151 (2012).
45. Castaño-Díez, D., Kudryashev, M. & Stahlberg, H. Dynamo Catalogue: geometrical tools and data management for particle picking in subtomogram averaging of cryo-electron tomograms. *J. Struct. Biol.* **197**, 135–144 (2017).
46. Li, X. et al. Electron counting and beam-induced motion correction enable near-atomic-resolution single-particle cryo-EM. *Nat. Methods* **10**, 584–590 (2013).
47. Frank, J. et al. SPIDER and WEB: processing and visualization of images in 3D electron microscopy and related fields. *J. Struct. Biol.* **116**, 190–199 (1996).
48. Desfosses, A., Ciuffa, R., Gutsche, I. & Sachse, C. SPRING – an image processing package for single-particle based helical reconstruction from electron cryomicrographs. *J. Struct. Biol.* **185**, 15–26 (2014).
49. Tang, G. et al. EMAN2: an extensible image processing suite for electron microscopy. *J. Struct. Biol.* **157**, 38–46 (2007).
50. Rohou, A. & Grigorieff, N. CTFFIND4: fast and accurate defocus estimation from electron micrographs. *J. Struct. Biol.* **192**, 216–221 (2015).
51. Diaz, R., Rice, W. J. & Stokes, D. L. in *Methods in Enzymology* (ed. Jensen, G. J.) 131–165 (Academic Press, Cambridge MA, 2010).
52. Egelman, E. H. The iterative helical real space reconstruction method: surmounting the problems posed by real polymers. *J. Struct. Biol.* **157**, 83–94 (2007).
53. Kucukelbir, A., Sigworth, F. J. & Tagare, H. D. Quantifying the local resolution of cryo-EM density maps. *Nat. Methods* **11**, 63–65 (2014).
54. Wang, R. Y.-R. et al. *De novo* protein structure determination from near-atomic resolution cryo-EM maps. *Nat. Methods* **12**, 335–338 (2015).
55. Emsley, P., Lohkamp, B., Scott, W. G. & Cowtan, K. Features and development of COOT. *Acta Crystallogr. D* **66**, 486–501 (2010).
56. Adams, P. D. et al. PHENIX: a comprehensive Python-based system for macromolecular structure solution. *Acta Crystallogr. D* **66**, (213–221 (2010).
57. Cole, C., Barber, J. D. & Barton, G. J. The Jpred 3 secondary structure prediction server. *Nucleic Acids Res* **36**, W197–W201 (2008).
58. Goddard, T. D., Huang, C. C. & Ferrin, T. E. Visualizing density maps with UCSF Chimera. *J. Struct. Biol.* **157**, 281–287 (2007).

Acknowledgements

The work was supported by Swiss National Science Foundation (SNSF) grant 31003A_159525 and the University of Basel. H.S. acknowledges support from the SNSF NCCR TransCure. Calculations were performed at sciCORE (http://scicore.unibas.ch/) scientific computing core facility at the University of Basel. We acknowledge S. Ursich for the help in sample preparation for cryo-ET.

Author contributions

J.W. collected cryo-electron microscopy data, performed image processing and generated atomic models. M.Br. isolated and purified the sheaths. M.K. performed some initial electron microscopy data collection and data analysis. D.C.-D. provided support and contributed to data analysis. K.N.G. and H.S. provided support and supervised data collection. T.M. contributed to and advised on atomic model building. M.Ba. conceived the project and analysed the data. M.Br., J.W. and M.Ba. wrote the manuscript. All authors read the manuscript.

Competing interests

The authors declare no competing financial interests.

Additional information

Supplementary information is available for this paper at doi:10.1038/s41564-017-0020-7.

Reprints and permissions information is available at www.nature.com/reprints.

Correspondence and requests for materials should be addressed to M.Ba.

nature research

Corresponding Author: Basler Marek

Date: Jul 27, 2017

Life Sciences Reporting Summary

Nature Research wishes to improve the reproducibility of the work we publish. This form is published with all life science papers and is intended to promote consistency and transparency in reporting. All life sciences submissions use this form; while some list items might not apply to an individual manuscript, all fields must be completed for clarity.

For further information on the points included in this form, see Reporting Life Sciences Research. For further information on Nature Research policies, including our data availability policy, see Authors & Referees and the Editorial Policy Checklist.

Experimental design

1. Sample size

   Describe how sample size was determined.

   Describe the statistical methods that were used to predetermine sample size OR if no sample size calculation was performed, describe how sample sizes were chosen and provide a rationale for why these sample sizes are sufficient.

2. Data exclusions

   Describe any data exclusions.

   If no data were excluded from the analyses, state this OR if data were excluded, describe the exclusions and the rationale behind them, indicating whether exclusion criteria were pre-established.

3. Replication

   Describe whether the experimental findings were reliably reproduced.

   For each experiment, note whether any attempts at replication failed OR state that all attempts at replication were successful.

4. Randomization

   Describe how samples/organisms/participants were allocated into experimental groups.

   Describe how samples were allocated to groups. If allocation was not random, describe how covariates were controlled. If this is not relevant to your study, explain why.

5. Blinding

   Describe whether the investigators were blinded to group allocation during data collection and/or analysis.

   Describe the extent of blinding used during data acquisition and analysis. If blinding was not possible, describe why OR explain why blinding was not relevant to your study.

Note: all studies involving animals and/or human research participants must disclose whether blinding and randomization were used.

6. Statistical parameters

   For all figures and tables that use statistical methods, confirm that the following items are present in relevant figure legends (or the Methods section if additional space is needed).

n/a	Confirmed	
☐	☐	The exact sample size (*n*) for each experimental group/condition, given as a discrete number and unit of measurement (animals, litters, cultures, etc.)
☐	☐	A description of how samples were collected, noting whether measurements were taken from distinct samples or whether the same sample was measured repeatedly.
☐	☐	A statement indicating how many times each experiment was replicated
☐	☐	The statistical test(s) used and whether they are one- or two-sided (note: only common tests should be described solely by name; more complex techniques should be described in the Methods section)
☐	☐	A description of any assumptions or corrections, such as an adjustment for multiple comparisons
☐	☐	The test results (e.g. *p* values) given as exact values whenever possible and with confidence intervals noted
☐	☐	A summary of the descriptive statistics, including central tendency (e.g. median, mean) and variation (e.g. standard deviation, interquartile range)
☐	☐	Clearly defined error bars

See the web collection on statistics for biologists for further resources and guidance.

Software

Policy information about availability of computer code

7. Software

Describe the software used to analyze the data in this study.	Relion2, Dynamo, SPRING, EMIP, COOT, Rosetta, Phenix, MotionCorr, IMOD

For all studies, we encourage code deposition in a community repository (e.g. GitHub). Authors must make computer code available to editors and reviewers upon request. The *Nature Methods* guidance for providing algorithms and software for publication may be useful for any submission.

Materials and reagents

Policy information about availability of materials

8. Materials availability

Indicate whether there are restrictions on availability of unique materials or if these materials are only available for distribution by a for-profit company.	No unique materials were used

9. Antibodies

Describe the antibodies used and how they were validated for use in the system under study (i.e. assay and species).	No antibodies were used

10. Eukaryotic cell lines

a. State the source of each eukaryotic cell line used.	No eukaryotic cell lines were used
b. Describe the method of cell line authentication used.	No eukaryotic cell lines were used
c. Report whether the cell lines were tested for mycoplasma contamination.	No eukaryotic cell lines were used
d. If any of the cell lines used in the paper are listed in the database of commonly misidentified cell lines maintained by ICLAC, provide a scientific rationale for their use.	No commonly misidentified cell lines were used

Animals and human research participants

Policy information about studies involving animals; when reporting animal research, follow the ARRIVE guidelines

11. Description of research animals

Provide details on animals and/or animal-derived materials used in the study.	No aminals were used

Policy information about studies involving human research participants

12. Description of human research participants

Describe the covariate-relevant population characteristics of the human research participants.	No human research participants were involved

II.5 Additional Results Related to Research Article III

II.1 Generation of minicells in *V. cholerae* and *P. aeruginosa* works different than in *E. coli*

As discussed before, we were not able to isolate native extended T6SS-sheaths from bacteria. However, cryo-ET combined with sub-tomogram averaging can reveal important features of protein complexes inside intact cells [233, 445–448]. The resolution of tomograms is, among other factors, limited by sample thickness. To reduce the thickness of bacteria, different approaches have been described to lead to the formation of either minicells (i.e. small cells without a chromosome) or cells with reduced size [449]. Advantages of the use of minicells have been exemplified in studies of phage infection of bacteria, architecture of the T3SS or arrays of chemoreceptors [172, 450–452]. However, most studies were conducted with *E. coli* or in one instance with *Shigella flexneri*, which is a close relative of *E. coli*.

Minicells were either generated by deletion of *minD*, a point mutation in *mreB* (A125V) or by overexpression of *ftsZ* [172, 445, 453, 454]. We implemented several approaches to generate minicells in *P. aeruginosa* as well as in *V. cholerae*. Some of them lead to the production of minicells, however, either we were not able to isolate the minicells, minicells were only shorter but not thinner, or did not exhibit T6SS-activity when observed by fluorescence microscopy (Figure II.5.1, [455]).

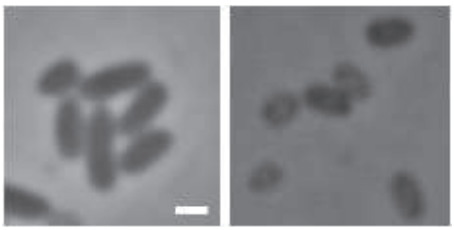

Figure II.5.1 *P. aeruginosa* produces smaller cells by over-expression of *ftsZ*. Light microscopy images of *P. aeruginosa* with pPSV35_*ftsZ*. *P. aeruginosa* cells are 1 μm or longer (left panel). When expression of ftsZ is induced from plasmid, shorter but not thinner cells can be isolated (right panel). *ftsZ*-expression was induced with 50 μM IPTG for 3 h. Scale bar is 1 μm.

Overexpression of *ftsZ* lead to the production of minicells, however, they only rarely were T6SS-active. Potentially, the probability of incorporating a membrane complex in minicells is lower due to the smaller surface area and/or cell curvature.

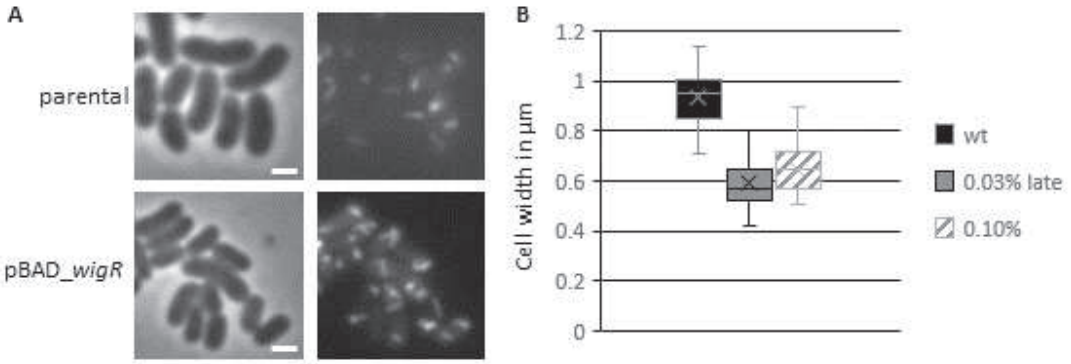

Figure II.5.2 *V. cholerae* over-expressing wigR are smaller. A, Fluorescence light microscopy images of *V. cholerae*. Cells over-expressing wigR are smaller in phase contrast (left) and are still T6SS-active (VipA-msfGFP, right). Expression of wigR was induced by addition of 0.03% arabinose for 3h. Scale bar is 1 μm. B, Measured cell widths of parental *V. cholerae* (black), expressing wigR for 3 h by induction with 0.03% arabinose (grey) and after1 h induction of wigR-expression by addition of 0.1% arabinose (diagonally striped). Between 25 and 60 cells were measured.

Recently, another report showed that *V. cholerae* are smaller when the transcriptional regulator *wigR* is overexpressed [456]. Overexpression of *wigR* lead to cells that were ≈30% thinner than wild-type cells with an intact and active T6SS (Figure II.5.2). This was not further followed up, as we were able to record tomograms of Ampicillin-treated cells and isolated a non-contractile sheath (Sections II.2 and II.4).

II.6 Research Article IV

Cryo-EM reconstruction of Type VI secretion system baseplate and sheath distal end

Sergey Nazarov, Johannes Schneider, Maximilian Brackmann, Kenneth Goldie, Henning Stahlberg and Marek Basler

The EMBO Journal, Volume 37, Issue 2, 17 January 2018, pages 161 - 320, DOI: 10.15252/embj.201797103

Statement of contribution

I performed initial proof-of-concept experiments and showed presence of baseplate and cap proteins in the sample. I performed sheath isolations and contributed to data interpretation.

Article

OPEN ACCESS

THE EMBO JOURNAL

Cryo-EM reconstruction of Type VI secretion system baseplate and sheath distal end

Sergey Nazarov[1], Johannes P Schneider[1], Maximilian Brackmann[1], Kenneth N Goldie[2], Henning Stahlberg[2,3] & Marek Basler[1,*]

Abstract

The bacterial Type VI secretion system (T6SS) assembles from three major parts: a membrane complex that spans inner and outer membranes, a baseplate, and a sheath–tube polymer. The baseplate assembles around a tip complex with associated effectors and connects to the membrane complex by TssK. The baseplate assembly initiates sheath–tube polymerization, which in some organisms requires TssA. Here, we analyzed both ends of isolated non-contractile *Vibrio cholerae* sheaths by cryo-electron microscopy. Our analysis suggests that the baseplate, solved to an average 8.0 Å resolution, is composed of six subunits of TssE/F_2/G and the baseplate periphery is decorated by six TssK trimers. The VgrG/PAAR tip complex in the center of the baseplate is surrounded by a cavity, which may accommodate up to ~450 kDa of effector proteins. The distal end of the sheath, resolved to an average 7.5 Å resolution, shows sixfold symmetry; however, its protein composition is unclear. Our structures provide an important step toward an atomic model of the complete T6SS assembly.

Keywords baseplate; contractile tails; cryo-electron microscopy; sheath; Type VI secretion system
Subject Categories Microbiology, Virology & Host Pathogen Interaction; Structural Biology
DOI 10.15252/embj.201797103 | Received 8 April 2017 | Revised 9 November 2017 | Accepted 16 November 2017

Introduction

Bacteria use phage-related contractile nanomachines to kill competition or manipulate the surrounding environment (Nakayama *et al*, 2000; Heymann *et al*, 2013; Shikuma *et al*, 2014; Ge *et al*, 2015). Evolutionarily related Type VI secretion system (T6SS) is used by bacteria to deliver proteins into both bacterial and eukaryotic cells (Mougous *et al*, 2006; Pukatzki *et al*, 2006; Hood *et al*, 2010; MacIntyre *et al*, 2010; Durand *et al*, 2014; Ho *et al*, 2014; Alcoforado Diniz *et al*, 2015; Hachani *et al*, 2016). The current model of T6SS biogenesis and mode of action is largely based on well-understood phage assembly (Leiman *et al*, 2009; Lossi *et al*, 2011, 2013; Ho *et al*, 2014; Zoued *et al*, 2014; Clemens *et al*, 2015; Kudryashev *et al*, 2015; Cianfanelli *et al*, 2016). However, many important features are unknown mostly due to the lack of high-resolution structural information of T6SS.

The whole T6SS was first observed at low resolution using cryo-electron tomography (cryo-ET) in *Vibrio cholerae* (Basler *et al*, 2012) and more recently in *Myxococcus xanthus* (Chang *et al*, 2017) and *Amoebophilus asiaticus* (Böck *et al*, 2017). The system is composed of a long sheath surrounding an inner tube attached to a baseplate and anchored to a membrane complex that spans both membranes (Brunet *et al*, 2014, 2015; Durand *et al*, 2015). T6SS biogenesis starts by formation of the membrane complex composed of TssJLM, which recruits TssK to connect a baseplate composed of TssEFG, as well as VgrG/PAAR spike and effectors (Brunet *et al*, 2015; Durand *et al*, 2015). The baseplate then serves as a nucleation platform for polymerization of the VipA/VipB (TssB/TssC) sheath and the inner Hcp tube (Zoued *et al*, 2016). Additionally, while one class of TssA proteins is required for baseplate assembly, another class of TssA proteins was shown to first bind to the baseplate and then stay associated with the distal end of the sheath during assembly (Planamente *et al*, 2016; Zoued *et al*, 2016).

The *V. cholerae* sheath subunits are interconnected by a mesh of VipA N-terminal and VipB C-terminal linkers (Kudryashev *et al*, 2015) similarly to T6SS sheath of *Francisella novicida* and R-type pyocin sheath (Clemens *et al*, 2015; Ge *et al*, 2015). The sheath was shown to assemble across the entire width of a cell, and this allowed to use live-cell fluorescence microscopy to study its dynamics and subcellular localization (Basler *et al*, 2012; Brunet *et al*, 2013; Gerc *et al*, 2015; Zoued *et al*, 2016; Vettiger *et al*, 2017). In *V. cholerae*, sheath assembly takes approximately 20 s (speed of assembly 30–40 nm/s) and is followed by fast contraction in less than 2 ms (speed of contraction higher than 800 μm/s) (Basler *et al*, 2012; Vettiger *et al*, 2017). Rapid sheath contraction propels the tip complex at the end of the inner tube formed from stacks of Hcp rings into the target cell periplasm or cytosol (Vettiger & Basler, 2016). In contrast to phages and many other contractile nanomachines, which translocate proteins only once by a single sheath contraction (Nakayama *et al*,

1 Focal Area Infection Biology, Biozentrum, University of Basel, Basel, Switzerland
2 Center for Cellular Imaging and NanoAnalytics, Biozentrum, University of Basel, Basel, Switzerland
3 Focal Area Structural Biology, Biozentrum, University of Basel, Basel, Switzerland
*Corresponding author. Tel: +41 61 207 21 10; E-mail: marek.basler@unibas.ch

2000; Ge *et al*, 2015; Hu *et al*, 2015), the contracted T6SS sheath is disassembled by a cytosolic unfoldase ClpV or ClpB to allow for repeated protein secretion (Bönemann *et al*, 2009; Pietrosiuk *et al*, 2011; Basler & Mekalanos, 2012; Basler *et al*, 2012; Kapitein *et al*, 2013; Förster *et al*, 2014; Brodmann *et al*, 2017).

The membrane complex seems to be stable at least in some organisms (Durand *et al*, 2015; Santin & Cascales, 2017); however, the whole T6SS was so far impossible to isolate from cells for *in vitro* studies. This is likely due to the highly dynamic behavior of T6SS, and it suggests that cell disruption triggers the sheath contraction, which in turn may lead to baseplate disassembly. Here, we analyzed both ends of a non-contractile T6SS sheath mutant, which has three amino acids inserted into the N-terminal VipA linker (VipA-N3) and was shown recently to co-purify with many components of T6SS baseplate (Brackmann *et al*, 2017; Wang *et al*, 2017). On one end, the sheath is attached to a 2.2-MDa complex with flattened cone geometry and dimensions of 240 × 124 Å. This complex resembles the phage T4 inner baseplate with a central sharp spike and is decorated by six protruding trimeric proteins. An extended-like sheath with a tube is docked onto the baseplate, and the overall structure resembles a typical contractile tail of bacteriophages. The opposite end of the sheath is covered with a flattened starlike complex with dimensions 190 × 67 Å and an estimated mass of 540 kDa and could represent either VipA/VipB sheath subunits without Hcp ring in an unusual conformation, or a cap composed of twelve copies of TssA protein. Together, our results indicate that blocking sheath contraction allows isolation of a largely intact T6SS and this may provide a path toward a detailed atomic model of the whole T6SS in a "ready-to-fire" conformation.

Results

Analysis of protein complexes associated with the ends of non-contractile sheaths

Non-contractile sheaths of *V. cholerae* were shown to be associated with certain baseplate components (Brackmann *et al*, 2017). We isolated the VipA-N3 sheath variant (3-amino acid insertion into the N-terminal VipA linker, tagged with msfGFP) from cells and purified it by ultracentrifugation as described previously (Kudryashev *et al*, 2015). Negative stain electron microscopy showed sheath assemblies of various lengths in apparently extended conformations (Fig 1A). On average, 39% of these sheath assemblies were decorated with distinct protein complexes at one of the two ends. Further image analysis and averaging revealed that one end resembles a phage-related baseplate and the second distal end has a distinct structure resembling a cap (Fig 1A).

To increase the resolution, we analyzed the non-contractile sheath sample by cryo-electron microscopy using Titan Krios and a K2 Summit direct electron detector in counting mode, operated at 300 kV and at a nominal magnification of 130,000×, corresponding to a calibrated pixel size of 1.06 Å. Overall, we collected 6,603 movies, performed specimen motion correction using MotionCorr2 (Zheng *et al*, 2017), and selected 21,446 particles from both ends of the non-contractile sheath assemblies. 8,309 baseplates and distal ends were identified after 2D classification, and 2,660 baseplates and 3,710 distal ends were further processed by RELION1.4 (Scheres, 2012) to obtain 3D density (Appendix Table S1). Based on available structural data of other contractile tail-like structures (Schwarzer *et al*, 2012; Heymann *et al*, 2013; Shikuma *et al*, 2014; Ge *et al*, 2015; Nováček *et al*, 2016; Taylor *et al*, 2016), we applied a sixfold symmetry (C6) during refinement of the baseplate and the distal end. The final resolution was estimated to be on average 8.7 Å (local resolution distribution from 7.2 to 14.2 Å) for the baseplate and 7.5 Å (from 6.7 to 13.7 Å) for the distal end (Fig EV1A). For the baseplate reconstruction, we also tested threefold (C3) symmetry during the refinement step using symmetry relaxation from C6 to C3. This resulted in a 11 Å resolution reconstruction (Appendix Fig S1A) with the same overall baseplate morphology, indicating that the C6 symmetry choice is correct and helps to improve the final resolution of the baseplate reconstruction.

The micrographs of non-contractile sheaths are mostly covered with long sheaths (Fig 1B), and this decreases the number of clearly observed sheath ends. It was recently shown that limiting Hcp availability in *V. cholerae* results in assembly of short, dynamic, and functional sheaths (Vettiger & Basler, 2016). In an attempt to increase the speed of data acquisition, we expressed limited amount of Hcp from an inducible pBAD24-*hcp* plasmid in the VipA-N3-msfGFP-expressing strain lacking both *hcp1* and *hcp2* genes (Fig EV2). We then purified the non-contractile sheaths as previously (Fig EV3) and characterized the sample by mass spectrometry. This showed that the sheaths prepared from Hcp-limited cells are associated with TssE,F,G,K, VgrG1/2/3, and PAAR (Fig EV3A and B, Tables EV1–EV3) similarly to the previous preparations. We collected 2,599 cryo-EM movies and selected 1,127 particles for the baseplate and 2,114 for the distal end. Combining this dataset with the dataset described above and selecting the best particles for the final 3D refinement, the final resolution of the baseplate increased from 8.7 to 8.0 Å (Fig EV1A), which improved overall interpretation of the protein density map. The resolution of the distal-end reconstruction did not improve, indicating dynamic nature of the complex. However, we also detected aberrant sheath fragments (Fig EV3C), which complicated single-particle analysis, and thus, these samples failed to provide a major increase in data acquisition rate.

Central spike and cavity for effector proteins

The cryo-EM reconstruction of the baseplate region revealed a 238-Å-wide sheath–tube assembly in its extended-like state attached to a compact hexagonal flattened conelike baseplate with a sharp tip in the center (Figs 1C and 2A–E). Overall dimensions of the baseplate are 182 Å in the narrow part, 240 Å in the broad part below the sheath–tube, and 195 Å in height including the protruding tip complex (Fig 2A and B). The central tip protrudes ~40 Å below base of the cone and clearly resembles a central spike present in all baseplates of phages with contractile tails (Browning *et al*, 2012; Leiman & Shneider, 2012; Schwarzer *et al*, 2012; Harada *et al*, 2013; Shneider *et al*, 2013; Habann *et al*, 2014; Taylor *et al*, 2016).

The T6SS spike complex is proposed to be formed by a VgrG trimer and a single PAAR protein (Leiman *et al*, 2009; Shneider *et al*, 2013). The central spike density has indeed well-resolved features in the threefold symmetry reconstruction (Appendix Fig S1A). The

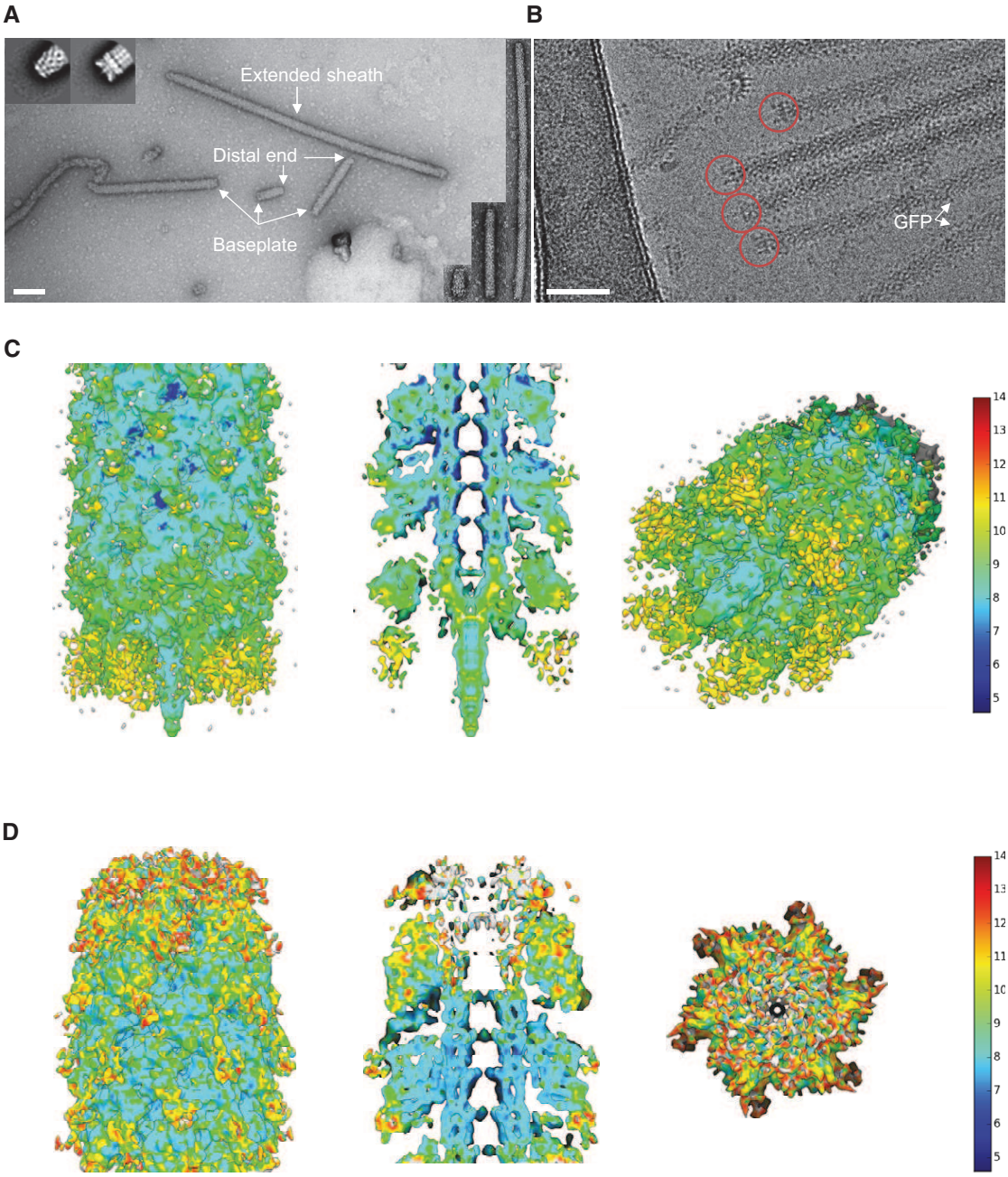

Figure 1. Raw images and cryo-EM structures of T6SS baseplate and distal-end complexes.

A A raw negative-stained image of VipA-N3 mutant sheath (scale bar: 100 nm). Extended sheath, baseplate, and distal end are highlighted with white arrows. Right insets: examples of T6SS assemblies of different lengths (shortest ~5 sheath rings, longest ~220 rings). Upper left insets: representative reference-free 2D class averages of baseplate (right) and distal-end (left) particles, extracted from negative-stained images.

B A raw cryo-EM image of VipA-N3 mutant (scale bar: 50 nm). Baseplate reconstruction was calculated for area highlighted with red circles.

C Side, cutaway, and tilted views of the sheath–baseplate cryo-EM reconstruction. 3D visualizations were rendered using UCSF Chimera. Baseplate model colored according to the local resolution variation, shown in the color bar on the right in Angstroms. Maps are shown at the contour level of 1.5σ.

D Side, cutaway, and top views of the sheath–distal-end cryo-EM reconstruction. 3D visualizations were rendered using UCSF Chimera. Distal-end model colored according to the local resolution variation, shown in the color bar on the right in Angstroms. Maps are shown at the contour level of 1.5σ.

available X-ray crystallographic structure of PA0091 VgrG-1 trimer (PDB 4MTK) and PAAR monomer (PDB 4JIV) fits well into both C3 (correlation coefficient (CC) = 0.93) and C6 reconstructions (CC = 0.88) (Fig 3A and Appendix Table S2). This fit was used to calculate the protein density volume-to-mass coefficient to estimate the mass of other protein complexes described below.

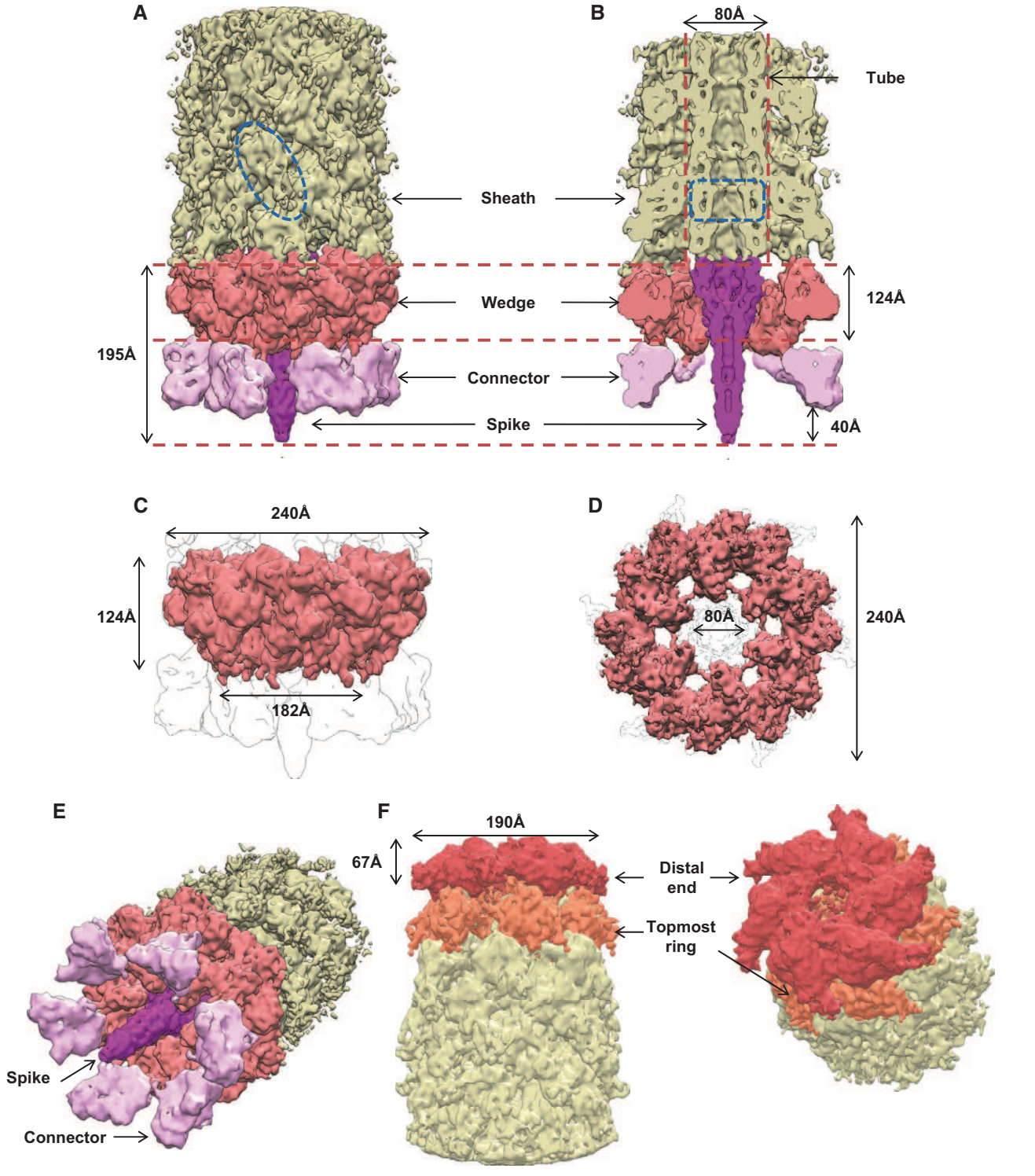

Figure 2. Overall dimensions, segmentation, and morphology of the baseplate and the distal end.

A, B Side and cutaway views of the sheath–baseplate cryo-EM reconstruction. The partially disordered connector density was replaced by the locally refined reconstruction calculated separately. The map is segmented, and protein complexes are colored and highlighted with black arrows. One VipA/VipB sheath subunit and one Hcp ring are outlined in blue.

C, D Side and bottom views of the putative baseplate density (1.15 MDa), highlighted in red in the sheath–baseplate cryo-EM reconstruction in (A, B).

E Tilted view of (A) with connector and spike densities highlighted with black arrows.

F Cutaway and tilted views of the sheath–distal-end cryo-EM reconstruction, locally filtered to the estimated resolution. The map is segmented and colored according to putative protein complexes.

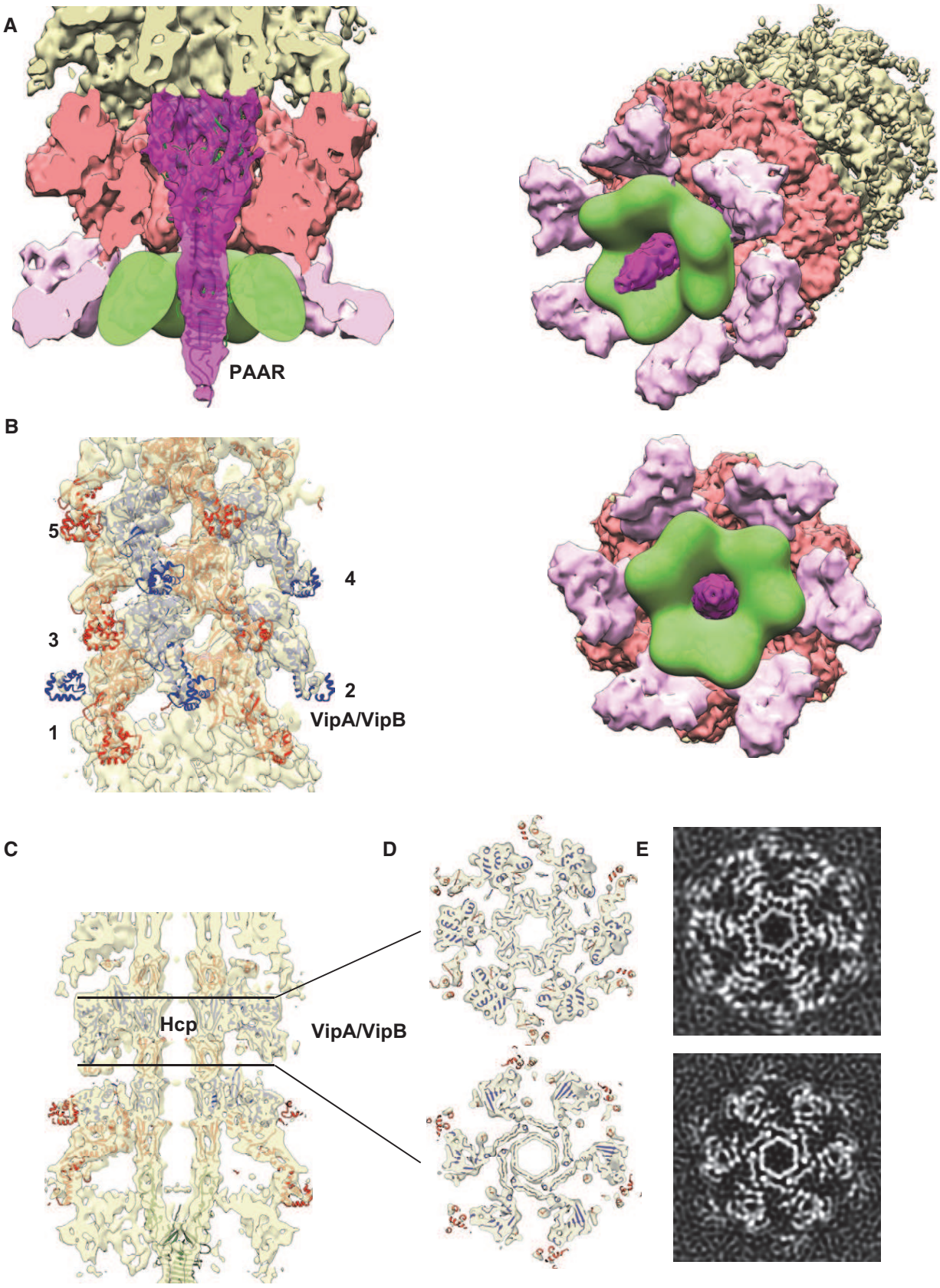

Figure 3.

Figure 3. Central spike, tube, and sheath densities with a cavity for effector proteins.

A Cutaway view of the density corresponding to the baseplate and spike with fitted X-ray crystallographic structures of VgrG-1 trimer (PDB 4MTK) and PAAR monomer (PDB 4JIV). Putative cavity for T6SS effectors is outlined in green.

B Side view of the density corresponding to the sheath next to the baseplate fitted with the atomic model of the VipA-N3 sheath–tube (PDB 5MXN). In panels (B–D), odd sheath rings are colored in red, even in blue. Sheath rings are numbered starting from the first ring next to the baseplate.

C Side cutaway view of the baseplate reconstruction with the fitted atomic model of VipA-N3 sheath–tube (PDB 5MXN).

D Top cutaway views of (C) with the fitted atomic model of VipA-N3 sheath–tube (PDB 5MXN).

E Slices through the raw sheath–baseplate reconstruction, as in (D).

T6SS effectors can be attached to the spike by several different mechanisms (Shneider *et al*, 2013). Mass spectrometry analysis identified T6SS effectors VasX and TseL associated with the non-contractile sheaths (Tables EV1–EV3). However, the cryo-EM reconstruction of VgrG/PAAR spike lacks any additional densities of possible effectors, and no density is observed inside VgrG or Hcp tube (Fig 3A and C–E). It is likely that each spike complex is decorated with a different set of effectors, and thus, the structures of the individual spikes are heterogeneous and the effector protein densities are missing after single-particle averaging. We estimate that the volume of the internal cavity formed around the central spike by the baseplate periphery is ~1,100 × 10^3 Å^3, which would be enough to accommodate multiple effectors with the overall molecular weight up to ~450 kDa, or three copies of ~150-kDa effector (Fig 3A).

Baseplate wedge and connection to the membrane complex

The central spike is surrounded by six copies of a structure resembling a phage baseplate wedge (Leiman & Shneider, 2012; Büttner *et al*, 2016; Taylor *et al*, 2016; Fig 2) and is decorated by a protein density, which is likely a connector between the baseplate and the membrane complex (Fig 2A–E). Overall, the T6SS baseplate resembles so-called minimal baseplate of contractile tail-like structures and is similar to the T4 phage inner baseplate in its pre-injection state (Appendix Fig S2; Leiman & Shneider, 2012; Taylor *et al*, 2016).

We estimate the molecular mass of a single baseplate wedge to be 191.2 kDa and 1.15 MDa for the overall dome-shaped assembly (Fig 2 and Table 1). Three conserved baseplate components, TssE, TssF, and TssG, share structural homology with T4 inner baseplate proteins: sheath initiator gp25, sheath platform gp6, and linker gp7 (Leiman *et al*, 2010; Taylor *et al*, 2016). Together, these proteins have been proposed to form a wedge subunit intermediate with a possible stoichiometry TssE–$(TssF)_2$–TssG (Taylor *et al*, 2016). Molecular mass of the TssE–$(TssF)_2$–TssG complex of *V. cholerae* based on their primary sequence is 189.2 kDa, which is in a good agreement with the mass estimation based on the baseplate reconstruction (Table 1).

Each baseplate wedge subunit is decorated with a ~85 Å long and ~65 Å wide protein density forming a continuation of the baseplate wedge flattened cone (Figs 2A, B, E and 4A, B, D). This protein density was initially resolved to the local resolution of only 14 Å, indicating that this protein complex or its domains are flexible and may be partially disordered. Another possibility is that this protein complex is occasionally present in less than six copies per baseplate, potentially due to instability during purification and the applied sixfold (C6) symmetry thus decreases the final resolution. To account for possible protein flexibility and low occupancy, we relaxed symmetry of the refined baseplate particles from C6 to C1 and performed 3D classification without alignment within a small mask around this decoration protein. The best 3D class was subsequently used for further focused 3D refinement, which increased the resolution to 10 Å and revealed clear trimeric features (Figs EV1 and 4A and B). Therefore, we estimate that this complex is composed of trimer of a 58-kDa protein (Table 1).

TssK was shown to form trimers in solution, it binds membrane complex proteins TssL/TssM as well as baseplate proteins TssF/TssG, and its spot localization correlates with T6SS activity (English *et al*, 2014; Brunet *et al*, 2015; Durand *et al*, 2015; Nguyen *et al*, 2017). Additionally, no wedge intermediate TssE–$(TssF)_2$–TssG was formed in the absence of TssK (Taylor *et al*, 2016). Taking these previous observations into account, the trimeric protein density on the periphery of the baseplate wedge is therefore likely formed by the 50-kDa TssK protein (Table 1; Figs 2A, B, E and 4A and B). Indeed, EAEC TssK protein structure (PDB 5M30) fits with a good agreement into our reconstruction (CC = 0.92) except for disordered C-terminal head domain (Fig 4B).

Each copy of the TssK protein complex has a threefold rotational axis oriented with ~48° relative to the baseplate sixfold axis with a left-handed twist and is thus similar to the domain IV of T4 peripheral baseplate protein gp10 (Appendix Fig S1). We suggest that TssK is likely interacting with TssG (MW = 38.4 kDa), which shares limited homology with T4 gp7 protein forming a link between the inner baseplate and the peripheral tail fiber network (Leiman *et al*, 2010; Taylor *et al*, 2016). TssK is also connected to the inner part of the baseplate

Table 1. Assignment of T6SS baseplate and distal-end proteins based on volume-to-mass coefficient calculated for fitted X-ray crystallographic structures of VgrG-1/PAAR (PDB 4MTK/4JIV).

Protein	Copies per assembly	$Mass_{EM}$, kDa	$Mass_{seq}$, kDa		Function	Homologues (T4)
TssE	6	192 for a single wedge	16	189 for a single wedge	Wedge	gp25
TssF	12		67		Wedge	gp6
TssG	6		38		Wedge	gp7/gp53
TssK	18	58	50		Connector	gp10
$TssA_1$ or VipA/VipB	12 or 6	90	53 or 74		Cap or Topmost sheath	–

wedge, likely the TssF dimer, through two fingerlike links (Fig 4C and D). Each link is about 22 Å long and 11 Å in diameter, suggesting that it may be formed by an α-helix or a β-hairpin loop. Together, those two connections would fix the TssK trimer to the baseplate wedge.

Sheath–tube attachment to the baseplate

The spike complex is predicted to be an extension of the Hcp tube, which is surrounded by the VipA/VipB sheath (Wang *et al*, 2017). Indeed, the central density resembles the structure of an Hcp tube and seems to be uniform from the first ring docked on top of the VgrG/PAAR spike (Fig 3C), suggesting that no additional proteins are in between the VgrG trimer and the Hcp tube. This is in an agreement with the fact that T6SS gene clusters lack orthologues of tubelike proteins such as gp48 and gp54 found between the spike and the tube in T4 phage (Taylor *et al*, 2016).

The structure of the extended sheath (PDB 5MNX) fits into the density just above the baseplate with CC = 0.87 (Fig 3B–E and Appendix Table S2), suggesting that this density represents the first ring of the sheath. An almost identical density, representing the second sheath ring, is 36.4 Å above and is twisted by 23.9 degrees, which is similar to the helical parameters determined for the extended sheath (37.8 Å rise and 23.5 degrees twist) (Wang *et al*, 2017). The density of the second ring correlates with the sheath-tube ring structure to CC = 0.86, further rings then to CC = 0.89 (Appendix Table S2).

Differences in correlation coefficients may be explained by slight changes in the conformation that the outer Domain 3 of the first and

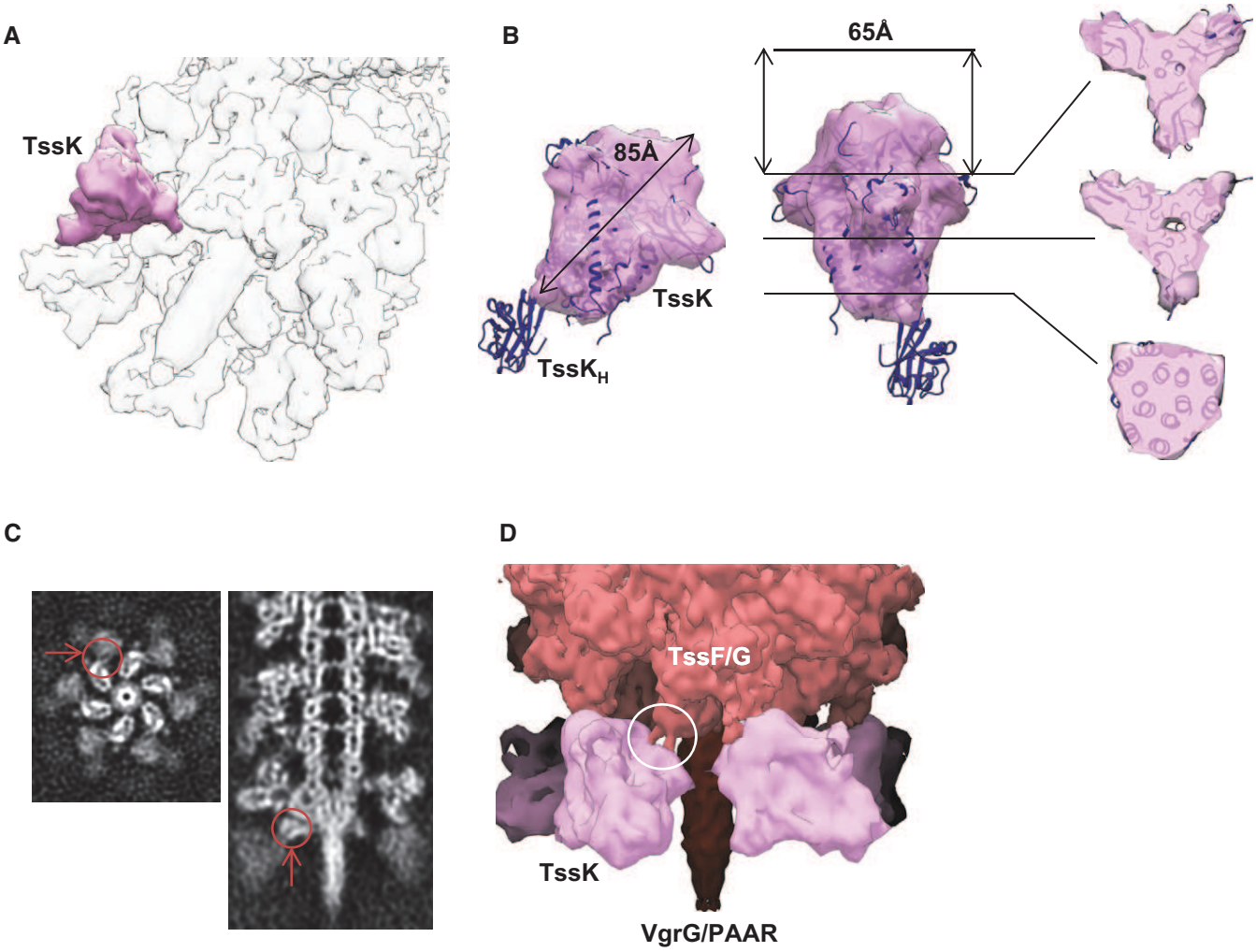

Figure 4. Trimeric connector protein and its interaction with the wedge.

A Tilted view of the composite baseplate cryo-EM reconstruction. One connector protein is superimposed with the locally refined reconstruction shown in pink.

B Orthogonal side views and slices perpendicular to the threefold axis through the locally refined reconstruction of the trimeric connector protein density. X-ray crystallographic structure of EAEC TssK protein (PDB 5M30) was fitted into connector reconstruction except for the disordered C-terminal head domain.

C Top and side slices through the raw sheath–baseplate reconstruction. Putative interface between connector and wedge highlighted with red arrows and circles.

D Side view of the sheath–baseplate cryo-EM reconstruction. The partially disordered connector density was replaced by the locally refined reconstruction. Putative coiled-coil interface between connector and wedge highlighted with white circle. Putative localization of the baseplate proteins is indicated.

second sheath rings adopts due to interactions with the baseplate (Fig 5A and B). Those interactions could be important for preventing ClpV-mediated sheath unfolding before contraction (Wang *et al*, 2017). One interface between the wedge and the adjacent sheath is between Domain 3 and the upper peripheral part of the wedge formed by TssF and TssG (Figs 3C and EV4A and C). This would be similar to T4 phage, where the external domain of the first sheath subunit gp18 potentially interacts with gp6/gp53 wedge proteins (Aksyuk *et al*, 2009; Taylor *et al*, 2016).

In the sheath, each subunit is connected by two β-stranded linkers to two adjacent subunits in the ring closer to the baseplate (Clemens *et al*, 2015; Ge *et al*, 2015; Kudryashev *et al*, 2015). Because of the structural homology between TssE and sheath inner Domain 1, TssE was proposed to accept the linkers from the first sheath ring and thus connect sheath to the baseplate (Kudryashev *et al*, 2015) similarly to TssE homolog gp25 in T4 phage (Taylor *et al*, 2016). However, the subunits of the non-contractile VipA-N3 mutant sheath are connected to the previous sheath ring only through VipB linker and the elongated VipA linker connects to a neighboring subunit on the same sheath ring (Wang *et al*, 2017). This also means that the first sheath ring can only be connected to the baseplate by six linkers and not by twelve as in the wild-type assembly or in the T4 phage (Kudryashev *et al*, 2015; Taylor *et al*, 2016). Even though our reconstruction lacks the resolution needed to resolve details of sheath–baseplate connection, there is a density originating from a sheath protomer likely corresponding to the VipB C-terminal linker, which is most likely connected to TssE in the wedge (Fig EV4). However, we would expect to detect a density corresponding to TssE more clearly. It is possible that the absence of the second VipA linker destabilizes TssE and its density is thus less resolved.

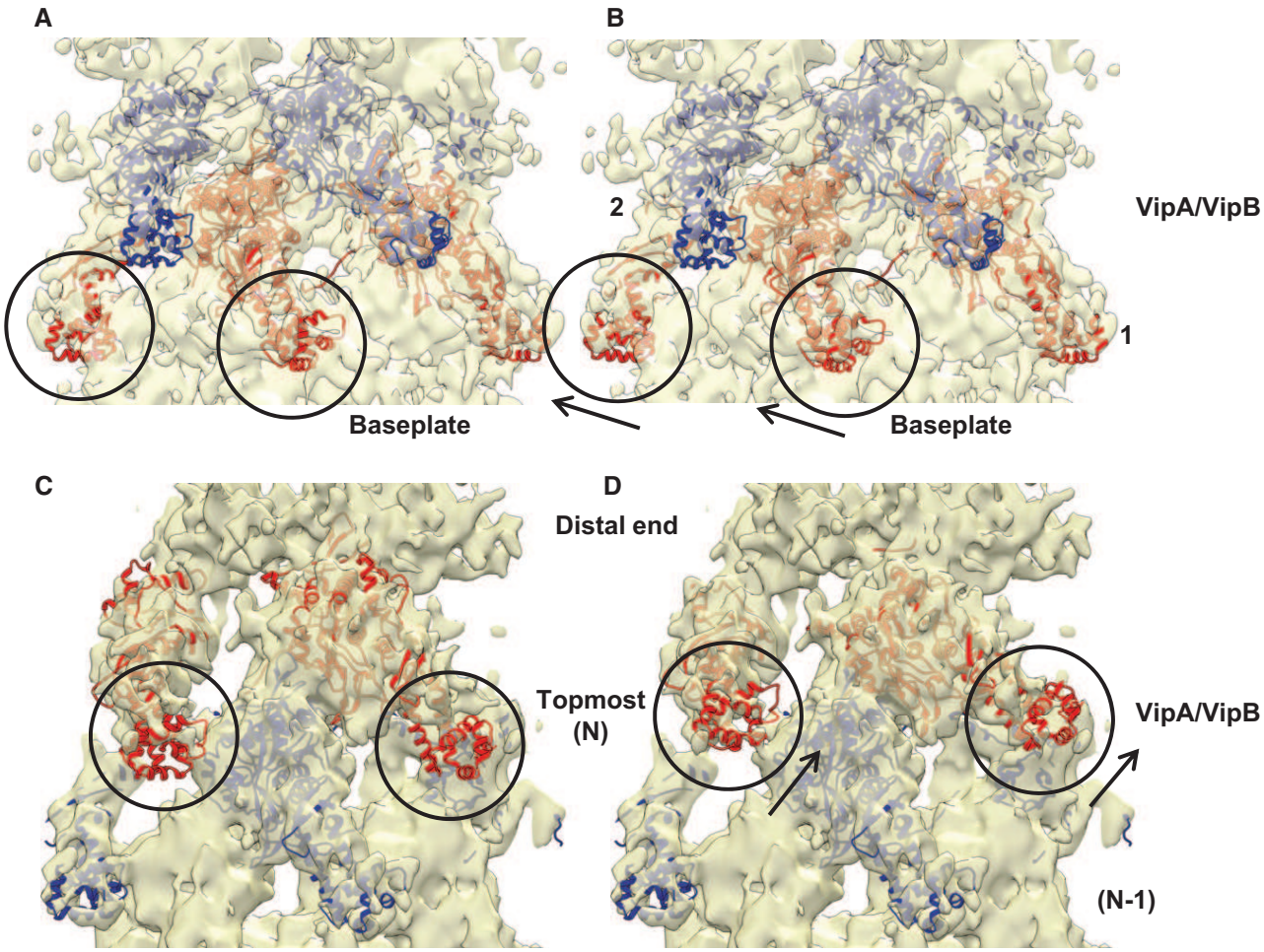

Figure 5. Rearrangements of the sheath rings next to the baseplate and the distal end.

A Side view of the density corresponding to the sheath next to the baseplate fitted with the atomic model of the VipA-N3 sheath–tube (PDB 5MXN).

B Same as (A), but with refitted sheath domain of the VipA-N3 sheath–tube (PDB 5MXN). Differences between original and refitted sheath domains are outlined with black circles and arrows. Ring numbers 1 and 2 correspond to the first and second rings above the baseplate wedge.

C Side view of the density corresponding to the sheath next to the distal end fitted with the atomic model of the VipA-N3 sheath–tube (PDB 5MXN).

D Same as (C), but with refitted sheath domain of the VipA-N3 sheath–tube (PDB 5MXN). Differences between original and refitted sheath domains are outlined with black circles and arrows. Ring numbers N and (N-1) correspond to the topmost ring and the previous ring.

Overall structure of the distal end

In our reconstruction, the side of the non-contractile sheath that is opposite to the baseplate is clearly distinct from the adjacent VipA/VipB sheath and Hcp tube rings (Figs 1D, 2F–G, and EV5). The sheath and tube densities were resolved to 7.5 Å resolution; however, the distal-end density was partially disordered. This density can be further split along the long sheath axis into two layers. The first layer was resolved to 14 Å resolution (shown in red in Figs 2E and EV5C), and the second layer was resolved to 10 Å resolution at the Hcp tube part and to 12 Å resolution at the VipA/VipB sheath periphery (orange in Figs 2E and EV5C), while rings below are resolved to 7.5 Å resolution as predicted by ResMap (Fig 1D; Kucukelbir *et al*, 2014). Six sheath subunits can be fitted into the layer that is next to the end of the regular sheath–tube polymer with a correlation coefficient 0.86, suggesting that this layer is composed of sheath–tube ring (topmost ring in Fig EV5C). However, the overall topology is different as the sheath subunits are rotated ~21 degree around the sheath axis and appear more flattened compared to the other sheath rings (Fig 5C and D). The layer at the very end of the complex is distinct and appears to be formed by six 90-kDa large protein complexes (Table 1; Figs 2F and EV5).

In *Escherichia coli*, TssA forms dodecamers colocalizing with the end of an assembling sheath that is distal from the baseplate, and it was proposed to prime and coordinate sheath–tube polymerization (Zoued *et al*, 2016). This suggests that the complex detected on the very end of the sheath could be formed by a homolog of *E. coli* TssA. *V. cholerae* has two TssA proteins, $TssA_1$ (locus name VCA0119) and $TssA_2$ (locus name VCA0121). $TssA_1$ is a close homolog of the *E. coli* TssA as it is also composed of an ImpA_N domain (PF06812) followed by T6SS_VasJ domain (PF16989) while $TssA_2$ only has the ImpA_N domain. $TssA_1$ has a molecular weight of 53.1 kDa and thus would likely form a dodecamer with a size close to 640 kDa. The fact that only approximately 540-kDa complex is detected at the end of the isolated sheaths could be explained by low resolution and partial disordering of the protein complex. However, the complex at the sheath end aligns poorly with the structure of the *E. coli* TssA dodecamer (EMD-3282) (Fig EV5D and E). This could be due to differences between TssA assemblies in solution and bound to sheath or could represent an actual difference in the overall structures of the *V. cholerae* $TssA_1$ and *E. coli* TssA.

It is important to note that only small amounts of $TssA_1$ protein were detected in our sheath preparations (Datasets EV4–EV7), and therefore, it is also possible that the distal-end density is composed of sheath subunits (74 kDa each) organized into flat starlike complex without the central Hcp hexamer. Indeed, sheath subunits fit the density with CC = 0.82 (Fig EV5C). The complex at the distal sheath end could therefore be a stable assembly intermediate rather than a cap composed of $TssA_1$ protein.

Discussion

Blocking sheath contraction helped to stabilize the T6SS and allowed us to isolate sheath with an attached baseplate and possibly a cap out of *V. cholerae* cells for high-resolution cryo-electron microscopy analysis. Although the 8 Å resolution of the baseplate reconstruction prevents precise segmentation of individual components, the overall baseplate structure clearly resembles T4 inner baseplate and represents the simplest type of baseplates conserved among other contractile tail-like systems (Leiman & Shneider, 2012; Büttner *et al*, 2016; Taylor *et al*, 2016).

The previous cryo-ET studies of *V. cholerae*, *M. xanthus*, and *A. asiaticus* showed that T6SS sheath–tube complex is connected to the cell envelope through a cone-shaped density (Basler *et al*, 2012; Böck *et al*, 2017; Chang *et al*, 2017). In our baseplate reconstruction, the periphery of the wedge likely composed of TssE/F/G is decorated by six copies of a trimeric protein TssK. It remains to be seen how six TssK trimers connect to the membrane complex with an apparent fivefold symmetry (Durand *et al*, 2015); however, it is possible that whole TssK or its parts are flexible and have certain degree of freedom to move and adopt to a structure with a different symmetry (Fig EV6). Recently solved structure of EAEC TssK protein (Nguyen *et al*, 2017) indeed revealed partially disordered C-terminal head domain, which indicates its flexibility. C-terminal head domain has been shown to interact with cytoplasmic domains of TssL and TssM proteins from membrane complex. The flexibility of TssK C-terminus probably provides more degree of freedom for the baseplate–membrane complex formation.

The signal to trigger sheath contraction is currently unknown for T6SS; however, in phages, the conformational switch of the baseplate triggers contraction of the assembled sheath, which then pushes the rigid tube with the sharp tip through the target cell membranes attached by tail fibers (Browning *et al*, 2012; Leiman & Shneider, 2012; Hu *et al*, 2015; Taylor *et al*, 2016). The signal for the phage baseplate component rearrangement comes from the attachment of the tail fibers to a target cell (Hu *et al*, 2015). Similarly, cell–cell contact could be a trigger for T6SS sheath contraction. In that case, the membrane complex could induce changes in TssK structure, which would propagate through its interaction with TssE/F/G wedge to trigger sheath contraction. However, live-cell imaging of T6SS sheath dynamics in *V. cholerae* provided no evidence for a triggering mechanism based on cell–cell contact (Basler & Mekalanos, 2012; Basler *et al*, 2012). Conversely, it is possible that rearrangement of baseplate proteins prior to sheath contraction changes TssK conformation, and this results in opening of the connected membrane complex to allow passage of the cargo-loaded spike and tube. Such membrane complex rearrangement was indeed proposed based on the structure of the isolated TssJLM membrane complex (Durand *et al*, 2015).

The cavity around VgrG/PAAR spike is ~$1{,}110 \times 10^3$ $Å^3$ large and may accommodate up to ~450-kDa large proteins, or three copies of up to ~150-kDa protein. This is consistent with sizes of known effectors: 129-kDa VgrG-1, 113-kDa VgrG-3, or 155-kDa pair VasX-VasW (Dong *et al*, 2013; Joshi *et al*, 2017). Since 77-kDa VgrG-2 with no extension domain is required for T6SS assembly (Appendix Fig S3; Pukatzki *et al*, 2007), there is also enough space for effectors interacting with VgrGs, such as 72-kDa TseL (Dong *et al*, 2013), in agreement with the model that many effectors bind to the VgrG/PAAR spike (Fig EV6; Shneider *et al*, 2013). However, the repertoire of secreted effectors is large (Durand *et al*, 2014; Alcoforado Diniz *et al*, 2015; Hachani *et al*, 2016), and therefore, it is likely that the overall shape of T6SS baseplate will vary between organisms. This could be achieved either by changes in the angle between TssF/G and TssK, or elongating the wedge or TssK assembly with a help of flexible C-terminal head domain (Nguyen *et al*,

2017). Our reconstruction also suggests that TssK protein may be involved in recruitment of certain effectors to the spike. Additionally, it is possible that some organisms evolved proteins that would serve as extensions for the wedge and would thus further increase the size of the baseplate cavity similarly to the variations in baseplate sizes seen in phages (Fu *et al*, 2011; Schwarzer *et al*, 2012; Hu *et al*, 2015; Büttner *et al*, 2016; Nováček *et al*, 2016; Taylor *et al*, 2016).

The cryo-electron microscopy reconstruction of the whole baseplate, sheath–tube, and distal end presented here provides an overall view of the system and will serve as a scaffold for placing high-resolution structures of individual T6SS components or their complexes. The approach used here can in principle be used to further improve the final resolution by collecting a significantly larger dataset. However, in contrast to phages, T6SS evolved into a highly dynamic nanomachine undergoing constant assembly and disassembly. Therefore, it is likely that the T6SS baseplate and cap are partially unstable during isolation. Moreover, even when limiting Hcp expression, most of each isolated T6SS complex is composed of the extended sheath–tube polymer, which further limits the number of particles that can be detected per single micrograph, thus complicating data collection. Additionally, particle heterogeneity and dynamic nature of the distal end and possibly of the baseplate decrease the final resolution and chances to resolve all structural features, which prevent us to unambiguously assign proteins to the densities. Nevertheless, a combination of mutagenesis, live-cell imaging, *in situ* cryo-electron tomography, and availability of atomic resolution models will eventually provide a complete model of T6SS mode of action.

Materials and Methods

VipA/VipB sheath preparation

Sheath preparation was done as described previously (Brackmann *et al*, 2017). Briefly, overnight cultures were diluted and regrown in fresh LB to a final optical density at 600 nm of 1. Cells were collected, resuspended, and lysed. After removal of cell debris, the supernatant was subjected to ultraspeed centrifugation in order to collect VipA/VipB sheath. The sample containing sheath was washed and then used for SDS–PAGE.

Preparation of sheath from Hcp-limited cells was done with following modifications: After reaching an optical density at 600 nm of 1, arabinose was added to the cells in a final concentration of 0.02% to induce Hcp expression. Cells were centrifuged immediately for 6 min at 5,000 × *g* and room temperature, resuspended, and lysed. Ultraspeed centrifugation and washing steps were performed as described previously (Brackmann *et al*, 2017).

Fluorescence microscopy

Fluorescence microscopy and image processing were carried out as described previously (Brackmann *et al*, 2017). Briefly, for *hcp* complementation experiments, overnight cultures were washed once in LB, diluted 1:100 into fresh medium supplemented with appropriated antibiotics, and cultivated to an optical density (OD) at 600 nm of 1. Cells were concentrated to OD 10, subsequently spotted on a LB 1% agarose pad containing 0.02% L-arabinose, and covered with a glass coverslip. Bacteria were directly imaged for 30–40 min at 25°C. To carry out fluorescence microscopy experiments, we used a Nikon Ti-E-inverted motorized microscope with Perfect Focus System and Plan Apo 100× Oil Ph3 DM (NA 1.4) objective lens. SPECTRA X light engine (Lumencor) and ET-GFP (Chroma #49002) filter set was used to excite and filter fluorescence. The setup further contained a sCMOS camera pco.edge 4.2 (PCO, Germany) (pixel size 65 nm) and VisiView software (Visitron Systems, Germany) to record images. Temperature was set to 30°C, and humidity was regulated to 95% by an Okolab T-unit (Okolab). Fiji (Schindelin *et al*, 2012) was used for additional image processing as described previously (Basler *et al*, 2013).

Mass spectrometry

Mass spectrometry was carried out as described previously (Brackmann *et al*, 2017). Briefly, samples were dissolved in TN-buffer, reduced, and alkylated. Proteins were digested overnight and supplemented with TFA to a final concentration of 1%. Peptides were cleaned up using PreOmics Cartridges (PreOmics, Martinsried, Germany) following the manufacturer's instructions. After drying the samples under vacuum, the peptides were resuspended in 0.1% aqueous formic acid solution at a concentration of 0.5 mg/ml. 0.5 µg of peptides of each sample was subjected to LC-MS analysis as described previously (Brackmann *et al*, 2017).

MS1 and MS2 scans were acquired at a target setting of 1E6 ions and 10,000 ions, respectively. The collision energy was set to 35%, and one microscan was acquired for each spectrum. All raw files acquired by DDA were converted to mgf format using msconvert (version 3.0, ProteoWizard, http://proteowizard.sourceforge.net/). The files were searched against a decoy (consisting of forward and reverse protein sequences) database of predicted protein sequence of *V. cholerae* (Uniprot, Organism ID: 243277, download date 11/07/2016, containing known contaminants, resulting in a total of 3,784 proteins) using Mascot (Matrix Science, version 2.4). The search parameters were set as follows: full tryptic specificity was required (cleavage after lysine and arginine residues unless followed by proline); up to three missed cleavages were allowed; carbamidomethyl (C) was set as a fixed modification; oxidation (M) and acetyl (Protein N-term) were set as variable modifications; 10 ppm precursor mass tolerance; and 0.6-Da fragment mass tolerance for CID tandem mass spectra. After importing the result files to Scaffold (http://www.proteomesoftware.com, version 4), the FDR rate was set to < 1% for protein identifications by the local Scaffold FDR algorithm based on the number of decoy hits.

Negative-stained sample preparation, data acquisition, and image processing

An aliquot of 3 µl of sheath sample was applied onto freshly glow-discharged carbon-coated 300-mesh copper grid, blotted, washed with 10 µl of TN-buffer, blotted again, and stained with 2% uranyl acetate for 10 s. 200 images were acquired using CM200FEG microscope (Philips) on TVIPS F416 CMOS camera, operated at 200 kV at a nominal magnification of 38,000×, corresponding to pixel size of 2.81 Å. Contrast transfer function for each micrograph was estimated using CTFFIND4 (Rohou & Grigorieff, 2015). 2,248 particles

corresponding to the ends of extended T6SS assemblies were picked using XMIPP manual picking utility within SCIPION framework (de la Rosa-Trevín *et al*, 2016). Extracted particles were phase-flipped and subjected for reference-free 2D classification without CTF correction in RELION1.4 (Scheres, 2012).

Cryo-EM sample preparation and data acquisition

An aliquot of 3 μl of sheath sample was applied onto freshly glow-discharged Quantifoil R2/1 holey carbon grids (Quantifoil Micro Tools GmbH, Germany), blotted for 3 s, and vitrified using a Vitrobot MK4 (FEI Corp., The Netherlands). The chamber was maintained at 4°C and 100% humidity during the blotting process.

Data of the isolated T6SS assemblies were acquired using Titan Krios microscope (FEI Corp.) equipped with an energy filter (slit width 20 eV) on a K2 Summit direct electron detector (Gatan Inc., USA) in counting mode, operated at 300 kV and at a nominal magnification of 130,000×, corresponding to a calibrated pixel size of 1.06 Å, and a defocus ranging from 1.5 to 3 μm. 9,202 movie series were collected automatically using the SerialEM software (Mastronarde, 2005). For each movie, 40-frame exposures were taken at 0.4 s per frame (16 s total exposure time), using a dose rate of 5e-/pixel/s.

Image processing

Movie frames were aligned using MotionCorr2 (Zheng *et al*, 2017) to correct for specimen motion. The averages of the aligned frames were used for data processing within SCIPION 1.0.1 (de la Rosa-Trevín *et al*, 2016). The contrast transfer function of each micrograph was estimated using the Gctf 1.06 program (Zhang, 2016). Baseplates and distal ends were manually selected from the micrographs using XMIPP manual picking utility in SCIPION 1.0.1 and extracted with a box size of 512 pixels. Particles were binned to have the box size of 256 pixels, corresponding to the pixel size of 2.12 Å. 21,446 baseplate and distal-end particles were classified into 20 classes using reference-free 2D classification with RELION1.4. After 2D classification, a total of 2,660 baseplates and 3,710 distal ends were used for 3D refinement and classification. Best baseplate and distal-end class averages were used for initial volume estimation using XMIPP RANSAC protocol in SCIPION (Vargas *et al*, 2014). Resulted volumes were low-pass-filtered to 60 Å and used as a reference model for 3D auto-refinement. C6 symmetry was imposed during 3D refinement. Better-resolved rigid sheath densities from baseplate and distal-end reconstructions were used for the soft mask creation for subsequent focused 3D refinement with small local angular sampling. Finally, refined particles and model were imported into RELION2.1 (Kimanius *et al*, 2016) for the auto-refinement using solvent-flattened FSCs. This procedure is suggested for elongated particles, when the protein complex represents a relatively small fraction of the reconstructed volume. This procedure resulted in 8.7 Å resolution baseplate and 7.5 Å resolution distal-end reconstructions. Tight mask around baseplate wedge and first sheath ring was created and focused 3D classification, and further refinement of the best class with 1,265 baseplate particles was performed with RELION2.1, which resulted in resolution improvement from 8.5 to 8 Å.

Straightforward baseplate reconstruction with C3 symmetry resulted in a map with strong artifacts. These artifacts most likely appeared due to the six-start sheath helix, occupying majority of the volume inside the particle. Instead, symmetry relaxation from C6 to C3 was performed with *relion_particle_symmetry_expand* utility from RELION2.1, followed by masked 3D classification without alignment. Smooth soft mask lacking sixfold-related features was created around the baseplate region. The resulting 11 Å resolution model showed the same features as a sixfold symmetrized model and trimeric features of the VgrG spike. Local resolution variations of the baseplate and distal-end maps were estimated with Resmap (Kucukelbir *et al*, 2014).

To perform focused refinement of the connector protein region, we low-pass filtered the refined baseplate map to 80 Å and generated a small mask around TssK region with Segger (Pintilie *et al*, 2010) in UCSF Chimera (Pettersen *et al*, 2004; Goddard *et al*, 2007). Mask was prepared for RELION2.1 with *relion_mask_create* with extended width and soft edge of five pixels. The subsequent masked 3D classification without alignment and focused 3D refinement of the best 3D class (Scheres, 2016) resulted in the connector protein density of 10 Å resolution.

Models segmentation and interpretation

Baseplate and distal-end reconstructions were rendered, segmented, and interpreted using UCSF Chimera (Pettersen *et al*, 2004; Pintilie *et al*, 2010). Volume-to-mass scale coefficient was calculated for the proteins with available X-ray crystallographic structure (Leiman *et al*, 2010).

Accession numbers

The EM map was deposited to EMDB (http://www.emdatabank.org) with accession number for the single-particle reconstruction of a distal-end EMD-3878, single-particle reconstruction of a baseplate EMD-3879.

Expanded View for this article is available online.

Acknowledgements
The work was supported by Swiss National Science Foundation (SNSF) grant 31003A_159525 and the University of Basel. HS acknowledges support from the SNSF NCCR TransCure. Calculations were performed at sciCORE (http://scicore.unibas.ch/) scientific computing core facility at University of Basel. We thank Emmanuelle Lezan form the Proteomics Core Facility at University of Basel for support with MS data processing and analysis.

Author contributions
SN collected electron microscopy data, performed image processing, and data analysis. MBr isolated and purified the sheaths and contributed to data collection and analysis. JPS isolated and purified sheaths from Hcp-limited cells and performed MS data collection and analysis. JPS performed imaging and image processing of Hcp-limited cells. KNG and HS provided support with and supervised data collection. MBa conceived the project and analyzed the data. SN and MBa wrote the manuscript. All authors read the manuscript.

Conflict of interest
The authors declare that they have no conflict of interest.

References

Aksyuk AA, Leiman PG, Shneider MM, Mesyanzhinov VV, Rossmann MG (2009) The structure of gene product 6 of bacteriophage T4, the hinge-pin of the baseplate. *Structure* 17: 800 – 808

Alcoforado Diniz J, Liu Y-C, Coulthurst SJ (2015) Molecular weaponry: diverse effectors delivered by the Type VI secretion system. *Cell Microbiol* 17: 1742 – 1751

Basler M, Mekalanos JJ (2012) Type 6 secretion dynamics within and between bacterial cells. *Science* 337: 815

Basler M, Pilhofer M, Henderson GP, Jensen GJ, Mekalanos JJ (2012) Type VI secretion requires a dynamic contractile phage tail-like structure. *Nature* 483: 182 – 186

Basler M, Ho BT, Mekalanos JJ (2013) Tit-for-tat: type VI secretion system counterattack during bacterial cell-cell interactions. *Cell* 152: 884 – 894

Böck D, Medeiros JM, Tsao H-F, Penz T, Weiss GL, Aistleitner K, Horn M, Pilhofer M (2017) *In situ* architecture, function, and evolution of a contractile injection system. *Science* 357: 713 – 717

Bönemann G, Pietrosiuk A, Diemand A, Zentgraf H, Mogk A (2009) Remodelling of VipA/VipB tubules by ClpV-mediated threading is crucial for type VI protein secretion. *EMBO J* 28: 315 – 325

Brackmann M, Wang J, Basler M (2017) Type VI secretion system sheath inter-subunit interactions modulate its contraction. *EMBO Rep* https://doi.org/10.15252/embr.201744416

Brodmann M, Dreier RF, Broz P, Basler M (2017) *Francisella* requires dynamic type VI secretion system and ClpB to deliver effectors for phagosomal escape. *Nat Commun* 8: 15853

Browning C, Shneider MM, Bowman VD, Schwarzer D, Leiman PG (2012) Phage pierces the host cell membrane with the iron-loaded spike. *Structure* 20: 326 – 339

Brunet YR, Espinosa L, Harchouni S, Mignot T, Cascales E (2013) Imaging type VI secretion-mediated bacterial killing. *Cell Rep* 3: 36 – 41

Brunet YR, Henin J, Celia H, Cascales E (2014) Type VI secretion and bacteriophage tail tubes share a common assembly pathway. *EMBO Rep* 15: 315 – 321

Brunet YR, Zoued A, Boyer F, Douzi B, Cascales E (2015) The Type VI secretion TssEFGK-VgrG phage-like baseplate is recruited to the TssJLM membrane complex via multiple contacts and serves as assembly platform for tail tube/sheath polymerization. *PLoS Genet* 11: e1005545

Büttner CR, Wu Y, Maxwell KL, Davidson AR (2016) Baseplate assembly of phage Mu: defining the conserved core components of contractile-tailed phages and related bacterial systems. *Proc Natl Acad Sci USA* 113: 10174 – 10179

Chang Y-W, Rettberg LA, Ortega DR, Jensen GJ (2017) *In vivo* structures of an intact type VI secretion system revealed by electron cryotomography. *EMBO Rep* 18: 1090 – 1099

Cianfanelli FR, Monlezun L, Coulthurst SJ (2016) Aim, load, fire: the type VI secretion system, a bacterial nanoweapon. *Trends Microbiol* 24: 51 – 62

Clemens DL, Ge P, Lee B-Y, Horwitz MA, Zhou ZH (2015) Atomic structure of T6SS reveals interlaced array essential to function. *Cell* 160: 940 – 951

Dong TG, Ho BT, Yoder-Himes DR, Mekalanos JJ (2013) Identification of T6SS-dependent effector and immunity proteins by Tn-seq in *Vibrio cholerae*. *Proc Natl Acad Sci USA* 110: 2623 – 2628

Durand E, Cambillau C, Cascales E, Journet L (2014) VgrG, Tae, Tle, and beyond: the versatile arsenal of Type VI secretion effectors. *Trends Microbiol* 22: 498 – 507

Durand E, Nguyen VS, Zoued A, Logger L, Péhau-Arnaudet G, Aschtgen M-S, Spinelli S, Desmyter A, Bardiaux B, Dujeancourt A, Roussel A, Cambillau C, Cascales E, Fronzes R (2015) Biogenesis and structure of a type VI secretion membrane core complex. *Nature* 523: 555 – 560

English G, Byron O, Cianfanelli FR, Prescott AR, Coulthurst SJ (2014) Biochemical analysis of TssK, a core component of the bacterial Type VI secretion system, reveals distinct oligomeric states of TssK and identifies a TssK-TssFG subcomplex. *Biochem J* 461: 291 – 304

Förster A, Planamente S, Manoli E, Lossi NS, Freemont PS, Filloux A (2014) Coevolution of the ATPase ClpV, the sheath proteins TssB and TssC, and the accessory protein TagJ/HsiE1 distinguishes type VI secretion classes. *J Biol Chem* 289: 33032 – 33043

Fu X, Walter MH, Paredes A, Morais MC, Liu J (2011) The mechanism of DNA ejection in the Bacillus anthracis spore-binding phage 8a revealed by cryo-electron tomography. *Virology* 421: 141 – 148

Ge P, Scholl D, Leiman PG, Yu X, Miller JF, Zhou ZH (2015) Atomic structures of a bactericidal contractile nanotube in its pre- and postcontraction states. *Nat Struct Mol Biol* 22: 377 – 382

Gerc AJ, Diepold A, Trunk K, Porter M, Rickman C, Armitage JP, Stanley-Wall NR, Coulthurst SJ (2015) Visualization of the *Serratia* Type VI secretion system reveals unprovoked attacks and dynamic assembly. *Cell Rep* 12: 2131 – 2142

Goddard TD, Huang CC, Ferrin TE (2007) Visualizing density maps with UCSF Chimera. *J Struct Biol* 157: 281 – 287

Habann M, Leiman PG, Vandersteegen K, Van den Bossche A, Lavigne R, Shneider MM, Bielmann R, Eugster MR, Loessner MJ, Klumpp J (2014) Listeria phage A511, a model for the contractile tail machineries of SPO1-related bacteriophages. *Mol Microbiol* 92: 84 – 99

Hachani A, Wood TE, Filloux A (2016) Type VI secretion and anti-host effectors. *Curr Opin Microbiol* 29: 81 – 93

Harada K, Yamashita E, Nakagawa A, Miyafusa T, Tsumoto K, Ueno T, Toyama Y, Takeda S (2013) Crystal structure of the C-terminal domain of Mu phage central spike and functions of bound calcium ion. *Biochim Biophys Acta* 1834: 284 – 291

Heymann JB, Bartho JD, Rybakova D, Venugopal HP, Winkler DC, Sen A, Hurst MRH, Mitra AK (2013) Three-dimensional structure of the toxin-delivery particle antifeeding prophage of *Serratia entomophila*. *J Biol Chem* 288: 25276 – 25284

Ho BT, Dong TG, Mekalanos JJ (2014) A view to a kill: the bacterial type VI secretion system. *Cell Host Microbe* 15: 9 – 21

Hood RD, Singh P, Hsu F, Güvener T, Carl MA, Trinidad RRS, Silverman JM, Ohlson BB, Hicks KG, Plemel RL, Li M, Schwarz S, Wang WY, Merz AJ, Goodlett DR, Mougous JD (2010) A type VI secretion system of *Pseudomonas aeruginosa* targets a toxin to bacteria. *Cell Host Microbe* 7: 25 – 37

Hu B, Margolin W, Molineux IJ, Liu J (2015) Structural remodeling of bacteriophage T4 and host membranes during infection initiation. *Proc Natl Acad Sci USA* 112: E4919 – E4928

Joshi A, Kostiuk B, Rogers A, Teschler J, Pukatzki S, Yildiz FH (2017) Rules of engagement: the type VI secretion system in *Vibrio cholerae*. *Trends Microbiol* 25: 267 – 279

Kapitein N, Bönemann G, Pietrosiuk A, Seyffer F, Hausser I, Locker JK, Mogk A (2013) ClpV recycles VipA/VipB tubules and prevents non-productive tubule formation to ensure efficient type VI protein secretion. *Mol Microbiol* 87: 1013 – 1028

Kimanius D, Forsberg BO, Scheres SH, Lindahl E (2016) Accelerated cryo-EM structure determination with parallelisation using GPUs in RELION-2. *Elife* 5: e18722

Kucukelbir A, Sigworth FJ, Tagare HD (2014) Quantifying the local resolution of cryo-EM density maps. *Nat Methods* 11: 63 – 65

Kudryashev M, Wang RY-R, Brackmann M, Scherer S, Maier T, Baker D, DiMaio F, Stahlberg H, Egelman EH, Basler M (2015) Structure of the type VI secretion system contractile sheath. *Cell* 160: 952 – 962

Leiman PG, Basler M, Ramagopal UA, Bonanno JB, Sauder JM, Pukatzki S, Burley SK, Almo SC, Mekalanos JJ (2009) Type VI secretion apparatus and phage tail-associated protein complexes share a common evolutionary origin. *Proc Natl Acad Sci USA* 106: 4154 – 4159

Leiman PG, Arisaka F, van Raaij MJ, Kostyuchenko VA, Aksyuk AA, Kanamaru S, Rossmann MG (2010) Morphogenesis of the T4 tail and tail fibers. *Virol J* 7: 355

Leiman PG, Shneider MM (2012) Contractile tail machines of bacteriophages. *Adv Exp Med Biol* 726: 93 – 114

Lossi NS, Dajani R, Freemont P, Filloux A (2011) Structure-function analysis of HsiF, a gp25-like component of the type VI secretion system, in *Pseudomonas aeruginosa*. *Microbiology* 157: 3292 – 3305

Lossi NS, Manoli E, Förster A, Dajani R, Pape T, Freemont P, Filloux A (2013) The HsiB1C1 (TssB-TssC) complex of the *Pseudomonas aeruginosa* type VI secretion system forms a bacteriophage tail sheathlike structure. *J Biol Chem* 288: 7536 – 7548

MacIntyre DL, Miyata ST, Kitaoka M, Pukatzki S (2010) The *Vibrio cholerae* type VI secretion system displays antimicrobial properties. *Proc Natl Acad Sci USA* 107: 19520 – 19524

Mastronarde DN (2005) Automated electron microscope tomography using robust prediction of specimen movements. *J Struct Biol* 152: 36 – 51

Mougous JD, Cuff ME, Raunser S, Shen A, Zhou M, Gifford CA, Goodman AL, Joachimiak G, Ordoñez CL, Lory S, Walz T, Joachimiak A, Mekalanos JJ (2006) A virulence locus of *Pseudomonas aeruginosa* encodes a protein secretion apparatus. *Science* 312: 1526 – 1530

Nakayama K, Takashima K, Ishihara H, Shinomiya T, Kageyama M, Kanaya S, Ohnishi M, Murata T, Mori H, Hayashi T (2000) The R-type pyocin of *Pseudomonas aeruginosa* is related to P2 phage, and the F-type is related to lambda phage. *Mol Microbiol* 38: 213 – 231

Nguyen VS, Logger L, Spinelli S, Legrand P, Pham TTH, Trinh TTN, Cherrak Y, Zoued A, Desmyter A, Durand E, Roussel A, Kellenberger C, Cascales E, Cambillau C (2017) Type VI secretion TssK baseplate protein exhibits structural similarity with phage receptor-binding proteins and evolved to bind the membrane complex. *Nat Microbiol* 2: 17103

Nováček J, Šiborová M, Benešík M, Pantůček R, Doškař J, Plevka P (2016) Structure and genome release of Twort-like Myoviridae phage with a double-layered baseplate. *Proc Natl Acad Sci USA* 113: 9351 – 9356

Pettersen EF, Goddard TD, Huang CC, Couch GS, Greenblatt DM, Meng EC, Ferrin TE (2004) UCSF Chimera–a visualization system for exploratory research and analysis. *J Comput Chem* 25: 1605 – 1612

Pietrosiuk A, Lenherr ED, Falk S, Bönemann G, Kopp J, Zentgraf H, Sinning I, Mogk A (2011) Molecular basis for the unique role of the AAA^+ chaperone ClpV in type VI protein secretion. *J Biol Chem* 286: 30010 – 30021

Pintilie GD, Zhang J, Goddard TD, Chiu W, Gossard DC (2010) Quantitative analysis of cryo-EM density map segmentation by watershed and scale-space filtering, and fitting of structures by alignment to regions. *J Struct Biol* 170: 427 – 438

Planamente S, Salih O, Manoli E, Albesa-Jové D, Freemont PS, Filloux A (2016) TssA forms a gp6-like ring attached to the type VI secretion sheath. *EMBO J* 35: 1613 – 1627

Pukatzki S, Ma AT, Sturtevant D, Krastins B, Sarracino D, Nelson WC, Heidelberg JF, Mekalanos JJ (2006) Identification of a conserved bacterial protein secretion system in *Vibrio cholerae* using the *Dictyostelium* host model system. *Proc Natl Acad Sci USA* 103: 1528 – 1533

Pukatzki S, Ma AT, Revel AT, Sturtevant D, Mekalanos JJ (2007) Type VI secretion system translocates a phage tail spike-like protein into target cells where it cross-links actin. *Proc Natl Acad Sci USA* 104: 15508 – 15513

Rohou A, Grigorieff N (2015) CTFFIND4: fast and accurate defocus estimation from electron micrographs. *J Struct Biol* 192: 216 – 221

de la Rosa-Trevín JM, Quintana A, Del Cano L, Zaldívar A, Foche I, Gutiérrez J, Gómez-Blanco J, Burguet-Castell J, Cuenca-Alba J, Abrishami V, Vargas J, Otón J, Sharov G, Vilas JL, Navas J, Conesa P, Kazemi M, Marabini R, Sorzano COS, Carazo JM (2016) Scipion: a software framework toward integration, reproducibility and validation in 3D electron microscopy. *J Struct Biol* 195: 93 – 99

Santin YG, Cascales E (2017) Domestication of a housekeeping transglycosylase for assembly of a Type VI secretion system. *EMBO Rep* 18: 138 – 149

Scheres SHW (2012) RELION: implementation of a Bayesian approach to cryo-EM structure determination. *J Struct Biol* 180: 519 – 530

Scheres SHW (2016) Processing of structurally heterogeneous Cryo-EM data in RELION. *Methods Enzymol* 579: 125 – 157

Schindelin J, Arganda-Carreras I, Frise E, Kaynig V, Longair M, Pietzsch T, Preibisch S, Rueden C, Saalfeld S, Schmid B, Tinevez J-Y, White DJ, Hartenstein V, Eliceiri K, Tomancak P, Cardona A (2012) Fiji: an open-source platform for biological-image analysis. *Nat Methods* 9: 676 – 682

Schwarzer D, Buettner FFR, Browning C, Nazarov S, Rabsch W, Bethe A, Oberbeck A, Bowman VD, Stummeyer K, Mühlenhoff M, Leiman PG, Gerardy-Schahn R (2012) A multivalent adsorption apparatus explains the broad host range of phage phi92: a comprehensive genomic and structural analysis. *J Virol* 86: 10384 – 10398

Shikuma NJ, Pilhofer M, Weiss GL, Hadfield MG, Jensen GJ, Newman DK (2014) Marine tubeworm metamorphosis induced by arrays of bacterial phage tail-like structures. *Science* 343: 529 – 533

Shneider MM, Buth SA, Ho BT, Basler M, Mekalanos JJ, Leiman PG (2013) PAAR-repeat proteins sharpen and diversify the type VI secretion system spike. *Nature* 500: 350 – 353

Taylor NMI, Prokhorov NS, Guerrero-Ferreira RC, Shneider MM, Browning C, Goldie KN, Stahlberg H, Leiman PG (2016) Structure of the T4 baseplate and its function in triggering sheath contraction. *Nature* 533: 346 – 352

Vargas J, Álvarez-Cabrera A-L, Marabini R, Carazo JM, Sorzano COS (2014) Efficient initial volume determination from electron microscopy images of single particles. *Bioinformatics* 30: 2891 – 2898

Vettiger A, Basler M (2016) Type VI secretion system substrates are transferred and reused among sister cells. *Cell* 167: 99 – 110.e12

Vettiger A, Winter J, Lin L, Basler M (2017) The type VI secretion system sheath assembles at the end distal from the membrane anchor. *Nat Commun* 8: 16088

Wang J, Brackmann M, Castaño-Díez D, Kudryashev M, Goldie KN, Maier T, Stahlberg H, Basler M (2017) Cryo-EM structure of the extended type VI secretion system sheath-tube complex. *Nat Microbiol* 2: 1507 – 1512

Zhang K (2016) Gctf: real-time CTF determination and correction. *J Struct Biol* 193: 1 – 12

Zheng SQ, Palovcak E, Armache J-P, Verba KA, Cheng Y, Agard DA (2017) MotionCor2: anisotropic correction of beam-induced motion for improved cryo-electron microscopy. *Nat Methods* 14: 331 – 332

Zoued A, Brunet YR, Durand E, Aschtgen M-S, Logger L, Douzi B, Journet L, Cambillau C, Cascales E (2014) Architecture and assembly of the Type VI secretion system. *Biochim Biophys Acta* 1843: 1664 – 1673

Zoued A, Durand E, Brunet YR, Spinelli S, Douzi B, Guzzo M, Flaugnatti N, Legrand P, Journet L, Fronzes R, Mignot T, Cambillau C, Cascales E (2016) Priming and polymerization of a bacterial contractile tail structure. *Nature* 531: 59 – 63

II.7 Additional Results Related to Research Article IV

As discussed above, the purification of sheaths with associated baseplates needs to be optimized to increase the number of baseplates in the sample. We decided to follow two different strategies; (i) we fused both sheath proteins and tagged VipB with an affinity tag to enable purification and inhibit further polymerization (Figure II.7.1) and (ii) we varied the existing protocol for sheath purification and used cushions for ultracentrifugation.

II.1 Affinity purification of baseplates with a truncated sheath

Affinity tags were placed at the side where polymerization happens. The addition of tags at the interface for the next protomer should inhibit the polymerization and still allow assembly of one or two sheath rings (depending on the location of the affinity tag) on the baseplate. A hexahistidine-tag and a FLAG-tag have been placed on VipB and the baseplate component TssE has been tagged with a StrepII-tag (Figure II.7.1) to allow orthogonal purification.

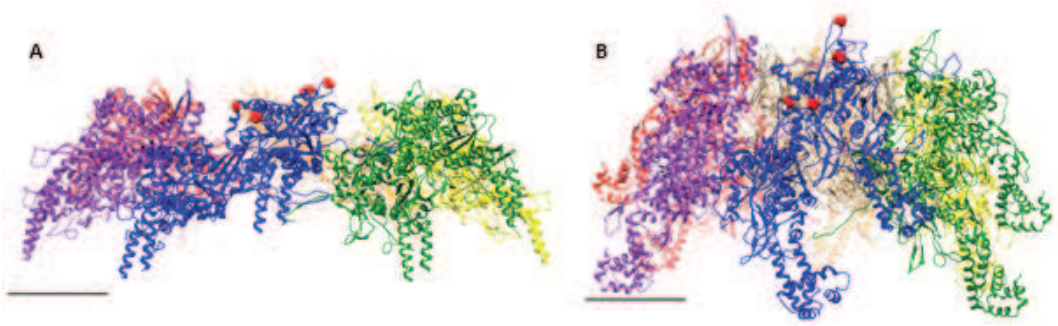

Figure II.7.1 Affinity tags were introduced at four different locations. A, Positions for introduction of affinity-tags were selected based on the structure of the contracted sheath. Locations are highlighted with red spheres on the blue protomer. Positions are in surface exposed loops. B, Positions of the introduced affinity tags are displayed on the extended sheath. The baseplate is located at the bottom of the structures. Scale bars are 50 Å.

Different attempts to purify baseplates with only one or two sheath rings failed, probably due to low binding of the protein to the resin of the affinity column.

Complementation of StrepII-tagged TssE was confirmed by fluorescence microscopy. However, gp25 (the homolog of TssE in phage T4) is deeply buried in the baseplate of phage T4 [372]. This explains, why binding of the StrepII-tag was low. The reason for low-binding of the hexahistidine- and FLAG-tagged VipA-VipB-fusion protein is currently unknown.

II.2 Altered sheath purification protocols for increased yield of baseplates

Presumably, sheaths are fragmented and baseplates disrupted during resuspension after ultra-centrifugation. To avoid excessive resuspension, the use of different cushions was tested. We tested glycerol, sucrose and Percoll® cushions. Sheaths were found in the glycerol- and sucrose-cushion, with the subsequent need to dialyse the sample to eliminate glycerol and sucrose. However, further dilution must be avoided, which makes the use of glycerol and sucrose not useful.

Percoll® is a silica-based colloidal density medium. Sheaths with baseplates were found to be on top of the Percoll®-cushion and ≈57% of sheaths (27 baseplates on 47 sheaths) contained baseplates. However, extraction of sheaths without significant amounts of Percoll® was not possible. Colloids have sizes from 15-30 nm, comparable to the width of sheaths. Purification of sheaths from contaminating Percoll® remained challenging. Further experiments will focus on the feasability of electron microscopy of Percoll®-purified sheaths and explore possibilities of further purification or enrichment of sheaths containing baseplates.

Chapter III

Discussion and Outlook

III.1 What did we learn?

In this thesis I described atomic structures of the T6SS-sheath in the contracted and extended state and the mechanism of sheath contraction. This led to insights into tube arrangement in the extended sheath and how specificity of ClpV for the contracted sheath is mediated. I also described the structure of the T6SS-baseplate and the cap at low resolution.

In a first publication, we showed that the integrity of a four-stranded β-sheet is crucial for assembly and contraction of the sheath, which is described in Section II.1. One of the β-strands (C-terminus of VipB) is essential for assembly, as it serves as a binding partner for the N-terminus of VipA, which is essential for contraction. Based on these findings, we designed further mutations that have an elongated linker region next to the N-terminal β-strand of VipA and lead to a project described in Section II.2. These mutations supported our hypothesis that the linker is involved in triggering sheath contraction. Once this linker is elongated, the signal of contraction cannot be transmitted through the sheath.

For the first time, we were able to isolate mutant sheaths in a non-contracted conformation. Interestingly, we identified components of the baseplate, the inner tube, a potential cap and even parts of the membrane complex in sheath samples of a non-contractile mutant. Cryo-EM of the non-contractile sheath lead to an atomic model of the T6SS-sheath with the associated Hcp-tube, which is described in Section II.4. We verified that the isolated mutant sheaths represent the wild-type sheaths *in vivo* by whole cell cryo-electron tomography.

Low-resolution structures of the baseplate and the cap, both of which are associated with the sheath, are described in Section II.6. Sheath and cap show a clear six-fold symmetry and the spike-tip complex of the baseplate is three-fold symmetric as described earlier [241]. Even though the resolution of the structure of the baseplate limits our insights, we could assign proteins to the electron densities. The structure of the baseplate also clarifies the location of the spike before the sheath contracts, which was speculative before [235]. A more detailed view of the role of the cap during polymerization can also be deduced (Section III.3) [365].

We now have a thorough understanding of how T6SS-sheath and potentially also other related contractile nanomachines work, however, many questions still remain.

III.2 What is the atomic structure of the baseplate and how is it connected to the membrane complex?

One of the biggest differences between T6SS and all other PLTSs, is the presence of a membrane complex in T6SS. T4 phage attaches to the target membrane with its tail fibers, which are connected to the peripheral baseplate. Neither tail fibers nor the peripheral baseplate components are present in T6SS and thus the connectivity to the membrane complex remains elusive.

Mass spectrometry analysis of purified extended VipA-N3 mutant sheath revealed high amounts of Hcp and baseplate components TssE, TssF, TssG and TssK. We also found this sample to be enriched in proteins of the membrane complex. Based on these observations and initial negative stain electron micrographs, we aimed at determining the architecture of the baseplate by cryo-EM, which resulted in a low-resolution description of the baseplate. Reasons for the limitations in resolution are challenges during sample preparation. Only ≈30% of sheaths contained a baseplate and large areas of the image were obstructed by overlaying sheaths. Additionally, the ends of sheath where presumably the baseplate is localized tend to cluster, which further complicates data processing. As discussed in Section II.6, the baseplate also exhibits some heterogeneity with regard to the components that are associated. We did not clearly identify an electron density for TssE, which is expected to reside in the inner baseplate at the sheath. Besides TssE, TssK appears to be the most weakly attached or most flexible component, whereas most other components are reasonably stable. The VgrG-trimer in the center is most likely a heterotrimer of different VgrGs and thus also not exactly three-fold symmetric. Additionally, some VgrG-proteins have C-terminal extensions or other associated effectors, which contribute to sample heterogeneity and further decrease the resolution that can be obtained by averaging.

As discussed in Section II.7, several attempts to purify the baseplate with only one or two rings of sheath failed because of low binding of the affinity tag to the resin of the purification column. The introduced affinity-tags on the fusion-protein should be large enough to prevent polymerization of sheath. Therefore, limits in sample preparation, obstruction of baseplates by sheath and low concentration of baseplates should be eliminated. Further optimization of this approach will be required for an atomic resolution structure of the baseplate.

Besides affinity purification of baseplates, the traditional protocol based on ultracentrifugation can be optimized. More gentle purification strategies showed promising preliminary data for enrichment of baseplates. The fraction of sheath with baseplates was increased ≈2-fold so that 60% of all sheaths were associated with baseplates. Further

optimization of the purification strategy will without doubt yield a higher concentration of baseplates and enable us to solve the structure of the baseplate at high resolution. As we also detected proteins of the membrane complex in mass spectrometry, the isolation of the baseplate, together with the membrane complex should be in reach and allow identification of interfaces. However, the purification of sheath with the associated membrane complex will require testing of various detergents to solubilize the membrane proteins and avoid their disruption.

III.3 What is the role of the cap during Type VI Secretion?

A recent report by Zoued et al. proposed that, in *E. coli,* TssA is involved in polymerization of the tail [365]. In this study, TssA is shown to be the initiator of sheath polymerization at the baseplate and stays attached to the growing sheath. It has a six-fold symmetry and its dimensions fit those of sheath and Hcp with a pore in the middle. This is further supported by data presented in Section II.6, which shows that the mass of the cap fits to a hexamer of TssA. Recent data point towards a breathing motion of TssA that potentially has a function in incorporating rings or monomers of Hcp at the growing end of the tail (Sergey Nazarov, unpublished data). Furthermore, recent reports showed that VipA and VipB are inserted at the side, where TssA1 (cap) is located (Andrea Vettiger, in revision and Johannes Schneider, unpublished data). The TssA ring could open its center and permit the incorporation of Hcp [365].

The association with the polymerizing end of the tail would be in agreement for findings in phage T4, in which tail terminator proteins gp3 and gp15 are first found in the baseplate but upon completion of tail biogenesis are found at the neck [457, 458]. Even though, these proteins are not essential, they are expected to support tail biogenesis and to stabilize the sheath in an extended conformation [458, 459].

Additionally, the cap could also play a role during contraction. By being tightly connected to the contracting sheath and being closed in the central part it pushes the inner tube out of the cell. Capping structures have been identified in T4 phage and in R-type pyocins, however, their role during contraction is not clear. The neck of phage T4 is closed during contraction and a similar structure is found in R-type pyocins but if they are required to minimize energy dissipation is still unclear [332, 417, 418].

The two functions of the cap do not mutually exclude each other, however, both need careful evaluation and further experiments. CryoEM could reveal different conformational states of TssA. Furthermore, fluorescence microscopy of the sheath in combination with truncated TssA with a larger central diameter can clarify the role during assembly and/or contraction.

III.4 What is the underlying molecular mechanism for recycling by ClpV?

The sheaths of phages, pyocins and most other contractile structures are composed of only one protein, whereas the T6SS-sheath is composed of VipA and VipB. Both genes are usually encoded next to each other, with VipA upstream of VipB. ClpV binds to the N-terminus of VipB. This prompts the hypothesis that the split of one gene of a common ancestor of the sheath occurred to enable binding of ClpV to the N-terminus of VipB. However, currently no experimental data supports this hypothesis.

To date, only little is known on how ClpV specifically recognizes the contracted sheath. In the extended state, domain 3 is buried in a groove and gets exposed after contraction [237, 242, 244, 388](Section II.4). Once contracted, ClpV binds to the N-terminus of VipB in the exposed domain 3 and presumably mainly unfolds VipB and as a side product also VipA. Most Clp-proteases recognize an either N- or C-terminal recognition peptide [460]. For ClpAP, it has been shown that an internal signal peptide can also be recognized, however, the current model proposes that either end is inserted into the peptidase but not the signal peptide itself [461–463].

Interestingly, in the H1-T6SS (Hcp Secretion Island 1-T6SS, one of three T6SS clusters in *P. aeruginosa*) of *P. aeruginosa,* an additional protein, TagJ, is postulated to mediate the interaction between ClpV and the contracted sheath [246]. In this context, TagJ is postulated to recognize the contracted sheath and ClpV binds TagJ and disassembles the sheath. In contrast to the T6SS of *V. cholerae* and *E. coli*, disassembly via TagJ/ClpV is mediated by binding to the N-terminus of HsiB (TssB/VipA-homolog), which is buried in the innermost part of the sheath [246, 464]. It remains to be shown how recognition of a deeply buried peptide is achieved. Additionally, details of these interactions remain unknown and how TagJ mediates disassembly by ClpV is unclear.

Progress on the structure of full-length ClpV bound to its substrate will further elucidate the mode of action and resolve if threading of two peptide strands adjacent to each other is possible and thus also potentially shed light on the evolutionary origin of the split of the sheath protein into two in the case of T6SS.

III.5 What triggers the baseplate to contract?

Studies from phage T4 showed that triggering of contraction is initiated at the baseplate upon recognition of a host. The T6SS of *V. cholerae* is active in the absence of potential target cells and kin cells. Currently, no trigger has been found that induces the contraction of the T6SS in *V. cholerae*, however it is reasonable to expect that contraction only takes

place after the sheath reaches a length that is sufficient to pierce a target cell. Different mechanisms of how contraction is triggered can be envisioned: (i) Contraction is triggered, when the polymerizing end reaches the cytoplasmic membrane at the distal end (opposite end of the baseplate). (ii) The cap (TssA) triggers contraction, when no more Hcp is present to elongate sheath. (iii) At a specific timepoint after initiation of polymerization, contraction is triggered. (iv) Instability in the baseplate triggers sheath contraction or (v) a completely independent mechanism that reacts to an unknown stimulus exists.

For most of the mentioned possibilities, some hints exist:

(i) Fluorescence microscopy of *Acinetobacter baylyi* indicates that as soon as the polymerizing sheath touches the opposed membrane, it contracts (Peter Ringel, unpublished data). However, extensive bending of the sheath when coming into contact with a membrane can also occur (Peter Ringel, unpublished data). Both observations are contradicting and thus make the possibility of contact dependent contraction unlikely.

(ii) When only limited amounts of Hcp are present, sheaths are significantly shorter, which is presumably based on lower availability of the protein [383]. This could result in lower speed of polymerization, which potentially can be sensed by the cap protein TssA. TssA would then signal the baseplate that sheath polymerization is completed and contraction can occur. Signaling could either occur through the sheath in which TssA would induce a conformational change "firing-ready" (which is different from "extended") or by a sheath independent pathway using post-translational modification of an unknown protein, which then triggers contraction at the baseplate. In the sheath-dependent scenario, a third conformational state is necessary; extended, firing-ready and contracted. The sheath-independent pathway would need an unidentified enzymatic function in TssA or in a yet unknown cognate binding protein, which then associates with the baseplate and triggers contraction.

(iii) Timing in biological systems can be based on many different mechanisms like membrane depolarization (action potential), variation of local protein concentration (FtsZ for bacterial division) or protein expression (cyclin-dependent kinases during mitosis) [465–468]. All mentioned mechanisms work on whole cells or at least parts of a bacterial cell. When observing T6SS-dynamics, we can observe structures directly adjacent to each other, however, they do not contract at the same time. Therefore, timing would have to be regulated separately for each sheath which makes this mechanism of triggering rather unlikely or at least more complex.

(iv) The observation that contraction does not appear to be precisely controlled, lead to the proposal that a random fluctuation in the stability of the baseplate leads to contraction. The extended sheath is in a meta-stable conformation. This is presumably also true for the baseplate when the sheath is extended. Mediated by fluctuations in the envi-

ronment, parts of the baseplate could adopt the energetically more favorable star-shaped conformation, which is adopted by the T4-phage baseplate after binding of the short tail fibers [372–374, 430]. This increases the chances that other parts also adopt the star-shaped conformation and by this trigger sheath contraction. This hypothesis is supported by the fact that we cannot isolate sheaths in an extended state, meaning that the integrity of its environment is crucial to stay in an extended state [233, 237].

(v) In *P. aeruginosa*, the T6SS-activity is tightly controlled at a post-translational level and is even targeted into a specific direction [329]. Up to now, no such targeting or regulation has been found in *V. cholerae*, however it is possible that, what is considered to be "constitutively active" actually is constant activation by an unknown stimulus.

The T6SSs of *A. baylyi*, *V. cholerae*, *F. novicida* and *P. aeruginosa* behave very different and up to now, little is known what the reason for these differences is. To find the initial trigger for the conformational change in the baseplate, a comparison of baseplate, cap and sheath structures is needed to unravel slight differences that change the behavior of the secretion system. Further studies will reveal modes of regulation of T6SSs in different organisms and shed light on the biological implications and reasons for different regulatory mechanisms.

References

[1] A. Popescu and R. J. Doyle. The Gram stain after more than a century. *Biotechnic & Histochemistry: Official Publication of the Biological Stain Commission*, 71(3):145–151, May 1996.

[2] Christian Hoffmann, Andrew Leis, Michael Niederweis, Jürgen M. Plitzko, and Harald Engelhardt. Disclosure of the mycobacterial outer membrane: Cryo-electron tomography and vitreous sections reveal the lipid bilayer structure. *Proceedings of the National Academy of Sciences*, 105(10):3963–3967, March 2008.

[3] Radhey S. Gupta. What are archaebacteria: life's third domain or monoderm prokaryotes related to Gram-positive bacteria? A new proposal for the classification of prokaryotic organisms. *Molecular Microbiology*, 29(3):695–707, August 1998.

[4] Effrosyni Papanikou, Spyridoula Karamanou, and Anastassios Economou. Bacterial protein secretion through the translocase nanomachine. *Nature Reviews Microbiology*, 5(11):839–851, November 2007.

[5] Paolo Natale, Thomas Brüser, and Arnold J. M. Driessen. Sec- and Tat-mediated protein secretion across the bacterial cytoplasmic membrane—Distinct translocases and mechanisms. *Biochimica et Biophysica Acta (BBA) - Biomembranes*, 1778(9):1735–1756, September 2008.

[6] G. Blobel and B. Dobberstein. Transfer of proteins across membranes. II. Reconstitution of functional rough microsomes from heterologous components. *The Journal of Cell Biology*, 67(3):852–862, December 1975.

[7] Thomas Nordahl Petersen, Søren Brunak, Gunnar von Heijne, and Henrik Nielsen. SignalP 4.0: discriminating signal peptides from transmembrane regions. *Nature Methods*, 8(10):785–786, October 2011.

[8] Jon Beckwith. The Sec-dependent pathway. *Research in Microbiology*, 164(6):497–504, July 2013.

[9] Mechthild Pohlschröder, Will A. Prinz, Enno Hartmann, and Jon Beckwith. Protein Translocation in the Three Domains of Life: Variations on a Theme. *Cell*, 91(5):563–566, November 1997.

[10] Mechthild Pohlschröder, Kieran Dilks, Nicholas J Hand, and R Wesley Rose. Translocation of proteins across archaeal cytoplasmic membranes. *FEMS Microbiology Reviews*, 28(1):3–24, February 2004.

[11] Ian Collinson. SecA—a New Twist in the Tale. *Journal of Bacteriology*, 199(2):e00736–16, January 2017.

[12] P. Walter and G. Blobel. Translocation of proteins across the endoplasmic reticulum. II. Signal recognition protein (SRP) mediates the selective binding to microsomal membranes of in-vitro-assembled polysomes synthesizing secretory protein. *The Journal of Cell Biology*, 91(2):551–556, November 1981.

[13] M. A. Poritz, H. D. Bernstein, K. Strub, D. Zopf, H. Wilhelm, and P. Walter. An E. coli ribonucleoprotein containing 4.5s RNA resembles mammalian signal recognition particle. *Science*, 250(4984):1111–1117, November 1990.

[14] Nancy D Ulbrandt, John A Newitt, and Harris D Bernstein. The E. coli Signal Recognition Particle Is Required for the Insertion of a Subset of Inner Membrane Proteins. *Cell*, 88(2):187–196, January 1997.

[15] Franz-Ulrich Hartl, Stewart Lecker, Elmar Schiebel, Joseph P. Hendrick, and William Wickner. The binding cascade of SecB to SecA to SecYE mediates preprotein targeting to the E. coli plasma membrane. *Cell*, 63(2):269–279, October 1990.

[16] Ottilie von Loeffelholz, Qiyang Jiang, Aileen Ariosa, Manikandan Karuppasamy, Karine Huard, Imre Berger, Shu-ou Shan, and Christiane Schaffitzel. Ribosome–SRP–FtsY cotranslational targeting complex in the closed state. *Proceedings of the National Academy of Sciences*, 112(13):3943–3948, March 2015.

[17] Robert T. Batey, Robert P. Rambo, Louise Lucast, Brian Rha, and Jennifer A. Doudna. Crystal Structure of the Ribonucleoprotein Core of the Signal Recognition Particle. *Science*, 287(5456):1232–1239, February 2000.

[18] Klemens Wild, Mario Halic, Irmgard Sinning, and Roland Beckmann. SRP meets the ribosome. *Nature Structural & Molecular Biology*, 11(11):1049–1053, November 2004.

[19] Goran Stjepanovic, Katja Kapp, Gert Bange, Christian Graf, Richard Parlitz, Klemens Wild, Matthias P. Mayer, and Irmgard Sinning. Lipids Trigger a Conformational Switch That Regulates Signal Recognition Particle (SRP)-mediated Protein Targeting. *Journal of Biological Chemistry*, 286(26):23489–23497, July 2011.

[20] Miryana Mircheva, Diana Boy, Benjamin Weiche, Friederike Hucke, Peter Graumann, and Hans-Georg Koch. Predominant membrane localization is an essential feature of the bacterial signal recognition particle receptor. *BMC Biology*, 7:76, 2009.

[21] Joen Luirink and Irmgard Sinning. SRP-mediated protein targeting: structure and function revisited. *Biochimica et Biophysica Acta (BBA) - Molecular Cell Research*, 1694(1–3):17–35, November 2004.

[22] Kakoli Mitra, Christiane Schaffitzel, Tanvir Shaikh, Florence Tama, Simon Jenni, Charles L. Brooks, Nenad Ban, and Joachim Frank. Structure of the E. coli protein-conducting channel bound to a translating ribosome. *Nature*, 438(7066):318–324, November 2005.

[23] Makoto Watanabe and Gunter Blobel. High-Affinity Binding of Escherichia coli SecB to the Signal Sequence Region of a Presecretory Protein. *Proceedings of the National Academy of Sciences of the United States of America*, 92(22):10133–10136, 1995.

[24] Franck Duong. Binding, activation and dissociation of the dimeric SecA ATPase at the dimeric SecYEG translocase. *The EMBO Journal*, 22(17):4375–4384, September 2003.

[25] Mark Paetzel, Andrew Karla, Natalie C. J. Strynadka, and Ross E. Dalbey. Signal Peptidases. *Chemical Reviews*, 102(12):4549–4580, December 2002.

[26] Anastassios Economou and William Wickner. SecA promotes preprotein translocation by undergoing ATP-driven cycles of membrane insertion and deinsertion. *Cell*, 78(5):835–843, September 1994.

[27] Bert van den Berg, William M. Clemons, Ian Collinson, Yorgo Modis, Enno Hartmann, Stephen C. Harrison, and Tom A. Rapoport. X-ray structure of a protein-conducting channel. *Nature*, 427(6969):36–44, January 2004.

[28] Yoshiki Tanaka, Yasunori Sugano, Mizuki Takemoto, Takaharu Mori, Arata Furukawa, Tsukasa Kusakizako, Kaoru Kumazaki, Ayako Kashima, Ryuichiro Ishitani, Yuji Sugita, Osamu Nureki, and Tomoya Tsukazaki. Crystal Structures of

SecYEG in Lipidic Cubic Phase Elucidate a Precise Resting and a Peptide-Bound State. *Cell Reports*, 13(8):1561–1568, November 2015.

[29] Johannes Scheuring, Nathalie Braun, Lars Nothdurft, Matthias Stumpf, Andreas K. J. Veenendaal, Stefan Kol, Chris van der Does, Arnold J. M. Driessen, and Sevil Weinkauf. The Oligomeric Distribution of SecYEG is Altered by SecA and Translocation Ligands. *Journal of Molecular Biology*, 354(2):258–271, November 2005.

[30] Karine Deville, Vicki A. M. Gold, Alice Robson, Sarah Whitehouse, Richard B. Sessions, Stephen A. Baldwin, Sheena E. Radford, and Ian Collinson. The Oligomeric State and Arrangement of the Active Bacterial Translocon. *Journal of Biological Chemistry*, 286(6):4659–4669, February 2011.

[31] Alexej Kedrov, Ilja Kusters, Victor V Krasnikov, and Arnold J M Driessen. A single copy of SecYEG is sufficient for preprotein translocation. *The EMBO Journal*, 30(21):4387–4397, November 2011.

[32] Eunyong Park and Tom A. Rapoport. Bacterial protein translocation requires only one copy of the SecY complex in vivo. *J Cell Biol*, 198(5):881–893, September 2012.

[33] Andrew R. Osborne and Tom A. Rapoport. Protein Translocation Is Mediated by Oligomers of the SecY Complex with One SecY Copy Forming the Channel. *Cell*, 129(1):97–110, April 2007.

[34] Anastassios Economou, Joseph A. Pogliano, Jonathan Beckwith, Donald B. Oliver, and William Wickner. SecA membrane cycling at SecYEG is driven by distinct ATP binding and hydrolysis events and is regulated by SecD and SecF. *Cell*, 83(7):1171–1181, December 1995.

[35] Jeroen P. W. van der Wolk, Janny G. de Wit, and Arnold J. M. Driessen. The catalytic cycle of the Escherichia coli SecA ATPase comprises two distinct preprotein translocation events. *The EMBO Journal*, 16(24):7297–7304, December 1997.

[36] Elmar Schiebel, Arnold J. M. Driessen, Franz-Ulrich Hartl, and William Wickner. H+ and ATP function at different steps of the catalytic cycle of preprotein translocase. *Cell*, 64(5):927–939, March 1991.

[37] Damon Huber, Mohammed Jamshad, Ruby Hanmer, Daniela Schibich, Kristina Döring, Isabella Marcomini, Günter Kramer, and Bernd Bukau. SecA cotranslationally interacts with nascent substrate proteins in vivo. *Journal of Bacteriology*, pages JB.00622–16, October 2016.

[38] Tracy Palmer and Ben C. Berks. The twin-arginine translocation (Tat) protein export pathway. *Nature Reviews Microbiology*, 10(7):483–496, July 2012.

[39] Philip A. Lee, Danielle Tullman-Ercek, and George Georgiou. The Bacterial Twin-Arginine Translocation Pathway. *Annual review of microbiology*, 60:373–395, 2006.

[40] Urs A. Ochsner, Aleksandra Snyder, Adriana I. Vasil, and Michael L. Vasil. Effects of the twin-arginine translocase on secretion of virulence factors, stress response, and pathogenesis. *Proceedings of the National Academy of Sciences*, 99(12):8312–8317, June 2002.

[41] Nathalie Pradel, Changyun Ye, Valérie Livrelli, Jianguo Xu, Bernard Joly, and Long-Fei Wu. Contribution of the Twin Arginine Translocation System to the Virulence of Enterohemorrhagic Escherichia coli O157:H7. *Infection and Immunity*, 71(9):4908–4916, September 2003.

[42] Emmy De Buck, Liesbeth Maes, Eef Meyen, Lieve Van Mellaert, Nick Geukens, Jozef Anné, and Elke Lammertyn. Legionella pneumophila Philadelphia-1 tatB and tatC affect intracellular replication and biofilm formation. *Biochemical and Biophysical Research Communications*, 331(4):1413–1420, June 2005.

[43] Enid T. González, Darby G. Brown, Jill K. Swanson, and Caitilyn Allen. Using the Ralstonia solanacearum Tat Secretome To Identify Bacterial Wilt Virulence Factors. *Applied and Environmental Microbiology*, 73(12):3779–3786, June 2007.

[44] Emmy De Buck, Elke Lammertyn, and Jozef Anné. The importance of the twin-arginine translocation pathway for bacterial virulence. *Trends in Microbiology*, 16(9):442–453, September 2008.

[45] Joanna D. Thomas, Richard A. Daniel, Jeff Errington, and Colin Robinson. Export of active green fluorescent protein to the periplasm by the twin-arginine translocase (Tat) pathway in Escherichia coli. *Molecular Microbiology*, 39(1):47–53, January 2001.

[46] Véronique Sauvé, Stefano Bruno, Ben C. Berks, and Andrew M. Hemmings. The SoxYZ Complex Carries Sulfur Cycle Intermediates on a Peptide Swinging Arm. *Journal of Biological Chemistry*, 282(32):23194–23204, August 2007.

[47] Steve Tottey, Kevin J. Waldron, Susan J. Firbank, Brian Reale, Conrad Bessant, Katsuko Sato, Timothy R. Cheek, Joe Gray, Mark J. Banfield, Christopher Dennison, and Nigel J. Robinson. Protein-folding location can regulate manganese-binding versus copper- or zinc-binding. *Nature*, 455(7216):1138–1142, October 2008.

[48] Kieran Dilks, R. Wesley Rose, Enno Hartmann, and Mechthild Pohlschröder. Prokaryotic Utilization of the Twin-Arginine Translocation Pathway: a Genomic Survey. *Journal of Bacteriology*, 185(4):1478–1483, February 2003.

[49] Wouter S. P. Jong, Corinne M. ten Hagen-Jongman, Pierre Genevaux, Josef Brunner, Bauke Oudega, and Joen Luirink. Trigger factor interacts with the signal peptide of nascent Tat substrates but does not play a critical role in Tat-mediated export. *European Journal of Biochemistry*, 271(23-24):4779–4787, December 2004.

[50] Elliott Crooke, Brenda Guthrie, Stewart Lecker, Roland Lill, and William Wickner. ProOmpA is stabilized for membrane translocation by either purified E. coli trigger factor or canine signal recognition particle. *Cell*, 54(7):1003–1011, September 1988.

[51] Wenke Graubner, Angelika Schierhorn, and Thomas Brüser. DnaK Plays a Pivotal Role in Tat Targeting of CueO and Functions beside SlyD as a General Tat Signal Binding Chaperone. *Journal of Biological Chemistry*, 282(10):7116–7124, March 2007.

[52] Olivier Genest, Farida Seduk, Laurence Théraulaz, Vincent Méjean, and Chantal Iobbi-Nivol. Chaperone protection of immature molybdoenzyme during molybdenum cofactor limitation. *FEMS Microbiology Letters*, 265(1):51–55, December 2006.

[53] Si-Yu Li, Bang-Yang Chang, and Sung-Chyr Lin. Coexpression of TorD enhances the transport of GFP via the TAT pathway. *Journal of Biotechnology*, 122(4):412–421, April 2006.

[54] Bo Hou, Stefan Frielingsdorf, and Ralf Bernd Klösgen. Unassisted Membrane Insertion as the Initial Step in pH/Tat-dependent Protein Transport. *Journal of Molecular Biology*, 355(5):957–967, February 2006.

[55] George L. Orriss, Michael J. Tarry, Bérengère Ize, Frank Sargent, Susan M. Lea, Tracy Palmer, and Ben C. Berks. TatBC, TatB, and TatC form structurally autonomous units within the twin arginine protein transport system of Escherichia coli. *FEBS Letters*, 581(21):4091–4097, August 2007.

[56] Michael J. Tarry, Eva Schäfer, Shuyun Chen, Grant Buchanan, Nicholas P. Greene, Susan M. Lea, Tracy Palmer, Helen R. Saibil, and Ben C. Berks. Structural analysis of substrate binding by the TatBC component of the twin-arginine protein transport system. *Proceedings of the National Academy of Sciences*, 106(32):13284–13289, August 2009.

[57] Kenneth Cline and Hiroki Mori. Thylakoid pH-dependent precursor proteins bind to a cpTatC–Hcf106 complex before Tha4-dependent transport. *J Cell Biol*, 154(4):719–730, August 2001.

[58] Fernanda Rodriguez, Sarah L. Rouse, Claudia E. Tait, Jeffrey Harmer, Antonio De Riso, Christiane R. Timmel, Mark S. P. Sansom, Ben C. Berks, and Jason R. Schnell. Structural model for the protein-translocating element of the twin-arginine transport system. *Proceedings of the National Academy of Sciences*, 110(12):E1092–E1101, March 2013.

[59] Mark C. Leake, Nicholas P. Greene, Rachel M. Godun, Thierry Granjon, Grant Buchanan, Shuyun Chen, Richard M. Berry, Tracy Palmer, and Ben C. Berks. Variable stoichiometry of the TatA component of the twin-arginine protein transport system observed by in vivo single-molecule imaging. *Proceedings of the National Academy of Sciences*, 105(40):15376–15381, October 2008.

[60] Sureshkumar Ramasamy, Ravinder Abrol, Christian J. M. Suloway, and William M. Clemons Jr. The Glove-like Structure of the Conserved Membrane Protein TatC Provides Insight into Signal Sequence Recognition in Twin-Arginine Translocation. *Structure*, 21(5):777–788, May 2013.

[61] Susana Cristóbal, Jan-Willem de Gier, Henrik Nielsen, and Gunnar von Heijne. Competition between Sec- and TAT-dependent protein translocation in Escherichia coli. *The EMBO Journal*, 18(11):2982–2990, June 1999.

[62] Hiroki Mori and Kenneth Cline. A twin arginine signal peptide and the pH gradient trigger reversible assembly of the thylakoid pH/Tat translocase. *The Journal of Cell Biology*, 157(2):205–210, April 2002.

[63] Julia Fröbel, Patrick Rose, Frank Lausberg, Anne-Sophie Blümmel, Roland Freudl, and Matthias Müller. Transmembrane insertion of twin-arginine signal peptides is driven by TatC and regulated by TatB. *Nature Communications*, 3:1311, December 2012.

[64] Timothy L. Yahr and William T. Wickner. Functional reconstitution of bacterial Tat translocation in vitro. *The EMBO Journal*, 20(10):2472–2479, May 2001.

[65] R. M. Mould and C. Robinson. A proton gradient is required for the transport of two lumenal oxygen-evolving proteins across the thylakoid membrane. *Journal of Biological Chemistry*, 266(19):12189–12193, July 1991.

[66] Eduard Bitto and David B. McKay. Crystallographic Structure of SurA, a Molecular Chaperone that Facilitates Folding of Outer Membrane Porins. *Structure*, 10(11):1489–1498, November 2002.

[67] S.W. Lazar and R. Kolter. SurA assists the folding of Escherichia coli outer membrane proteins. *Journal of Bacteriology*, 178(6):1770–1773, 1996.

[68] B. M. Thome and M. Müller. Skp is a periplasmic Escherichia coli protein requiring SecA and SecY for export. *Molecular Microbiology*, 5(11):2815–2821, November 1991.

[69] Kathrin Ramm and Andreas Plückthun. High enzymatic activity and chaperone function are mechanistically related features of the dimeric E. coli peptidyl-prolyl-isomerase FkpA1. *Journal of Molecular Biology*, 310(2):485–498, July 2001.

[70] Jesper E. Mogensen and Daniel E. Otzen. Interactions between folding factors and bacterial outer membrane proteins. *Molecular Microbiology*, 57(2):326–346, July 2005.

[71] Ingo P. Korndörfer, Monica K. Dommel, and Arne Skerra. Structure of the periplasmic chaperone Skp suggests functional similarity with cytosolic chaperones despite differing architecture. *Nature Structural & Molecular Biology*, 11(10):1015–1020, October 2004.

[72] Nigel Mackman and I. Barry Holland. Functional characterization of a cloned haemolysin determinant from E. coli of human origin, encoding information for the secretion of a 107k polypeptide. *Molecular and General Genetics MGG*, 196(1):129–134, August 1984.

[73] C. Wandersman and P. Delepelaire. TolC, an Escherichia coli outer membrane protein required for hemolysin secretion. *Proceedings of the National Academy of Sciences of the United States of America*, 87(12):4776–4780, June 1990.

[74] V. Koronakis, M. Cross, and C. Hughes. Transcription antitermination in an Escherichia coli haemolysin operon is directed progressively by cis-acting DNA sequences upstream of the promoter region. *Molecular Microbiology*, 3(10):1397–1404, October 1989.

[75] P. Stanley, V. Koronakis, and C. Hughes. Mutational analysis supports a role for multiple structural features in the C-terminal secretion signal of Escherichia coli haemolysin. *Molecular Microbiology*, 5(10):2391–2403, October 1991.

[76] Sabrina Thomas, I. Barry Holland, and Lutz Schmitt. The Type 1 secretion pathway — The hemolysin system and beyond. *Biochimica et Biophysica Acta (BBA) - Molecular Cell Research*, 1843(8):1629–1641, August 2014.

[77] Kanna Nagamatsu, Thomas J. Hannan, Randi L. Guest, Maria Kostakioti, Maria Hadjifrangiskou, Jana Binkley, Karen Dodson, Tracy L. Raivio, and Scott J. Hultgren. Dysregulation of Escherichia coli -hemolysin expression alters the course of acute and persistent urinary tract infection. *Proceedings of the National Academy of Sciences*, 112(8):E871–E880, February 2015.

[78] Kheng B. Lim, Carthene R. Bazemore Walker, Lin Guo, Shahaireen Pellett, Jeffrey Shabanowitz, Donald F. Hunt, Erik L. Hewlett, Albrecht Ludwig, Werner Goebel, Rodney A. Welch, and Murray Hackett. Escherichia coli -Hemolysin (HlyA) Is Heterogeneously Acylated in Vivo with 14-, 15-, and 17-Carbon Fatty Acids. *Journal of Biological Chemistry*, 275(47):36698–36702, November 2000.

[79] Peter Stanley, Len C. Packman, Vassilis Koronakis, and Colin Hughes. Fatty Acylation of Two Internal Lysine Residues Required for the Toxic Activity Escherichia coli Hemolysin. *Science*, 266(5193):1992–1996, 1994.

[80] Jelena Zaitseva, Stefan Jenewein, Alexander Wiedenmann, Houssain Benabdelhak, I. Barry Holland, and Lutz Schmitt. Functional Characterization and ATP-Induced Dimerization of the Isolated ABC-Domain of the Haemolysin B Transporter. *Biochemistry*, 44(28):9680–9690, July 2005.

[81] Jelena Zaitseva, Christine Oswald, Thorsten Jumpertz, Stefan Jenewein, Alexander Wiedenmann, I. Barry Holland, and Lutz Schmitt. A structural analysis of asymmetry required for catalytic activity of an ABC-ATPase domain dimer. *The EMBO Journal*, 25(14):3432–3443, July 2006.

[82] S. Létoffé, P. Delepelaire, and C. Wandersman. Protein secretion in Gram-negative bacteria: Assembly of the three components of ABC protein-mediated exporters is ordered and promoted by substrate binding. *EMBO Journal*, 15(21):5804–5811, 1996.

[83] Lekshmy Balakrishnan, Colin Hughes, and Vassilis Koronakis. Substrate-triggered recruitment of the TolC channel-tunnel during type I export of hemolysin by Escherichia coli1. *Journal of Molecular Biology*, 313(3):501–510, October 2001.

[84] Houssain Benabdelhak, Stephan Kiontke, Carsten Horn, Robert Ernst, Mark A. Blight, I. Barry Holland, and Lutz Schmitt. A Specific Interaction Between the

NBD of the ABC-transporter HlyB and a C-Terminal Fragment of its Transport Substrate Haemolysin A. *Journal of Molecular Biology*, 327(5):1169–1179, April 2003.

[85] Shahid Mehmood, Carmen Domene, Eric Forest, and Jean-Michel Jault. Dynamics of a bacterial multidrug ABC transporter in the inward- and outward-facing conformations. *Proceedings of the National Academy of Sciences*, 109(27):10832–10836, July 2012.

[86] Dheeraj Khare, Michael L. Oldham, Cedric Orelle, Amy L. Davidson, and Jue Chen. Alternating Access in Maltose Transporter Mediated by Rigid-Body Rotations. *Molecular Cell*, 33(4):528–536, February 2009.

[87] Michael L. Oldham and Jue Chen. Snapshots of the maltose transporter during ATP hydrolysis. *Proceedings of the National Academy of Sciences*, 108(37):15152–15156, September 2011.

[88] Roger J. P. Dawson and Kaspar P. Locher. Structure of a bacterial multidrug ABC transporter. *Nature*, 443(7108):180–185, September 2006.

[89] Matthew K. Higgins, Evert Bokma, Eva Koronakis, Colin Hughes, and Vassilis Koronakis. Structure of the periplasmic component of a bacterial drug efflux pump. *Proceedings of the National Academy of Sciences of the United States of America*, 101(27):9994–9999, July 2004.

[90] R. Schülein, I. Gentschev, H.-J. Mollenkopf, and W. Goebel. A topological model for the haemolysin translocator protein HlyD. *MGG Molecular & General Genetics*, 234(1):155–163, 1992.

[91] Vassilis Koronakis, Andrew Sharff, Eva Koronakis, Ben Luisi, and Colin Hughes. Crystal structure of the bacterial membrane protein TolC central to multidrug efflux and protein export. *Nature*, 405(6789):914–919, June 2000.

[92] Alexandre Chenal, Johanna C. Karst, Ana Cristina Sotomayor Pérez, Anna Katarzyna Wozniak, Bruno Baron, Patrick England, and Daniel Ladant. Calcium-Induced Folding and Stabilization of the Intrinsically Disordered RTX Domain of the CyaA Toxin. *Biophysical Journal*, 99(11):3744–3753, December 2010.

[93] Ana-Cristina Sotomayor-Pérez, Daniel Ladant, and Alexandre Chenal. Disorder-to-Order Transition in the CyaA Toxin RTX Domain: Implications for Toxin Secretion. *Toxins*, 7(1):1–20, December 2014.

[94] Alexandre Chenal, J. Iñaki Guijarro, Bertrand Raynal, Muriel Delepierre, and Daniel Ladant. RTX Calcium Binding Motifs Are Intrinsically Disordered in the Absence of Calcium IMPLICATION FOR PROTEIN SECRETION. *Journal of Biological Chemistry*, 284(3):1781–1789, January 2009.

[95] Ladislav Bumba, Jiri Masin, Pavel Macek, Tomas Wald, Lucia Motlova, Ilona Bibova, Nela Klimova, Lucie Bednarova, Vaclav Veverka, Michael Kachala, Dmitri I. Svergun, Cyril Barinka, and Peter Sebo. Calcium-Driven Folding of RTX Domain -Rolls Ratchets Translocation of RTX Proteins through Type I Secretion Ducts. *Molecular Cell*, 62(1):47–62, April 2016.

[96] Romé Voulhoux, Geneviève Ball, Bérengère Ize, Michael L. Vasil, Andrée Lazdunski, Long-Fei Wu, and Alain Filloux. Involvement of the twin-arginine translocation system in protein secretion via the type II pathway. *The EMBO Journal*, 20(23):6735–6741, December 2001.

[97] Kris Pauwels, Ariel Lustig, Lode Wyns, Jan Tommassen, Savvas N. Savvides, and Patrick Van Gelder. Structure of a membrane-based steric chaperone in complex with its lipase substrate. *Nature Structural & Molecular Biology*, 13(4):374–375, April 2006.

[98] Samuel Wagner, Lisa Königsmaier, María Lara-Tejero, Matthew Lefebre, Thomas C. Marlovits, and Jorge E. Galán. Organization and coordinated assembly of the type III secretion export apparatus. *Proceedings of the National Academy of Sciences*, 107(41):17745–17750, October 2010.

[99] A. P. Pugsley. Translocation of a folded protein across the outer membrane in Escherichia coli. *Proceedings of the National Academy of Sciences*, 89(24):12058–12062, December 1992.

[100] H. M. Lu, S. Mizushima, and S. Lory. A periplasmic intermediate in the extracellular secretion pathway of Pseudomonas aeruginosa exotoxin A. *Journal of Bacteriology*, 175(22):7463–7467, November 1993.

[101] Amanda L. Horstman and Meta J. Kuehn. Bacterial Surface Association of Heat-labile Enterotoxin through Lipopolysaccharide after Secretion via the General Secretory Pathway. *Journal of Biological Chemistry*, 277(36):32538–32545, September 2002.

[102] M. Sandkvist, L. O. Michel, L. P. Hough, V. M. Morales, M. Bagdasarian, M. Koomey, V. J. DiRita, and M. Bagdasarian. General secretion pathway (eps)

genes required for toxin secretion and outer membrane biogenesis in Vibrio cholerae. *Journal of Bacteriology*, 179(22):6994–7003, November 1997.

[103] Sophie Le Blastier, Aurore Hamels, Matthew Cabeen, Lionel Schille, Françoise Tilquin, Marc Dieu, Martine Raes, and Jean-Yves Matroule. Phosphate Starvation Triggers Production and Secretion of an Extracellular Lipoprotein in Caulobacter crescentus. *PLOS ONE*, 5(12):e14198, December 2010.

[104] Camila Ramos Santos, Zaira Bruna Hoffmam, Vanesa Peixoto de Matos Martins, Leticia Maria Zanphorlin, Leandro Henrique de Paula Assis, Rodrigo Vargas Honorato, Paulo Sérgio Lopes de Oliveira, Roberto Ruller, and Mario Tyago Murakami. Molecular Mechanisms Associated with Xylan Degradation by Xanthomonas Plant Pathogens. *Journal of Biological Chemistry*, 289(46):32186–32200, November 2014.

[105] Konstantin V. Korotkov, Maria Sandkvist, and Wim G. J. Hol. The type II secretion system: biogenesis, molecular architecture and mechanism. *Nature Reviews Microbiology*, 10(5):336–351, May 2012.

[106] Marija Tauschek, Rebecca J. Gorrell, Richard A. Strugnell, and Roy M. Robins-Browne. Identification of a protein secretory pathway for the secretion of heat-labile enterotoxin by an enterotoxigenic strain of Escherichia coli. *Proceedings of the National Academy of Sciences*, 99(10):7066–7071, May 2002.

[107] T. R. Hirst and J. Holmgren. Conformation of protein secreted across bacterial outer membranes: a study of enterotoxin translocation from Vibrio cholerae. *Proceedings of the National Academy of Sciences*, 84(21):7418–7422, November 1987.

[108] Kaushik Bharati and Nirmal K. Ganguly. Cholera toxin: A paradigm of a multifunctional protein. *The Indian Journal of Medical Research*, 133(2):179–187, February 2011.

[109] Olivera Francetic, Nienke Buddelmeijer, Shawn Lewenza, Carol A. Kumamoto, and Anthony P. Pugsley. Signal Recognition Particle-Dependent Inner Membrane Targeting of the PulG Pseudopilin Component of a Type II Secretion System. *Journal of Bacteriology*, 189(5):1783–1793, March 2007.

[110] Jorik Arts, Ria van Boxtel, Alain Filloux, Jan Tommassen, and Margot Koster. Export of the Pseudopilin XcpT of the Pseudomonas aeruginosa Type II Secretion System via the Signal Recognition Particle-Sec Pathway. *Journal of Bacteriology*, 189(5):2069–2076, March 2007.

[111] Badreddine Douzi, Alain Filloux, and Romé Voulhoux. On the path to uncover the bacterial type II secretion system. *Phil. Trans. R. Soc. B*, 367(1592):1059–1072, April 2012.

[112] C d'Enfert, A Ryter, and A P Pugsley. Cloning and expression in Escherichia coli of the Klebsiella pneumoniae genes for production, surface localization and secretion of the lipoprotein pullulanase. *The EMBO Journal*, 6(11):3531–3538, November 1987.

[113] Melissa Ayers, P Lynne Howell, and Lori L Burrows. Architecture of the type II secretion and type IV pilus machineries. *Future Microbiology*, 5(8):1203–1218, August 2010.

[114] Matthew Hobbs and John S. Mattick. Common components in the assembly of type 4 fimbriae, DNA transfer systems, filamentous phage and protein-secretion apparatus: a general system for the formation of surface-associated protein complexes. *Molecular Microbiology*, 10(2):233–243, October 1993.

[115] Mangayarkarasi Nivaskumar and Olivera Francetic. Type II secretion system: A magic beanstalk or a protein escalator. *Biochimica et Biophysica Acta (BBA) - Molecular Cell Research*, 1843(8):1568–1577, August 2014.

[116] Mickaël Desvaux, Nicholas J. Parham, Anthony Scott-Tucker, and Ian R. Henderson. The general secretory pathway: a general misnomer? *Trends in Microbiology*, 12(7):306–309, July 2004.

[117] David A Cisneros, Peter J Bond, Anthony P Pugsley, Manuel Campos, and Olivera Francetic. Minor pseudopilin self-assembly primes type II secretion pseudopilus elongation. *The EMBO Journal*, 31(4):1041–1053, February 2012.

[118] Steve L. Reichow, Konstantin V. Korotkov, Wim G. J. Hol, and Tamir Gonen. Structure of the cholera toxin secretion channel in its closed state. *Nature Structural & Molecular Biology*, 17(10):1226–1232, October 2010.

[119] Suzanne R. Lybarger, Tanya L. Johnson, Miranda D. Gray, Aleksandra E. Sikora, and Maria Sandkvist. Docking and Assembly of the Type II Secretion Complex of Vibrio cholerae. *Journal of Bacteriology*, 191(9):3149–3161, May 2009.

[120] Miranda D. Gray, Michael Bagdasarian, Wim G. J. Hol, and Maria Sandkvist. In vivo cross-linking of EpsG to EpsL suggests a role for EpsL as an ATPase-pseudopilin coupling protein in the Type II secretion system of Vibrio cholerae. *Molecular microbiology*, 79(3):786–798, February 2011.

[121] Éric Durand, Gérard Michel, Romé Voulhoux, Julia Kürner, Alain Bernadac, and Alain Filloux. XcpX Controls Biogenesis of the Pseudomonas aeruginosa XcpT-containing Pseudopilus. *Journal of Biological Chemistry*, 280(36):31378–31389, September 2005.

[122] Jodi L. Camberg and Maria Sandkvist. Molecular Analysis of the Vibrio cholerae Type II Secretion ATPase EpsE. *Journal of Bacteriology*, 187(1):249–256, January 2005.

[123] Marcella Patrick, Konstantin V. Korotkov, Wim G. J. Hol, and Maria Sandkvist. Oligomerization of EpsE Coordinates Residues from Multiple Subunits to Facilitate ATPase Activity. *Journal of Biological Chemistry*, 286(12):10378–10386, March 2011.

[124] D. N. Nunn and S. Lory. Cleavage, methylation, and localization of the Pseudomonas aeruginosa export proteins XcpT, -U, -V, and -W. *Journal of Bacteriology*, 175(14):4375–4382, July 1993.

[125] Rolf Köhler, Karsten Schäfer, Shirley Müller, Guillaume Vignon, Kay Diederichs, Ansgar Philippsen, Philippe Ringler, Anthony P. Pugsley, Andreas Engel, and Wolfram Welte. Structure and assembly of the pseudopilin PulG. *Molecular Microbiology*, 54(3):647–664, November 2004.

[126] Manuel Campos, David A. Cisneros, Mangayarkarasi Nivaskumar, and Olivera Francetic. The type II secretion system – a dynamic fiber assembly nanomachine. *Research in Microbiology*, 164(6):545–555, July 2013.

[127] M Sandkvist, M Bagdasarian, S P Howard, and V J DiRita. Interaction between the autokinase EpsE and EpsL in the cytoplasmic membrane is required for extracellular secretion in Vibrio cholerae. *The EMBO Journal*, 14(8):1664–1673, April 1995.

[128] David Nunn. Bacterial Type II protein export and pilus biogenesis: more than just homologies? *Trends in Cell Biology*, 9(10):402–408, October 1999.

[129] Brianne J. Burkinshaw and Natalie C. J. Strynadka. Assembly and structure of the T3ss. *Biochimica et Biophysica Acta (BBA) - Molecular Cell Research*, 1843(8):1649–1663, August 2014.

[130] Jorge E. Galán and Hans Wolf-Watz. Protein delivery into eukaryotic cells by type III secretion machines. *Nature*, 444(7119):567–573, November 2006.

[131] Fabien Habyarimana and Brian M. M. Ahmer. More Evidence for Secretion Signals within the mRNA of Type 3 Secreted Effectors. *Journal of Bacteriology*, 195(10):2117–2118, May 2013.

[132] George S. Niemann, Roslyn N. Brown, Ivy T. Mushamiri, Nhu T. Nguyen, Rukayat Taiwo, Afke Stufkens, Richard D. Smith, Joshua N. Adkins, Jason E. McDermott, and Fred Heffron. RNA Type III Secretion Signals That Require Hfq. *Journal of Bacteriology*, 195(10):2119–2125, May 2013.

[133] Martin Löwer and Gisbert Schneider. Prediction of Type III Secretion Signals in Genomes of Gram-Negative Bacteria. *PLOS ONE*, 4(6):e5917, June 2009.

[134] Oliver Schraidt and Thomas C. Marlovits. Three-Dimensional Model of Salmonella's Needle Complex at Subnanometer Resolution. *Science*, 331(6021):1192–1195, March 2011.

[135] Antoine Loquet, Nikolaos G. Sgourakis, Rashmi Gupta, Karin Giller, Dietmar Riedel, Christian Goosmann, Christian Griesinger, Michael Kolbe, David Baker, Stefan Becker, and Adam Lange. Atomic model of the type III secretion system needle. *Nature*, 486(7402):276–279, June 2012.

[136] Andrea Puhar and Philippe J. Sansonetti. Type III secretion system. *Current Biology*, 24(17):R784–R791, September 2014.

[137] Guy R. Cornelis. The type III secretion injectisome. *Nature Reviews Microbiology*, 4(11):811–825, November 2006.

[138] J. E. Shea, M. Hensel, C. Gleeson, and D. W. Holden. Identification of a virulence locus encoding a second type III secretion system in Salmonella typhimurium. *Proceedings of the National Academy of Sciences*, 93(6):2593–2597, March 1996.

[139] T Michiels, P Wattiau, R Brasseur, J M Ruysschaert, and G Cornelis. Secretion of Yop proteins by Yersiniae. *Infection and Immunity*, 58(9):2840–2849, September 1990.

[140] Jon C. Haller, Sharon Carlson, Kristin J. Pederson, and Dorothy E. Pierson. A chromosomally encoded type III secretion pathway in Yersinia enterocolitica is important in virulence. *Molecular Microbiology*, 36(6):1436–1446, June 2000.

[141] W Goebel and J Hedgpeth. Cloning and functional characterization of the plasmid-encoded hemolysin determinant of Escherichia coli. *Journal of Bacteriology*, 151(3):1290–1298, September 1982.

[142] Wolf-Dietrich Hardt, Li-Mei Chen, Kornel E Schuebel, Xosé R Bustelo, and Jorge E Galán. S. typhimurium Encodes an Activator of Rho GTPases that Induces Membrane Ruffling and Nuclear Responses in Host Cells. *Cell*, 93(5):815–826, May 1998.

[143] Henry N. Higgs and Thomas D. Pollard. Activation by Cdc42 and Pip2 of Wiskott-Aldrich Syndrome Protein (Wasp) Stimulates Actin Nucleation by Arp2/3 Complex. *The Journal of Cell Biology*, 150(6):1311–1320, September 2000.

[144] Jayesh C Patel and Jorge E Galán. Manipulation of the host actin cytoskeleton by Salmonella — all in the name of entry. *Current Opinion in Microbiology*, 8(1):10–15, February 2005.

[145] Juan Du, Analise Z. Reeves, Jessica A. Klein, Donna J. Twedt, Leigh A. Knodler, and Cammie F. Lesser. The type III secretion system apparatus determines the intracellular niche of bacterial pathogens. *Proceedings of the National Academy of Sciences*, 113(17):4794–4799, April 2016.

[146] Garth L. Abrahams, Petra Müller, and Michael Hensel. Functional Dissection of SseF, a Type III Effector Protein Involved in Positioning the Salmonella-Containing Vacuole. *Traffic*, 7(8):950–965, August 2006.

[147] Rita Figueira and David W. Holden. Functions of the Salmonella pathogenicity island 2 (SPI-2) type III secretion system effectors. *Microbiology*, 158(5):1147–1161, 2012.

[148] Julia Radics, Lisa Königsmaier, and Thomas C. Marlovits. Structure of a pathogenic type 3 secretion system in action. *Nature Structural & Molecular Biology*, 21(1):82–87, January 2014.

[149] Thomas C. Marlovits, Tomoko Kubori, Anand Sukhan, Dennis R. Thomas, Jorge E. Galán, and Vinzenz M. Unger. Structural Insights into the Assembly of the Type III Secretion Needle Complex. *Science*, 306(5698):1040–1042, November 2004.

[150] Dalian Zhong, Matthew Lefebre, Kawaljit Kaur, Melanie A. McDowell, Courtney Gdowski, Sunhwan Jo, Yu Wang, Stephen H. Benedict, Susan M. Lea, Jorge E. Galan, and Roberto N. De Guzman. The Salmonella Type III Secretion System Inner Rod Protein PrgJ Is Partially Folded. *Journal of Biological Chemistry*, 287(30):25303–25311, July 2012.

[151] Thomas C. Marlovits, Tomoko Kubori, María Lara-Tejero, Dennis Thomas, Vinzenz M. Unger, and Jorge E. Galán. Assembly of the inner rod determines needle length in the type III secretion injectisome. *Nature*, 441(7093):637–640, June 2006.

[152] Frank S. Cordes, Kaoru Komoriya, Eric Larquet, Shixin Yang, Edward H. Egelman, Ariel Blocker, and Susan M. Lea. Helical Structure of the Needle of the Type III Secretion System of Shigella flexneri. *Journal of Biological Chemistry*, 278(19):17103–17107, May 2003.

[153] Laure Journet, Céline Agrain, Petr Broz, and Guy R. Cornelis. The Needle Length of Bacterial Injectisomes Is Determined by a Molecular Ruler. *Science*, 302(5651):1757–1760, December 2003.

[154] Julien R. C. Bergeron, Lucia Fernández, Gregory A. Wasney, Marija Vuckovic, Fany Reffuveille, Robert E. W. Hancock, and Natalie C. J. Strynadka. The Structure of a Type 3 Secretion System (T3ss) Ruler Protein Suggests a Molecular Mechanism for Needle Length Sensing. *Journal of Biological Chemistry*, 291(4):1676–1691, January 2016.

[155] Daniel H. Wee and Kelly T. Hughes. Molecular ruler determines needle length for the Salmonella Spi-1 injectisome. *Proceedings of the National Academy of Sciences*, 112(13):4098–4103, March 2015.

[156] Petr Broz, Catherine A. Mueller, Shirley A. Müller, Ansgar Philippsen, Isabel Sorg, Andreas Engel, and Guy R. Cornelis. Function and molecular architecture of the Yersinia injectisome tip complex. *Molecular Microbiology*, 65(5):1311–1320, September 2007.

[157] C. A. Mueller, P. Broz, and G. R. Cornelis. The type III secretion system tip complex and translocon. *Molecular Microbiology*, 68(5):1085–1095, June 2008.

[158] Zhi Peng Gao, Pin Nie, Jin Fang Lu, Lu Yi Liu, Tiao Yi Xiao, Wei Liu, Jia Shou Liu, and Hai Xia Xie. Type III Secretion System Translocon Component EseB Forms Filaments on and Mediates Autoaggregation of and Biofilm Formation by Edwardsiella tarda. *Applied and Environmental Microbiology*, 81(17):6078–6087, September 2015.

[159] H.U. Ferris, Y. Furukawa, T. Minamino, M.B. Kroetz, M. Kihara, K. Namba, and R.M. Macnab. FlhB regulates ordered export of flagellar components via autocleavage mechanism. *Journal of Biological Chemistry*, 280(50):41236–41242, 2005.

[160] Isabel Sorg, Stefanie Wagner, Marlise Amstutz, Shirley A. Müller, Petr Broz, Yvonne Lussi, Andreas Engel, and Guy R. Cornelis. YscU recognizes translocators as export substrates of the Yersinia injectisome. *The EMBO Journal*, 26(12):3015–3024, June 2007.

[161] Andrea Nans, Mikhail Kudryashev, Helen R. Saibil, and Richard D. Hayward. Structure of a bacterial type III secretion system in contact with a host membrane in situ. *Nature Communications*, 6:10114, December 2015.

[162] Roma Kenjale, Justin Wilson, Sebastian F. Zenk, Saroj Saurya, Wendy L. Picking, William D. Picking, and Ariel Blocker. The Needle Component of the Type III Secreton of Shigella Regulates the Activity of the Secretion Apparatus. *Journal of Biological Chemistry*, 280(52):42929–42937, December 2005.

[163] Cécile Neyt and Guy R. Cornelis. Insertion of a Yop translocation pore into the macrophage plasma membrane by Yersinia enterocolitica: requirement for translocators YopB and YopD, but not LcrG. *Molecular Microbiology*, 33(5):971–981, September 1999.

[164] Caroline Montagner, Christian Arquint, and Guy R. Cornelis. Translocators YopB and YopD from Yersinia enterocolitica Form a Multimeric Integral Membrane Complex in Eukaryotic Cell Membranes. *Journal of Bacteriology*, 193(24):6923–6928, December 2011.

[165] María Lara-Tejero, Junya Kato, Samuel Wagner, Xiaoyun Liu, and Jorge E. Galán. A Sorting Platform Determines the Order of Protein Secretion in Bacterial Type III Systems. *Science*, 331(6021):1188–1191, March 2011.

[166] Bo Hu, Dustin R. Morado, William Margolin, John R. Rohde, Olivia Arizmendi, Wendy L. Picking, William D. Picking, and Jun Liu. Visualization of the type III secretion sorting platform of Shigella flexneri. *Proceedings of the National Academy of Sciences*, 112(4):1047–1052, January 2015.

[167] Junya Kato, Matthew Lefebre, and Jorge E. Galán. Structural Features Reminiscent of ATP-Driven Protein Translocases Are Essential for the Function of a Type III Secretion-Associated ATPase. *Journal of Bacteriology*, 197(18):3007–3014, September 2015.

[168] Yukihiro Akeda and Jorge E. Galán. Chaperone release and unfolding of substrates in type III secretion. *Nature*, 437(7060):911–915, October 2005.

[169] Koushik Paul, Marc Erhardt, Takanori Hirano, David F. Blair, and Kelly T. Hughes. Energy source of flagellar type III secretion. *Nature*, 451(7177):489–492, January 2008.

[170] Gottfried Wilharm, Verena Lehmann, Kristina Krauss, Beatrix Lehnert, Susanna Richter, Klaus Ruckdeschel, Jürgen Heesemann, and Konrad Trülzsch. Yersinia enterocolitica Type III Secretion Depends on the Proton Motive Force but Not on the Flagellar Motor Components MotA and MotB. *Infection and Immunity*, 72(7):4004–4009, July 2004.

[171] Marc Erhardt, Max E. Mertens, Florian D. Fabiani, and Kelly T. Hughes. ATPase-Independent Type-III Protein Secretion in Salmonella enterica. *PLOS Genetics*, 10(11):e1004800, November 2014.

[172] Bo Hu, Maria Lara-Tejero, Qingke Kong, Jorge E. Galán, and Jun Liu. In Situ Molecular Architecture of the Salmonella Type III Secretion Machine. *Cell*, 168(6):1065–1074.e10, March 2017.

[173] Antonello Covacci and Rino Rappuoli. Pertussis toxin export requires accessory genes located downstream from the pertussis toxin operon. *Molecular Microbiology*, 8(3):429–434, May 1993.

[174] Peter J. Christie and Eric Cascales. Structural and dynamic properties of bacterial type IV secretion systems (review). *Molecular Membrane Biology*, 22(1-2):51–61, April 2005.

[175] Jack A. Heinemann and George F. Sprague. Bacterial conjugative plasmids mobilize DNA transfer between bacteria and yeast. *Nature*, 340(6230):205–209, July 1989.

[176] Gunnar Schröder, Ralf Schuelein, Maxime Quebatte, and Christoph Dehio. Conjugative DNA transfer into human cells by the VirB/VirD4 type IV secretion system of the bacterial pathogen Bartonella henselae. *Proceedings of the National Academy of Sciences of the United States of America*, 108(35):14643–14648, August 2011.

[177] Eric Cascales and Peter J. Christie. The versatile bacterial type IV secretion systems. *Nature Reviews Microbiology*, 1(2):137–149, November 2003.

[178] Eric Cascales and Peter J. Christie. Agrobacterium VirB10, an ATP energy sensor required for type IV secretion. *Proceedings of the National Academy of Sciences of the United States of America*, 101(49):17228–17233, December 2004.

[179] Stefano Censini, Christina Lange, Zhaoying Xiang, Jean E. Crabtree, Paolo Ghiara, Mark Borodovsky, Rino Rappuoli, and Antonello Covacci. cag, a pathogenicity island of Helicobacter pylori, encodes type I-specific and disease-associated virulence factors. *Proceedings of the National Academy of Sciences*, 93(25):14648–14653, December 1996.

[180] Natalia S. Akopyants, Sandra W. Clifton, Dangeruta Kersulyte, Jean E. Crabtree, Bryan E. Youree, C. Adonis Reece, Nick O. Bukanov, E. Susan Drazek, Bruce A. Roe, and Douglas E. Berg. Analyses of the cag pathogenicity island of Helicobacter pylori. *Molecular Microbiology*, 28(1):37–53, April 1998.

[181] David Burstein, Tal Zusman, Elena Degtyar, Ram Viner, Gil Segal, and Tal Pupko. Genome-Scale Identification of Legionella pneumophila Effectors Using a Machine Learning Approach. *PLOS Pathogens*, 5(7):e1000508, July 2009.

[182] Camille Locht, Loic Coutte, and Nathalie Mielcarek. The ins and outs of pertussis toxin. *FEBS Journal*, 278(23):4668–4682, December 2011.

[183] Drusilla L. Burns, Stefanie Fiddner, Anissa M. Cheung, and Anita Verma. Analysis of Subassemblies of Pertussis Toxin Subunits In Vivo and Their Interaction with the Ptl Transport Apparatus. *Infection and Immunity*, 72(9):5365–5372, September 2004.

[184] Mario Pantoja, Lishan Chen, Yuching Chen, and Eugene W. Nester. Agrobacterium type IV secretion is a two-step process in which export substrates associate with the virulence protein VirJ in the periplasm. *Molecular Microbiology*, 45(5):1325–1335, September 2002.

[185] Peter J Christie and Joseph P Vogel. Bacterial type IV secretion: conjugation systems adapted to deliver effector molecules to host cells. *Trends in Microbiology*, 8(8):354–360, August 2000.

[186] Hiroki Nagai and Tomoko Kubori. Type IVB Secretion Systems of Legionella and Other Gram-Negative Bacteria. *Frontiers in Microbiology*, 2, 2011.

[187] Barbara Schrammeijer, Alice Beijersbergen, Ken B. Idler, Leo S. Melchers, David V. Thompson, and Paul J. J. Hooykaas. Sequence analysis of the vir-region from Agrobacterium tumefaciens octopine Ti plasmid pTi15955. *Journal of Experimental Botany*, 51(347):1167–1169, June 2000.

[188] Gretchen A. Kuldau, Guido De Vos, John Owen, Gretchen McCaffrey, and Patricia Zambryski. The virB operon of Agrobacterium tumefaciens pTiC58 encodes 11 open reading frames. *Molecular and General Genetics MGG*, 221(2):256–266, April 1990.

[189] Mark Simone, Colleen A. McCullen, Lisa E. Stahl, and Andrew N. Binns. The carboxy-terminus of VirE2 from Agrobacterium tumefaciens is required for its transport to host cells by the virB-encoded type IV transport system. *Molecular Microbiology*, 41(6):1283–1293, September 2001.

[190] Ralf Schulein, Patrick Guye, Thomas A. Rhomberg, Michael C. Schmid, Gunnar Schröder, Annette C. Vergunst, Ilaria Carena, and Christoph Dehio. A bipartite signal mediates the transfer of type IV secretion substrates of Bartonella henselae into human cells. *Proceedings of the National Academy of Sciences of the United States of America*, 102(3):856–861, January 2005.

[191] Christopher Parker and Richard J. Meyer. The R1162 relaxase/primase contains two, type IV transport signals that require the small plasmid protein MobB. *Molecular Microbiology*, 66(1):252–261, October 2007.

[192] Marc Roger Couturier, Elizabetta Tasca, Cesare Montecucco, and Markus Stein. Interaction with CagF Is Required for Translocation of CagA into the Host via the Helicobacter pylori Type IV Secretion System. *Infection and Immunity*, 74(1):273–281, January 2006.

[193] Cristina E. Alvarez-Martinez and Peter J. Christie. Biological Diversity of Prokaryotic Type IV Secretion Systems. *Microbiology and Molecular Biology Reviews*, 73(4):775–808, December 2009.

[194] Qing Yuan, Anna Carle, Chan Gao, Durga Sivanesan, Khaled Ahmed Aly, Christoph Höppner, Lilian Krall, Natalie Domke, and Christian Baron. Identification of the VirB4-VirB8-VirB5-VirB2 Pilus Assembly Sequence of Type IV Secretion Systems. *Journal of Biological Chemistry*, 280(28):26349–26359, July 2005.

[195] D. Fernandez, G. M. Spudich, X. R. Zhou, and P. J. Christie. The Agrobacterium tumefaciens VirB7 lipoprotein is required for stabilization of VirB proteins during assembly of the T-complex transport apparatus. *Journal of Bacteriology*, 178(11):3168–3176, June 1996.

[196] Erh-Min Lai, Ralf Eisenbrandt, Markus Kalkum, Erich Lanka, and Clarence I. Kado. Biogenesis of T Pili in Agrobacterium tumefaciens Requires Precise VirB2

Propilin Cleavage and Cyclization. *Journal of Bacteriology*, 184(1):327–330, January 2002.

[197] Ralf Eisenbrandt, Markus Kalkum, Erh-Min Lai, Rudi Lurz, Clarence I. Kado, and Erich Lanka. Conjugative Pili of IncP Plasmids, and the Ti Plasmid T Pilus Are Composed of Cyclic Subunits. *Journal of Biological Chemistry*, 274(32):22548–22555, August 1999.

[198] Erh-Min Lai and Clarence I. Kado. Processed VirB2 Is the Major Subunit of the Promiscuous Pilus of Agrobacterium tumefaciens. *Journal of Bacteriology*, 180(10):2711–2717, May 1998.

[199] Harry H. Low, Francesca Gubellini, Angel Rivera-Calzada, Nathalie Braun, Sarah Connery, Annick Dujeancourt, Fang Lu, Adam Redzej, Rémi Fronzes, Elena V. Orlova, and Gabriel Waksman. Structure of a type IV secretion system. *Nature*, 508(7497):550–553, April 2014.

[200] Eric Cascales and Peter J. Christie. Definition of a Bacterial Type IV Secretion Pathway for a DNA Substrate. *Science*, 304(5674):1170–1173, May 2004.

[201] Matxalen Llosa, John Zupan, Christian Baron, and Patricia Zambryski. The N- and C-Terminal Portions of theAgrobacterium VirB1 Protein Independently Enhance Tumorigenesis. *Journal of Bacteriology*, 182(12):3437–3445, June 2000.

[202] C. Baron, M. Llosa, S. Zhou, and P. C. Zambryski. VirB1, a component of the T-complex transfer machinery of Agrobacterium tumefaciens, is processed to a C-terminal secreted product, VirB1. *Journal of Bacteriology*, 179(4):1203–1210, February 1997.

[203] Peter J. Christie, Neal Whitaker, and Christian González-Rivera. Mechanism and structure of the bacterial type IV secretion systems. *Biochimica et Biophysica Acta (BBA) - Molecular Cell Research*, 1843(8):1578–1591, August 2014.

[204] John Zupan, Cheryl A. Hackworth, Julieta Aguilar, Doyle Ward, and Patricia Zambryski. VirB1* Promotes T-Pilus Formation in the vir-Type IV Secretion System of Agrobacterium tumefaciens. *Journal of Bacteriology*, 189(18):6551–6563, September 2007.

[205] Heike Schmidt-Eisenlohr, Natalie Domke, Christina Angerer, Gerhard Wanner, Patricia C. Zambryski, and Christian Baron. Vir Proteins Stabilize VirB5 and Mediate Its Association with the T Pilus of Agrobacterium tumefaciens. *Journal of Bacteriology*, 181(24):7485–7492, December 1999.

[206] Erh-Min Lai, Olga Chesnokova, Lois M. Banta, and Clarence I. Kado. Genetic and Environmental Factors Affecting T-Pilin Export and T-Pilus Biogenesis in Relation to Flagellation of Agrobacterium tumefaciens. *Journal of Bacteriology*, 182(13):3705–3716, July 2000.

[207] Yoann G Santin and Eric Cascales. Domestication of a housekeeping transglycosylase for assembly of a Type VI secretion system. *EMBO reports*, December 2016.

[208] Lois M. Banta, Jennifer E. Kerr, Eric Cascales, Meghan E. Giuliano, Megan E. Bailey, Cedar McKay, Vidya Chandran, Gabriel Waksman, and Peter J. Christie. An Agrobacterium VirB10 Mutation Conferring a Type IV Secretion System Gating Defect`[U+25BF]`. *Journal of Bacteriology*, 193(10):2566–2574, May 2011.

[209] Ellen L. Zechner, Silvia Lang, and Joel F. Schildbach. Assembly and mechanisms of bacterial type IV secretion machines. *Phil. Trans. R. Soc. B*, 367(1592):1073–1087, April 2012.

[210] Angel Rivera-Calzada, Rémi Fronzes, Christos G. Savva, Vidya Chandran, Pei W. Lian, Toon Laeremans, Els Pardon, Jan Steyaert, Han Remaut, Gabriel Waksman, and Elena V. Orlova. Structure of a bacterial type IV secretion core complex at subnanometre resolution. *The EMBO Journal*, 32(8):1195–1204, April 2013.

[211] Erin R. Green and Joan Mecsas. Bacterial Secretion Systems: An Overview. *Microbiology Spectrum*, 4(1), February 2016.

[212] Travis J. Barnard, Nathalie Dautin, Petra Lukacik, Harris D. Bernstein, and Susan K. Buchanan. Autotransporter structure reveals intra-barrel cleavage followed by conformational changes. *Nature Structural & Molecular Biology*, 14(12):1214–1220, December 2007.

[213] Jack C. Leo, Iwan Grin, and Dirk Linke. Type V secretion: mechanism(s) of autotransport through the bacterial outer membrane. *Philosophical Transactions of the Royal Society B: Biological Sciences*, 367(1592):1088–1101, April 2012.

[214] Ian R. Henderson, Fernando Navarro-Garcia, Mickaël Desvaux, Rachel C. Fernandez, and Dlawer Ala'Aldeen. Type V Protein Secretion Pathway: the Autotransporter Story. *Microbiology and Molecular Biology Reviews*, 68(4):692–744, December 2004.

[215] Bert van den Berg. Crystal Structure of a Full-Length Autotransporter. *Journal of Molecular Biology*, 396(3):627–633, February 2010.

[216] Joel Selkrig, Khedidja Mosbahi, Chaille T. Webb, Matthew J. Belousoff, Andrew J. Perry, Timothy J. Wells, Faye Morris, Denisse L. Leyton, Makrina Totsika, Minh-Duy Phan, Nermin Celik, Michelle Kelly, Clare Oates, Elizabeth L. Hartland, Roy M. Robins-Browne, Sri Harsha Ramarathinam, Anthony W. Purcell, Mark A. Schembri, Richard A. Strugnell, Ian R. Henderson, Daniel Walker, and Trevor Lithgow. Discovery of an archetypal protein transport system in bacterial outer membranes. *Nature Structural & Molecular Biology*, 19(5):506–510, May 2012.

[217] Fabian Gruss, Franziska Zähringer, Roman P. Jakob, Björn M. Burmann, Sebastian Hiller, and Timm Maier. The structural basis of autotransporter translocation by TamA. *Nature Structural & Molecular Biology*, 20(11):1318–1320, November 2013.

[218] Y. Ohnishi, M. Nishiyama, S. Horinouchi, and T. Beppu. Involvement of the COOH-terminal pro-sequence of Serratia marcescens serine protease in the folding of the mature enzyme. *Journal of Biological Chemistry*, 269(52):32800–32806, December 1994.

[219] Nami Tajima, Fumihiro Kawai, Sam-Yong Park, and Jeremy R. H. Tame. A Novel Intein-Like Autoproteolytic Mechanism in Autotransporter Proteins. *Journal of Molecular Biology*, 402(4):645–656, October 2010.

[220] Nathalie Dautin, Travis J. Barnard, D. Eric Anderson, and Harris D. Bernstein. Cleavage of a bacterial autotransporter by an evolutionarily convergent autocatalytic mechanism. *The EMBO Journal*, 26(7):1942–1952, April 2007.

[221] Peter van Ulsen, Sadeeq ur Rahman, Wouter S. P. Jong, Maria H. Daleke-Schermerhorn, and Joen Luirink. Type V secretion: From biogenesis to biotechnology. *Biochimica et Biophysica Acta (BBA) - Molecular Cell Research*, 1843(8):1592–1611, August 2014.

[222] Emmanuelle Dé, Nathalie Saint, Karine Glinel, Albano C. Meli, Daniel Lévy, and Françoise Jacob-Dubuisson. Influence of the passenger domain of a model autotransporter on the properties of its translocator domain. *Molecular Membrane Biology*, 25(3):192–202, January 2008.

[223] Syma Khalid and Mark S. P. Sansom. Molecular dynamics simulations of a bacterial autotransporter: NalP from Neisseria meningitidis. *Molecular Membrane Biology*, 23(6):499–508, January 2006.

[224] V. Roussel-Jazédé, Gelder Van, R. Sijbrandi, L. Rutten, B.R. Otto, J. Luirink, P. Gros, J. Tommassen, and Ulsen Van. Channel properties of the translocator do-

main of the autotransporter Hbp of Escherichia coli. *Molecular Membrane Biology*, 28(3):157–169, 2011.

[225] Clasien J. Oomen, Peter van Ulsen, Patrick Van Gelder, Maya Feijen, Jan Tommassen, and Piet Gros. Structure of the translocator domain of a bacterial autotransporter. *The EMBO Journal*, 23(6):1257–1266, March 2004.

[226] Esteban Veiga, Etsuko Sugawara, Hiroshi Nikaido, Víctor de Lorenzo, and Luis Angel Fernández. Export of autotransported proteins proceeds through an oligomeric ring shaped by C-terminal domains. *The EMBO Journal*, 21(9):2122–2131, May 2002.

[227] B Lipinska, M Zylicz, and C Georgopoulos. The HtrA (DegP) protein, essential for Escherichia coli survival at high temperatures, is an endopeptidase. *Journal of Bacteriology*, 172(4):1791–1797, April 1990.

[228] Wouter S. P. Jong, Corinne M. Ten Hagen-Jongman, Tanneke Den Blaauwen, Dirk Jan Slotboom, Jeremy R. H. Tame, David Wickström, Jan-Willem De Gier, Ben R. Otto, and Joen Luirink. Limited tolerance towards folded elements during secretion of the autotransporter Hbp. *Molecular Microbiology*, 63(5):1524–1536, March 2007.

[229] Tobias Krojer, Justyna Sawa, Eva Schäfer, Helen R. Saibil, Michael Ehrmann, and Tim Clausen. Structural basis for the regulated protease and chaperone function of DegP. *Nature*, 453(7197):885–890, June 2008.

[230] Stephanie K. Aoki, Rupinderjit Pamma, Aaron D. Hernday, Jessica E. Bickham, Bruce A. Braaten, and David A. Low. Contact-Dependent Inhibition of Growth in Escherichia coli. *Science*, 309(5738):1245–1248, August 2005.

[231] Stephanie K. Aoki, Juliana C. Malinverni, Kyle Jacoby, Benjamin Thomas, Rupinderjit Pamma, Brooke N. Trinh, Susan Remers, Julia Webb, Bruce A. Braaten, Thomas J. Silhavy, and David A. Low. Contact-dependent growth inhibition requires the essential outer membrane protein BamA (YaeT) as the receptor and the inner membrane transport protein AcrB. *Molecular Microbiology*, 70(2):323–340, October 2008.

[232] Julia S. Webb, Kiel C. Nikolakakis, Julia L. E. Willett, Stephanie K. Aoki, Christopher S. Hayes, and David A. Low. Delivery of CdiA Nuclease Toxins into Target Cells during Contact-Dependent Growth Inhibition. *PLOS ONE*, 8(2):e57609, February 2013.

[233] M. Basler, M. Pilhofer, G. P. Henderson, G. J. Jensen, and J. J. Mekalanos. Type VI secretion requires a dynamic contractile phage tail-like structure. *Nature*, 483(7388):182–186, March 2012.

[234] Yannick R. Brunet, Abdelrahim Zoued, Frédéric Boyer, Badreddine Douzi, and Eric Cascales. The Type VI Secretion TssEFGK-VgrG Phage-Like Baseplate Is Recruited to the TssJLM Membrane Complex via Multiple Contacts and Serves As Assembly Platform for Tail Tube/Sheath Polymerization. *PLoS Genet*, 11(10):e1005545, October 2015.

[235] Eric Durand, Van Son Nguyen, Abdelrahim Zoued, Laureen Logger, Gérard Péhau-Arnaudet, Marie-Stéphanie Aschtgen, Silvia Spinelli, Aline Desmyter, Benjamin Bardiaux, Annick Dujeancourt, Alain Roussel, Christian Cambillau, Eric Cascales, and Rémi Fronzes. Biogenesis and structure of a type VI secretion membrane core complex. *Nature*, 523(7562):555–560, July 2015.

[236] Eric Durand, Abdelrahim Zoued, Silvia Spinelli, Paul J. H. Watson, Marie-Stéphanie Aschtgen, Laure Journet, Christian Cambillau, and Eric Cascales. Structural Characterization and Oligomerization of the TssL Protein, a Component Shared by Bacterial Type VI and Type IVb Secretion Systems. *Journal of Biological Chemistry*, 287(17):14157–14168, April 2012.

[237] Mikhail Kudryashev, Ray Yu-Ruei Wang, Maximilian Brackmann, Sebastian Scherer, Timm Maier, David Baker, Frank DiMaio, Henning Stahlberg, Edward H. Egelman, and Marek Basler. Structure of the Type VI Secretion System Contractile Sheath. *Cell*, 160(5):952–962, February 2015.

[238] Julie M. Silverman, Danielle M. Agnello, Hongjin Zheng, Benjamin T. Andrews, Mo Li, Carlos E. Catalano, Tamir Gonen, and Joseph D. Mougous. Haemolysin Coregulated Protein Is an Exported Receptor and Chaperone of Type VI Secretion Substrates. *Molecular Cell*, 51(5):584–593, September 2013.

[239] Stefan Pukatzki, Amy T. Ma, Derek Sturtevant, Bryan Krastins, David Sarracino, William C. Nelson, John F. Heidelberg, and John J. Mekalanos. Identification of a conserved bacterial protein secretion system in Vibrio cholerae using the Dictyostelium host model system. *Proceedings of the National Academy of Sciences*, 103(5):1528–1533, January 2006.

[240] Stefan Pukatzki, Steven B McAuley, and Sarah T Miyata. The type VI secretion system: translocation of effectors and effector-domains. *Current Opinion in Microbiology*, 12(1):11–17, February 2009.

[241] Mikhail M. Shneider, Sergey A. Buth, Brian T. Ho, Marek Basler, John J. Mekalanos, and Petr G. Leiman. PAAR-repeat proteins sharpen and diversify the type VI secretion system spike. *Nature*, 500(7462):350–353, August 2013.

[242] Sebastian Kube, Nicole Kapitein, Tomasz Zimniak, Franz Herzog, Axel Mogk, and Petra Wendler. Structure of the VipA/B Type VI Secretion Complex Suggests a Contraction-State-Specific Recycling Mechanism. *Cell Reports*, 8(1):20–30, July 2014.

[243] Aleksandra Pietrosiuk, Esther D. Lenherr, Sebastian Falk, Gabriele Bönemann, Jürgen Kopp, Hanswalter Zentgraf, Irmgard Sinning, and Axel Mogk. Molecular Basis for the Unique Role of the AAA+ Chaperone ClpV in Type VI Protein Secretion. *Journal of Biological Chemistry*, 286(34):30010–30021, August 2011.

[244] Gabriele Bönemann, Aleksandra Pietrosiuk, Alexander Diemand, Hanswalter Zentgraf, and Axel Mogk. Remodelling of VipA/VipB tubules by ClpV-mediated threading is crucial for type VI protein secretion. *The EMBO Journal*, 28(4):315–325, February 2009.

[245] Marek Basler. Type VI secretion system: secretion by a contractile nanomachine. *Phil. Trans. R. Soc. B*, 370(1679):20150021, October 2015.

[246] Andreas Förster, Sara Planamente, Eleni Manoli, Nadine S. Lossi, Paul S. Freemont, and Alain Filloux. Coevolution of the ATPase ClpV, the Sheath Proteins TssB and TssC, and the Accessory Protein TagJ/HsiE1 Distinguishes Type VI Secretion Classes. *Journal of Biological Chemistry*, 289(47):33032–33043, November 2014.

[247] Sarah A. Stanley, Sridharan Raghavan, William W. Hwang, and Jeffery S. Cox. Acute infection and macrophage subversion by Mycobacterium tuberculosis require a specialized secretion system. *Proceedings of the National Academy of Sciences*, 100(22):13001–13006, October 2003.

[248] Agnese Serafini, Francesca Boldrin, Giorgio Palù, and Riccardo Manganelli. Characterization of a Mycobacterium tuberculosis ESX-3 Conditional Mutant: Essentiality and Rescue by Iron and Zinc. *Journal of Bacteriology*, 191(20):6340–6344, October 2009.

[249] Alka Mehra, Aleena Zahra, Victor Thompson, Natalie Sirisaengtaksin, Ashley Wells, Maura Porto, Stefan Köster, Kristen Penberthy, Yoshihisha Kubota, Amelie Dricot, Daniel Rogan, Marc Vidal, David E. Hill, Andrew J. Bean, and Jennifer A.

Philips. Mycobacterium tuberculosis Type VII Secreted Effector EsxH Targets Host ESCRT to Impair Trafficking. *PLOS Pathogens*, 9(10):e1003734, October 2013.

[250] Daria Bottai, Mariagrazia Di Luca, Laleh Majlessi, Wafa Frigui, Roxane Simeone, Fadel Sayes, Wilbert Bitter, Michael J. Brennan, Claude Leclerc, Giovanna Batoni, Mario Campa, Roland Brosch, and Semih Esin. Disruption of the ESX-5 system of Mycobacterium tuberculosis causes loss of PPE protein secretion, reduction of cell wall integrity and strong attenuation. *Molecular Microbiology*, 83(6):1195–1209, March 2012.

[251] Laleh Majlessi, Priscille Brodin, Roland Brosch, Marie-Jésus Rojas, Huot Khun, Michel Huerre, Stewart T. Cole, and Claude Leclerc. Influence of ESAT-6 secretion system 1 (RD1) of Mycobacterium tuberculosis on the interaction between mycobacteria and the host immune system. *Journal of Immunology (Baltimore, Md.: 1950)*, 174(6):3570–3579, March 2005.

[252] Ben Warne, Catriona P. Harkins, Simon R. Harris, Alexandra Vatsiou, Nicola Stanley-Wall, Julian Parkhill, Sharon J. Peacock, Tracy Palmer, and Matthew T. G. Holden. The Ess/Type VII secretion system of Staphylococcus aureus shows unexpected genetic diversity. *BMC Genomics*, 17:222, 2016.

[253] Ramasubramanian Sundaramoorthy, Paul K. Fyfe, and William N. Hunter. Structure of Staphylococcus aureus EsxA Suggests a Contribution to Virulence by Action as a Transport Chaperone and/or Adaptor Protein. *Journal of Molecular Biology*, 383(3):603–614, November 2008.

[254] Edith N. G. Houben, Konstantin V. Korotkov, and Wilbert Bitter. Take five — Type VII secretion systems of Mycobacteria. *Biochimica et Biophysica Acta (BBA) - Molecular Cell Research*, 1843(8):1707–1716, August 2014.

[255] Monica L. Burts, Wade A. Williams, Kristin DeBord, and Dominique M. Missiakas. EsxA and EsxB are secreted by an ESAT-6-like system that is required for the pathogenesis of Staphylococcus aureus infections. *Proceedings of the National Academy of Sciences of the United States of America*, 102(4):1169–1174, January 2005.

[256] Abdallah M. Abdallah, Theo Verboom, Fredericke Hannes, Mohamad Safi, Michael Strong, David Eisenberg, René J. P. Musters, Christina M. J. E. Vandenbroucke-Grauls, Ben J. Appelmelk, Joen Luirink, and Wilbert Bitter. A specific secretion

system mediates PPE41 transport in pathogenic mycobacteria. *Molecular Microbiology*, 62(3):667–679, November 2006.

[257] Abdallah M. Abdallah, Theo Verboom, Eveline M. Weerdenburg, Nicolaas C. Gey van Pittius, Phetole W. Mahasha, Connie Jiménez, Marcela Parra, Nathalie Cadieux, Michael J. Brennan, Ben J. Appelmelk, and Wilbert Bitter. PPE and PE_pgrs proteins of Mycobacterium marinum are transported via the type VII secretion system ESX-5. *Molecular Microbiology*, 73(3):329–340, August 2009.

[258] T. J. Doran, A. L. M. Hodgson, J. K. Davies, and A. J. Radford. Characterisation of a novel repetitive DNA sequence from Mycobacterium bovis. *FEMS Microbiology Letters*, 96(2-3):179–185, September 1992.

[259] Nicolaas C. Gey van Pittius, Samantha L. Sampson, Hyeyoung Lee, Yeun Kim, Paul D. van Helden, and Robin M. Warren. Evolution and expansion of the Mycobacterium tuberculosis PE and PPE multigene families and their association with the duplication of the ESAT-6 (esx) gene cluster regions. *BMC Evolutionary Biology*, 6:95, 2006.

[260] Patricia A. DiGiuseppe Champion, Sarah A. Stanley, Matthew M. Champion, Eric J. Brown, and Jeffery S. Cox. C-Terminal Signal Sequence Promotes Virulence Factor Secretion in Mycobacterium tuberculosis. *Science*, 313(5793):1632–1636, September 2006.

[261] Jonathan M. Wagner, Timothy J. Evans, and Konstantin V. Korotkov. Crystal structure of the N-terminal domain of EccA1 ATPase from the ESX-1 secretion system of Mycobacterium tuberculosis. *Proteins*, 82(1):159–163, January 2014.

[262] Wilbert Bitter, Edith N. G. Houben, Daria Bottai, Priscille Brodin, Eric J. Brown, Jeffery S. Cox, Keith Derbyshire, Sarah M. Fortune, Lian-Yong Gao, Jun Liu, Nicolaas C. Gey van Pittius, Alexander S. Pym, Eric J. Rubin, David R. Sherman, Stewart T. Cole, and Roland Brosch. Systematic Genetic Nomenclature for Type VII Secretion Systems. *PLOS Pathogens*, 5(10):e1000507, October 2009.

[263] Patricia A. DiGiuseppe Champion, Matthew M. Champion, Paolo Manzanillo, and Jeffery S. Cox. ESX-1 secreted virulence factors are recognized by multiple cytosolic AAA ATPases in pathogenic mycobacteria. *Molecular Microbiology*, 73(5):950–962, September 2009.

[264] Edith N. G. Houben, Jovanka Bestebroer, Roy Ummels, Louis Wilson, Sander R. Piersma, Connie R. Jiménez, Tom H. M. Ottenhoff, Joen Luirink, and Wilbert

Bitter. Composition of the type VII secretion system membrane complex. *Molecular Microbiology*, 86(2):472–484, October 2012.

[265] Xiao-Li Zhang, De-Feng Li, Joy Fleming, Li-Wei Wang, Ying Zhou, Da-Cheng Wang, Xian-En Zhang, and Li-Jun Bi. Core component EccB1 of the Mycobacterium tuberculosis type VII secretion system is a periplasmic ATPase. *The FASEB Journal*, 29(12):4804–4814, December 2015.

[266] Jonathan M. Wagner, Sum Chan, Timothy J. Evans, Sara Kahng, Jennifer Kim, Mark A. Arbing, David Eisenberg, and Konstantin V. Korotkov. Structures of EccB1 and EccD1 from the core complex of the mycobacterial ESX-1 type VII secretion system. *BMC Structural Biology*, 16:5, 2016.

[267] Keiko Sato, Mariko Naito, Hideharu Yukitake, Hideki Hirakawa, Mikio Shoji, Mark J. McBride, Ryan G. Rhodes, and Koji Nakayama. A protein secretion system linked to bacteroidete gliding motility and pathogenesis. *Proceedings of the National Academy of Sciences*, 107(1):276–281, January 2010.

[268] Keiko Sato, Hideharu Yukitake, Yuka Narita, Mikio Shoji, Mariko Naito, and Koji Nakayama. Identification of Porphyromonas gingivalis proteins secreted by the Por secretion system. *FEMS microbiology letters*, 338(1):68–76, January 2013.

[269] Mark J McBride and Daisuke Nakane. Flavobacterium gliding motility and the type IX secretion system. *Current Opinion in Microbiology*, 28:72–77, December 2015.

[270] Sampada S. Kharade and Mark J. McBride. Flavobacterium johnsoniae PorV Is Required for Secretion of a Subset of Proteins Targeted to the Type IX Secretion System. *Journal of Bacteriology*, 197(1):147–158, January 2015.

[271] Sampada S. Kharade and Mark J. McBride. Flavobacterium johnsoniae Chitinase ChiA Is Required for Chitin Utilization and Is Secreted by the Type IX Secretion System. *Journal of Bacteriology*, 196(5):961–970, March 2014.

[272] P. N. Papapanou. Epidemiology of periodontal diseases: an update. *Journal of the International Academy of Periodontology*, 1(4):110–116, October 1999.

[273] U. M. Irfan, D. V. Dawson, and N. F. Bissada. Epidemiology of periodontal disease: a review and clinical perspectives. *Journal of the International Academy of Periodontology*, 3(1):14–21, January 2001.

[274] S. Sugawara, E. Nemoto, H. Tada, K. Miyake, T. Imamura, and H. Takada. Proteolysis of human monocyte CD14 by cysteine proteinases (gingipains) from Porphyromonas gingivalis leading to lipopolysaccharide hyporesponsiveness. *Journal of Immunology (Baltimore, Md.: 1950)*, 165(1):411–418, July 2000.

[275] T Imamura, S Tanase, T Hamamoto, J Potempa, and J Travis. Activation of blood coagulation factor IX by gingipains R, arginine-specific cysteine proteinases from Porphyromonas gingivalis. *Biochemical Journal*, 353(Pt 2):325–331, January 2001.

[276] T. Imamura, R. N. Pike, J. Potempa, and J. Travis. Pathogenesis of periodontitis: a major arginine-specific cysteine proteinase from Porphyromonas gingivalis induces vascular permeability enhancement through activation of the kallikrein/kinin pathway. *The Journal of Clinical Investigation*, 94(1):361–367, July 1994.

[277] Takahisa Imamura, Agnieszka Banbula, Pedro J. B. Pereira, James Travis, and Jan Potempa. Activation of Human Prothrombin by Arginine-specific Cysteine Proteinases (Gingipains R) from Porphyromonas gingivalis. *Journal of Biological Chemistry*, 276(22):18984–18991, June 2001.

[278] Maxence S. Vincent, Mickaël J. Canestrari, Philippe Leone, Julien Stathopoulos, Bérengère Ize, Abdelrahim Zoued, Christian Cambillau, Christine Kellenberger, Alain Roussel, and Eric Cascales. Characterization of the Porphyromonas gingivalis Type IX Secretion Trans-Envelope PorKLMNP Core Complex. *Journal of Biological Chemistry*, page jbc.M116.765081, January 2017.

[279] Dhana G. Gorasia, Paul D. Veith, Eric G. Hanssen, Michelle D. Glew, Keiko Sato, Hideharu Yukitake, Koji Nakayama, and Eric C. Reynolds. Structural Insights into the PorK and PorN Components of the Porphyromonas gingivalis Type IX Secretion System. *PLOS Pathogens*, 12(8):e1005820, August 2016.

[280] Iñaki de Diego, Miroslaw Ksiazek, Danuta Mizgalska, Lahari Koneru, Przemyslaw Golik, Borys Szmigielski, Magdalena Nowak, Zuzanna Nowakowska, Barbara Potempa, John A. Houston, Jan J. Enghild, Ida B. Thøgersen, Jinlong Gao, Ann H. Kwan, Jill Trewhella, Grzegorz Dubin, F. Xavier Gomis-Rüth, Ky-Anh Nguyen, and Jan Potempa. The outer-membrane export signal of Porphyromonas gingivalis type IX secretion system (T9ss) is a conserved C-terminal -sandwich domain. *Scientific Reports*, 6:23123, March 2016.

[281] Filippo Pacini. *Osservazioni microscopiche e deduzioni patologiche sul cholera asiatico*. tip. di F. Bencini, 1854.

[282] N Howard-Jones. Robert Koch and the cholera vibrio: a centenary. *British Medical Journal (Clinical research ed.)*, 288(6414):379–381, February 1984.

[283] Carla Lutz, Martina Erken, Parisa Noorian, Shuyang Sun, and Diane McDougald. Environmental reservoirs and mechanisms of persistence of Vibrio cholerae. *Frontiers in Microbiology*, 4, 2013.

[284] John F. Heidelberg, Jonathan A. Eisen, William C. Nelson, Rebecca A. Clayton, Michelle L. Gwinn, Robert J. Dodson, Daniel H. Haft, Erin K. Hickey, Jeremy D. Peterson, Lowell Umayam, Steven R. Gill, Karen E. Nelson, Timothy D. Read, Herve Tettelin, Delwood Richardson, Maria D. Ermolaeva, Jessica Vamathevan, Steven Bass, Haiying Qin, Ioana Dragoi, Patrick Sellers, Lisa McDonald, Teresa Utterback, Robert D. Fleishmann, William C. Nierman, Owen White, Steven L. Salzberg, Hamilton O. Smith, Rita R. Colwell, John J. Mekalanos, J. Craig Venter, and Claire M. Fraser. DNA sequence of both chromosomes of the cholera pathogen Vibrio cholerae. *Nature*, 406(6795):477–483, August 2000.

[285] Matthew K. Waldor and John J. Mekalanos. Lysogenic Conversion by a Filamentous Phage Encoding Cholera Toxin. *Science*, 272(5270):1910–1914, June 1996.

[286] Brigid M Davis and Matthew K Waldor. Filamentous phages linked to virulence of Vibrio cholerae. *Current Opinion in Microbiology*, 6(1):35–42, February 2003.

[287] Asish K. Mukhopadhyay, Soumen Chakraborty, Yoshifumi Takeda, G. Balakrish Nair, and Douglas E. Berg. Characterization of VPI Pathogenicity Island and CTX Prophage in Environmental Strains of Vibrio cholerae. *Journal of Bacteriology*, 183(16):4737–4746, August 2001.

[288] Matthew K. Waldor and John J. Mekalanos. Emergence of a New Cholera Pandemic: Molecular Analysis of Virulence Determinants in Vibrio cholerae 0139 and Development of a Live Vaccine Prototype. *The Journal of Infectious Diseases*, 170(2):278–283, August 1994.

[289] T. R. Hirst, J. Sanchez, J. B. Kaper, S. J. Hardy, and J. Holmgren. Mechanism of toxin secretion by Vibrio cholerae investigated in strains harboring plasmids that encode heat-labile enterotoxins of Escherichia coli. *Proceedings of the National Academy of Sciences*, 81(24):7752–7756, December 1984.

[290] S. J. Streatfield, M. Sandkvist, T. K. Sixma, M. Bagdasarian, W. G. Hol, and T. R. Hirst. Intermolecular interactions between the A and B subunits of heat-labile

enterotoxin from Escherichia coli promote holotoxin assembly and stability in vivo. *Proceedings of the National Academy of Sciences*, 89(24):12140–12144, December 1992.

[291] D. M. Gill and R. Meren. ADP-ribosylation of membrane proteins catalyzed by cholera toxin: basis of the activation of adenylate cyclase. *Proceedings of the National Academy of Sciences of the United States of America*, 75(7):3050–3054, July 1978.

[292] Jun Sakurai, Masahiro Nagahama, Masataka Oda, Hideaki Tsuge, and Keiko Kobayashi. Clostridium perfringens Iota-Toxin: Structure and Function. *Toxins*, 1(2):208–228, December 2009.

[293] Penelope E Stein, Amechand Boodhoo, Glen D Armstrong, Stephen A Cockle, Michel H Klein, and Randy J Read. The crystal structure of pertussis toxin. *Structure*, 2(1):45–57, January 1994.

[294] P.E. Stein, A. Boodhoo, G.J. Tyrrell, J.L. Brunton, and R.J. Read. Crystal structure of the cell-binding B oligomer of verotoxin-1 from E. coli. *Nature*, 355(6362):748–750, 1992.

[295] D. A. Bobak, M. M. Bliziotes, M. Noda, S. C. Tsai, R. Adamik, and J. Moss. Mechanism of activation of cholera toxin by ADP-ribosylation factor (ARF): both low- and high-affinity interactions of ARF with guanine nucleotides promote toxin activation. *Biochemistry*, 29(4):855–861, January 1990.

[296] Anne A. Wolf, Michael G. Jobling, Susan Wimer-Mackin, Margaret Ferguson-Maltzman, James L. Madara, Randall K. Holmes, and Wayne I. Lencer. Ganglioside Structure Dictates Signal Transduction by Cholera Toxin and Association with Caveolae-like Membrane Domains in Polarized Epithelia. *The Journal of Cell Biology*, 141(4):917–927, May 1998.

[297] Jay R. Thiagarajah and A. S. Verkman. New drug targets for cholera therapy. *Trends in Pharmacological Sciences*, 26(4):172–175, April 2005.

[298] Arpita Chatterjee, Pradeep K. Dutta, and Rukhsana Chowdhury. Effect of Fatty Acids and Cholesterol Present in Bile on Expression of Virulence Factors and Motility of Vibrio cholerae. *Infection and Immunity*, 75(4):1946–1953, April 2007.

[299] Eric S Krukonis and Victor J DiRita. From motility to virulence: sensing and responding to environmental signals in Vibrio cholerae. *Current Opinion in Microbiology*, 6(2):186–190, April 2003.

[300] Darren A. Schuhmacher and Karl E. Klose. Environmental Signals Modulate ToxT-Dependent Virulence Factor Expression in Vibrio cholerae. *Journal of Bacteriology*, 181(5):1508–1514, March 1999.

[301] Alex Toftgaard Nielsen, Nadia A. Dolganov, Glen Otto, Michael C. Miller, Cheng Yen Wu, and Gary K. Schoolnik. RpoS Controls the Vibrio cholerae Mucosal Escape Response. *PLOS Pathogens*, 2(10):e109, October 2006.

[302] Lisa Craig, Ronald K Taylor, Michael E Pique, Brian D Adair, Andrew S Arvai, Mona Singh, Sarah J Lloyd, David S Shin, Elizabeth D Getzoff, Mark Yeager, Katrina T Forest, and John A Tainer. Type IV Pilin Structure and Assembly: X-Ray and EM Analyses of Vibrio cholerae Toxin-Coregulated Pilus and Pseudomonas aeruginosa PAK Pilin. *Molecular Cell*, 11(5):1139–1150, May 2003.

[303] Juliana Li, Mindy S. Lim, Sheng Li, Melissa Brock, Michael E. Pique, Virgil L. Woods Jr., and Lisa Craig. Vibrio cholerae Toxin-Coregulated Pilus Structure Analyzed by Hydrogen/Deuterium Exchange Mass Spectrometry. *Structure*, 16(1):137–148, January 2008.

[304] Richard A. Finkelstein. Cholera, Vibrio cholerae O1 and O139, and Other Pathogenic Vibrios. In Samuel Baron, editor, *Medical Microbiology*. University of Texas Medical Branch at Galveston, Galveston (TX), 4th edition, 1996.

[305] Ezra J. Barzilay, Nicolas Schaad, Roc Magloire, Kam S. Mung, Jacques Boncy, Georges A. Dahourou, Eric D. Mintz, Maria W. Steenland, John F. Vertefeuille, and Jordan W. Tappero. Cholera Surveillance during the Haiti Epidemic — The First 2 Years. *New England Journal of Medicine*, 368(7):599–609, February 2013.

[306] WHO | Weekly Epidemiological Record, 23 September 2016, vol. 91, 38 (pp. 433–440).

[307] W. B. O'Shaughnessy. Proposal of a new method of treating the blue epidemic cholerae by the injection of highly oxygenised salts into the venous system. *The Lancet*, 17(432):366–371, December 1831.

[308] G H Rabbani, M R Islam, T Butler, M Shahrier, and K Alam. Single-dose treatment of cholera with furazolidone or tetracycline in a double-blind randomized trial. *Antimicrobial Agents and Chemotherapy*, 33(9):1447–1450, September 1989.

[309] WHO | Cholera.

[310] B.K. Hammer and B.L. Bassler. Quorum sensing controls biofilm formation in Vibrio cholerae. *Molecular Microbiology*, 50(1):101–114, 2003.

[311] Jun Zhu, Melissa B. Miller, Russell E. Vance, Michelle Dziejman, Bonnie L. Bassler, and John J. Mekalanos. Quorum-sensing regulators control virulence gene expression in Vibrio cholerae. *Proceedings of the National Academy of Sciences*, 99(5):3129–3134, March 2002.

[312] Yi Shao and Bonnie L. Bassler. Quorum regulatory small RNAs repress type VI secretion in Vibrio cholerae. *Molecular Microbiology*, 92(5):921–930, June 2014.

[313] Elena S. Antonova, Eryn E. Bernardy, and Brian K. Hammer. Natural competence in Vibrio cholerae is controlled by a nucleoside scavenging response that requires CytR-dependent anti-activation. *Molecular Microbiology*, 86(5):1215–1231, December 2012.

[314] Melanie Blokesch. Chitin colonization, chitin degradation and chitin-induced natural competence of Vibrio cholerae are subject to catabolite repression. *Environmental Microbiology*, 14(8):1898–1912, August 2012.

[315] Verena Bachmann, Benjamin Kostiuk, Daniel Unterweger, Laura Diaz-Satizabal, Stephen Ogg, and Stefan Pukatzki. Bile Salts Modulate the Mucin-Activated Type VI Secretion System of Pandemic Vibrio cholerae. *PLOS Neglected Tropical Diseases*, 9(8):e0004031, August 2015.

[316] Lisa C. Metzger, Sandrine Stutzmann, Tiziana Scrignari, Charles Van der Henst, Noémie Matthey, and Melanie Blokesch. Independent Regulation of Type VI Secretion in Vibrio cholerae by TfoX and TfoY. *Cell Reports*, 15(5):951–958, May 2016.

[317] Sandrine Borgeaud, Lisa C. Metzger, Tiziana Scrignari, and Melanie Blokesch. The type VI secretion system of Vibrio cholerae fosters horizontal gene transfer. *Science*, 347(6217):63–67, January 2015.

[318] Mirella Lo Scrudato and Melanie Blokesch. A transcriptional regulator linking quorum sensing and chitin induction to render Vibrio cholerae naturally transformable. *Nucleic Acids Research*, 41(6):3644–3658, April 2013.

[319] Karin L. Meibom, Melanie Blokesch, Nadia A. Dolganov, Cheng-Yen Wu, and Gary K. Schoolnik. Chitin Induces Natural Competence in Vibrio cholerae. *Science*, 310(5755):1824–1827, December 2005.

[320] Daniel Unterweger, Sarah T. Miyata, Verena Bachmann, Teresa M. Brooks, Travis Mullins, Benjamin Kostiuk, Daniele Provenzano, and Stefan Pukatzki. The Vibrio cholerae type VI secretion system employs diverse effector modules for intraspecific competition. *Nature Communications*, 5:3549, April 2014.

[321] Takahiko Ishikawa, Pramod Kumar Rompikuntal, Barbro Lindmark, Debra L. Milton, and Sun Nyunt Wai. Quorum Sensing Regulation of the Two hcp Alleles in Vibrio cholerae O1 Strains. *PLOS ONE*, 4(8):e6734, August 2009.

[322] Jun Zheng, Ok S. Shin, D. Ewen Cameron, and John J. Mekalanos. Quorum sensing and a global regulator TsrA control expression of type VI secretion and virulence in Vibrio cholerae. *Proceedings of the National Academy of Sciences*, 107(49):21128–21133, December 2010.

[323] Christopher M. Waters, Wenyun Lu, Joshua D. Rabinowitz, and Bonnie L. Bassler. Quorum Sensing Controls Biofilm Formation in Vibrio cholerae through Modulation of Cyclic Di-GMP Levels and Repression of vpsT. *Journal of Bacteriology*, 190(7):2527–2536, April 2008.

[324] Avatar Joshi, Benjamin Kostiuk, Andrew Rogers, Jennifer Teschler, Stefan Pukatzki, and Fitnat H. Yildiz. Rules of Engagement: The Type VI Secretion System in Vibrio cholerae. *Trends in Microbiology*, 2017.

[325] Amy T. Ma and John J. Mekalanos. In vivo actin cross-linking induced by Vibrio cholerae type VI secretion system is associated with intestinal inflammation. *Proceedings of the National Academy of Sciences*, 107(9):4365–4370, March 2010.

[326] Andrew T. Cheng, Karen M. Ottemann, and Fitnat H. Yildiz. Vibrio cholerae Response Regulator VxrB Controls Colonization and Regulates the Type VI Secretion System. *PLOS Pathogens*, 11(5):e1004933, May 2015.

[327] FoSheng Hsu, Sandra Schwarz, and Joseph D. Mougous. TagR promotes PpkA-catalysed type VI secretion activation in Pseudomonas aeruginosa. *Molecular Microbiology*, 72(5):1111–1125, June 2009.

[328] Joseph D. Mougous, Marianne E. Cuff, Stefan Raunser, Aimee Shen, Min Zhou, Casey A. Gifford, Andrew L. Goodman, Grazyna Joachimiak, Claudia L. Ordoñez, Stephen Lory, Thomas Walz, Andrzej Joachimiak, and John J. Mekalanos. A Virulence Locus of Pseudomonas aeruginosa Encodes a Protein Secretion Apparatus. *Science*, 312(5779):1526–1530, June 2006.

[329] Marek Basler, Brian T. Ho, and John J. Mekalanos. Tit-for-Tat: Type VI Secretion System Counterattack during Bacterial Cell-Cell Interactions. *Cell*, 152(4):884–894, February 2013.

[330] Joseph D. Mougous, Casey A. Gifford, Talia L. Ramsdell, and John J. Mekalanos. Threonine phosphorylation post-translationally regulates protein secretion in Pseudomonas aeruginosa. *Nature Cell Biology*, 9(7):797–803, July 2007.

[331] M. Basler and J. J. Mekalanos. Type 6 Secretion Dynamics Within and Between Bacterial Cells. *Science*, 337(6096):815–815, August 2012.

[332] Peng Ge, Dean Scholl, Petr G. Leiman, Xuekui Yu, Jeff F. Miller, and Z. Hong Zhou. Atomic structures of a bactericidal contractile nanotube in its pre- and postcontraction states. *Nature Structural & Molecular Biology*, 22(5):377–382, May 2015.

[333] Petr G. Leiman, Marek Basler, Udupi A. Ramagopal, Jeffrey B. Bonanno, J. Michael Sauder, Stefan Pukatzki, Stephen K. Burley, Steven C. Almo, and John J. Mekalanos. Type VI secretion apparatus and phage tail-associated protein complexes share a common evolutionary origin. *Proceedings of the National Academy of Sciences*, 106(11):4154–4159, March 2009.

[334] Daniel L. Clemens, Peng Ge, Bai-Yu Lee, Marcus A. Horwitz, and Z. Hong Zhou. Atomic Structure of T6ss Reveals Interlaced Array Essential to Function. *Cell*, 160(5):940–951, February 2015.

[335] Nicholas J. Shikuma, Martin Pilhofer, Gregor L. Weiss, Michael G. Hadfield, Grant J. Jensen, and Dianne K. Newman. Marine Tubeworm Metamorphosis Induced by Arrays of Bacterial Phage Tail–Like Structures. *Science*, 343(6170):529–533, January 2014.

[336] J. Bernard Heymann, Joseph D. Bartho, Daria Rybakova, Hari P. Venugopal, Dennis C. Winkler, Anindito Sen, Mark R. H. Hurst, and Alok K. Mitra. Three-dimensional Structure of the Toxin-delivery Particle Antifeeding Prophage of Serratia entomophila. *Journal of Biological Chemistry*, 288(35):25276–25284, August 2013.

[337] Paula J. Wilderman, Adriana I. Vasil, Zaiga Johnson, and Michael L. Vasil. Genetic and biochemical analyses of a eukaryotic-like phospholipase D of Pseudomonas aeruginosa suggest horizontal acquisition and a role for persistence in a chronic pulmonary infection model. *Molecular Microbiology*, 39(2):291–304, January 2001.

[338] S G Williams, L T Varcoe, S R Attridge, and P A Manning. Vibrio cholerae Hcp, a secreted protein coregulated with HlyA. *Infection and Immunity*, 64(1):283–289, January 1996.

[339] Christian Schlieker, Hanswalter Zentgraf, Petra Dersch, and Axel Mogk. ClpV, a unique Hsp100/Clp member of pathogenic proteobacteria. *Biological Chemistry*, 386(11):1115–1127, 2005.

[340] Sakshi Shrivastava and Sharmila S. Mande. Identification and Functional Characterization of Gene Components of Type VI Secretion System in Bacterial Genomes. *PLoS ONE*, 3(8), August 2008.

[341] Sandra Schwarz, T. Eoin West, Frédéric Boyer, Wen-Chi Chiang, Mike A. Carl, Rachel D. Hood, Laurence Rohmer, Tim Tolker-Nielsen, Shawn J. Skerrett, and Joseph D. Mougous. Burkholderia Type VI Secretion Systems Have Distinct Roles in Eukaryotic and Bacterial Cell Interactions. *PLoS Pathogens*, 6(8), August 2010.

[342] Abderrahman Hachani, Thomas E Wood, and Alain Filloux. Type VI secretion and anti-host effectors. *Current Opinion in Microbiology*, 29:81–93, February 2016.

[343] Andrea J. Jani and Peggy A. Cotter. Type VI Secretion: Not Just for Pathogenesis Anymore. *Cell Host & Microbe*, 8(1):2–6, July 2010.

[344] Feng Jiang, Nicholas R. Waterfield, Jian Yang, Guowei Yang, and Qi Jin. A Pseudomonas aeruginosa Type VI Secretion Phospholipase D Effector Targets Both Prokaryotic and Eukaryotic Cells. *Cell Host & Microbe*, 15(5):600–610, May 2014.

[345] Dana L. MacIntyre, Sarah T. Miyata, Maya Kitaoka, and Stefan Pukatzki. The Vibrio cholerae type VI secretion system displays antimicrobial properties. *Proceedings of the National Academy of Sciences*, 107(45):19520–19524, November 2010.

[346] Jeanette Bröms, Anders Sjöstedt, and Moa Lavander. The Role of the Francisella Tularensis Pathogenicity Island in Type VI Secretion, Intracellular Survival, and Modulation of Host Cell Signaling. *Frontiers in Microbiology*, 1, 2010.

[347] Shaohui Wang, Jianjun Dai, Qingmei Meng, Xiangan Han, Yue Han, Yichao Zhao, Denghui Yang, Chan Ding, and Shengqing Yu. DotU expression is highly induced during in vivo infection and responsible for virulence and Hcp1 secretion in avian pathogenic Escherichia coli. *Frontiers in Microbiology*, 5, 2014.

[348] Eryn E. Bernardy, Maryann A. Turnsek, Sarah K. Wilson, Cheryl L. Tarr, and Brian K. Hammer. Diversity of Clinical and Environmental Isolates of Vibrio

cholerae in Natural Transformation and Contact-Dependent Bacterial Killing Indicative of Type VI Secretion System Activity. *Applied and Environmental Microbiology*, 82(9):2833–2842, May 2016.

[349] Sarah T. Miyata, Maya Kitaoka, Lukasz Wieteska, Christian Frech, Nansheng Chen, and Stefan Pukatzki. The Vibrio Cholerae Type VI Secretion System: Evaluating its Role in the Human Disease Cholera. *Frontiers in Microbiology*, 1, November 2010.

[350] Mark A. Schell, Ricky L. Ulrich, Wilson J. Ribot, Ernst E. Brueggemann, Harry B. Hines, Dan Chen, Lyla Lipscomb, H. Stanley Kim, Jan Mrázek, William C. Nierman, and David DeShazer. Type VI secretion is a major virulence determinant in Burkholderia mallei. *Molecular Microbiology*, 64(6):1466–1485, June 2007.

[351] Gil Shalom, Jonathan G. Shaw, and Mark S. Thomas. In vivo expression technology identifies a type VI secretion system locus in Burkholderia pseudomallei that is induced upon invasion of macrophages. *Microbiology*, 153(8):2689–2699, 2007.

[352] Alistair B. Russell, Rachel D. Hood, Nhat Khai Bui, Michele LeRoux, Waldemar Vollmer, and Joseph D. Mougous. Type VI secretion delivers bacteriolytic effectors to target cells. *Nature*, 475(7356):343–347, July 2011.

[353] Tao G. Dong, Brian T. Ho, Deborah R. Yoder-Himes, and John J. Mekalanos. Identification of T6ss-dependent effector and immunity proteins by Tn-seq in Vibrio cholerae. *Proceedings of the National Academy of Sciences*, 110(7):2623–2628, February 2013.

[354] Alistair B. Russell, Pragya Singh, Mitchell Brittnacher, Nhat Khai Bui, Rachel D. Hood, Mike A. Carl, Danielle M. Agnello, Sandra Schwarz, David R. Goodlett, Waldemar Vollmer, and Joseph D. Mougous. A widespread bacterial type VI secretion effector superfamily identified using a heuristic approach. *Cell host & microbe*, 11(5):538–549, May 2012.

[355] Stefan Pukatzki, Amy T. Ma, Andrew T. Revel, Derek Sturtevant, and John J. Mekalanos. Type VI secretion system translocates a phage tail spike-like protein into target cells where it cross-links actin. *Proceedings of the National Academy of Sciences*, 104(39):15508–15513, September 2007.

[356] John C. Whitney, Christina M. Beck, Young Ah Goo, Alistair B. Russell, Brittany N. Harding, Justin A. De Leon, David A. Cunningham, Bao Q. Tran, David A.

Low, David R. Goodlett, Christopher S. Hayes, and Joseph D. Mougous. Genetically distinct pathways guide effector export through the type VI secretion system. *Molecular Microbiology*, 92(3):529–542, May 2014.

[357] Emrah Altindis, Tao Dong, Christy Catalano, and John Mekalanos. Secretome Analysis of Vibrio cholerae Type VI Secretion System Reveals a New Effector-Immunity Pair. *mBio*, 6(2):e00075–15, May 2015.

[358] Chacko Jobichen, Smarajit Chakraborty, Mo Li, Jun Zheng, Lissa Joseph, Yu-Keung Mok, Ka Yin Leung, and J. Sivaraman. Structural Basis for the Secretion of EvpC: A Key Type VI Secretion System Protein from Edwardsiella tarda. *PLOS ONE*, 5(9):e12910, September 2010.

[359] Xiaoye Liang, Richard Moore, Mike Wilton, Megan J. Q. Wong, Linh Lam, and Tao G. Dong. Identification of divergent type VI secretion effectors using a conserved chaperone domain. *Proceedings of the National Academy of Sciences*, 112(29):9106–9111, July 2015.

[360] Sarah T. Miyata, Maya Kitaoka, Teresa M. Brooks, Steven B. McAuley, and Stefan Pukatzki. Vibrio cholerae Requires the Type VI Secretion System Virulence Factor VasX To Kill Dictyostelium discoideum. *Infection and Immunity*, 79(7):2941–2949, July 2011.

[361] Marie-Stéphanie Aschtgen, Abdelrahim Zoued, Roland Lloubès, Laure Journet, and Eric Cascales. The C-tail anchored TssL subunit, an essential protein of the enteroaggregative Escherichia coli Sci-1 Type VI secretion system, is inserted by YidC. *MicrobiologyOpen*, 1(1):71–82, March 2012.

[362] Marie-Stéphanie Aschtgen, Christophe S. Bernard, Sophie De Bentzmann, Roland Lloubès, and Eric Cascales. SciN Is an Outer Membrane Lipoprotein Required for Type VI Secretion in Enteroaggregative Escherichia coli. *Journal of Bacteriology*, 190(22):7523–7531, November 2008.

[363] Catarina Felisberto-Rodrigues, Eric Durand, Marie-Stéphanie Aschtgen, Stéphanie Blangy, Miguel Ortiz-Lombardia, Badreddine Douzi, Christian Cambillau, and Eric Cascales. Towards a Structural Comprehension of Bacterial Type VI Secretion Systems: Characterization of the TssJ-TssM Complex of an Escherichia coli Pathovar. *PLOS Pathogens*, 7(11):e1002386, November 2011.

[364] Marie-Stéphanie Aschtgen, Marthe Gavioli, Andrea Dessen, Roland Lloubès, and Eric Cascales. The SciZ protein anchors the enteroaggregative Escherichia coli

Type VI secretion system to the cell wall. *Molecular Microbiology*, 75(4):886–899, February 2010.

[365] Abdelrahim Zoued, Eric Durand, Yannick R. Brunet, Silvia Spinelli, Badreddine Douzi, Mathilde Guzzo, Nicolas Flaugnatti, Pierre Legrand, Laure Journet, Rémi Fronzes, Tâm Mignot, Christian Cambillau, and Eric Cascales. Priming and polymerization of a bacterial contractile tail structure. *Nature*, 531(7592):59–63, March 2016.

[366] V. A. Rao, S. M. Shepherd, G. English, S. J. Coulthurst, and W. N. Hunter. The structure of Serratia marcescens Lip, a membrane-bound component of the type VI secretion system. *Acta Crystallographica Section D: Biological Crystallography*, 67(12):1065–1072, December 2011.

[367] C. S. Robb, M. Assmus, F. E. Nano, and A. B. Boraston. Structure of the T6ss lipoprotein TssJ1 from Pseudomonas aeruginosa. *Acta Crystallographica Section F: Structural Biology and Crystallization Communications*, 69(6):607–610, June 2013.

[368] Craig S. Robb, Francis E. Nano, and Alisdair B. Boraston. The Structure of the Conserved Type Six Secretion Protein TssL (DotU) from Francisella novicida. *Journal of Molecular Biology*, 419(5):277–283, June 2012.

[369] James C. Samuelson, Minyong Chen, Fenglei Jiang, Ines Möller, Martin Wiedmann, Andreas Kuhn, Gregory J. Phillips, and Ross E. Dalbey. YidC mediates membrane protein insertion in bacteria. *Nature*, 406(6796):637–641, August 2000.

[370] Laureen Logger, Marie-Stéphanie Aschtgen, Marie Guérin, Eric Cascales, and Eric Durand. Molecular Dissection of the Interface between the Type VI Secretion TssM Cytoplasmic Domain and the TssG Baseplate Component. *Journal of Molecular Biology*, 428(22):4424–4437, November 2016.

[371] Abdelrahim Zoued, Chloé J. Cassaro, Eric Durand, Badreddine Douzi, Alexandre P. España, Christian Cambillau, Laure Journet, and Eric Cascales. Structure–Function Analysis of the TssL Cytoplasmic Domain Reveals a New Interaction between the Type VI Secretion Baseplate and Membrane Complexes. *Journal of Molecular Biology*, 428(22):4413–4423, November 2016.

[372] Nicholas M. I. Taylor, Nikolai S. Prokhorov, Ricardo C. Guerrero-Ferreira, Mikhail M. Shneider, Christopher Browning, Kenneth N. Goldie, Henning Stahlberg, and Petr G. Leiman. Structure of the T4 baseplate and its function in triggering sheath contraction. *Nature*, 533(7603):346–352, May 2016.

[373] Bo Hu, William Margolin, Ian J. Molineux, and Jun Liu. Structural remodeling of bacteriophage T4 and host membranes during infection initiation. *Proceedings of the National Academy of Sciences*, 112(35):E4919–E4928, September 2015.

[374] R. A. Crowther, Elaine V. Lenk, Yoshiko Kikuchi, and Jonathan King. Molecular reorganization in the hexagon to star transition of the baseplate of bacteriophage T4. *Journal of Molecular Biology*, 116(3):489–523, November 1977.

[375] Victor A. Kostyuchenko, Grigorii A. Navruzbekov, Lidia P. Kurochkina, Sergei V. Strelkov, Vadim V. Mesyanzhinov, and Michael G. Rossmann. The structure of bacteriophage T4 gene product 9: the trigger for tail contraction. *Structure*, 7(10):1213–1222, October 1999.

[376] Sara Planamente, Osman Salih, Eleni Manoli, David Albesa-Jové, Paul S Freemont, and Alain Filloux. TssA forms a gp6-like ring attached to the type VI secretion sheath. *The EMBO Journal*, page e201694024, June 2016.

[377] Grant English, Olwyn Byron, Francesca R. Cianfanelli, Alan R. Prescott, and Sarah J. Coulthurst. Biochemical analysis of TssK, a core component of the bacterial Type VI secretion system, reveals distinct oligomeric states of TssK and identifies a TssK–TssFG subcomplex. *Biochemical Journal*, 461(2):291–304, July 2014.

[378] Petr G. Leiman, Fumio Arisaka, Mark J. van Raaij, Victor A. Kostyuchenko, Anastasia A. Aksyuk, Shuji Kanamaru, and Michael G. Rossmann. Morphogenesis of the T4 tail and tail fibers. *Virology Journal*, 7:355, 2010.

[379] Petr G. Leiman and Mikhail M. Shneider. Contractile Tail Machines of Bacteriophages. In Michael G. Rossmann and Venigalla B. Rao, editors, *Viral Molecular Machines*, number 726 in Advances in Experimental Medicine and Biology, pages 93–114. Springer US, 2012. DOI: 10.1007/978-1-4614-0980-9_5.

[380] Y. R. Brunet, J. Henin, H. Celia, and E. Cascales. Type VI secretion and bacteriophage tail tubes share a common assembly pathway. *EMBO reports*, 15(3):315–321, March 2014.

[381] Abdelrahim Zoued, Eric Durand, Cecilia Bebeacua, Yannick R. Brunet, Badreddine Douzi, Christian Cambillau, Eric Cascales, and Laure Journet. TssK Is a Trimeric Cytoplasmic Protein Interacting with Components of Both Phage-like and Membrane Anchoring Complexes of the Type VI Secretion System. *Journal of Biological Chemistry*, 288(38):27031–27041, September 2013.

[382] Carina R. Büttner, Yingzhou Wu, Karen L. Maxwell, and Alan R. Davidson. Baseplate assembly of phage Mu: Defining the conserved core components of contractile-tailed phages and related bacterial systems. *Proceedings of the National Academy of Sciences*, 113(36):10174–10179, September 2016.

[383] Andrea Vettiger and Marek Basler. Type VI Secretion System Substrates Are Transferred and Reused among Sister Cells. *Cell*, 167(1):99–110.e12, September 2016.

[384] Jerzy Osipiuk, Xiaohui Xu, Hong Cui, Alexei Savchenko, Aled Edwards, and Andrzej Joachimiak. Crystal structure of secretory protein Hcp3 from Pseudomonas aeruginosa. *Journal of Structural and Functional Genomics*, 12(1):21, March 2011.

[385] Badreddine Douzi, Silvia Spinelli, Stéphanie Blangy, Alain Roussel, Eric Durand, Yannick R. Brunet, Eric Cascales, and Christian Cambillau. Crystal Structure and Self-Interaction of the Type VI Secretion Tail-Tube Protein from Enteroaggregative Escherichia coli. *PLOS ONE*, 9(2):e86918, February 2014.

[386] Panagiotis F. Sarris, Emmanuel D. Ladoukakis, Nickolas J. Panopoulos, and Effie V. Scoulica. A Phage Tail-Derived Element with Wide Distribution among Both Prokaryotic Domains: A Comparative Genomic and Phylogenetic Study. *Genome Biology and Evolution*, 6(7):1739–1747, July 2014.

[387] Frédéric Boyer, Gwennaële Fichant, Jérémie Berthod, Yves Vandenbrouck, and Ina Attree. Dissecting the bacterial type VI secretion system by a genome wide in silico analysis: what can be learned from available microbial genomic resources? *BMC Genomics*, 10:104, 2009.

[388] Nicole Kapitein, Gabriele Bönemann, Aleksandra Pietrosiuk, Fabian Seyffer, Ingrid Hausser, Jacomine Krijnse Locker, and Axel Mogk. ClpV recycles VipA/VipB tubules and prevents non-productive tubule formation to ensure efficient type VI protein secretion. *Molecular Microbiology*, 87(5):1013–1028, March 2013.

[389] Kerri-Lynn Sheahan, Christina L. Cordero, and Karla J. Fullner Satchell. Identification of a domain within the multifunctional Vibrio cholerae RTX toxin that covalently cross-links actin. *Proceedings of the National Academy of Sciences of the United States of America*, 101(26):9798–9803, June 2004.

[390] Daniel Unterweger, Benjamin Kostiuk, Rina Ötjengerdes, Ashley Wilton, Laura Diaz-Satizabal, and Stefan Pukatzki. Chimeric adaptor proteins translocate di-

verse type VI secretion system effectors in Vibrio cholerae. *The EMBO Journal*, 34(16):2198–2210, August 2015.

[391] Sebastian Kube and Petra Wendler. Structural comparison of contractile nanomachines. *biophysics 2015, Vol. 2, Pages 88-115*, May 2015.

[392] Mark R. H. Hurst, Travis R. Glare, and Trevor A. Jackson. Cloning Serratia entomophila Antifeeding Genes—a Putative Defective Prophage Active against the Grass Grub Costelytra zealandica. *Journal of Bacteriology*, 186(15):5116–5128, August 2004.

[393] Thomas B. Higerd, Charles A. Baechler, and Richard S. Berk. In Vitro and In Vivo Characterization of Pyocin. *Journal of Bacteriology*, 93(6):1976–1986, June 1967.

[394] M. Kageyama. STUDIES OF A PYOCIN. I. PHYSICAL AND CHEMICAL PROPERTIES. *Journal of Biochemistry*, 55:49–53, January 1964.

[395] Keisuke Nakayama, Kayoko Takashima, Hiroshi Ishihara, Tomoyuki Shinomiya, Makoto Kageyama, Shigehiko Kanaya, Makoto Ohnishi, Takahiro Murata, Hirotada Mori, and Tetsuya Hayashi. The R-type pyocin of Pseudomonas aeruginosa is related to P2 phage, and the F-type is related to lambda phage. *Molecular Microbiology*, 38(2):213–231, October 2000.

[396] G. Yang, A. J. Dowling, U. Gerike, R. H. ffrench Constant, and N. R. Waterfield. Photorhabdus Virulence Cassettes Confer Injectable Insecticidal Activity against the Wax Moth. *Journal of Bacteriology*, 188(6):2254–2261, March 2006.

[397] Kazufumi Kuroda and Makoto Kageyama. Biochemical Properties of a New Flexuous Bacteriocin, Pyocin F1, Produced by *Pseudomonas aeruginosa*. *The Journal of Biochemistry*, 85(1):7–19, 1979.

[398] Yvon Michel-Briand and Christine Baysse. The pyocins of Pseudomonas aeruginosa. *Biochimie*, 84(5–6):499–510, May 2002.

[399] Younghoon Seo and D. R. Galloway. Purification of the pyocin S2 complex from Pseudomonas aeruginosa PAO1: Analysis of DNase activity. *Biochemical and Biophysical Research Communications*, 172(2):455–461, October 1990.

[400] Catherine Duport, Christine Baysse, and Yvon Michel-Briand. Molecular Characterization of Pyocin S3, a Novel S-type Pyocin from Pseudomonas aeruginosa. *Journal of Biological Chemistry*, 270(15):8920–8927, April 1995.

[401] Heleen L. Coetzee, H. C. de Klerk, J. N. Coetzee, and J. A. Smit. Bacteriophage-tail-like Particles Associated with Intra-species Killing of Proteus vulgaris. *Journal of General Virology*, 2(1):29–36, 1968.

[402] Eckhard Strauch, Heike Kaspar, Christoph Schaudinn, Petra Dersch, Kazimierz Madela, Christina Gewinner, Stefan Hertwig, Jörg Wecke, and Bernd Appel. Characterization of Enterocoliticin, a Phage Tail-Like Bacteriocin, and Its Effect on Pathogenic Yersinia enterocolitica Strains. *Applied and Environmental Microbiology*, 67(12):5634–5642, December 2001.

[403] Sonia Fischer, Agustina Godino, José Miguel Quesada, Paula Cordero, Edgardo Jofré, Gladys Mori, and Manuel Espinosa-Urgel. Characterization of a phage-like pyocin from the plant growth-promoting rhizobacterium Pseudomonas fluorescens SF4c. *Microbiology*, 158(6):1493–1503, 2012.

[404] Jon Penterman, Pradeep K. Singh, and Graham C. Walker. Biological Cost of Pyocin Production during the SOS Response in Pseudomonas aeruginosa. *Journal of Bacteriology*, 196(18):3351–3359, September 2014.

[405] H. Matsui, Y. Sano, H. Ishihara, and T. Shinomiya. Regulation of pyocin genes in Pseudomonas aeruginosa by positive (prtN) and negative (prtR) regulatory genes. *Journal of Bacteriology*, 175(5):1257–1263, March 1993.

[406] Steven R. Williams, Dana Gebhart, David W. Martin, and Dean Scholl. Retargeting R-Type Pyocins To Generate Novel Bactericidal Protein Complexes. *Applied and Environmental Microbiology*, 74(12):3868–3876, June 2008.

[407] Thilo Köhler, Viviane Donner, and Christian van Delden. Lipopolysaccharide as Shield and Receptor for R-Pyocin-Mediated Killing in Pseudomonas aeruginosa. *Journal of Bacteriology*, 192(7):1921–1928, April 2010.

[408] Y. Uratani and T. Hoshino. Pyocin R1 inhibits active transport in Pseudomonas aeruginosa and depolarizes membrane potential. *Journal of Bacteriology*, 157(2):632–636, February 1984.

[409] Jennifer M. Ritchie, Jennifer L. Greenwich, Brigid M. Davis, Roderick T. Bronson, Dana Gebhart, Steven R. Williams, David Martin, Dean Scholl, and Matthew K. Waldor. An Escherichia coli O157-Specific Engineered Pyocin Prevents and Ameliorates Infection by E. coli O157:H7 in an Animal Model of Diarrheal Disease. *Antimicrobial Agents and Chemotherapy*, 55(12):5469–5474, December 2011.

[410] Dean Scholl, Mike Cooley, Steve R. Williams, Dana Gebhart, David Martin, Anna Bates, and Robert Mandrell. An Engineered R-Type Pyocin Is a Highly Specific and Sensitive Bactericidal Agent for the Food-Borne Pathogen Escherichia coli O157:H7. *Antimicrobial Agents and Chemotherapy*, 53(7):3074–3080, July 2009.

[411] Andrew MQ King, Elliot Lefkowitz, Michael J. Adams, and Eric B. Carstens, editors. *Virus Taxonomy: Ninth Report of the International Committee on Taxonomy of Viruses*. Elsevier, London ; Waltham, MA, 1 edition edition, November 2011.

[412] Anastasia A. Aksyuk, Lidia P. Kurochkina, Andrei Fokine, Farhad Forouhar, Vadim V. Mesyanzhinov, Liang Tong, and Michael G. Rossmann. Structural Conservation of the Myoviridae Phage Tail Sheath Protein Fold. *Structure*, 19(12):1885–1894, December 2011.

[413] Eric S. Miller, Elizabeth Kutter, Gisela Mosig, Fumio Arisaka, Takashi Kunisawa, and Wolfgang Rüger. Bacteriophage T4 Genome. *Microbiology and Molecular Biology Reviews*, 67(1):86–156, March 2003.

[414] Lee D. Simon. Infection of Escherichia coli by T2 and T4 Bacteriophages as Seen in the Electron Microscope: T4 Head Morphogenesis. *Proceedings of the National Academy of Sciences*, 69(4):907–911, April 1972.

[415] Victor A. Kostyuchenko, Petr G. Leiman, Paul R. Chipman, Shuji Kanamaru, Mark J. van Raaij, Fumio Arisaka, Vadim V. Mesyanzhinov, and Michael G. Rossmann. Three-dimensional structure of bacteriophage T4 baseplate. *Nature Structural & Molecular Biology*, 10(9):688–693, September 2003.

[416] N. R. Watts and D. H. Coombs. Structure of the bacteriophage T4 baseplate as determined by chemical cross-linking. *Journal of Virology*, 64(1):143–154, January 1990.

[417] Andrei Fokine, Zhihong Zhang, Shuji Kanamaru, Valorie D. Bowman, Anastasia A. Aksyuk, Fumio Arisaka, Venigalla B. Rao, and Michael G. Rossmann. The Molecular Architecture of the Bacteriophage T4 Neck. *Journal of Molecular Biology*, 425(10):1731–1744, May 2013.

[418] Anastasia A Aksyuk, Petr G Leiman, Lidia P Kurochkina, Mikhail M Shneider, Victor A Kostyuchenko, Vadim V Mesyanzhinov, and Michael G Rossmann. The tail sheath structure of bacteriophage T4: a molecular machine for infecting bacteria. *The EMBO Journal*, 28(7):821–829, April 2009.

[419] Victor A. Kostyuchenko, Paul R. Chipman, Petr G. Leiman, Fumio Arisaka, Vadim V. Mesyanzhinov, and Michael G. Rossmann. The tail structure of bacteriophage T4 and its mechanism of contraction. *Nature Structural & Molecular Biology*, 12(9):810–813, September 2005.

[420] David H. Coombs and Frederick A. Eiserling. Studies on the structure, protein composition and assembly of the neck of bacteriophage T4. *Journal of Molecular Biology*, 116(3):375–405, November 1977.

[421] Tahmina Akhter, Li Zhao, Atsushi Kohda, Kazuhiro Mio, Shuji Kanamaru, and Fumio Arisaka. The neck of bacteriophage T4 is a ring-like structure formed by a hetero-oligomer of gp13 and gp14. *Biochimica et Biophysica Acta (BBA) - Proteins and Proteomics*, 1774(8):1036–1043, August 2007.

[422] L. W. Black and D. T. Brown. Head morphologies in bacteriophage T4 head and internal protein mutant infections. *Journal of Virology*, 17(3):894–905, March 1976.

[423] Andrei Fokine, Paul R. Chipman, Petr G. Leiman, Vadim V. Mesyanzhinov, Venigalla B. Rao, and Michael G. Rossmann. Molecular architecture of the prolate head of bacteriophage T4. *Proceedings of the National Academy of Sciences of the United States of America*, 101(16):6003–6008, April 2004.

[424] Michael S. Mitchell and Venigalla B. Rao. Functional Analysis of the Bacteriophage T4 DNA-packaging ATPase Motor. *Journal of Biological Chemistry*, 281(1):518–527, January 2006.

[425] Gerald Leffers and Venigalla B. Rao. Biochemical Characterization of an ATPase Activity Associated with the Large Packaging Subunit gp17 from Bacteriophage T4. *Journal of Biological Chemistry*, 275(47):37127–37136, November 2000.

[426] Yuriy Chaban, Rudi Lurz, Sandrine Brasilès, Charlène Cornilleau, Matthia Karreman, Sophie Zinn-Justin, Paulo Tavares, and Elena V. Orlova. Structural rearrangements in the phage head-to-tail interface during assembly and infection. *Proceedings of the National Academy of Sciences*, 112(22):7009–7014, June 2015.

[427] Ayaka Washizaki, Tetsuro Yonesaki, and Yuichi Otsuka. Characterization of the interactions between Escherichia coli receptors, LPS and OmpC, and bacteriophage T4 long tail fibers. *MicrobiologyOpen*, 5(6):1003–1015, December 2016.

[428] Sergio G. Bartual, José M. Otero, Carmela Garcia-Doval, Antonio L. Llamas-Saiz, Richard Kahn, Gavin C. Fox, and Mark J. van Raaij. Structure of the bacteriophage

T4 long tail fiber receptor-binding tip. *Proceedings of the National Academy of Sciences*, 107(47):20287–20292, November 2010.

[429] F Yu and S Mizushima. Roles of lipopolysaccharide and outer membrane protein OmpC of Escherichia coli K-12 in the receptor function for bacteriophage T4. *Journal of Bacteriology*, 151(2):718–722, August 1982.

[430] Moh Lan Yap, Thomas Klose, Fumio Arisaka, Jeffrey A. Speir, David Veesler, Andrei Fokine, and Michael G. Rossmann. Role of bacteriophage T4 baseplate in regulating assembly and infection. *Proceedings of the National Academy of Sciences*, 113(10):2654–2659, March 2016.

[431] Shuji Kanamaru, Petr G. Leiman, Victor A. Kostyuchenko, Paul R. Chipman, Vadim V. Mesyanzhinov, Fumio Arisaka, and Michael G. Rossmann. Structure of the cell-puncturing device of bacteriophage T4. *Nature*, 415(6871):553–557, January 2002.

[432] Lance K. Ishimoto, Karyn S. Ishimoto, Antonio Cascino, Marilena Cipollaro, and Frederick A. Eiserling. The structure of three bacteriophage T4 genes required for tail-tube assembly. *Virology*, 164(1):81–90, May 1988.

[433] Fumio Arisaka, Jürg Tschopp, Roel van Driel, and Jürgen Engel. Reassembly of the bacteriophage T4 tail from the core-baseplate and the monomeric sheath protein P18: A co-operative association process. *Journal of Molecular Biology*, 132(3):369–386, August 1979.

[434] Petr G. Leiman, Paul R. Chipman, Victor A. Kostyuchenko, Vadim V. Mesyanzhinov, and Michael G. Rossmann. Three-Dimensional Rearrangement of Proteins in the Tail of Bacteriophage T4 on Infection of Its Host. *Cell*, 118(4):419–429, August 2004.

[435] Robert L. Duda, Mari Gingery, and Frederick A. Eiserling. Potential length determiner and dna injection protein is extruded from bacteriophage T4 tail tubes in vitro. *Virology*, 151(2):296–314, June 1986.

[436] Natalia K. Abuladze, Mari Gingery, Jerry Tsai, and Frederick A. Eiserling. Tail Length Determination in Bacteriophage T4. *Virology*, 199(2):301–310, March 1994.

[437] Venigalla B. Rao and Lindsay W. Black. Structure and assembly of bacteriophage T4 head. *Virology Journal*, 7:356, 2010.

[438] Werner Baschong, Ueli Aebi, Cristina Baschong-Prescianotto, Jaques Dubochet, Lukas Landmann, Eduard Kellenberger, and Michel Wurtz. Head structure of bacteriophages T2 and T4. *Journal of Ultrastructure and Molecular Structure Research*, 99(3):189–202, June 1988.

[439] Anastasia A. Aksyuk and Michael G. Rossmann. Bacteriophage Assembly. *Viruses*, 3(3):172–203, February 2011.

[440] M. F. Moody. Sheath of bacteriophage T4. *Journal of Molecular Biology*, 80(4):613–635, November 1973.

[441] Boris F. Poglazov, Andrei V. Efimov, Sergio Marco, Jose Carrascosa, Tanya A. Kuznetsova, Larisa G. Aijrich, Lidia P. Kurochkina, and Vadim V. Mesyanzhinov. Polymerization of Bacteriophage T4 Tail Sheath Protein Mutants Truncated at the C-Termini. *Journal of Structural Biology*, 127(3):224–230, October 1999.

[442] Amirali Sattarzadeh, Reza Saberianfar, Warren R. Zipfel, Rima Menassa, and Maureen R. Hanson. Green to red photoconversion of GFP for protein tracking in vivo. *Scientific Reports*, 5:11771, July 2015.

[443] Dana Gebhart, Stephen Lok, Simon Clare, Myreen Tomas, Mark Stares, Dean Scholl, Curtis J. Donskey, Trevor D. Lawley, and Gregory R. Govoni. A Modified R-Type Bacteriocin Specifically Targeting Clostridium difficile Prevents Colonization of Mice without Affecting Gut Microbiota Diversity. *mBio*, 6(2):e02368–14, May 2015.

[444] Xiaoqiu Liu, Huifeng Jiang, Zhenglong Gu, and Jeffrey W. Roberts. High-resolution view of bacteriophage lambda gene expression by ribosome profiling. *Proceedings of the National Academy of Sciences*, 110(29):11928–11933, July 2013.

[445] Morgan Beeby, Deborah A. Ribardo, Caitlin A. Brennan, Edward G. Ruby, Grant J. Jensen, and David R. Hendrixson. Diverse high-torque bacterial flagellar motors assemble wider stator rings using a conserved protein scaffold. *Proceedings of the National Academy of Sciences*, 113(13):E1917–E1926, March 2016.

[446] Patrizia Abrusci, Marta Vergara-Irigaray, Steven Johnson, Morgan D. Beeby, David R. Hendrixson, Pietro Roversi, Miriam E. Friede, Janet E. Deane, Grant J. Jensen, Christoph M. Tang, and Susan M. Lea. Architecture of the major component of the type III secretion system export apparatus. *Nature Structural & Molecular Biology*, 20(1):99–104, January 2013.

[447] Xiaowei Zhao, Steven J. Norris, and Jun Liu. Molecular Architecture of the Bacterial Flagellar Motor in Cells. *Biochemistry*, 53(27):4323–4333, July 2014.

[448] Yi-Wei Chang, Lee A. Rettberg, Davi R. Ortega, and Grant J. Jensen. In vivo structures of an intact type VI secretion system revealed by electron cryotomography. *EMBO reports*, page e201744072, May 2017.

[449] Madeline M. Farley, Bo Hu, William Margolin, and Jun Liu. Minicells, Back in Fashion. *Journal of Bacteriology*, 198(8):1186–1195, April 2016.

[450] Mikhail Kudryashev, Marco Stenta, Stefan Schmelz, Marlise Amstutz, Ulrich Wiesand, Daniel Castaño-Díez, Matteo T. Degiacomi, Stefan Münnich, Christopher KE Bleck, Julia Kowal, Andreas Diepold, Dirk W. Heinz, Matteo Dal Peraro, Guy R. Cornelis, and Henning Stahlberg. In situ structural analysis of the Yersinia enterocolitica injectisome. *eLife*, 2:e00792, July 2013.

[451] Bo Hu, William Margolin, Ian J. Molineux, and Jun Liu. The Bacteriophage T7 Virion Undergoes Extensive Structural Remodeling During Infection. *Science*, 339(6119):576–579, February 2013.

[452] Jun Liu, Bo Hu, Dustin R. Morado, Sneha Jani, Michael D. Manson, and William Margolin. Molecular architecture of chemoreceptor arrays revealed by cryoelectron tomography of Escherichia coli minicells. *Proceedings of the National Academy of Sciences*, 109(23):E1481–E1488, June 2012.

[453] Jun Liu, Cheng-Yen Chen, Daisuke Shiomi, Hironori Niki, and William Margolin. Visualization of bacteriophage P1 infection by cryo-electron tomography of tiny Escherichia coli. *Virology*, 417(2):304–311, September 2011.

[454] Qin Sun and William Margolin. Influence of the Nucleoid on Placement of FtsZ and MinE Rings in Escherichia coli. *Journal of Bacteriology*, 183(4):1413–1422, February 2001.

[455] Sebatian Ursich. Cryo-electron tomography structure of type vi secretion system. Master's thesis, Universität Basel, 2016.

[456] Tobias Dörr, Laura Alvarez, Fernanda Delgado, Brigid M. Davis, Felipe Cava, and Matthew K. Waldor. A cell wall damage response mediated by a sensor kinase/response regulator pair enables beta-lactam tolerance. *Proceedings of the National Academy of Sciences*, 113(2):404–409, January 2016.

[457] Peter L. Ferguson and David H. Coombs. Pulse-chase analysis of the in Vivo assembly of the bacteriophage T4 tail1. *Journal of Molecular Biology*, 297(1):99–117, March 2000.

[458] Jonathan King. Assembly of the tail of bacteriophage T4. *Journal of Molecular Biology*, 32(2):231–262, March 1968.

[459] A. Vianelli, G. R. Wang, M. Gingery, R. L. Duda, F. A. Eiserling, and E. B. Goldberg. Bacteriophage T4 Self-Assembly: Localization of gp3 and Its Role in Determining Tail Length. *Journal of Bacteriology*, 182(3):680–688, February 2000.

[460] Catherine K. Smith, Tania A. Baker, and Robert T. Sauer. Lon and Clp family proteases and chaperones share homologous substrate-recognition domains. *Proceedings of the National Academy of Sciences of the United States of America*, 96(12):6678–6682, June 1999.

[461] Joel R. Hoskins, Katsuhiko Yanagihara, Kiyoshi Mizuuchi, and Sue Wickner. ClpAP and ClpXP degrade proteins with tags located in the interior of the primary sequence. *Proceedings of the National Academy of Sciences*, 99(17):11037–11042, August 2002.

[462] Cheolju Lee, Michael P Schwartz, Sumit Prakash, Masahiro Iwakura, and Andreas Matouschek. ATP-Dependent Proteases Degrade Their Substrates by Processively Unraveling Them from the Degradation Signal. *Molecular Cell*, 7(3):627–637, March 2001.

[463] Brian G. Reid, Wayne A. Fenton, Arthur L. Horwich, and Eilika U. Weber-Ban. ClpA mediates directional translocation of substrate proteins into the ClpP protease. *Proceedings of the National Academy of Sciences*, 98(7):3768–3772, March 2001.

[464] Nadine S. Lossi, Eleni Manoli, Pete Simpson, Cerith Jones, Kailyn Hui, Rana Dajani, Sarah J. Coulthurst, Paul Freemont, and Alain Filloux. The archetype Pseudomonas aeruginosa proteins TssB and TagJ form a novel subcomplex in the bacterial type VI secretion system. *Molecular Microbiology*, 86(2):437–456, October 2012.

[465] A. L. Hodgkin and A. F. Huxley. A quantitative description of membrane current and its application to conduction and excitation in nerve. *The Journal of Physiology*, 117(4):500–544, August 1952.

[466] Mark W. Barnett and Philip M. Larkman. The action potential. *Practical Neurology*, 7(3):192–197, June 2007.

[467] Qin Sun and William Margolin. FtsZ Dynamics during the Division Cycle of Live Escherichia coli Cells. *Journal of Bacteriology*, 180(8):2050–2056, April 1998.

[468] Marcos Malumbres. Cyclin-dependent kinases. *Genome Biology*, 15:122, 2014.

Abbreviations

ABC-	ATP-binding cassette
Afp	antifeeding prophage
CDI	Contact Dependent Inhibition
CFTR	cystic fibrosis transmembrane conductance regulator
cryo-EM	cryo-electron microscopy
cryo-ET	cryo-electron tomography
CT	Cholera Toxin
EM	electron microscopy
GSP	General Secretion Pathway
HlyA	Hemolysin A
hoc	highly antigenic outer capsid
IMC	inner membrane complex
LPS	lipopolysaccharide
MAC	metamorphosis-associated contractile
MERV	multiple effector translocation VgrG
MFP	Membrane Fusion Protein
OMC	outer membrane complex
PLTS	phage tail-like protein translocation system
PMF	proton motive force

PorSS	Porphyromonas secretion system
POTRA	polypeptide transport-associated
PTX	pertussis toxin
PVC	Photorabdus virulence cassette
RTX	repeats-in-toxin
SAXS	small angle X-ray scattering
SCV	Salmonella-Containing Vacuole
Sec-	Secretion-
SLTs	Shiga-like toxins
soc	small outer capsid
SPI	Salmonella Pathogenicity Island
SRP	signal recognition particle
Stx	Shiga toxin
T4CP	Type 4 Coupling Protein
T6SS	Type 6 Secretion System
Tap	T6SS adaptor protein
Tat-	Twin Arginine Translocation
TCP	Toxin coregulated pilus
TEC	T6SS effector chaperones
TISS	Type I Secretion System
TMD	Transmembrane Domain
TPS	Two-partner Secretion
UPEC	uropathogenic E. coli
VPI	Vibrio pathogenicity island

List of Figures

Acknowledgments

I would like to thank...

- ... Prof. Dr. Marek Basler for giving me the opportunity to work on this fascinating project and for an excellent introduction to microbiology. I also thank him for constant support and frequent discussions about, but not only my project(s). Especially in the beginning of my PhD I learnt a lot from him.
- ... Prof. Dr. Henning Stahlberg and Prof. Dr. Timm Maier for serving as my PhD advisory committee and supporting me throughout the years with scientific and career advice. Furthermore for fruitful discussions about my project and sharing a passion for structural biology.
- ... Prof. Dr. Markus Seeger for serving as a co-referee.
- ... Dr. Misha Kudryashev, Dr. Jing Wang and Dr. Sergey Nazarov for working on different exciting projects with me.
- ... Clara Greiner for support with lab work and insights in supervision.
- ... my co-workers Clara Greiner, Maj Brodmann, Anna Hagmann, Peter Ringel, Andrea Vettiger, Dr. Lin Lin, Dr. Sergey Nazarov, Dr. Johannes Schneider and Dr. Jing Wang for a nice every-day lab life.
- ... Dr. Mihai Ionescu for scientific advice and running the laboratory smoothly.
- ... Michaela Hanisch for taking care of all administrative issues and frequent updates on the swiss runnning community.
- ... Marina Kuhn and Patric Hänni for taking care of all equipment on the floor that one can really focus on science.
- ... the media and cleaning kitchen staff for excellent services.

- ... Dr. Christoph Schmutz, Maj Brodmann, Anna Hagmann and Andrea Vettiger for input and comments on parts of this thesis.
- ... all friends from the Biozentrum, outside the Biozentrum, from the Stuttgart area and from Munich to retreat from science and a different perspective.
- ... my family for constant support and interest in the abstract world of secretion systems.

Chapter IV

Appendix

IV.1 Review Article I

Using Force to Punch Holes: Mechanics of Contractile Nanomachines

Maximilian Brackmann, Sergey Nazarov, Jing Wang and Marek Basler

Trends in Cell Biology, Volume 27, Issue 9, September 2017, pages 623-632, DOI: 10.1016/j.tcb.2017.05.003.

Statement of contribution

I drafted the section about TssA, prepared Figure 1 and contributed to the preparation of other figures and sections.

Trends in Cell Biology

CellPress
REVIEWS

Review

Using Force to Punch Holes: Mechanics of Contractile Nanomachines

Maximilian Brackmann,[1,2] Sergey Nazarov,[1,2] Jing Wang,[1,2] and Marek Basler[1,*]

Using physical force to translocate macromolecules across a membrane has the advantage of being a universal solution independent of the properties of the target membrane. However, physically punching a stiff membrane is not a trivial task and three things are necessary for success: a sharp tip, a source of energy, and the ability to strongly bind to the target. In this review we describe the basic mechanism of membrane puncturing by contractile nanomachines with a focus on the T4 phage, R-type pyocin, and the bacterial Type VI secretion system (T6SS) based on recent studies of the structures and dynamics of their assembly.

Trends

Many bacterial nanomachines share a common ancestry and mode of action with contractile-tailed phages.

Recent advances in cryoelectron microscopy have allowed unprecedented insight into the structures of R-type pyocin and the T4 baseplate in both the pre- and post-contraction state.

Studies on the structures and dynamics of several components of the Type VI secretion system (T6SS) provide a detailed picture of T6SS's mode of action and assembly.

These recent studies unravel a unique mechanism for the penetration of cellular membranes.

Punching Holes into Membranes

With the evolution of membranes as partitions of cells and their compartments, a new challenge emerged: how can hydrophilic molecules be efficiently translocated across a barrier? Various mechanisms have evolved, including contractile nanomachines, which are effective and powerful systems for physically piercing membranes and allowing the translocation of macromolecules such as DNA or proteins. All contractile nanomachines comprise three major parts: a baseplate, a long tube with a sharp tip, and a contractile helical sheath that wraps around the tube and attaches to the baseplate. The process of membrane penetration is initiated by rearrangement of the baseplate components with two consequences: initiation of sheath contraction and opening of the middle of the baseplate to allow passage of the tip and tube. As the sheath irreversibly transitions to its contracted state, it releases the tube by widening its inner diameter, while at the same time shortening its length and rotating around its helical axis as it increases its overall twist. Since the sheath is firmly attached to both the baseplate and the distal end of the inner tube, its contraction results in a rotation and a translation of the inner tube through the baseplate and thus piercing of the attached target membrane (see the scheme in Figure 1).

The most abundant contractile nanomachines are phages with contractile tails that punch holes into bacterial membranes to deliver DNA into host cells [1,2]. R-type pyocins of *Pseudomonas aeruginosa* and related diffocins of *Clostridium difficile* punch a hole into the bacterial envelope to efficiently kill target cells [3–6]. Structurally related particles are also used to deliver proteins into eukaryotic cells: *Photorhabdus* virulence cassettes [7], antifeeding prophages [8], and metamorphosis-associated contractile structures of *Pseudoalteromonas luteoviolacea* [9]. All of these systems are assembled inside bacterial cells and are released to the environment after cell lysis. An interesting adaptation of these contractile tails is the T6SS [10,11]. Bacteria use the T6SS to puncture both bacterial and eukaryotic membranes and to deliver large effectors across membranes to fight their competition [12–14]. In this review we cover recent advances in cryoelectron microscopy (cryo-EM) and studies of the dynamics of T6SS assembly, which have provided unprecedented insights into the mode of action of these sophisticated nanomachines.

[1]Focal Area Infection Biology, Biozentrum, University of Basel, Basel, Switzerland
[2]These authors contributed equally.

*Correspondence: marek.basler@unibas.ch (M. Basler).

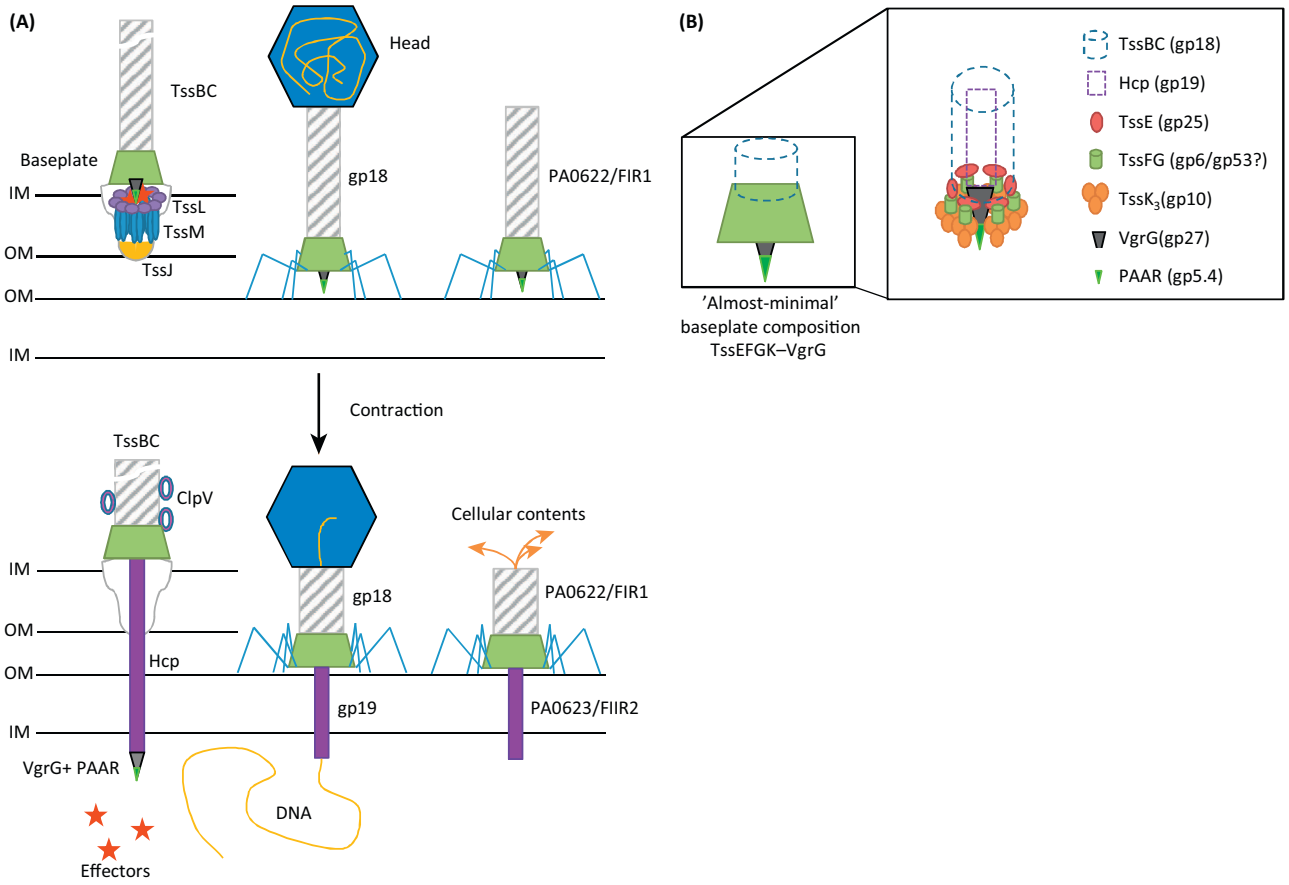

Figure 1. Scheme of Contractile Nanomachines. (A) The Type VI secretion system (T6SS) delivers effectors from the bacterial cytosol to the cytosol of a target cell. Phage T4 delivers its DNA into the target cell and R-type pyocins generate holes in the cell envelope, comprising an inner membrane (IM) and outer membrane (OM), of closely related species. (B) Close-up view of the baseplate of T6SS. TssK presumably attaches the baseplate to the membrane complex. TssF and TssG form a wedge and a core bundle of the baseplate and TssE is a sheath initiator. The VgrG and PAAR proteins form the spike and spike tip complex and Hcp forms the tube. ClpV (or TssH) disassembles the contracted T6SS sheath. Respective phage gene products (gp) are in parentheses.

Baseplate

The complexity of contractile nanomachines is commonly located in the baseplate [15,16]. The baseplate serves as a nucleation site for polymerization of the tube and sheath and a change in structure of the baseplate triggers sheath contraction [1,15,17]. Most of our knowledge of baseplate-like structures comes from extensive studies of bacteriophage T4, a model system for all contractile-sheath-like complexes despite enormous structural complexity. Recently, atomic-resolution maps of the T4 baseplate in both pre- and post-attachment states have been derived from high-resolution cryo-EM maps [17]. T4 baseplate is a ~6.5-MDa complex comprising multiple copies of at least 15 different proteins organized into a central spike complex that is surrounded by inner, intermediate, and peripheral sections of the baseplate. Importantly, the components of the inner baseplate are conserved in tailed phages and other contractile injection systems (Table 1) [1,17].

The T4 inner baseplate comprises a ring of 12 copies of core bundle gp6, six copies of sheath assembly initiator gp25, six copies of core bundle clamp gp53, and six copies of core bundle gp7, which is also part of the intermediate baseplate and a link to the peripheral tail fiber network [17]. The T4 central spike, comprising the monomeric gp5.4 spike tip, trimeric gp5

Table 1. Protein Composition of Various Contractile Nanomachines

	Location/function	Copies/Bp	Phage P2	Phage T4 [17]	T6SS	R-type pyocin
Central hub complex	Spike tip	1	gpV	gp5.4	PAAR repeat	PA0616
	Spike	3		gp5	VgrG	PA0616
	Baseplate hub	3	gpD	gp27	VgrG	PA0628
Wedge	Core bundle clamp, sheath platform	6	gpI	gp53	Part of TssF/TssG	PA0627
	Sheath assembly initiator	6	gpW	gp25	TssE	PA0617
	Core bundle, sheath platform	12	gpJ	gp6	TssF	PA0618
	Core bundle, link to periphery	6	gpI	gp7	TssG	PA0619

spike, and trimeric gp27 hub, is located at the front end of the tube and pierces the host cell membrane during infection [17,18]. The central spike complex is also crucial for assembly of the high-energy, dome-shaped baseplate, which is a precursor for tube and extended sheath polymerization [1,15,19]. All T4 inner baseplate components except gp53 are found in contractile injection systems [17].

Many critical T6SS components share remarkable structural and functional homology with proteins of the membrane-piercing contractile tails of bacteriophages (Table 1). The first such homology was identified for the VgrG proteins, which are secreted by the T6SS and in some cases carry C-terminal extension domains, which have been shown to be effectors [11,20]. VgrG proteins form a trimer at the tip of the Hcp tube and are structurally homologous to the T4 spike complex [21]. A PAAR-repeat protein, stabilized by a zinc ion, caps the VgrG trimer and forms the tip, which pierces the target cell envelope [18]. The PAAR proteins are structural homologs of T4 phage gp5.4 protein [17,18]. Interestingly, both PAAR and VgrG proteins may bind effectors or carry effector domains into target cells, which is conceptually similar to the lysozyme domain on the gp5 spike protein that is required for T4 phage host infection [21,22,69].

One of the most conserved components of all contractile phages is also conserved in T6SS. TssE is an homolog of T4 baseplate component gp25 [21,23] and, together with TssF, TssG, and TssK, forms the T6SS baseplate [24]. The $(TssF)_2$–TssG module may be similar to the T4 $(gp6)_2$–gp7-like heterotrimer [17]. Therefore, these T6SS proteins could constitute a conserved assembly intermediate that forms the core bundle, the trifurcation unit, and the sheath polymerization platform (Table 1).

T6SS Membrane Complex

In T4 phage, the short tail fibers are assembled from trimeric gp12, attached to trimeric gp10, and connect the baseplate to the host cell surface by irreversibly binding to LPS [25], which is important for efficient infection of target cells [17,19]. By contrast, the T6SS baseplate is anchored to the cell envelope from the cytosolic side by associating with a membrane complex comprising TssJ, TssL, and TssM [26] (Figure 1). The details are unclear; however, the trimeric TssK interacts with both the membrane-anchoring TssJLM complex and baseplate components [27,28] and has been proposed to initiate T6SS wedge assembly, similar to the gp10 trimer in T4 [17,19]. TssK is first recruited to TssL and together with TssG, which binds to TssM, serves as the major connector between the baseplate and the membrane complex [24,27,28]. These interactions have to be as firm as the corresponding connections in phage T4–maybe even stronger to account for the greater length of the T6SS sheath. Interestingly, there is a symmetry mismatch between the fivefold-symmetric membrane complex and the presumably

sixfold-symmetric baseplate [26]. It will be important to address how these two large complexes connect to provide the strong attachment needed for successful piercing of target membranes. An important step forward is the recent visualization of the intact T6SS in *Myxococcus xanthus* by electron cryotomography [69].

Sheath–Tube Assembly

In all contractile tails, both tubes and sheaths are likely to be built via similar assembly pathways. Despite the low sequence similarity among tube proteins, their structures are almost identical among contractile tails (Figure 2) [3,10,21,29]. Tube proteins fold as β-sheet rolls flanked by a short α-helix and an extended loop. The monomers form hexameric rings that then stack head to tail with a twist to form a helical tube. The main difference among the structures of tube proteins is in the length of the loops connecting the β-strands of subunits, which may be involved in ring stacking or, in the case of T6SS, effector binding. The secretion of small effectors such as EvpP in *Edwardsiella tarda* [30] and Tse1-4 in *P. aeruginosa* [31,32] requires direct interaction with the inner surface of Hcp hexamers.

In phages, the tube protein polymer serves as a template for guiding the assembly of the extended sheath [33,34]. The atomic model of extended R-type pyocin showed that a positively charged α-helix of the sheath (named the 'attachment helix') and a negatively charged patch on the tube surface are likely to drive sheath–tube assembly [3]. The tube and the sheath have identical helical symmetry in both T4 phage and R-type pyocin and it is likely that the T6SS tube–sheath complex assembles similarly [69], although the Hcp may form tubes with no twist in a crystal lattice [10,35]. Hcp is required for the assembly of extended T6SS sheaths [35,36]; however, a polymer resembling the contracted sheath can form in the absence of other T6SS components [36–38]. Similarly, phage polysheaths self-assemble from the gp18 sheath protein when overexpressed in *Escherichia coli* [39,40].

In many contractile nanomachines, the length of the sheath–tube is constant (Table 2) and is regulated by a tape-measure protein [41–43]. Interestingly, the T6SS sheath can assemble across the full size of bacteria without an apparent mode of regulation [26,44,45]. The sheaths of various contractile nanomachines assemble as helical polymers of hexameric rings. However, the helical parameters, rise and twist, per subunit, vary among sheaths (Table 2). All contractile sheaths described at high resolution were shown to be related to each other (Figure 3A) [3,46–49]. The smallest sheath subunit is found in R-type pyocin. It comprises two domains (domain 1 and domain 2) that are highly conserved in contractile phages and the T6SS [1,47,49]. These domains form the inner layers of the sheaths. Domain 1 forms the inner most layer and starts and ends with two β-stranded linkers that interconnect the sheath subunits (Figure 3B). Each

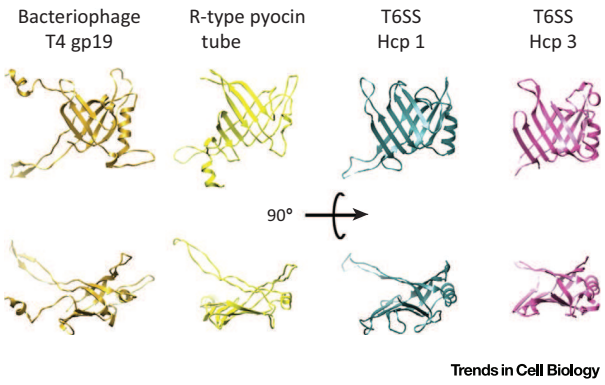

Figure 2. Tube Proteins Are Similar in All Contractile-Tail-Like Structures. The tube structures shown here are from bacteriophage T4 (PDB: 5iv5), R-type pyocin (PDB: 3j9q), and Type VI secretion system (T6SS) Hcp1 (PDB: 1Y12) and T6SS Hcp3 (PDB: 3HE3), both from *Pseudomonas aeruginosa*.

Table 2. Helix Parameters of Contractile-Tail-Like Structures

	Contractile bacteriophage				R-type pyocin		T6SS				Antifeeding prophage		MAC	
	T4 [67]		ΦKZ [68]		*Pseudomonas aeruginosa* [3]		*Vibrio cholerae* [49]		*Francisella novicida* [48]		*Serratia entomophila* [8]		*Pseudoalteromonas luteoviolacea* [9]	
Tube protein	gp19		ND		PA0623		Hcp		IglC		Afp1 or 5		MacT1, MacT2	
Sheath protein	gp18		gp29		PA0622		TssB/TssC (VipA, VipB)		IglA, IglB		Afp2–4		MacS	
Number of rings	23		44		27		V[c]		V		10		ND[d]	
State	E[a]	C[b]	E	C	E	C	E	C	E	C	E	C	E	C
Diameter (nm)	24	33	25	32	18	24	20	26	ND	ND	18	23	13	16
Rise/sub (Å)	40.6 (40.2)	16.4	36.7	17.9	38.4	16.2	ND	21.8	ND	20.8	81.4	ND	ND	ND
Twist/sub (°)	17.2 (17.9)	32.9	22	34.1	18.3	33.1	ND	29.4	ND	26.6	40.5	ND	ND	ND

[a]E, extended.
[b]C, contracted.
[c]V, variable.
[d]ND, not determined.

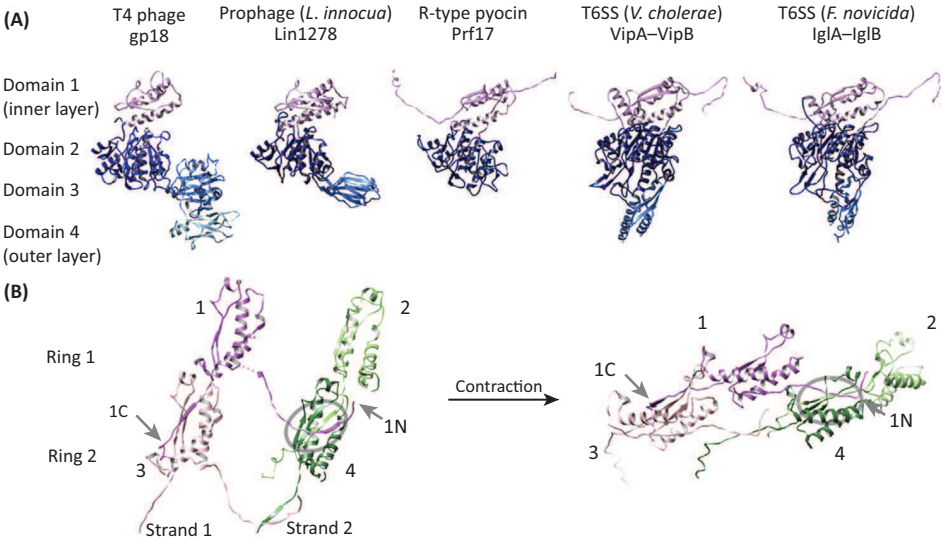

Figure 3. Sheath Proteins of Contractile-Tail-Like Structures. (A) T4 phage gp18 model (PDB: 3J2 M), Lin1278 of prophage from *Listeria innocua* (PDB: 3LML), R-type pyocin sheath (PDB: 3J9Q), Type VI secretion system (T6SS) sheath (*Vibrio cholerae*) (PDB: 3J9G), T6SS sheath (*Francisella novicida*) (PDB: 3J9O). (B) Connectivity of domain 1 (R-type pyocin). This domain starts and ends with β-stranded linkers that connect three subunits together: subunit 1 with subunit 3 on the same strand but one ring closer to the baseplate and subunit 4, which is on the neighboring strand. Together the three connected subunits form 4-stranded β-sheets of the inner domain (gray circle). After contraction, subunits on ring 1 are pulled closer to ring 2 but the connectivity is unchanged. Abbreviations: 1N, N terminus of subunit 1; 1C, C terminus of subunit 1.

subunit is connected with two neighboring subunits, which are located on the ring closer to the baseplate. The first subunit is on the same sheath strand and the second subunit is on the neighboring strand. Together the three connected subunits form the 4-stranded β-sheet of domain 1. Domain 2, which is exposed on the surface of the sheath, inserts into domain 1 [3] (Figure 3). Phage sheaths often contain additional domains inserted into domain 2 [46,47].

By contrast, T6SS sheath subunits assemble from two proteins, TssB (VipA) and TssC (VipB), which together fold into three domains. Domains 1 and 2 are highly similar to those of phage sheaths; however, the third α-helical domain inserted into domain 2 is T6SS specific [38,48,49]. In most T6SS clusters, the two sheath proteins are encoded directly after each other and domain 3 is formed from the TssB C terminus and TssC N terminus. This surface-exposed domain 3 contains the binding site for ClpV, which is a T6SS-specific AAA+ unfoldase that recycles the contracted sheath to allow the assembly of new extended sheaths [36,37,44]. A split of the ancestral sheath-encoding gene is likely to have occurred during the evolution of new functions required for the T6SS, such as unfolding by ClpV. Uncoupling the N terminus of TssC from the C terminus of TssB may help to preserve the proper folding of existing domains while accommodating the coevolution of TssC with its cognate ClpV [50,51].

Many T6SS clusters encode one protein or sometimes two that have been grouped into the family of TssA proteins [52]. Whereas TssA is essential for T6SS activity in *E. coli* [53], its deletion in *P. aeruginosa* causes only a reduction in T6SS activity [54]. Originally, all TssA proteins were grouped in the same protein family because of the presence of a common ImpA_N-domain (Pfam ID: PF06812), despite otherwise differing domain architectures [52]. Thus, it is unsurprising that TssA proteins with differing domain architectures have different functions.

E. coli TssA, which has an ImpA_N-domain and a C-terminal VasJ domain (Pfam ID: PF16989), was shown to act as a primer for sheath polymerization and to remain associated with the growing end of the sheath [53]. The location of *E. coli* TssA also suggests that it may form a cap needed to propel the inner Hcp tube during contraction [53]. Despite low sequence homology, the same study reported *E. coli* TssA to be a functional homolog of gp15 of phage T4, in which it stabilizes the sheath in an extended conformation [53,55,56]. By contrast, TssA of the H1-T6SS of *P. aeruginosa* is a baseplate component with low homology to gp6 of phage T4 [54]. Twelve copies of gp6 in two different conformations are present in the inner baseplate of T4 phage [17]. However, two other studies suggested that gp6 is a homolog of TssF in *E. coli* [17,24]. Both characterized TssA proteins were shown to be dodecamers in solution by either analytical ultracentrifugation or multiangle light scattering, and electron microscopy of the TssA protein complexes further supports these findings [53,54]. Currently, no structural information is available for the conserved ImpA_N domain and little is known about its role; however, an atomic model has been proposed for most of the N-terminal portion of *E. coli* TssA (VasJ-domain) [53]. Both *E. coli* and *P. aeruginosa* have a single *tssA* per T6SS cluster, but the *Vibrio cholerae* T6SS cluster encodes two unrelated *tssA* genes; one contains a VasJ domain similar to *E. coli* TssA. It will be interesting to see what roles these two different TssAs play in the assembly of the *V. cholerae* T6SS. It is possible that VasJ-domain-containing TssAs are involved in the priming and polymerization of the tube–sheath complex and TssAs that are similar to the TssA of *P. aeruginosa* are baseplate components that remain attached to the baseplate.

Contraction

The contraction of the T4 phage sheath was proposed to progress from the baseplate towards the phage head in a wave of contracting sheath rings [57]. This is a transition from a high-energy conformation with the sheath tightly wrapped around the inner tube to a short, low-energy state while propelling the inner tube (Figure 4). The common ancestry of the sheath proteins suggests that all sheaths undergo similar reorganization during contraction [1]. Domain 1 maintains connectivity throughout contraction and is likely to provide stability to the sheath. Contraction is

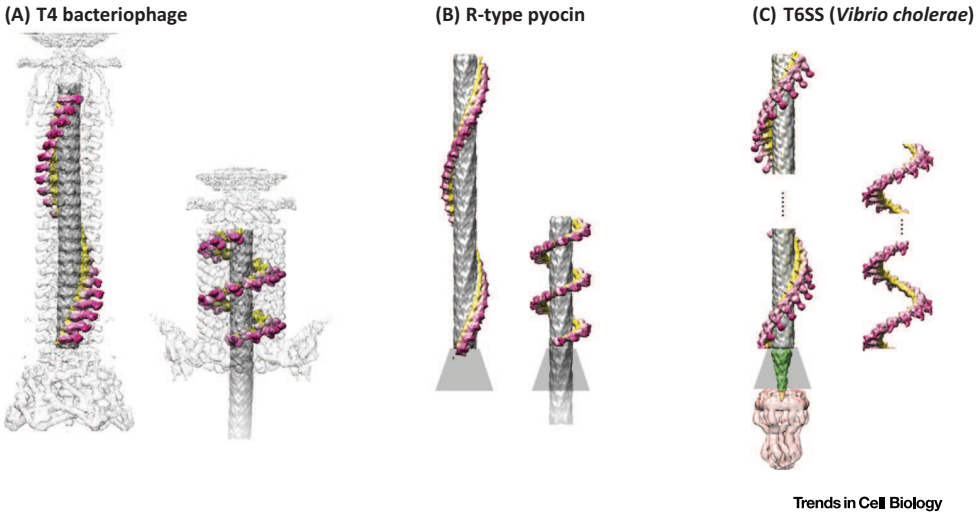

Figure 4. Comparison of the Type VI Secretion System (T6SS) with the Phage-Tail-Like Contractile System. (A) T4 phage extended state compiled with an electron microscopy map (emd_1126, emd_3374). T4 phage contracted state (emd_5528). (B) R-type pyocin pre- and post-contraction states (emd_6270, emd_6271) both associated with the baseplate (structure unknown). (C) T6SS extended-state sheath–tube complex (modeled on R-type pyocin), VgrG and PAAR complex (modeled on PDB: 4IJV and 4MTK), baseplate (unknown), and membrane complex (emd_2927). Contracted sheath (PDB: 3J9G).

driven by solvation free energy gain due to increased intersubunit binding [3,46]. It was also proposed that interactions between the inner domains of the sheath subunits could be responsible for generating the pulling force needed for ring-by-ring contraction of the R-type pyocin sheath [3]. The comparison of the extended and contracted sheath structures of R-type pyocin suggests that the contraction of a single sheath ring generates 72 kcal/mol of energy [3].

Although the helical parameters of both extended and contracted sheaths vary among known contractile-tail-like structures, rotation increases and rise decreases during contraction in all structures. This results in movement and rotation of the inner tube during contraction (Table 2). The speed of sheath contraction has so far been monitored only for T6SS by live-cell fluorescence imaging, and a single sheath has been shown to contract in less than 5 ms to about 50% of its extended length [45]. Assuming that the T6SS sheath undergoes a transition similar to that of the related sheaths, a 1-μm-long T6SS sheath may undergo ten rotations with the inner tube in less than 5 ms (120 000 RPM) and push it by about 500 nm while releasing over 15 000 kcal/mol of energy. Such an enormous amount of power is likely to be needed to push large effectors across target membranes.

Disassembly

After sheath contraction the contractile tail is in a low-energy conformation. Since most contractile nanomachines act outside cells without an additional source of energy, reassembly to a high-energy state is impossible; thus, each tail acts only once. The exception is the T6SS, which assembles inside bacterial cells. Almost all T6SS clusters encode the AAA+ protein ClpV, which is crucial for T6SS efficiency but not strictly required for T6SS function [45,58]. Importantly, ClpV recognizes the N terminus of TssC and catalyzes sheath unfolding within tens of seconds [37,44,59,60]. Since ClpV specifically recognizes only the contracted sheath [44], it has been proposed that sheath contraction exposes the TssC N terminus on the sheath surface [38,49,69]. However, the structure of the extended T6SS sheath is unknown and therefore the exact mechanism by which ClpV mediates unfolding remains to be described.

Concluding Remarks

With recent atomic models of the T4 phage baseplate and R-type pyocin tube–sheath in precontraction and post-contraction states [3,17], we are approaching a detailed mechanistic understanding of the assembly and contraction of the most-studied contractile tails. It is reasonable to expect that atomic models of related contractile nanomachines, including those puncturing eukaryotic membranes, will become available in the near future. This will help us to understand how the systems evolved to puncture various target membranes.

A similar level of detailed description of T6SS assembly is, however, challenging because the system is highly dynamic and assembles inside bacterial cells, which complicates obtaining structures with atomic resolution. Electron cryotomography has yielded low-resolution structures of the system [45,61,69] and the use of thin bacterial cells, or assembling the T6SS in minicells together with subtomogram averaging, will be necessary to significantly improve resolution [62,63]. Medium-resolution tomography structures will be further used to fit atomic models of individual isolated proteins or their complexes obtained by other methods. However, isolation of T6SS components natively assembled in an inherently unstable precontraction state might require crosslinking or mutagenesis of certain T6SS components.

The function of the T6SS inside cells provides an opportunity to monitor its assembly and mode of action by fluorescence microscopy with temporal resolution approaching the millisecond range and spatial resolution limited by live-cell-imaging technologies. Eight core T6SS components [TssA, TssB (VipA), TssF, TssH (ClpV), TssJ, TssK, TssL, and TssM] have been successfully fused to fluorescent proteins and monitored in live cells [24,26,44,45,53,59].

Outstanding Questions

What are the basic principles behind spatial and temporal regulation of T6SS assembly?

What is the signal that triggers sheath contraction?

What structural reorganization does the baseplate undergo?

What is the fate of the baseplate and membrane complex after contraction?

What are the main advantages of the unique mode of action of T6SS compared with other bacterial secretion systems?

Translocation of Hcp and VgrG between live cells was imaged indirectly [64]; however, with progress on labeling and imaging techniques we might expect even more components to be visualized directly. Importantly, imaging of T6SS dynamics will enlighten our understanding of related contractile nanomachines, which are often too small to be visualized by fluorescence microscopy.

Future research will unravel additional strategies that contractile nanomachines utilize to puncture membranes and will show how these sophisticated tools can be used for a wide variety of functions. While many questions remain (see Outstanding Questions), with a better understanding of the principles behind their assembly and mode of action we could begin designing new systems for efficient delivery of macromolecules into target cells. This may be helpful for treating infectious diseases [4,65] or triggering signaling cascades in eukaryotic cells [66] for various therapeutic purposes.

References

1. Leiman, P.G. and Shneider, M.M. (2012) Contractile tail machines of bacteriophages. *Adv. Exp. Med. Biol.* 726, 93–114
2. Yap, M.L. and Rossmann, M.G. (2014) Structure and function of bacteriophage T4. *Future Microbiol.* 9, 1319–1327
3. Ge, P. *et al.* (2015) Atomic structures of a bactericidal contractile nanotube in its pre- and postcontraction states. *Nat. Struct. Mol. Biol.* 22, 377–382
4. Gebhart, D. *et al.* (2015) A modified R-type bacteriocin specifically targeting *Clostridium difficile* prevents colonization of mice without affecting gut microbiota diversity. *mBio* 6, e02368-14
5. Kageyama, M. *et al.* (1964) Studies of a pyocin. III. Biological properties of the pyocin. *J. Biochem.* 55, 59–64
6. Nakayama, K. *et al.* (2000) The R-type pyocin of *Pseudomonas aeruginosa* is related to P2 phage, and the F-type is related to lambda phage. *Mol. Microbiol.* 38, 213–231
7. Yang, G. *et al.* (2006) *Photorhabdus* virulence cassettes confer injectable insecticidal activity against the wax moth. *J. Bacteriol.* 188, 2254–2261
8. Heymann, J.B. *et al.* (2013) Three-dimensional structure of the toxin-delivery particle antifeeding prophage of *Serratia entomophila*. *J. Biol. Chem.* 288, 25276–25284
9. Shikuma, N.J. *et al.* (2014) Marine tubeworm metamorphosis induced by arrays of bacterial phage tail-like structures. *Science* 343, 529–533
10. Mougous, J.D. *et al.* (2006) A virulence locus of *Pseudomonas aeruginosa* encodes a protein secretion apparatus. *Science* 312, 1526–1530
11. Pukatzki, S. *et al.* (2006) Identification of a conserved bacterial protein secretion system in *Vibrio cholerae* using the *Dictyostelium* host model system. *Proc. Natl. Acad. Sci. U. S. A.* 103, 1528–1533
12. Alcoforado Diniz, J. *et al.* (2015) Molecular weaponry: diverse effectors delivered by the Type VI secretion system. *Cell. Microbiol.* 17, 1742–1751
13. Durand, E. *et al.* (2014) VgrG, Tae, Tle, and beyond: the versatile arsenal of Type VI secretion effectors. *Trends Microbiol.* 22, 498–507
14. Hachani, A. *et al.* (2016) Type VI secretion and anti-host effectors. *Curr. Opin. Microbiol.* 29, 81–93
15. Leiman, P.G. *et al.* (2010) Morphogenesis of the T4 tail and tail fibers. *Virol. J.* 7, 355
16. Schwarzer, D. *et al.* (2012) A multivalent adsorption apparatus explains the broad host range of phage phi92: a comprehensive genomic and structural analysis. *J. Virol.* 86, 10384–10398
17. Taylor, N.M.I. *et al.* (2016) Structure of the T4 baseplate and its function in triggering sheath contraction. *Nature* 533, 346–352
18. Shneider, M.M. *et al.* (2013) PAAR-repeat proteins sharpen and diversify the Type VI secretion system spike. *Nature* 500, 350–353
19. Yap, M.L. *et al.* (2016) Role of bacteriophage T4 baseplate in regulating assembly and infection. *Proc. Natl. Acad. Sci. U. S. A.* 113, 2654–2659
20. Pukatzki, S. *et al.* (2007) Type VI secretion system translocates a phage tail spike-like protein into target cells where it cross-links actin. *Proc. Natl. Acad. Sci. U. S. A.* 104, 15508–15513
21. Leiman, P.G. *et al.* (2009) Type VI secretion apparatus and phage tail-associated protein complexes share a common evolutionary origin. *Proc. Natl. Acad. Sci. U. S. A.* 106, 4154–4159
22. Kanamaru, S. *et al.* (2002) Structure of the cell-puncturing device of bacteriophage T4. *Nature* 415, 553–557
23. Lossi, N.S. *et al.* (2011) Structure–function analysis of HsiF, a gp25-like component of the Type VI secretion system, in *Pseudomonas aeruginosa*. *Microbiology* 157, 3292–3305
24. Brunet, Y.R. *et al.* (2015) The Type VI secretion TssEFGK–VgrG phage-like baseplate is recruited to the TssJLM membrane complex via multiple contacts and serves as assembly platform for tail tube/sheath polymerization. *PLoS Genet.* 11, e1005545
25. Thomassen, E. *et al.* (2003) The structure of the receptor-binding domain of the bacteriophage T4 short tail fibre reveals a knitted trimeric metal-binding fold. *J. Mol. Biol.* 331, 361–373
26. Durand, E. *et al.* (2015) Biogenesis and structure of a Type VI secretion membrane core complex. *Nature* 523, 555–560
27. English, G. *et al.* (2014) Biochemical analysis of TssK, a core component of the bacterial Type VI secretion system, reveals distinct oligomeric states of TssK and identifies a TssK–TssFG subcomplex. *Biochem. J.* 461, 291–304
28. Zoued, A. *et al.* (2013) TssK is a trimeric cytoplasmic protein interacting with components of both phage-like and membrane anchoring complexes of the Type VI secretion system. *J. Biol. Chem.* 288, 27031–27041
29. Pell, L.G. *et al.* (2009) The phage lambda major tail protein structure reveals a common evolution for long-tailed phages and the Type VI bacterial secretion system. *Proc. Natl. Acad. Sci. U. S. A.* 106, 4160–4165
30. Zheng, J. and Leung, K.Y. (2007) Dissection of a Type VI secretion system in *Edwardsiella tarda*. *Mol. Microbiol.* 66, 1192–1206
31. Silverman, J.M. *et al.* (2013) Haemolysin coregulated protein is an exported receptor and chaperone of Type VI secretion substrates. *Mol. Cell* 51, 584–593
32. Whitney, J.C. *et al.* (2014) Genetically distinct pathways guide effector export through the Type VI secretion system. *Mol. Microbiol.* 92, 529–542
33. Arisaka, F. *et al.* (1979) Reassembly of the bacteriophage T4 tail from the core–baseplate and the monomeric sheath protein P18: a co-operative association process. *J. Mol. Biol.* 132, 369–386
34. Tschopp, J. *et al.* (1979) Purification, characterization and reassembly of the bacteriophage T4D tail sheath protein P18. *J. Mol. Biol.* 128, 247–258

35. Brunet, Y.R. *et al.* (2014) Type VI secretion and bacteriophage tail tubes share a common assembly pathway. *EMBO Rep.* 15, 315–321
36. Kapitein, N. *et al.* (2013) ClpV recycles VipA/VipB tubules and prevents non-productive tubule formation to ensure efficient Type VI protein secretion. *Mol. Microbiol.* 87, 1013–1028
37. Bönemann, G. *et al.* (2009) Remodelling of VipA/VipB tubules by ClpV-mediated threading is crucial for Type VI protein secretion. *EMBO J.* 28, 315–325
38. Kube, S. *et al.* (2014) Structure of the VipA/B Type VI secretion complex suggests a contraction-state-specific recycling mechanism. *Cell Rep.* 8, 20–30
39. Moody, M.F. (1967) Structure of the sheath of bacteriophage T4. I. Structure of the contracted sheath and polysheath. *J. Mol. Biol.* 25, 167–200
40. Poglazov, B.F. *et al.* (1999) Polymerization of bacteriophage T4 tail sheath protein mutants truncated at the C-termini. *J. Struct. Biol.* 127, 224–230
41. Abuladze, N.K. *et al.* (1994) Tail length determination in bacteriophage T4. *Virology* 199, 301–310
42. Ghequire, M.G.K. *et al.* (2015) Different Ancestries of R tailocins in rhizospheric *Pseudomonas* isolates. *Genome Biol. Evol.* 7, 2810–2828
43. Rybakova, D. *et al.* (2015) Afp14 is involved in regulating the length of anti-feeding prophage (Afp). *Mol. Microbiol.* 96, 815–826
44. Basler, M. and Mekalanos, J.J. (2012) Type 6 secretion dynamics within and between bacterial cells. *Science* 337, 815
45. Basler, M. *et al.* (2012) Type VI secretion requires a dynamic contractile phage tail-like structure. *Nature* 483, 182–186
46. Aksyuk, A.A. *et al.* (2009) The tail sheath structure of bacteriophage T4: a molecular machine for infecting bacteria. *EMBO J.* 28, 821–829
47. Aksyuk, A.A. *et al.* (2011) Structural conservation of the myoviridae phage tail sheath protein fold. *Structure* 19, 1885–1894
48. Clemens, D.L. *et al.* (2015) Atomic structure of T6SS reveals interlaced array essential to function. *Cell* 160, 940–951
49. Kudryashev, M. *et al.* (2015) Structure of the Type VI secretion system contractile sheath. *Cell* 160, 952–962
50. Douzi, B. *et al.* (2016) Structure and specificity of the Type VI secretion system ClpV–TssC interaction in enteroaggregative *Escherichia coli*. *Sci. Rep.* 6, 34405
51. Förster, A. *et al.* (2014) Coevolution of the ATPase ClpV, the sheath proteins TssB and TssC, and the accessory protein TagJ/HsiE1 distinguishes Type VI secretion classes. *J. Biol. Chem.* 289, 33032–33043
52. Shalom, G. *et al.* (2007) *In vivo* expression technology identifies a Type VI secretion system locus in *Burkholderia pseudomallei* that is induced upon invasion of macrophages. *Microbiology* 153, 2689–2699
53. Zoued, A. *et al.* (2016) Priming and polymerization of a bacterial contractile tail structure. *Nature* 531, 59–63
54. Planamente, S. *et al.* (2016) TssA forms a gp6-like ring attached to the Type VI secretion sheath. *EMBO J.* 35, 1613–1627
55. Fokine, A. *et al.* (2013) The molecular architecture of the bacteriophage T4 neck. *J. Mol. Biol.* 425, 1731–1744
56. Pell, L.G. *et al.* (2009) The X-ray crystal structure of the phage lambda tail terminator protein reveals the biologically relevant hexameric ring structure and demonstrates a conserved mechanism of tail termination among diverse long-tailed phages. *J. Mol. Biol.* 389, 938–951
57. Moody, M.F. (1973) Sheath of bacteriophage T4. 3. Contraction mechanism deduced from partially contracted sheaths. *J. Mol. Biol.* 80, 613–635
58. Zheng, J. *et al.* (2011) Genetic analysis of anti-amoebae and anti-bacterial activities of the Type VI secretion system in *Vibrio cholerae*. *PLoS One* 6, e23876
59. Gerc, A.J. *et al.* (2015) Visualization of the *Serratia* Type VI secretion system reveals unprovoked attacks and dynamic assembly. *Cell Rep.* 12, 2131–2142
60. Pietrosiuk, A. *et al.* (2011) Molecular basis for the unique role of the AAA+ chaperone ClpV in Type VI protein secretion. *J. Biol. Chem.* 286, 30010–30021
61. Chang, Y.-W. *et al.* (2014) Correlated cryogenic photoactivated localization microscopy and cryo-electron tomography. *Nat. Methods* 11, 737–739
62. Farley, M.M. *et al.* (2016) Minicells, back in fashion. *J. Bacteriol* 198, 1186–1195
63. Oikonomou, C.M. and Jensen, G.J. (2016) A new view into prokaryotic cell biology from electron cryotomography. *Nat. Rev. Microbiol.* 14, 205–220
64. Vettiger, A. and Basler, M. (2016) Type VI secretion system substrates are transferred and reused among sister cells. *Cell* 167, 99–110 e12
65. Ritchie, J.M. *et al.* (2011) An *Escherichia coli* O157-specific engineered pyocin prevents and ameliorates infection by *E. coli* O157:H7 in an animal model of diarrheal disease. *Antimicrob. Agents Chemother.* 55, 5469–5474
66. Shikuma, N.J. *et al.* (2016) Stepwise metamorphosis of the tubeworm *Hydroides elegans* is mediated by a bacterial inducer and MAPK signaling. *Proc. Natl. Acad. Sci. U. S. A.* 113, 10097–10102
67. Kostyuchenko, V.A. *et al.* (2005) The tail structure of bacteriophage T4 and its mechanism of contraction. *Nat. Struct. Mol. Biol.* 12, 810–813
68. Fokine, A. *et al.* (2007) Cryo-EM study of the *Pseudomonas* bacteriophage phiKZ. *Structure* 15, 1099–1104
69. Chang, Y.W. *et al.* (2017) In vivo structures of an intact type VI secretion system revealed by electron cryotomography. *EMBO Rep.* e201744072